ELECTRICALLY SMALL
HIGH-TEMPERATURE SUPERCONDUCTING Y-Ba-Cu-O
MEANDER DIPOLE ANTENNAS
FOR SPACE-LIMITED APPLICATIONS

by

MAZLINA ESA

A thesis submitted to the Faculty of Engineering
of The University of Birmingham
for the degree of
DOCTOR OF PHILOSOPHY

School of Electronic and Electrical Engineering
University of Birmingham
Edgbaston
Birmingham
B15 2TT
England

August 1996

SYNOPSIS

Two sets of electrically small antennas in the form of coplanar meander dipoles have been designed and tested in this study. The meander dipoles are the anti-symmetrical and the symmetrical meander structures. Both sets were based on the 1.0 GHz linear half-wavelength dipole, i.e., all the meander dipole antennas have equal total arm lengths of 150.0 mm. Each set consists of several antennas, with different number of meander sections. The anti-symmetrical meander antennas were fabricated from copper (on RT/duroid substrate) whilst the symmetrical meander antennas were fabricated from copper, thick- and thin-film high temperature superconducting (HTS) materials. The first type of meander antennas was fed from underneath the circuit, through the substrate. The meander antennas are electrically small. However, as the physical size decreases, the frequency of operation increases resulting in an electrical size increase. The antennas were found to be inefficient, which is inherent to their small size. In addition, the far-field radiation pattern was close to that of a short dipole. Although they are inefficient as compared with large antennas, they can potentially have increased gain and increased efficiency with the use of superconducting material. This potential has been demonstrated by the second design, even though they have much smaller electrical and physical size. Coplanar strip (CPS) feeding line was employed to help reduce radiation pattern distortion. No matching network was designed because the antennas are reasonably well-matched to the input. Instead, a quarter-wavelength sleeve balun was incorporated to reduce the feeding loss and stray radiation. It also behaves as a matching network. The HTS symmetrical meander antennas were found to outperform the corresponding copper structures in terms of gain and efficiency. They also exhibit the supergain ratio in the range 10 to 45 over the corresponding copper structures. The symmetrical meander antennas operate at almost the same frequency as that of a linear half-wavelength dipole which has the same track length. This shows that the linear dipole can be miniaturised by meandering its radiating structure, whilst maintaining the frequency of operation. Numerical simulations were also done on all the designed antennas. The suitability of the HTS meander antennas for space-limited applications has been demonstrated.

kesyukuran hanya sanya kepada Rabb alam semesta yang sempurna ini

terima kasih kepada seluruh keluarga dan sahabat handai

semuga semua amal kita diredhaiNya

ACKNOWLEDGEMENTS

I would like to thank Dr M. J. Lancaster for giving such a wonderful guidance throughout the work done in preparation of this dissertation. I would also like to extend my gratitude to Dr L. P. Ivrissimtzis (now at COMSAT RSI, CSA Antenna Systems, Kent) for being such a great help. I am also grateful to Dr F. Huang for his valuable assistance especially during the second year of this study. Stimulating discussion sessions spent with Dr J. S. Hong, Prof. P. S. Hall, Dr C. C. Constantinou and Dr D. G. Checketts are greatly appreciated. Much thank to all members of the Superconductivity Group and the previous COPS group; for their co-operation and worthy help.

In addition, I would like to thank the Universiti Teknologi Malaysia, Malaysia, and the Malaysian Government for approving my study-leave and sponsoring my studies.

CONTENTS PAGE

CHAPTER 1 INTRODUCTION

1.0 OBJECTIVES AND SCOPE OF STUDY

The purpose of this study is to develop a practical printed electrically small antenna made of high-temperature superconducting (HTS) material. HTS materials have low loss characteristics superior to conventional conductors such as silver and copper. The use of superconductors in the antenna construction does not predominantly affect their radiation characteristics in terms of radiation pattern and directivity. This implies that the antenna radiation resistance and external reactance are independent of the conducting material. The material will, however, affect the input impedance, radiation efficiency and bandwidth of particular types of antennas.

The advantageous characteristics of HTS antennas include small size, directive radiation pattern in a small antenna, integrated low-loss matching, improved efficiency and improved gain. It is useful to develop a planar antenna structure which can be flatly mounted onto any body surface. For example, an antenna may have to be placed on the side of an aircraft, where no protrusions are allowed. This antenna will then have a broadside radiation pattern. Antenna miniaturisation has future potential since demands for small antennas have been increasing in order to fulfil various specifications such as limited space and portable equipment.

The objective of this study is to develop an electrically small HTS antenna with the following characteristics and features:

- high gain and high efficiency
- dual-broadside E-plane radiation pattern
- operational frequency in the region 1 to 10 GHz
- integrated low-loss matching and balun
- planar structure

This dissertation reports the work done on several small antennas as shown in Fig. 1.1. Experimental work and numerical simulations on anti-symmetrical meander dipoles of Fig. 1.1(a) were carried out. The geometry of all three generic antenna types in Fig. 1.1(a) has been altered to produce the required performance. A dipole of the same axial length was also built and tested for comparison to these meander dipoles. A second set of symmetrical generic meander dipoles similar to Fig. 1.1(a) was also designed and fabricated. The first structure is illustrated in Fig. 1.1(b). A complete set of copper antennas has been fabricated and tested. In addition, one thick-film HTS antenna and a set of thin-film HTS antennas were also fabricated and tested. Experimental as well as numerical simulation results will be presented and discussed. The performance of these two sets of meander dipole antennas is then compared.

Altogether there are twenty-nine different antennas built and tested as transmitters in this work. A linear half-wavelength dipole was used as the receiver in the transmission and radiation pattern measurements. Full *S*-parameter and radiation pattern measurements were performed on all the designed antennas.

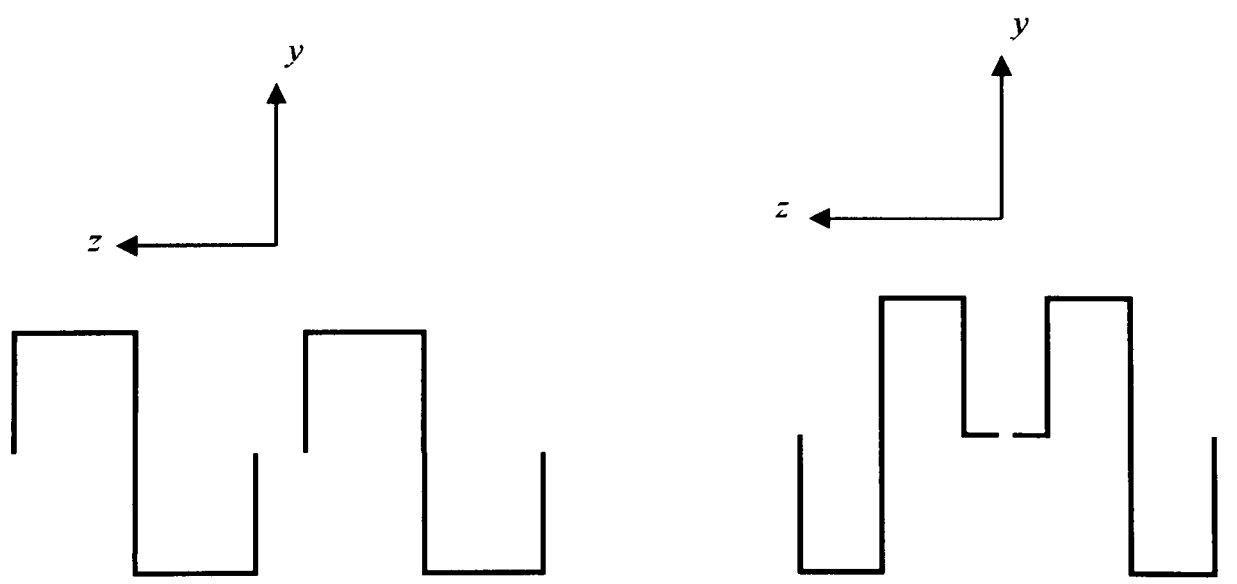

(a) (b)

Fig. 1.1. Designed antenna circuits: (a) anti-symmetrical meander dipole, b) symmetrical meander dipole.

The rest of Chapter 1 discusses the relevant available literature on small antennas and work on meander antennas. A short discussion of low-temperature small superconducting antenna designs before 1986 is also presented.

Chapter 2 presents antenna properties related to this study. This includes discussion of radiation pattern, directivity and gain, input impedance, matching networks, efficiency and bandwidth. This is followed by a section devoted specially on small antennas. The last section of this chapter discusses several forms of dipole antennas related to this study.

In-depth discussion of superconducting antennas is made in Chapter 3. A review of superconductivity is initially given. This chapter then discusses two important parameters that determines the quality of a superconducting material for practical antenna applications, that is, the surface impedance and penetration depth. This is followed by the discussion of the surface impedance of superconducting films with finite thickness. Recent work on HTS small antennas is then discussed. A brief discussion of HTS matching networks ends the chapter.

Chapter 4 discusses the antenna gain, efficiency and radiation pattern measurement methods.

Details of all the antenna designs are laid out in Chapter 5. This chapter discusses the antenna design procedures as well as presenting all the physical geometry's. The underlying design principles are also presented. This is followed by a discussion of matching networks and baluns.

Chapter 6 discusses the numerical simulations used for all the designed and tested antennas. Some examples of the simulated results are presented.

Chapter 7 initially discusses the materials involved and the fabrication techniques carried out. Suitable cables and connectors involved in the measurements are also presented.

A discussion of the experimental set-up begins Chapter 8. This is followed by a detailed presentation of the experimental and numerical simulation results. These results are then discussed in depth.

Finally, conclusion and recommendations for future developments are laid down in Chapter 9.

1.1 SMALL ANTENNAS

This section reviews the available literature on small antennas before 1980. Literature on antennas can be found in many textbooks such as references [1] to [3]. However, there has been little extensive experimental work done on small antennas. This could be due to the fact that smaller antennas are generally less efficient, especially for wideband operation. Background design theory on small antennas are confined to numerical methods. Researchers tend to use quantitative analysis such as Method of Moments to predict their proposed design performances, for instance references [4] to [9].

The work of small antennas dates back as early as 1947 when Wheeler [10] discussed the radiation power factor of capacitor and inductor radiators of equal volume. Radiation power factor is descriptive of the radiation of real power from a small antenna taking a much larger value of reactive power. In this work, the fundamental limits of antennas whose maximum dimension is less than the radianlength, i.e., $1/2\pi$ of the wavelength, was also defined. It was pointed out that such a small antenna behaves essentially as a dipole with a coaxial doughnut radiation pattern.

In 1948, Chu [11] presented a more generalised work on physical limitations of omni-directional antennas. He determined the optimum performance of an antenna in free space and the corresponding relation between its gain and the bandwidth of the input impedance under various criteria. The field outside a sphere enclosing the omni-directional antenna can be described by spherical wave functions. Due to their orthogonal properties, this spherical waves can be replaced by a number of independent equivalent circuits. A

minimum Q-factor which can be achieved from omnidirectional antennas in relation to their volume was quantified. These results can be applied to small antenna structures. It was found that antennas which generated an infinitesimally small dipole fields have the smallest possible Q of all possible antenna types, with a gain of 1.5. This corresponds to potentially having the broadest bandwidth. This analysis gave a useful worst case expression for Q. However, antenna losses were not accounted for.

Based on Chu's work, Harrington [12] developed a formula for the maximum gain of antennas in terms of their size. Formulas for the relationship between beamwidth and sidelobe level were also derived.

Harrington [13] extended Chu's analysis by including ohmic loss effects on antenna Q-factor for an idealised lossy metal sphere. This is the simplest antenna case since the wave functions are orthogonal over its surface. It was noted that if higher gain is desired, the antenna must necessarily be a narrowband device. Further, it was pointed out that small antennas are potentially supergain antennas.

Harrington's work, however, does not account for matching circuit losses. Wheeler [10] had already pointed out that these losses can significantly affect overall system performance. Also Smith [14] had laid down basic rules for matching circuits design using dissipative elements.

Wheeler [15] presented further basic concepts and rules of small antennas as was discussed in his earlier 1947 paper. He suggested the use of the fact that for an electrically small antenna, assumed centred at the origin of a spherical coordinate system, the near field is to a good approximation confined to the interior of the radiansphere. The concept of "radiation shield" was proposed. The purpose of this shield is to avoid radiation of power while leaving the inherent dissipation in the resonant circuit of a small antenna. Its shape and size are not critical but the theoretical ideal is a radiansphere. The essence of this method is to remove the radiation resistance of an antenna under test from its input impedance by enclosing it within a conducting shell and thereby preventing radiation. This method is very simple and convenient. However, its serious limitation at lower frequencies is that the size

of the required radiation shield becomes impractically large. The radiation shield concept is very useful in evaluating power efficiency of the useful radiation. It was emphasised that for any antenna configuration, the efficiency and/or bandwidth is ultimately limited by size.

Later Wheeler [16] further elaborated the radiation shield concept. It was proposed that a "small" antenna is one somewhat smaller than the radiansphere, i.e., a sphere of radius equals its radianlength, but it has a "sphere of influence" occupying the radiansphere. The power that theoretically can be intercepted by a hypothetical isotropic antenna is that which flows through the radiansphere or its cross-section, the "radiancircle".

Recently, McLean [17] re-examined the fundamental limits on the radiation Q of electrically small antennas discussed earlier by Chu [11] and Harrington [13]. McLean obtained an exact formulation of the minimum attainable radiation Q of a linearly polarised antenna. The formulation agrees with that obtained by Chu and Harrington at the lower limit. However, at the higher limit, the formulations differ by a factor of 4/3. This is an interesting finding, since the design of antennas whose electrical size are closer to the higher limit, can be more accurately catered for.

Other work related to small antennas (made from normal conductors) before 1980 deal with efficiency measurements. These will be reviewed next. The different methods of determining the radiation efficiency of antennas are further discussed in Section 4.2.

The method [16] was used by Newman *et al.* [18] together with their proposed Q-method on electrically small antennas, specifically multiturn loop antennas. These two methods were compared, due to their principal advantages of being quick and easy to apply. Also, both relate the antenna efficiency to the input impedance rather than a far-field pattern integration. Two methods were used to define accuracy limits of the Wheeler method. It was found that Wheeler's method accurately predicts the relative efficiencies of two designed antennas and it also yields a reasonable approximation to the absolute efficiency, for variable frequency operation. Both methods were found to have accurately predicted relative changes in efficiency and to a lesser extent absolute efficiency.

Crowley [19] devised a method for determining antenna efficiency in 1953. It was claimed that this method is simple, requires no special equipment, indoors measurements can be made and measurements can also be made over a band of frequencies. This method employs two diffferent antennas which are geometrically identical but constructed of metals with different conductivities and surface resistivities, one of which is the antenna under test. These antennas can also be made as scaled models. From ratios measurements antenna efficiency can be obtained.

An adaptation of Crowley's method to antennas with well-defined set of terminals, a resistance-comparison method was proposed and performed on multiturn loop antennas by Flaig [20] in 1968. He agreed that this technique is capable of reducing the problem of site-errors, i.e., reflections at the walls of the anaechoic chamber and the support structure, that influenced the field intensity. These problems are particularly troublesome below 150 MHz. In the Flaig development, a tacit assumption used was that the antenna input resistance can be adequately represented as series loss-radiation resistances. By having exactly geometrically identical antennas with the same radiation patterns, these site-error problems can be eliminated. Flaig concluded that this is a practical method especially at frequencies below 100 MHz.

Smith [21] discussed the radiation efficiency of electrically small multiturn loop antennas. Multiturn structures were chosen since these structures were often employed to increase the radiation efficiency. Smith's results confirmed that the proximity effect contributes to making accurate calculations of the radiation efficiency, particularly for loops whose efficiencies are below ten percent.

Smith considered both the antenna and its matching network [14] in which the principle of conservation of energy was applied. Further analysis on overall antenna system performance was made. The antenna system was composed of the antenna and its matching network. It was noted that, in applications where electrically small antennas are necessary and transmitter power is limited, the system efficiency may be a critical factor in determining the feasibility of the system. The experimental examples on the cryogenic loop antenna and

the ferrite loaded loop antenna showed the importance of including the matching network in efficiency calculations for electrically small antennas. The cryogenic loop antenna was previously discussed by Hoang and Fournier [22] where cooling was proposed as a method to improve radiation efficiency and the signal-to-noise of electrically small antennas. The ferrite loaded loop antenna was proposed by Weeks [23] for increasing the radiation efficiency.

Smith [24] analysed the Wheeler's method by formulating a model problem to evaluate its accuracy. Initially, the available four methods for determining antenna efficiency; namely the pattern integration method, the Q-factor method, the resistance-comparison method and the Wheeler's cap method, were reviewed. Wheeler method was chosen in this particular work for its attractive feature of being easy to implement in practice, requiring only two measurements of the input resistance. It was concluded that this method can be quite accurate for shields with dimensions a substantial fraction of a wavelength and provided that the antenna under test is not operated near a critical point like at antiresonance. The shield conductivity does not have to be very high to produce accurate results. He also set guidelines for its applications.

Four fundamental limitations in antennas were discussed by Hansen [25] in 1981. These were in the categories of electrically small antennas, superdirective antennas, super-resolution antennas and high-gain antennas. These limitations exhibit a steeply rising cost with performance. Hence, operation beyond the robust region is often desirable. In electrically small antennas, the bandwidth or Q varies with size. These antennas were analysed via spherical mode theory with the antenna enclosed in a virtual sphere. A minimum Q exists that varies inversely with the cube of sphere radius, when the radius is much less than the radianlength. This limits the achievable bandwidth for a given antenna size. The results of Harrington's analysis [13] that involved ohmic loss effects on the antenna Q-factor for an idealised lossy metal sphere, were also presented. The trade-off between efficiency and Q-factor for this particular antenna was clearly demonstrated. It was noted that the antenna bandwidth can be improved only if the antenna configuration utilizes efficiently the available volume within the minimum sphere that encloses the antenna. It was

also claimed that electrically small antennas are superdirective in nature and they exhibit the properties associated with superdirective antennas, that is, low radiation resistance and narrow bandwidth. Superdirective arrays have less than half-wavelength spacings between elements. For small spacings, a constraint is needed to limit factors such as Q, mechanical and electrical tolerances, sidelobes and efficiency [26], [27]. This can be obtained by expressing constrained directivity as a ratio of two Hermitian quadratic forms, for which a solution exists. Super-resolution was described as the production of an array pattern with one or more main beams that are appreciably narrower than the nominal Rayleigh resolution. Super-resolution arrays made use of maximum entropy processing. This improves spatial frequency resolution for short samples, analogous to spectral analysis processing. A power ratio expression as the fundamental super-resolution limit for the simplest case of two equal sources was also presented. In the final category, high-gain antennas are mainly large antennas. They exhibit high-gain due to large square wavelengths area and not due to superdirectivity. Hansen discussed only reflectors which are steerable in both directions and with achievable gain limited by their cost.

Wheeler [28] proposed a wide-band matching circuit which can maximise the poor matching efficiency of a small antenna. A special inverse-cubed frequency scale, which is used in describing the fundamental limitation on wide-band matching of a small antenna, was presented. This made use of a fixed reactive network. The matching efficiency is defined as the fraction of available power that is delivered through the matching network.

Hikada [29] clarified analytically that it is possible to realise an electrically small loop antenna capable of changing matching-frequency over a one octave frequency range, only by varying one variable capacitor. Good impedance matching at resonance frequencies is maintained throughout the range. The condition of no removal of the feed point location was used.

1.2 SMALL MEANDER ANTENNAS

Work on small modified or meander antennas made from normal metals was carried out by various researchers. Rashed and Tai [4] attempted a compact resonant antenna design without using lumped loading. A type of wire meander monopole antenna was proposed and results for reducing the antenna size were obtained. The design is as shown in Fig. 1.2(a). A reduction factor for a meander antenna was introduced. Impedance measurements were performed to understand the characteristics of meander antennas. Experimentally, it was found that as the number of sections per wavelength increases, its resonant frequency also increases. It was also found that when the width of rectangular loops increases, the reduction factor decreases, but the resonant resistance drops drastically. In order to maintain linear polarisation, this width has to be chosen to be small compared to the antenna length. A slow wave structure model was developed and used for the antenna as a basis to approximate analysis. Due to coupling between adjacent wire elements, numerical methods were used which gave precise formulation. A meander version of log-periodic dipole arrays and folded monopoles was also considered.

Later, Rashed and Tai [5] presented further work on a threefold resonant antenna, as depicted in Fig. 1.2(b), with considerable size reduction. The antenna was treated as a monopole with a distributed loading. The coupling between elements within the structure and the load contributed to a current distribution with a marked peak near the feeding point. This shape differs from that of a conventional monopole. It was found that antenna efficiency was affected only by the ohmic losses in the antenna wire. This was considered a clear advantage over the antennas with lumped loading. It was also found that the bandwidth is narrower compared with a conventional monopole but comparable to that of other size reduction techniques such as base loaded or top-loaded antennas. It was claimed that there is very little horizontal expansion of structure. This contributes to negligible undesirable radiation.

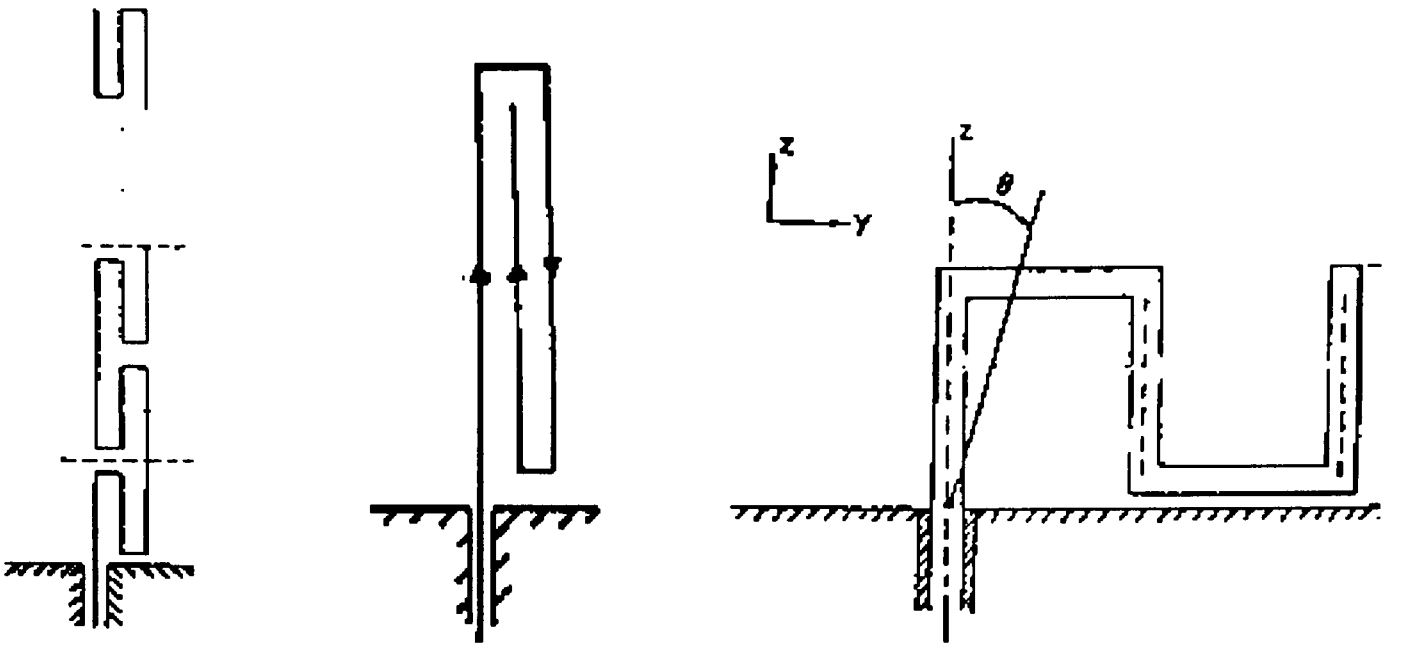

(a) (b) (c)

Fig. 1.2. Meander monopole antennas: (a) general structure [4], (b) threefold [5], (c) [7].

Rashed and Tai [6] extended the work on their first design [4] as shown in Fig. 1.2(a). Meander antennas were proposed as possible elements for size reduction. These antennas consist of continously folded wires intended to reduce the resonant length. It was found that size reduction increases as the wire radius decreases. It was concluded that for a constant wire length, there is a possibility of greater size reduction by increasing the width-to-wire radius ratio. The antennas introduced has size reduction in the resonant length typically from 25-40%. Efficiency is only affected by the ohmic losses in the wire, and there is negligible cross polarisation. More size reduction can be obtained by decreasing the wire radius or increasing the folded arms separation. With an increase in the number of meander sections, there is less size reduction introduced in return for an improved bandwidth. This is an interesting finding.

In another work, Rashed [7] studied further the characteristics of the meander line section of Fig. 1.2(c). The far-field components and further effect of the wire radius were considered. The transition from a simple meander monopole as a compact radiator to a meander line section was investigated. The measurements indicated that increasing the meander section width resulted in a drastic drop of the resistance at resonance. However, since the resonant frequency also diminished, that indicated a reduction in resonant length of the section when compared with a monopole at the same resonant frequency. A thickness

parameter was used to analyse the wire radius effect. Using numerical methods, it was verifed that with decreasing wire radius, the resonant frequency decreases, with improved size reduction. From the radiation point of view and for shortening antenna size, difference in reducing radius and increasing width is fundamental. Increasing the width results in cross-polarisation but this is not the case when decreasing the wire radius. It was found experimentally that a considerable increase in the meander section width ended up in field pattern asymmetry and undesirable radiation. However, for small width values, considerable size reduction of typically 40% can be achieved. It was concluded that although both methods gave smaller radiation resistance, a smaller wire radius is preferred for shortening the antenna even though the resonant frequency decreases. However, the penalty to be paid is a lower efficiency which is inherent to all small antennas.

Nakano *et al.* [8] investigated both numerically and experimentally, two cases of bent dipole antennas as shown in Fig. 1.3, in 1983. Effects of arm bend was considered as well as asymmetric feeding on dipole antennas. Firstly, a centre-fed half-wave bent dipole of Fig. 1.3(a). It was found that for right-angled bending, the dipole resonates with almost a pure resistance of 50 ohms. As bending angle is changed, the radiation pattern is essentially conserved, although polarisation plane inclination is observed. Secondly, an asymmetric-fed full-wave bent dipole of Fig. 1.3(b) was found to achieve a bidirectional beam of increased directivity. It was concluded that the arm bend served to reduce the input impedance to a desirable value which is easily matched to common coaxial cables. This work has the advantage of having direct feeds without the need of any matching network.

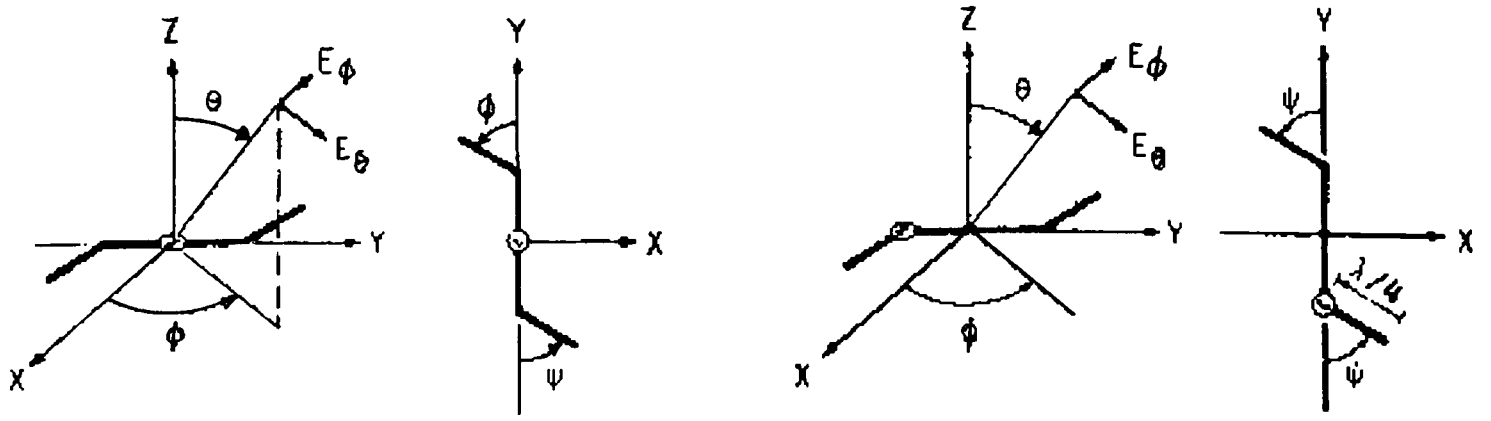

(a) (b)

Fig. 1.3. Bent dipole antennas [8]: (a) centre-fed half-wave (b) asymmetric-fed full-wave.

Nakano [9] then analysed numerically and experimentally two types of modified dipole antennas, namely the zig-zag (Fig. 1.4(a)) and the meander-line (Fig. 1.4(b)) types. This work concentrated on shortening the axial length, and a shortening ratio was defined. This was introduced earlier by Rashed [4] who used the term size reduction. Current distribution along the arm was determined by applying a simplified integral equation. Calculations of the input impedance, radiation pattern and absolute gain were made. The experimental radiation patterns of both antennas considered were found to be similar to that of a conventional half-wave linear dipole antenna. The zig-zag dipole resonated at the axial length of less than a self-resonant length of the half-wave linear dipole. The findings showed that the linear dipole can be miniaturised by changing the geometrical shape whilst still maintaining the radiation pattern.

(a) (b)

Fig. 1.4. Modified dipole antennas [9]: (a) zig-zag, (b) meander-line.

Another form of bent dipole antenna was designed by Parker and El-Sheikh [30]. These can be seen in Fig. 1.5. They designed a convoluted dipole array of frequency selective surfaces while retaining the cell dimensions. The axial length was kept constant. The total arm length was increased by convoluting (meandering). It was found that this produced a major reduction in the resonant frequency, giving a substantial improved stability at the same time. The optimum designs of these elements have yet to be explored. This includes the effect of the number of cycles and depths of the convolutions and their design forms. However it was also found that a three-cycled element (zig-zag) does not so effectively stabilise the transmission response.

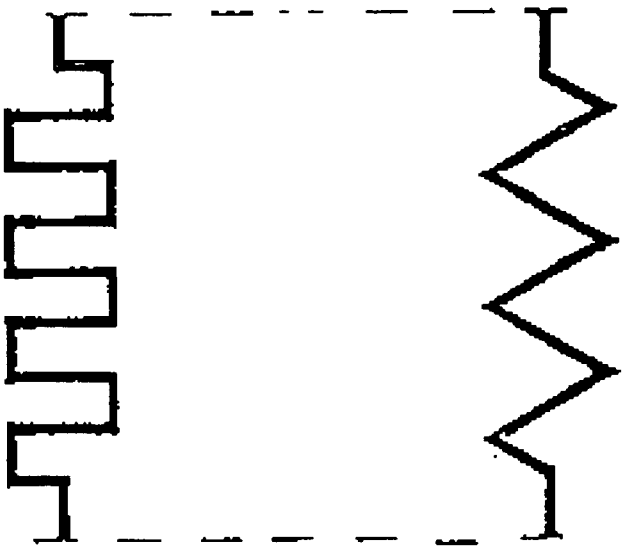

Fig. 1.5. Convoluted dipoles [30].

Other work on small antennas are related to several efficiency measurement methods. These will be discussed in-depth in Section 4.2. The discussion of high-temperature small superconducting antennas is given in Section 3.4.

1.3 LOW-TEMPERATURE SMALL SUPERCONDUCTING ANTENNAS

Earlier work on low-temperature electrically small superconducting antennas operating at the temperature of liquid helium showed that these antennas exhibit an increase in the radiation efficiency [31], [32].

Walker and Haden demonstrated a highly efficient electrically and physically small superconducting antenna [31]. The antenna configuration was in the form of a loop structure suspended through a ground plane and matched with a coaxial transmission cavity. Such configuration enabled the antenna characteristics to be predicted and controlled in an orderly fashion. Theoretical predictions were compared with experimental results, showing good agreement in the Q-factor and efficiency. They obtained a 27 dBm improvement in the power level of the received signal. They further concluded that one advantage of the system investigated is that it is effectively wideband, since the antenna can be excited at all the near-harmonics of the fundamental frequency of the cavity.

The above loop antenna design was extended by Walker *et al.* to form an array [32]. A good demonstration of a tremendous increase in the array efficiency was made. In the experiment, an 18.9% increase in efficiency was observed. This was pointed out to be due to the reduction in the matching circuit losses and the VSWR.

However, the increase in efficiency of the above loop array was at the expense of the bandwidth [33]. It was suggested that, in practice, the limit on reducing the length of an array is probably not significantly changed by use of superconductors.

CHAPTER 2

ANTENNA PROPERTIES

2.0 INTRODUCTION

This chapter initially discusses the standard definitions of various parameters that contribute to antenna performance. All italic text is taken from reference [34]. A short discussion of input impedance is then given. This is followed by a discussion of matching networks and formulations related to the radiation efficiency of the designed antennas. Discussions of bandwidth and of small antennas are then presented. Lastly, formulations related to the input impedance of the designed antenas are discussed. Related measurements are made in Chapter 4 whilst reference to the experimental set-up can be made in Chapter 8.

2.1 RADIATION PATTERN

An antenna radiation pattern is *a graphical representation of the radiation properties of the antenna as a function of space co-ordinates. In most cases, the radiation pattern is determined in the far-field region and is represented as a function of the directional co-ordinates. Radiation properties include radiation intensity, field strength, phase or polarisation.* This is usually in the form of a three-dimensional spatial distribution of radiated energy as a function of the observer's position along a constant radius. The pattern is measured on the surface of a constant radius sphere. The standard spherical co-ordinate system of Fig. 2.1 can be used to identify any position of the sphere.

This pattern in a representation of the radiation characteristics of the antenna as a function of the elevation or vertical angle, θ, and the azimuth or horizontal angle, ϕ. Generally, an antenna pattern is three-dimensional, but this is an impractical measurement. Hence, a number of two-dimensional patterns are adequate for the construction of a three-

dimensional pattern. Nevertheless, antenna performance is often described in terms of its two principal two-dimensional patterns, namely the orthogonal principal E- and H-plane patterns. For a linearly-polarised antenna, the E-plane pattern is defined as *the plane containing the electric-field vector and the direction of maximum radiation*; whilst the H-plane as *the plane containing the magnetic-field vector and the direction of maximum radiation*. In practice, most antennas are oriented so that at least one of the principal plane patterns coincide with one of the geometrical principal planes.

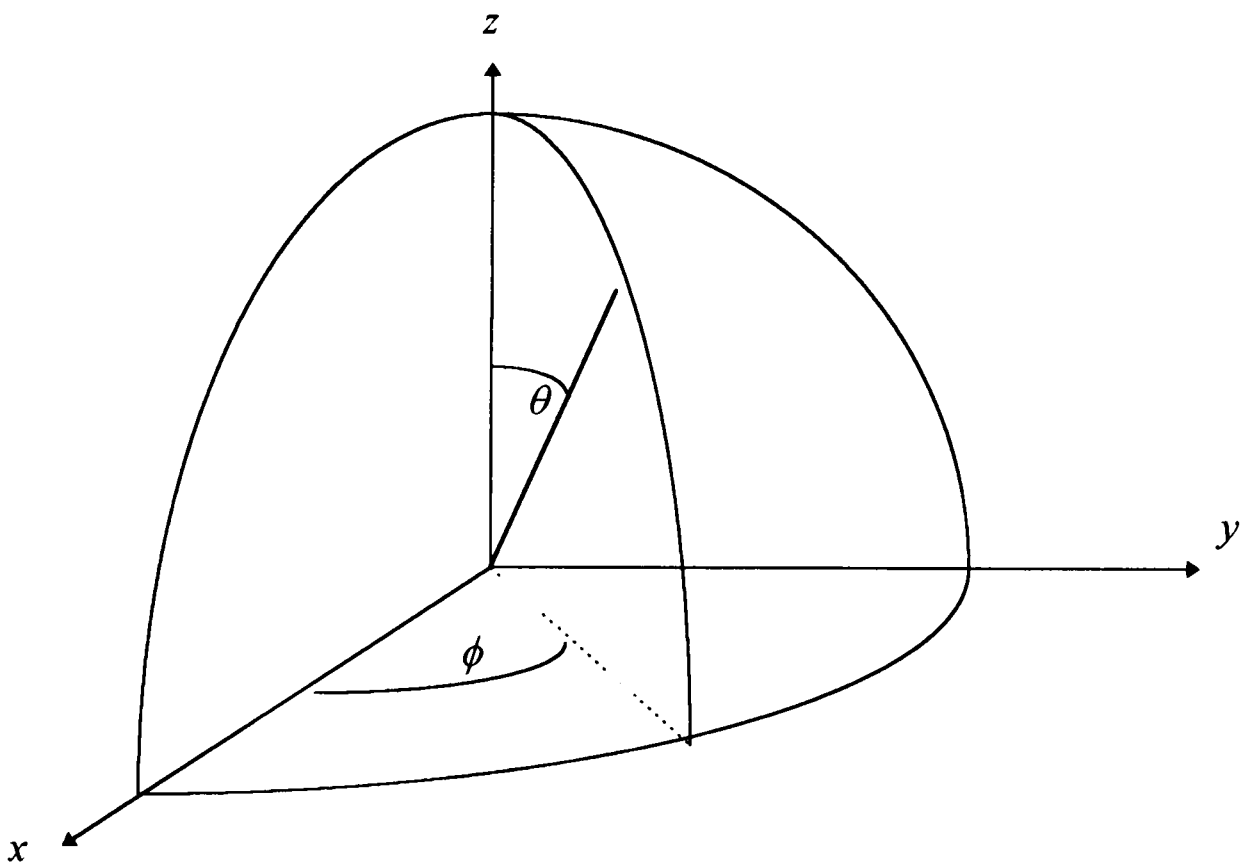

Fig. 2.1. Spherical co-ordinate system geometry.

A radiation pattern may contain parts known as lobes, which can be further sub-classified as major, minor, side and back lobes. The definitions are as follows :

(a) Radiation lobe : *portion of the radiation pattern bounded by regions of relatively weak radiation intensity.*

(b) Major lobe (also known as main beam) : *the radiation lobe containing the direction of maximum radiation.*

(c) Minor lobe : any lobe except the major lobe, usually represent undesirable radiation which should be minimised.

(d) Side lobe : *a radiation lobe in any direction other than the intended lobe*.

(e) Back lobe : a minor lobe occupying the hemisphere in a direction opposite to that of the major lobe.

From the major lobe, the half-power beamwidth (HPBW) can be obtained. The definition is, *in a plane containing the direction of the maximum of a beam, the angle between the two directions in which the radiation intensity is one-half the maximum value of the beam*. Though the term beamwidth is understood as the 3-dB beamwidth, one may use this term to describe the angle between any two points on the pattern. In this case, one has to state clearly the referred specific points in order to avoid confusion.

An example of illustration showing the linear power pattern plot with its associated lobes and beamwidth is given in Fig. 2.2.

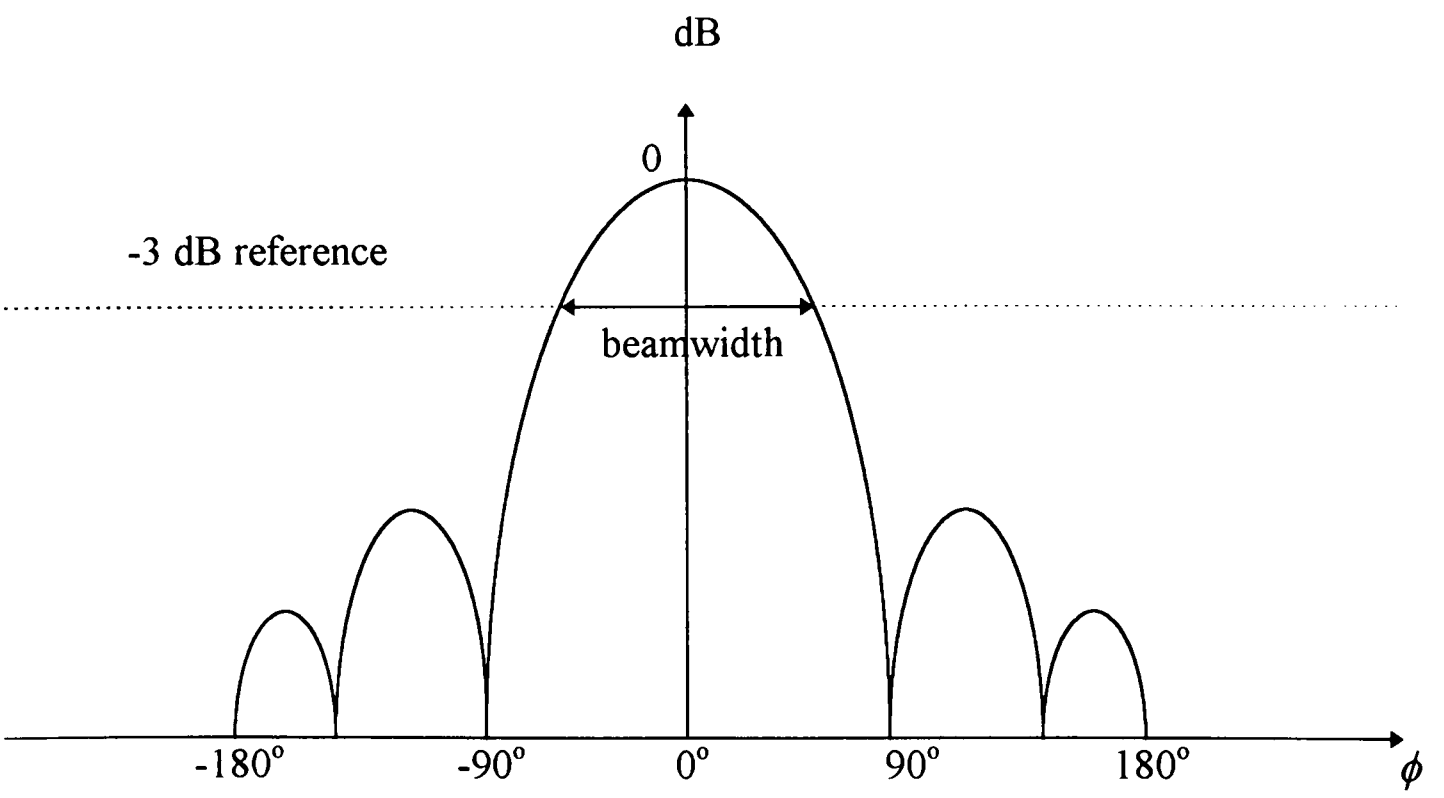

Fig. 2.2. An example of a power pattern linear plot.

There are three regions of space that surround an antenna; reactive near-field region, radiating near-field or Fresnel region and far-field or Fraunhofer region, as illustrated in Fig. 2.3. These regions are only meant to identify the field structure in each region.

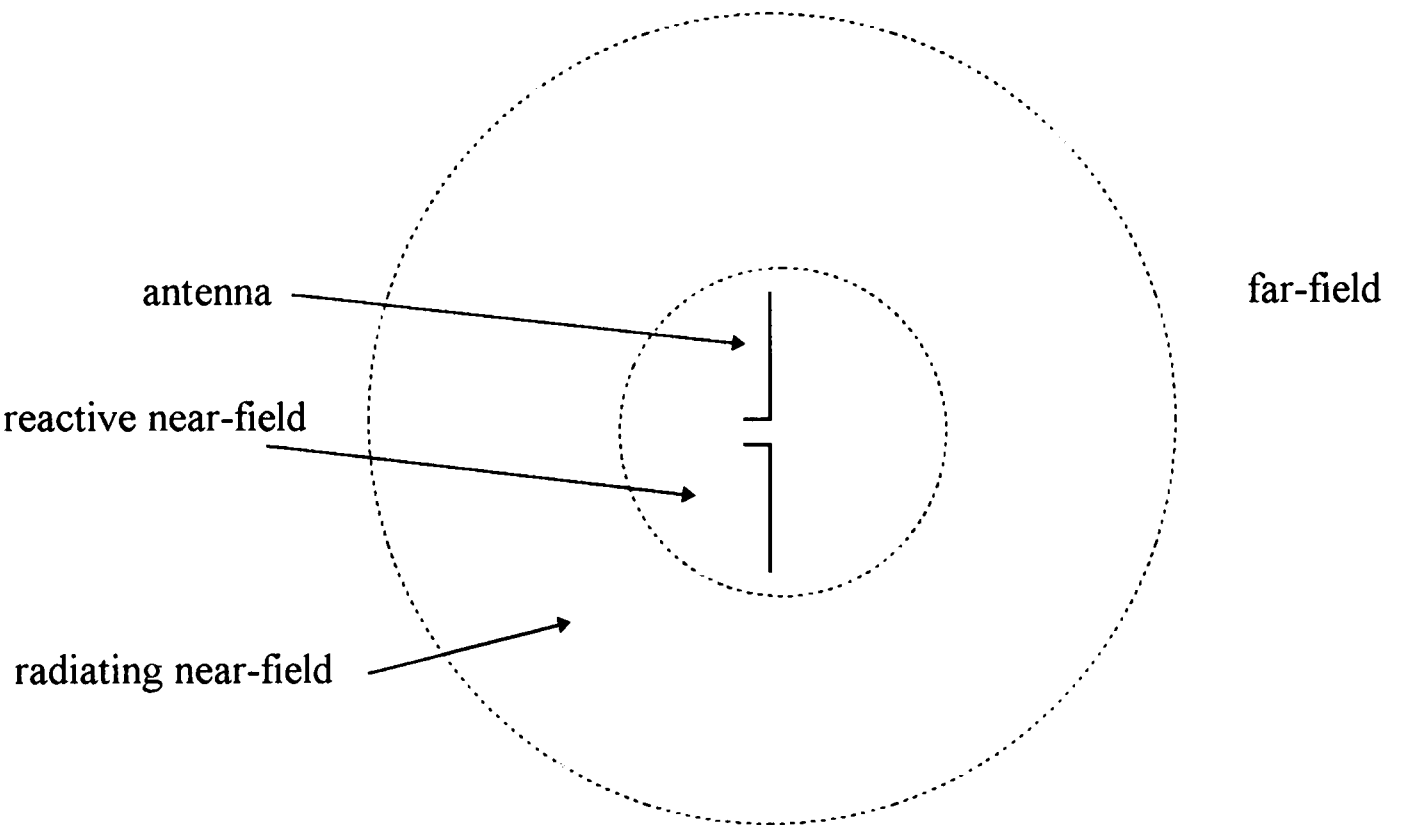

Fig. 2.3. Antenna field regions.

The definitions of the antenna field regions are listed below:

(a) reactive near-field region : *that region of the field immediately surrounding the antenna wherein the reactive field predominates.*

(b) radiating near-field region : *that region of the field of an antenna between the reactive near-field region and the far-field region wherein radiation fields predominate and wherein the angular field distribution is dependent upon the distance from the antenna. For an antenna focused at infinity, the radiating near-field region is sometimes referred to as the Fresnel region on the basis of analogy to optical terminology. If the antenna has a*

maximum overall dimension which is very small compared to the wavelength, this field region may not exist.

(c) far-field region : *that region of the field of an antenna where the angular field distribution is essentially independent of the distance from the antenna. If the antenna has a maximum overall dimension* d_m , *the far-field region is commonly taken to exist at distances greater that* $2d_m^2/\lambda$ *from the antenna,* λ *being the wavelength. For an antenna focused at infinity, the far-field region is sometimes referred to as the Fraunhofer region on the basis of analogy to optical terminology.*

In a given direction, radiation intensity is *the power radiated from an antenna per unit solid angle*. This is simply

$$U = r^2 W_{rad} \tag{2.1}$$

where U is the radiation intensity in watts per unit solid angle, r is the distance and W_{rad} is the radiation density in watts per square meter. A solid angle is measured in steradian (or sr), one steradian being the solid angle with its vertex at the centre of a sphere of radius r that is subtended by a spherical surface area equal to that of a square with each side of length r. A closed sphere has a solid angle of 4π steradians.

The power pattern discussed earlier is also a measure of the radiation intensity. The total power radiated by an antenna can be obtained by integrating the radiation intensity in eqn. (2.1), over the entire sphere solid angle, as follows

$$P_{rad} = \oint_{\Omega} U \, d\Omega = \int_0^{2\pi} \int_0^{\pi} U \sin\theta \, d\theta \, d\phi \tag{2.2}$$

where $d\Omega$ is the element solid angle.

2.2 DIRECTIVITY AND GAIN

Directivity is *the value of the directive gain in the direction of its maximum value*. It is a measure describing only the antenna directional properties. For a nonisotropic source, its directivity is equal to the ratio of its maximum radiation intensity over that of an isotropic source. The directive gain in a given direction is *the ratio of the radiation intensity in that direction to the radiation intensity of a reference antenna*, where an isotropic source being taken as the reference antenna. This isotropic source radiates in all directions.

We can write [1], [3]

$$D_g = \frac{U}{U_0} = \frac{4\pi U}{P_{rad}} \tag{2.3}$$

$$D_0 = \frac{U|_{max}}{U_0} = \frac{U_{max}}{U_0} = \frac{4\pi U_{max}}{P_{rad}} \tag{2.4}$$

where D_g is the directive gain (dimensionless), D_0 is the directivity (dimensionless), U is the radiation intensity, U_{max} is the maximum radiation intensity, U_0 is the radiation intensity of an isotropic source and P_{rad} is the total radiated power. Note that, for an isotropic source, eqns. (2.3) and (2.4) are equal to unity, since U, U_{max} and U_0 are equal to each other.

Antenna gain is a quantity which takes into account the antenna efficiency as well as its directional capabilities. Antenna power gain in a given direction is *4π times the ratio of the radiation intensity in that direction to the net power accepted by the antenna from a connected transmitter*. However, the power gain is usually taken in the direction of maximum radiation.

In general,

$$\text{Gain} = 4\pi \frac{\text{radiation intensity}}{\text{total input power}}$$

$$= 4\pi \frac{U(\theta,\phi)}{P_{in}} \tag{2.5}$$

Relative gain is also referred to. It is *the ratio of the power gain in a given direction to the power gain of a reference antenna in its referenced direction*. Both antenna must have the same input power. The reference antenna may be a dipole, horn or any antenna whose gain can be calculated or is known. It can also be a lossless isotropic source. In general form,

$$G_g(\theta, \phi) = \eta\ D_g(\theta, \phi) \tag{2.6}$$

where η is the total antenna efficiency. Further discussion of the antenna gain measurement methods will be given in Section 4.3.

In practice, the gain maximum value is usually referred to. Hence, eqn. (2.6) can be written as

$$G_0 = \eta D_0 \tag{2.7}$$

where η is the antenna overall efficiency that takes into account the losses at the input terminals and within the antenna structure.

2.3 INPUT IMPEDANCE

Input impedance is *the impedance presented by an antenna at its terminals, or the ratio of the voltage to current at a pair of terminals, or the ratio of the appropriate components of the electric to magnetic fields at a point* (or at the antenna input).

A transmitting antenna in the form of a wire dipole is illustrated in Fig. 2.4(a) [1]. The excitation of the antenna is represented by a generator of internal impedance Z_g The terminals of the antenna is designated by terminal a-b, which is also the output terminals of the generator. The equivalent circuit of the antenna and its excitation is given in Fig. 2.4(b) [1]. Current I_g is flowing from the generator into the antenna. The generator can be represented by its generated voltage V_g, generator resistance R_g and generator reactance X_g.

On the other hand, the antenna can be represented by an impedance which consists of the antenna resistance R_a and antenna reactance X_a. For small antennas with very low dielectric loss, the antenna resistance is made up of its radiation resistance R_{rad} and its loss resistance R_{loss}. Further considerations for small antennas are discussed in Section 2.7.

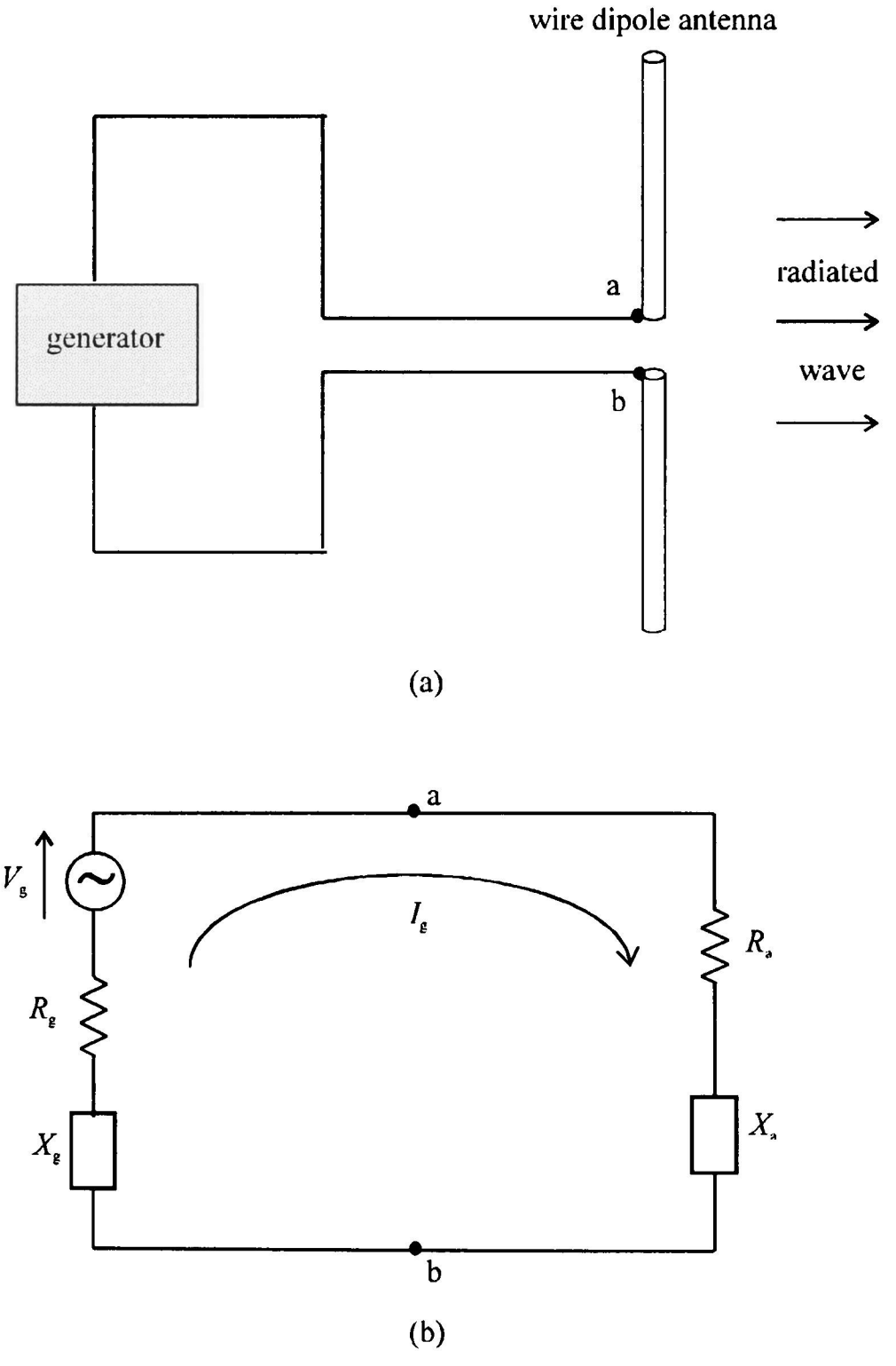

Fig. 2.4. (a) A transmitting antenna, (b) the equivalent circuit.

The power generated by the generator is divided as follows:

1. Power dissipated in the loss resistance as heat loss. This amount has to be kept as low as possible, for an antenna to be efficient.

2. Power radiated through the radiation resistance. This amount has to be made as high as possible, for an antenna to be efficient.

3. Power dissipated as heat on the internal resistance of the generator.

In order to achieve maximum power transfer from the generator to the antenna, half of the power generated by the generator has to be dissipated as heat in R_g, whilst the other half is delivered to the antenna. This condition occurs when there is conjugate matching.

Mathematically, the conjugate matching happens when

$$R_a + R_{loss} = R_g \tag{2.8}$$

and

$$X_a = -X_g \tag{2.9}$$

In practise, an amount of mismatch loss may present between the antenna and the interconnecting transmission line. This will reduce the overall efficiency of the antenna. Factors which contribute to the antenna overall efficiency is discussed in Section 2.5.

Further discussion of the input impedance of the dipole antennas is given in Section 2.8. In addition, the loss resistance of a superconductor is discussed further in Chapter 3.

2.4 MATCHING NETWORKS

A matching network may be employed between the antenna radiating structure and the antenna feed. This is to provide the conjugate matching condition for maximum power transfer as discussed in Section 2.3. The operation of the antenna system over a frequency range depends on the frequency characteristics of the combination between the transmission feeding line and the antenna radiating structure. Usually, the transmission line has real characteristic impedance whilst the input impedance of the antenna is complex. For example, one may use a 50 ohm coaxial cable for the feeding or the antenna may have a 50 ohm coplanar strip feeding line. The coaxial cable and the coplanar strip line are discussed in Sections 7.4 and 2.8.6, respectively.

Three standard yet simple matching networks suitable for this study are the stub-matching, the quarter-wavelength transformer and the taper section. These will be briefly discussed as follows:

(a) Stub-matching

A short- or open-circuited shunt stub of length l_2 can be placed at a distance l_1 from the terminals of the antenna radiating structure. The short-circuited shunt is illustrated in Fig. 2.5.

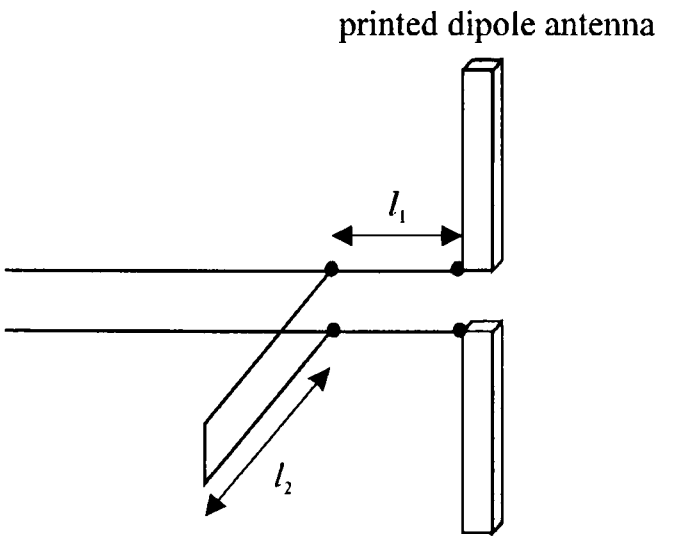

Fig. 2.5. Shunt matching.

A simple linear printed dipole is shown here as the antenna. The length l_1 is adjusted to make the input resistance of the antenna radiating structure equals the real characteristic impedance of the transmission line. The length l_2 is adjusted to cancel out the reactive part of the antenna input impedance. In some cases, more than one stub may be required to provide the perfect match. However, compromise has to be made to the size of the antenna and the available space for the matching network.

(b) Quarter-wavelength transformer

This is essentially a transmission line with the desired characteristic impedance. It is directly connected to the radiating structure terminals, if the antenna input impedance is real. For complex input impedance of the antenna, the transformer is positioned a distance l_3 away, as illustrated in Fig. 2.6. A linear printed dipole is shown as the antenna. This distance will cancel out the reactive part of the antenna input impedance. In order to match the antenna input resistance, R_{in}, with the real characteristic impedance, Z_0, of the transmission line, the characteristic impedance of the transformer can be calculated as [35]

$$Z_1 = \sqrt{Z_0 R_{in}} \tag{2.10}$$

Multiple sections of such transformer may be designed for antennas with broad bandwidth.

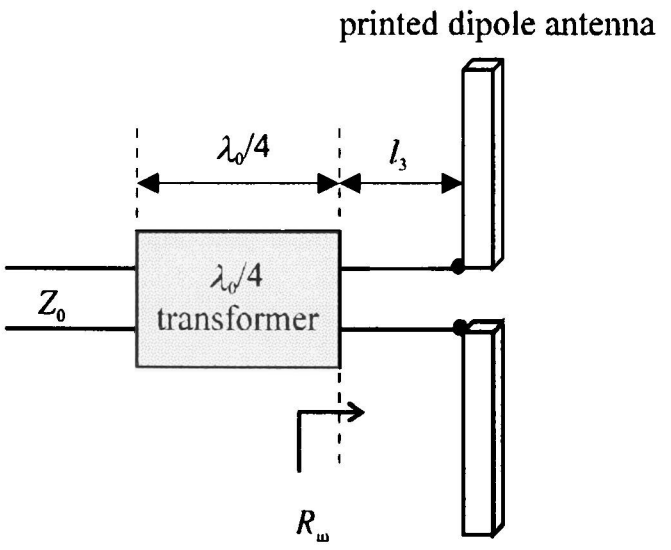

Fig. 2.6. Quarter-wavelength transformer

(c) Taper section

The taper section is essentially an impedance transformation network. It is a length of transmission line with varying cross-section. The impedance of a cross-section is inversely proportional to the cross-section. The impedance change along the line may be chosen to be a function of line length, which results in smooth variations of the line impedance. Abrupt change between adjacent small line sections can be reduced. This will minimise discontinuities; i.e., sudden change in the line impedance. Consequently, reflections will be minimised.

One such mathematical function is the exponential function. An example of a taper matching circuit of length l_t, is illustrated in Fig. 2.7.

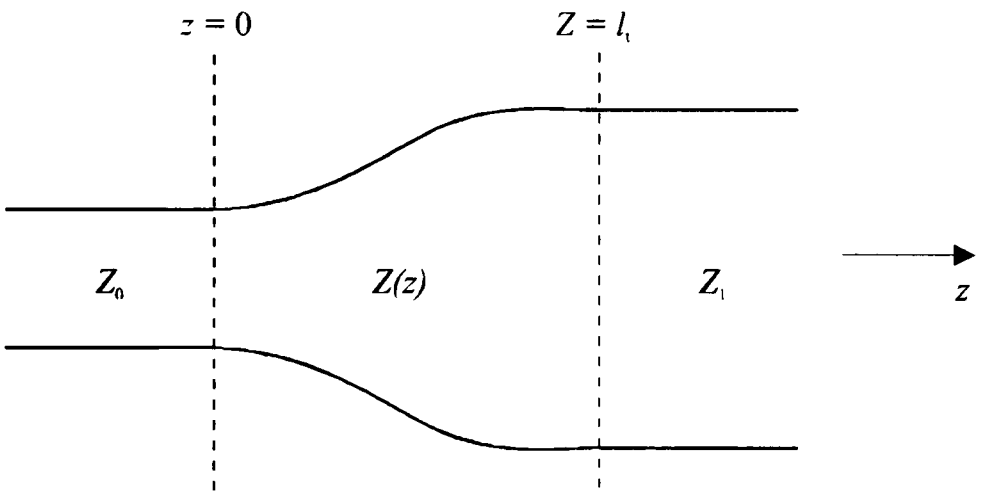

Fig. 2.7. Taper matching circuit.

Z_1 is the impedance of the antenna, Z_2 is the characteristic impedance of the feeding line and $Z(z)$ is the characteristic impedance of the taper section. The latter varies from $z = 0$ to $z = l_t$. $Z(z)$ can be calculated from the expression [36]

$$Z(z) = Z_0 \exp\left[z \frac{\ln\left(\frac{Z_1}{Z_0}\right)}{l_t} \right] \tag{2.11}$$

where the term $\ln\left(\frac{Z_1}{Z_0}\right)$ is known as the taper rate. At the ends of the taper section, $Z(z=0) = Z_0$ and $Z(z = l_t) = Z_1$. This shows that matching occurs at both cross-sections.

2.5 EFFICIENCY

The antenna radiation efficiency can be defined as the ratio of the total power radiated by the antenna to the total power accepted by the antenna at its input terminals during radiation. This is equivalent to the ratio of the antenna radiation resistance, R_{rad} , to the antenna total resistance, i.e.,

$$\eta_{rad} = \frac{R_{rad}}{R_{rad} + R_{loss}} \tag{2.12}$$

where R_{loss} is the antenna loss resistance. This assumes that the antenna is perfectly matched to its source or the load cable. However, matching to a 50 ohm system is difficult to be implemented for small structures.

A matching network may be employed between the radiating structure and the antenna feed, as discussed earlier in Section 2.4 and further in Section 3.4 related to the superconducting devices. The losses that occur in this network are usually very small. It can be incorporated by an equivalent resistance R_m . If the antenna is not well-matched, losses due to reflection at the antenna feed may be present. This can be accounted for, by another small resistance R_f . Hence, the overall antenna efficiency can be written as

$$\eta_{tot} = \frac{R_{rad}}{R_{loss} + R_{rad} + R_m + R_t} \tag{2.13}$$

However, R_f can be neglected since it is very difficult to be determined. The denominator of eqn. (2.13) is also the antenna input impedance. Knowing its value using eqn. (2.35), R_m can be calculated by neglecting R_f . Thus the total antenna efficiency can be deduced using eqn. (2.13) again.

Since small antennas have directivities of 1.5, it is very convenient to perform only the transmission measurement, and then calculate the antenna gain using eqn. (4.4), or more accurately using eqn. (4.5). Consequently, antenna efficiency can be easily calculated from eqn. (2.7). Further discussions of the different measurement methods of the antenna radiation efficiency will be given in Section 4.2.

2.6 BANDWIDTH

The antenna bandwidth is *the range of frequencies within which the performance of the antenna, with respect to some characteristic, conforms to a specified standard.* It is normally considered as the frequency range that lie on both sides of the antenna centre frequency, where the antenna characteristics are within an acceptable value of those at the centre frequency. The centre frequency can be the antenna resonant frequency. For a narrowband antenna, this is expressed as a percentage of the frequency difference over the bandwidth centre frequency. On the other hand, for a broadband antenna, it is expressed as the ratio of the upper-to-lower frequencies of acceptable operation.

In general, the useful bandwidth of an antenna depends solely on its impedance characteristics. If the bandwidth is broad, one has to ensure that, within the required bandwidth, the antenna pattern maintains an acceptable shape. The bandwidth can also be specified by the lower and upper frequency limits at which the voltage standing wave ratio (VSWR) on the transmission line exceeds an acceptable value. In practise, VSWR close to unity is desirable (perfect match or zero reflection). However, the acceptable value varies widely with application. Nevertheless, a higher limit of 2.0 is usually accepted.

The VSWR is related to the measured reflection coefficient $|S_{11}|$ by

$$\text{VSWR} = \frac{1 + |S_{11}|}{1 - |S_{11}|} \tag{2.14}$$

This corresponds to $|S_{11}| = 0.333$ or ~ -10.0 dB.

2.7 SMALL ANTENNAS

An electrically small antenna is defined as an antenna occupying a small fraction of one radiansphere in space [16]. The greatest dimension is typically less than a quarter wavelength, which includes any image in a ground plane. The radiansphere is the spherical volume having a radius of $1/2\pi$ wavelength (= 0.16 wavelength) [15]. The significance of this term is that stored energy dominates inside the radiansphere while radiated energy is important outside. A small antenna is essentially a magnetic dipole (behaving as an inductor) or an electric dipole (behaving as a capacitor), or possibly a combination of both [10].

The radiation power factor (PF_{rad}) is a figure-of-merit for an electrically small antenna [10]. It is defined by

$$\mathrm{PF}_{rad} = \frac{\text{radiated power}}{\text{reactive power}} = \frac{R_{rad}}{X} << 1 \qquad (2.15)$$

where R_{rad} and X are the antenna radiation resistance and reactance, respectively. This has been shown to be equal to the ratio of the antenna volume to a radiansphere as

$$\mathrm{PF}_{rad} = \frac{\text{antenna volume}}{\text{radiansphere}} = (kr)^3 \qquad (2.16)$$

PF_{rad} is in fact not an inverse of the Q-factor, since

$$Q = \frac{\text{energy stored per unit time}}{\text{energy lost per unit time}} = \frac{X}{R_{loss} + R_{rad}} = \frac{\text{centre (or operational frequency)}}{\text{bandwidth}} \qquad (2.17)$$

It can be seen that, by increasing either R_{rad} or R_{loss} , or both, Q-factor will be reduced and the bandwidth will be broadened. But from eqn. (2.15), only an increase in R_{rad} will increase the radiation power factor.

The lowest achievable Q-factor of an electrically small antenna system is related to the antenna largest linear dimension, given by [25]

$$Q \approx \frac{1}{(kr)^3} \tag{2.18}$$

This Q-factor is independent of the geometrical configuration of the antenna within the sphere of radius r. It also represents the fundamental limit on the electrical size of an antenna. It is interesting to note that this value is equivalent to the inverse of PF_{rad} in eqn. (2.15) when there is no loss resistance.

The term radiation power factor is descriptive of the radiation of real power from a small antenna taking a much larger value of reactive power. The small value of radiation power factor is limited by some measure of the antenna size. The radiation efficiency of a transmitting antenna is the fraction of available power from a source that is radiated into space whilst that of a receiving antenna, it is the fraction of available power from a source to a load representing the receiver (this is really a measure of the ability of a received signal to overcome the noise level in the circuits).

This small value of radiation power factor is directly proportional to ω^3, and hence to the relative operational bandwidth. Since the operating efficiency of a small antenna is limited by its radiation power factor, which is proportional to its size, this in turn depends on the relative operational bandwidth as compared with the radiation power factor. For narrowband operation, the relative operational bandwidth of a small antenna is taken to be less than the radiation power factor. Antenna efficiency is limited by dissipation or heat losses in the whole antenna structure. Similar to eqn. (2.15), the loss power factor can be defined as

$$\mathrm{PF}_{loss} = \frac{\text{loss power}}{\text{reactive power}} = \frac{R_{loss}}{X} \tag{2.19}$$

Since the radiation power factor of a small antenna is small, its efficiency is substantially reduced according to the formulation

$$\text{Radiation efficiency} = \frac{\mathrm{PF}_{rad}}{\mathrm{PF}_{rad} + \mathrm{PF}_{loss}} \tag{2.20}$$

This is in fact equivalent to that of eqn. (2.12), rewritten here for convenience as

$$\eta_{rad} = \frac{R_{rad}}{R_{rad} + R_{loss}} \tag{2.21}$$

This means that large antennas yield higher efficiency since the radiation power factor is greatly increased whereas the loss power factor is greatly decreased. However, a specified efficiency can lead to desirable size requirement where a small value is sufficient to serve a purpose.

On the other extreme, a small antenna may be needed for wideband operation. The relative bandwidth is taken to be so much greater than the radiation power factor. Efficiency may then be limited by the ability of the matching network [28].

The radiation power factor of small antennas is also related to the effective volume, V_{effec} , and its spherical radius, a', by the relationships [10]

$$V_{\text{effec}} = \frac{9}{2} \text{PF}_{rad} V_{rsph} \qquad \text{and} \qquad a' = \frac{\lambda}{2\pi} \left(\frac{9}{2} \text{PF}_{rad} \right)^{1/3} \tag{2.22}$$

where is V_{rsph} the radiansphere volume of radius equal the radianlength, i.e., $\lambda/2\pi$. This effective volume includes any image in an adjoining ground plane regarded as integral with the antenna.

Fig. 2.8 illustrates four examples of antennas with their corresponding effective volume drawn in dotted circle. It can be clearly seen that the effective volumes of Figs. 2.8(a) and (b) do not differ significantly as the occupied volumes, and they are largely affected by the antennas length. Similarly in Figs. 2.8(c) and (d), the effective volumes also do not differ significantly as the occupied volume, since they are largely influenced by the loop square size.

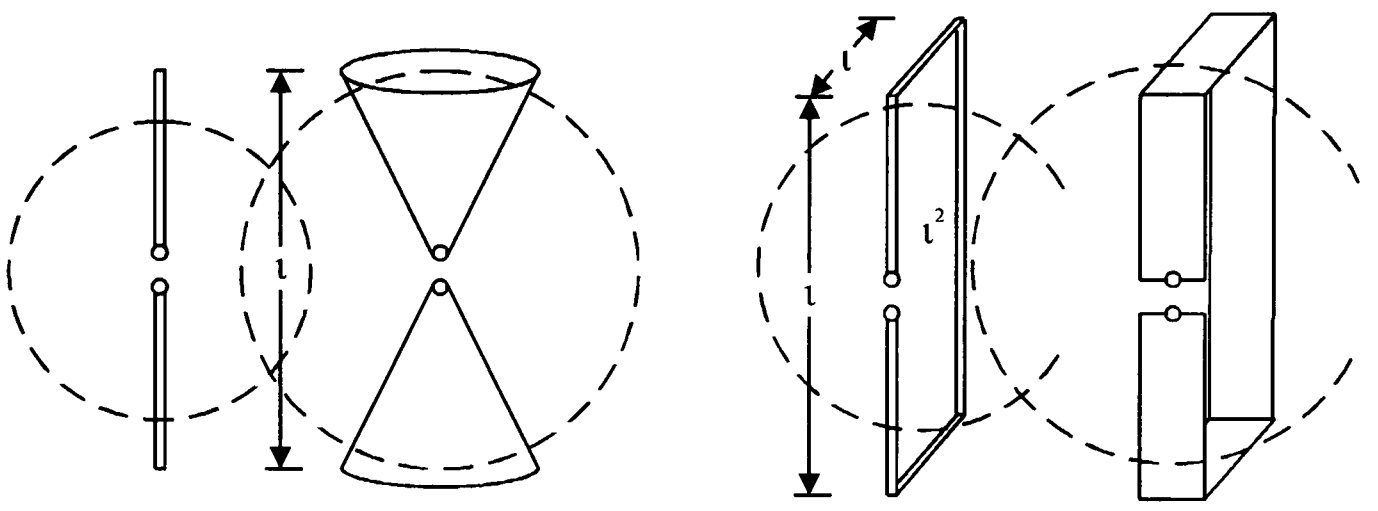

Fig. 2.8. Effective volume [10], (a) wire dipole (b) cone dipole (c) wire square loop (d) strip square loop.

2.8 DIPOLES

In this section, the formulation of the input impedance of all the designed antenna circuits are described. Current distribution curves are also given where appropriate. All the discussion applies to normal and superconducting antennas. However, several considerations relevant to HTS antennas will be emphasised where appropriate. Far-field radiation patterns are also described.

2.8.1 Short Dipoles

The geometry of a centre-fed short wire dipole antenna of length d_s and wire radius a_s in free space is illustrated in Fig. 2.9(a). The corresponding triangular current distribution is illustrated in Fig. 2.9(b). Note that $a_s << d_s$. The antenna is considered short when [1]

$$\lambda_0/50 < d_s < \lambda_0/10 \tag{2.23}$$

where λ_0 is the operating wavelength. In Fig. 2.9(a), (x', y', z') represent the co-ordinates of the source, (x, y, z) represent the observation point co-ordinates and R is the distance from any point on the source to the observation point. These dipoles are assumed to be very thin, i.e., $x' = y' = 0$. To a good approximation, the current distribution for a short dipole of length d_s can be written as [1]

$$\begin{aligned} \mathbf{I}_{es}(x', y', z') &= a_z\ I_{0s}\,[\,1 - (2/d_s)z'\,] && \text{for}\quad 0 \le z' \le d_s/2 \\ &= a_z\ I_{0s}\,[1 + (2/d_s)z'\,] && \text{for}\quad -d_s/2 \le z' \le 0 \end{aligned} \tag{2.24}$$

where $\mathbf{I}_{es}$ is the electric current along the short dipole, a_z is the radial unit vector and I_{0s} is the constant peak current. This triangular distribution assumes that the antenna is centre-fed and the current vanishes at the end points ($z' = \pm d_s/2$).

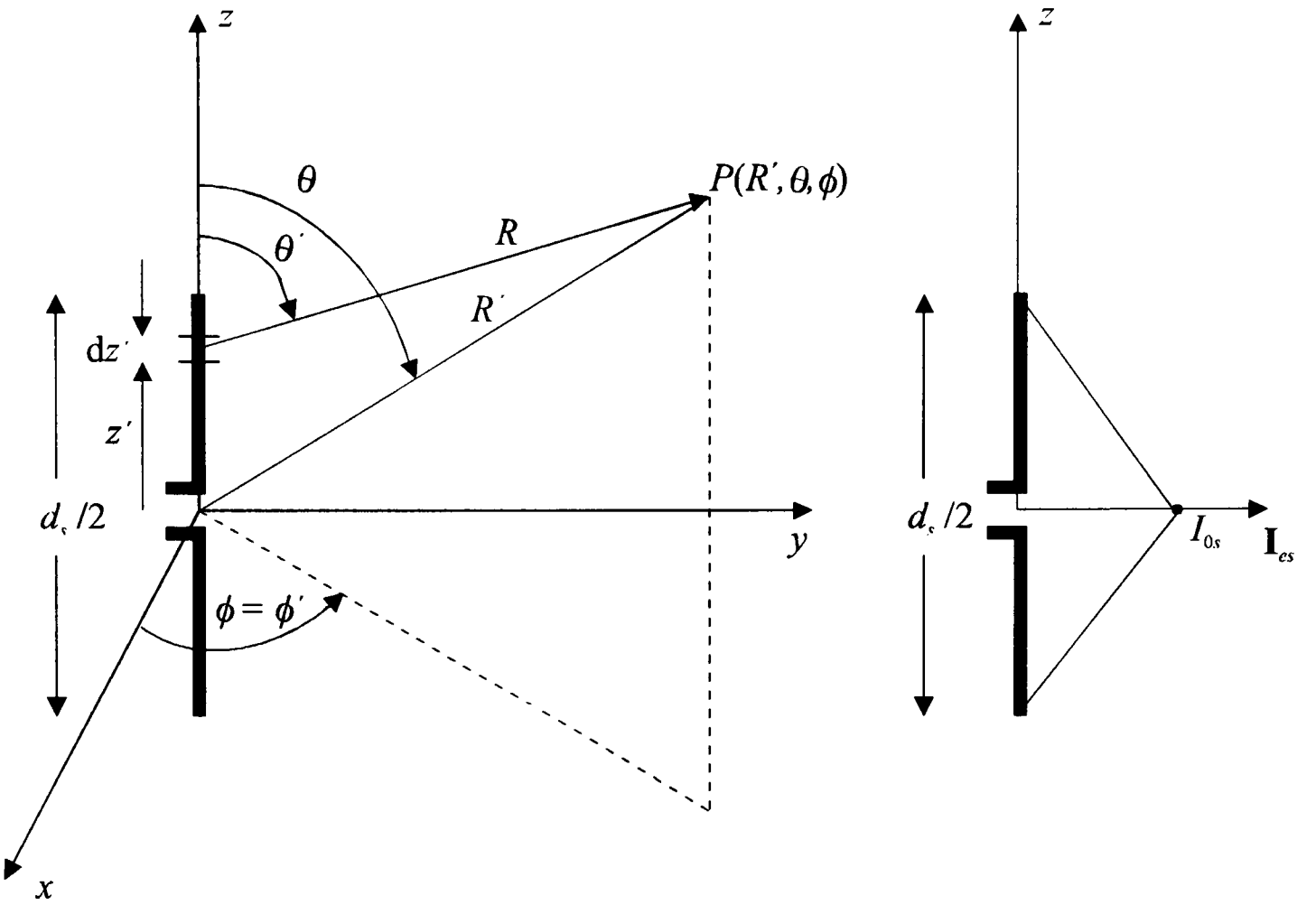

(a) (b)

Fig. 2.9. Linear short dipole antenna a) geometry, b) current distribution along the dipole length.

Such current distribution leads to the expression for the total power radiated as

$$P_{rad} = Z_0 \left(\frac{\pi}{3}\right) \left| \frac{I_{0s}\, d_s}{\lambda_0} \right|^2 \tag{2.25}$$

where Z_0 is the intrinsic impedance of free space, i.e., 120π. λ_0 is related to the frequency of operation f_0 through the expression

$$\lambda_0 = c/f_0 \tag{2.26}$$

where c is the speed of light in free space.

Using the expression [1]

$$R_{rad} = \frac{2P_{rad}}{|I_{0s}{}^2|} \tag{2.27}$$

the radiation resistance for the short wire dipole can be written as

$$R_{rad} = Z_0 \left(\frac{\pi}{6}\right) \left|\frac{d_s}{\lambda_0}\right|^2 \tag{2.28}$$

Eqn. (2.28) can also be written as

$$R_{rad} = \frac{Z_0 d_s^2 k_0^2}{24\pi} \tag{2.29}$$

where k_0 is the propagation constant in free space,

$$k_0 = 2\pi/\lambda_0 \tag{2.30}$$

R_{rad} constitutes one component of the antenna input impedance Z_{in} . The short dipole antenna of Fig. 2.9(a), as with all antennas, can be represented by an equivalent network as shown in Fig. 2.10.

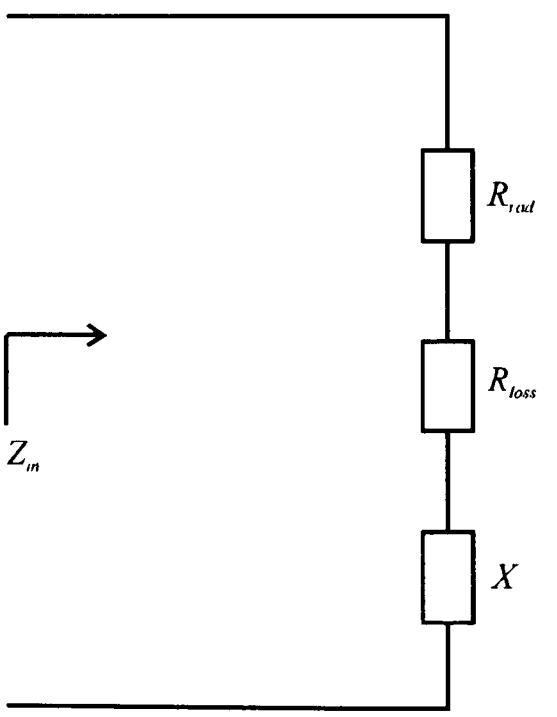

Fig. 2.10. Equivalent circuit of a short dipole antenna.

The input impedance consists of series R_{rad} , ohmic loss resistance R_{loss} a reactance X , i.e.,

$$Z_{in} = R_{in} + \mathrm{j}\, X_{in} = (R_{rad} + R_{loss}) + \mathrm{j}\, X_{in} \tag{2.31}$$

The radiation resistance is the resistance associated with the power radiated from the dipole antenna. The ohmic loss resistance has to be accounted as a component of the antenna input impedance since it may be comparable to the radiation resistance.

The loss resistance can be written as [1]

$$R_{loss} = \frac{1}{P_s}\sqrt{\frac{\omega\,\mu_0}{2\sigma}} \tag{2.32}$$

where $P_s = 2\pi a_s$, i.e., the perimeter of the wire dipole of radius a_s , $\omega = 2\pi f_0$, i.e., the angular frequency, $\mu_0 = 4\pi \times 10^{-7}$ Hm^{-1} , i.e., the permeability of vacuum, and σ is the conductivity of the wire.

Eqn. (2.32) can also be written as

$$R_{loss} = R_s \frac{d_s}{6\pi a_s} \tag{2.33}$$

where R_s is the surface resistance of the dipole conductor. The expression for surface resistance of a normal metal is

$$R_s = \sqrt{\frac{\omega\mu_0}{2\sigma}} \tag{2.34}$$

Since σ is real and constant for normal metals, the surface resistance has an $f^{1/2}$ frequency dependence. At room temperature (300K), σ for copper is 5.882×10^7 Sm^{-1} [37]. It is important to note here that, for a superconductor, σ is not real and constant. Instead, it is complex and is a function of frequency, temperature and material properties. Consequently, the surface resistance of a superconductor has an f^2 frequency dependence and is given by

$$R_s = \omega^2 \mu_0^2 \lambda_L^3(T) \sigma_1 / 2 \tag{2.35}$$

where σ_1 is the normal state conductivity, $\lambda_L(T)$ is the London's penetration depth = $\lambda_L(0)[1-(T/T_c)^4]^{-1/2}$ for $T \leq T_c$, T_c is the critical temperature and $\lambda_L(0)$ is the London's penetration depth as T approaches 0K. The surface resistance of a superconductor is discussed further in Chapter 3.

Ohmic loss describes the heat dissipation which is mainly caused by the finite surface resistance of the antenna. It should be noted that the radiation resistance should be larger than the surface resistance, in order to maintain high radiation efficiency. This is because, the radiation resistance is the component that contributes to the radio wave emission.

The reactance of a short dipole is capacitive. For a dipole with wire radius a_s , it can be written as [2]

$$X_{in} = X_C = Z_0 \frac{2}{\pi k_0 d_s} \left[\ln\left(d_s / a_s\right) - 1 \right] \tag{2.36}$$

If the dipole is fabricated as a printed circuit on a semi-infinite substrate, modifications have to be made on the values of a_s , k_0 , the permittivity of the substrate (ε_r) and Z_0. However, the overall effect on the antenna performance is very small. a_s has to be modified as the electrical equivalent radius a. Since the cross-sectional geometry of the conductor is rectangular with a_w width and a_h height, the equivalent radius can be approximated using (see, for example, in [1], [3])

$$a = 0.25\, a_h + 0.35\, a_w \tag{2.37}$$

The geometrical shape of the conductor with its corresponding equivalent circular cylinder radius a are illustrated in Fig. 2.11.

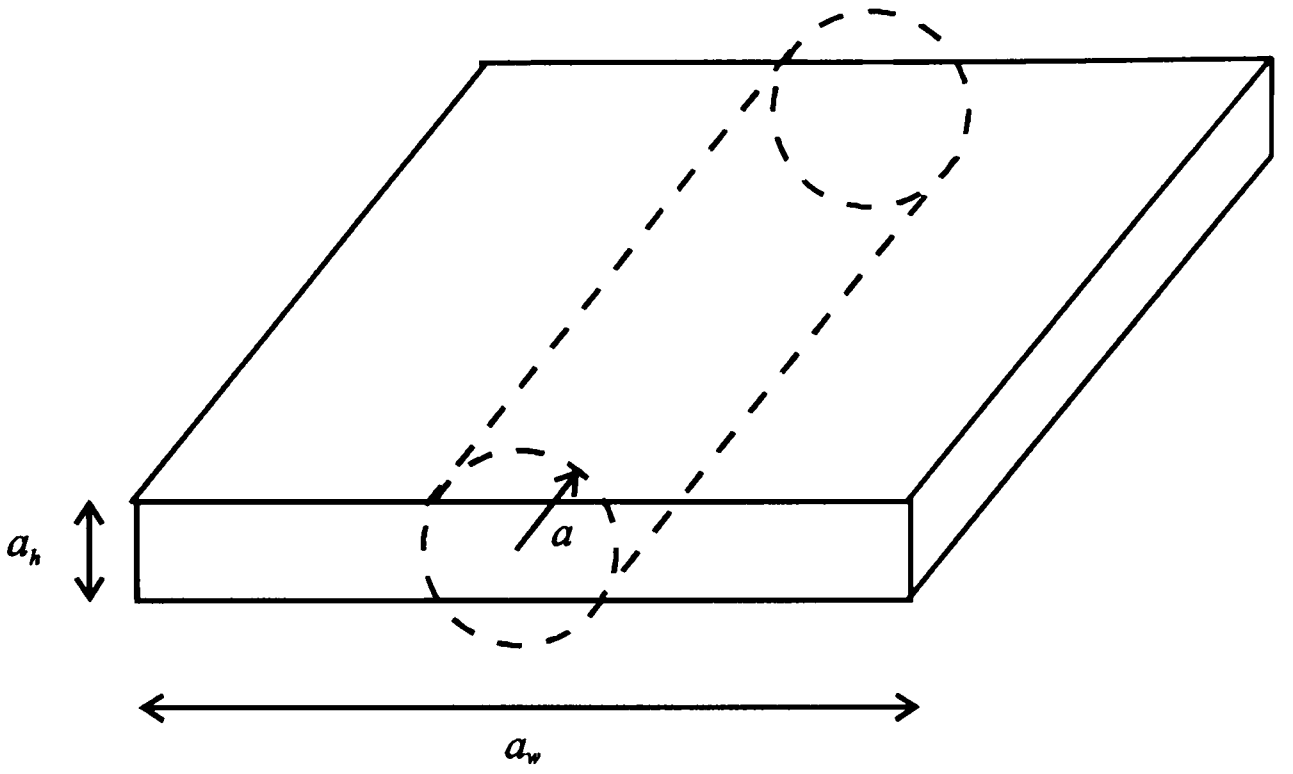

Fig. 2.11. Rectangular conductor geometrical shape and its equivalent circular cylinder radius (the relative dimensions are to scale).

In general, eqn. (2.26) can also be written as

$$\lambda_0 = v_{ph} / f_0 \tag{2.38}$$

where v_{ph} is the velocity of the wave in a medium. In free space, $v_{ph} = c$. With the presence of semi-infinite dielectric substrate onto which the dipole antenna is fabricated, the limit of v_{ph} can be taken as

$$v_{ph} = c\,[(\varepsilon_r + 1)/2]^{-1/2} \tag{2.39}$$

where ε_r is the relative permittivity of the dielectric substrate. The term $(\varepsilon_r + 1)/2$ is the effective permittivity ε_{eff}, taking into account the presence of two different mediums, i.e., air and dielectric. With the presence of such substrate, the propagation constant k_0 of eqn. (2.30) effectively becomes

$$k_{\text{eff}} = k_0 \left[(\varepsilon_r + 1)/2 \right]^{1/2} \tag{2.40}$$

However, eqns. (2.39) and (2.40) are valid only for a thick semi-infinite dielectric substrate, where the width of the printed dipole s_w is less than a third of the substrate thickness h. For infinite dielectric substrate, $[(\varepsilon_r + 1)/2]^{1/2}$ reduces to merely $\varepsilon_r^{1/2}$. Hence, the exact effective permittivity of a thin finite dielectric substrate lies between these two limits, as can be very closely approximated by [38]

$$\varepsilon_{\text{eff}} = 1 + \frac{\varepsilon_r + 1}{2} \left[1 - \left(\frac{s_w / h}{1 + s_w / h} \right) \right] \tag{2.41}$$

and eqns. (2.39), (2.38), (2.40) and (2.41) simplify to

$$v_{\text{eff}} = c\, \varepsilon_{\text{eff}}^{-1/2} \tag{2.42}$$

$$\lambda_{\text{eff}} = v_{\text{eff}} / f_0 \tag{2.43}$$

$$k_{\text{eff}} = k_0\, \varepsilon_{\text{eff}}^{1/2} \tag{2.44}$$

$$Z_{\text{eff}} = Z_0\, \varepsilon_{\text{eff}}^{-1/2} \tag{2.45}$$

Hence, the components of the antenna input impedance of eqns. (2.29), (2.33) and (2.36) can be rewritten as

$$R_{rad} = \frac{Z_{\text{eff}}\, d_s^2\, k_{\text{eff}}^2}{24\pi} \tag{2.46}$$

$$R_{loss} = R_s \frac{d_s}{6\pi a} \tag{2.47}$$

$$X_{in} = X_C = Z_{\text{eff}} \frac{2}{\pi k_{\text{eff}} d_s} \left[\ln(d_s / a) - 1\right] \tag{2.48}$$

Both R_{rad} and R_{loss} decrease with decreasing length of dipole. However, R_{rad} decreases more rapidly. The use of a superconductor in the fabrication of the dipole, as with all antennas, will only reduce the loss resistance. This will contribute to an improved radiation efficiency. There is a small effect from the internal (kinetic) inductance on the reactance of the antenna but this is small and neglected here. The kinetic inductance is discussed in Section 3.2.

From the series equivalent circuit of Fig. 2.10, the Q of an antenna is

$$Q = \frac{X_C}{R_{rad} + R_{loss}} \tag{2.49}$$

Substituting eqns. (2.46) to (2.48) into eqn. (2.49) gives

$$Q = \frac{Z_{\text{eff}} \frac{2}{\pi k_{\text{eff}} d_s} \left[\ln(d_s / a) - 1\right]}{\frac{Z_{\text{eff}} d_s^2 k_{\text{eff}}^2}{24\pi} + R_s \frac{d_s}{6\pi a}} \tag{2.50}$$

which simplifies to

$$Q = \frac{48 Z_{\text{eff}} a}{k_{\text{eff}} d_s^2} \frac{\left[\ln(d_s / a) - 1\right]}{\left(4R_s + Z_{\text{eff}} d_s k_{\text{eff}}^2 a\right)} \tag{2.51}$$

Substituting eqns. (2.46) and (2.47) into eqn. (2.12) gives the radiation efficiency as

$$\eta_{rad} = \frac{\frac{Z_{\text{eff}} d_s^2 k_{\text{eff}}^2}{24\pi}}{\frac{Z_{\text{eff}} d_s^2 k_{\text{eff}}^2}{24\pi} + R_s \frac{d_s}{6\pi a}} \tag{2.52}$$

which simplifies to

$$\eta_{rad} = \frac{Z_{\text{eff}} d_s^2 k_{\text{eff}}^2 a}{Z_{\text{eff}} d_s^2 k_{\text{eff}}^2 a + 4R_s d_s} \tag{2.53}$$

From eqns. (2.21) and (2.49), Q can also be written in terms of η_{rad} as

$$Q = \frac{X_C}{R_{rad}} \eta_{rad} \tag{2.54}$$

Substituting eqns. (2.46) and (2.48) into eqn. (2.54) gives

$$Q = \frac{48}{d_s^3 \, k_{\text{eff}}^3} \left[\ln(d_s / a) - 1 \right] \eta_{rad} \tag{2.55}$$

The semi-infinite substrate and air environment applies to room temperature measurements (i.e., at 300K). When making measurements with cryogenic environment (i.e., at 77K), the test antenna is totally immersed in the liquid nitrogen (ε_r =1.44) [39]. The presence of the liquid nitrogen may be accounted for in the effective permittivity of eqn. (2.39). Nevertheless, this effect is almost negligible on the antenna overall performance and hence it can be neglected. A slight shift in the antenna resonating frequency may be observed.

The phase velocity in the superconducting line which accounts for the London's penetration depth is given by the relationship [40]

$$v_{\text{ph}} = c \, [\, \varepsilon_{\text{eff}} \, (1 + \lambda_L / t_s) \,]^{-1/2} \tag{2.56}$$

where t_s is the superconducting film thickness. If t_s is small compared with λ_L , then an effective penetration depth, λ_e , has to be used with the relationship [40]

$$\lambda_e = \lambda_L \coth (t_s / \lambda_L) \tag{2.57}$$

Further discussion of the London's penetration depth is given in Section 3.2.

The reflection coefficient of the short dipole, as with all antennas, can be determined from the known input impedance using

$$S_{11} = \frac{Z_{in} - Z_c}{Z_{in} + Z_c} \qquad \text{(dimensionless)} \tag{2.58}$$

where Z_c is the line characteristic impedance, equals 50 ohms. In decibels,

$$(S_{11})_{\text{dB}} = 20 \log | S_{11} | \tag{2.59}$$

If the antenna is well-matched, $Z_{in} = Z_c = 50$ ohms. Hence, $S_{11} = 0$ or $-\infty$ dB.

The far-field radiation pattern of a linear printed short dipole is doughnut-shaped [1]. It is a figure-of-revolution of the pattern in Fig. 2.12 about the axis of the dipole. The 3 dB beamwidth is 90°. The far-field electric, E_θ, and magnetic, H_ϕ, field components can be written as

$$E_\theta = \frac{\mathrm{j}\, Z_{\text{eff}} \left[I_s \right] \sin\theta \; d_s}{2R' \; \lambda_{\text{eff}}} \tag{2.60}$$

$$H_\phi = \frac{\mathrm{j} \left[I_s \right] \sin\theta \; d_s}{2R' \; \lambda_{\text{eff}}} \tag{2.61}$$

where $[I_s]$ is the retarded current equals $I_{0s}\, \mathrm{e}^{\mathrm{j}\omega\left[t-(R'/v_{\text{ph}})\right]}$ and R'/v_{ph} is the retardation time.

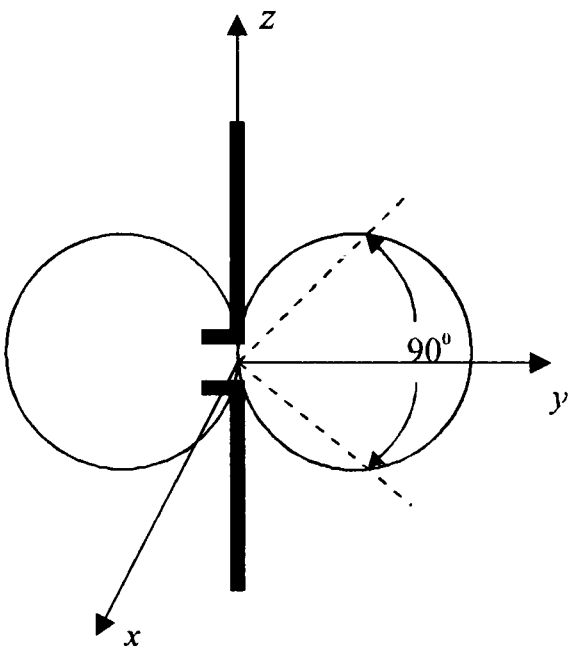

Fig. 2.12. Far-field patterns of a short dipole.

2.8.2 Half-wavelength Linear Dipoles

The geometry of a centre-fed linear half-wavelength ($\lambda/2$) wire dipole antenna of length d and radius a_d , and its corresponding current distribution are illustrated in Fig. 2.13. Note that $a_d << d$.

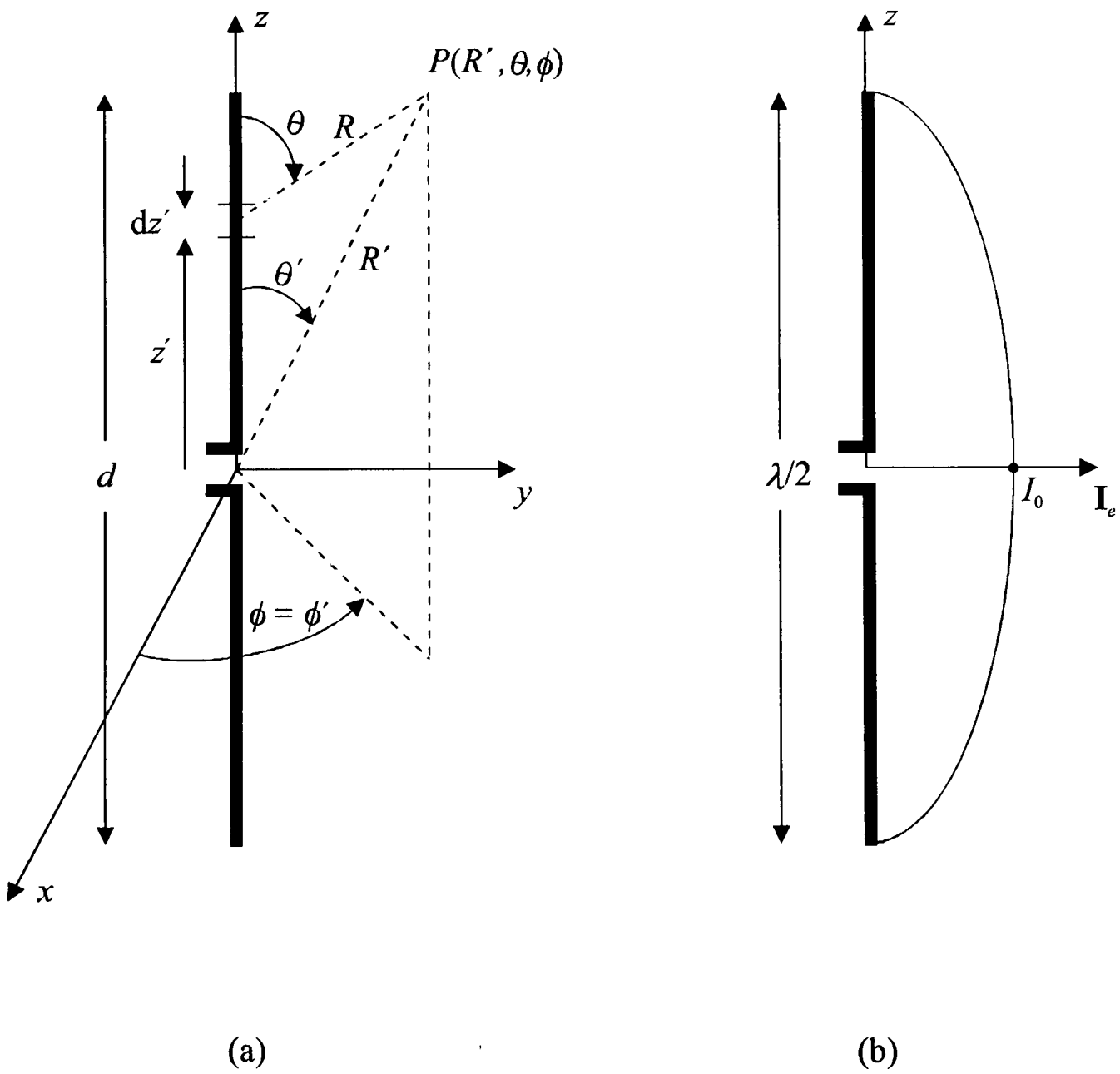

(a) (b)

Fig. 2.13. Linear $\lambda/2$ dipole antenna a) geometry, b) current distribution along the dipole length.

In Fig. 2.13(a), (x', y', z') represent the co-ordinates of the source, (x, y, z) represent the observation point co-ordinates and R is the distance from any point on the source to the observation point. These dipoles are assumed to be very thin, i.e., $x' = y' = 0$. To a good approximation, the current distribution for a $\lambda/2$ dipole of length d can be written as [1]

$$\mathbf{I}_{ed}(x', y', z') = a_z\ I_0 \sin[k_0(d/2 - z')] \qquad \text{for} \quad 0 \le z' \le d/2$$

$$= a_z\ I_0 \sin[k_0(d/2 + z')] \qquad \text{for} \quad -d/2 \le z' \le 0 \tag{2.63}$$

where $\mathbf{I}_{ed}$ is the electric current, a_z is the radial unit vector and I_0 is the constant peak current. This distribution assumes that the antenna is centre-fed and the current vanishes at the end points ($z' = \pm d/2$).

Such current distribution leads to the expression for the total power radiated as

$$P_{rad} = Z_0 \frac{|I_0|^2}{8\pi} \int_0^{2\pi} \frac{\cos^2\left(\frac{\pi}{2}\cos\theta\right)}{\sin\theta} \mathrm{d}\theta \tag{2.64}$$

Using the expression [1] similar to eqn. (2.27), the radiation resistance of a $\lambda/2$ linear wire dipole is given by

$$R_{rad} = \frac{2\,P_{rad}}{|I_0|^2} \tag{2.65}$$

which simplifies to

$$R_{rad} = 73 \text{ ohms} \tag{2.66}$$

Similar to the short dipole, the input impedance of the linear $\lambda/2$ dipole can be represented by an equivalent circuit of Fig. 2.10. The loss resistance of the $\lambda/2$ wire dipole is [1]

$$R_{loss} = \frac{1}{P_d}\sqrt{\frac{\omega\,\mu_0}{2\sigma}} \tag{2.67}$$

where $P_d = 2\pi a_d$, i.e., the perimeter of the $\lambda/2$ wire dipole of wire radius a_d.

Eqn. (2.67) can also be written as

$$R_{loss} = R_s \frac{d}{2\pi a_d} \tag{2.68}$$

where d is the length of the $\lambda/2$ dipole. The expression for R_s is the same as eqn. (2.34) for normal metal dipoles and as eqn. (2.35) for superconductor dipoles.

The reactance of the $\lambda/2$ dipole is inductive and is given by [1]

$$X_{in} = X_L = 30 \text{ Si}(2\pi) = 42.5 \text{ ohms} \tag{2.69}$$

where $\text{Si}(2\pi)$ is the sin integral of 2π and equals 1.42. The $\lambda/2$ dipole can be made resonant, i.e., making the reactance zero, by shortening the antenna by a few percent. Consequently, R_{rad} will decrease. For printed $\lambda/2$ dipoles, a_d has to be modified as the equivalent radius a using eqn. (2.37).

From the series equivalent circuit of Fig. 2.10, the Q of the linear $\lambda/2$ dipole antenna is

$$Q = \frac{X_L}{R_{rad} + R_{loss}} \tag{2.70}$$

Substituting eqns. (2.66), (2.68) and (2.69) into eqn. (2.70) gives

$$Q = \frac{42.5}{73 + R_s \frac{d}{2\pi a}} \tag{2.71}$$

Substituting eqns. (2.66) and (2.68) into eqn. (2.12) gives the radiation efficiency as

$$\eta_{rad} = \frac{73}{73 + R_s \frac{d}{2\pi a}} \tag{2.72}$$

From eqns. (2.21) and (2.70), Q can also be written in terms of η_{rad} as

$$Q = \frac{X_L}{R_{rad}} \eta_{rad} \tag{2.73}$$

Substituting eqns. (2.66) and (2.69) into eqn. (2.73) gives

$$Q = \frac{42.5}{73.0} \eta_{rad} = 0.582 \eta_{rad} \tag{2.74}$$

The reflection coefficient of the linear printed $\lambda/2$ dipole can then be determined from the known input impedance using eqn. (2.58), as with the short dipole.

The far-field radiation pattern of a linear printed $\lambda/2$ dipole is doughnut-shaped [1]. It is a figure-of-revolution of the pattern in Fig. 2.14 about the axis of the dipole. The 3 dB beamwidth is 78°, which is 12° less than that of a short dipole. The pattern is slightly more directional than that of a short dipole. The far-field electric, E_θ, and magnetic, H_ϕ, field components can be written as

$$E_\theta = \frac{\mathrm{j}\, Z_{\mathrm{eff}} \left[I_d\right]}{2\pi R'} \left[\frac{\cos\left[\left(k_{\mathrm{eff}}\, d \cos\theta\right) / 2\right] - \cos\left(k_{\mathrm{eff}}\, d / 2\right)}{\sin\theta} \right] \tag{2.75}$$

$$H_\phi = \frac{\mathrm{j} \left[I_d\right]}{2\pi R'} \left[\frac{\cos\left[\left(k_{\mathrm{eff}}\, d \cos\theta\right) / 2\right] - \cos\left(k_{\mathrm{eff}}\, d / 2\right)}{\sin\theta} \right] \tag{2.76}$$

where $[I_d]$ is the retarded current equals $I_0\, \mathrm{e}^{\mathrm{j}\,\omega\left[t-(R'/v_{\mathrm{ph}})\right]}$ and R'/v_{ph} is the retardation time.

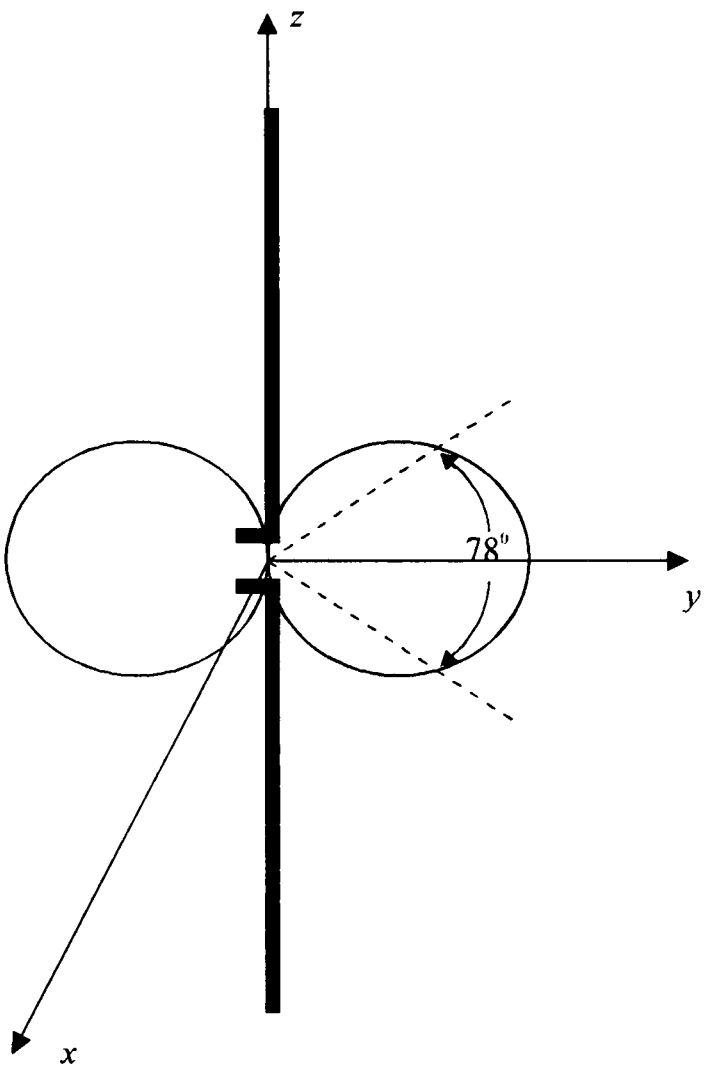

Fig. 2.14. Far-field patterns of a linear $\lambda/2$ dipole.

2.8.3 Meander Dipoles

The geometry of the centre-fed meander wire dipole antennas of wire radius a_{dm} are illustrated in Fig. 2.15. d_{am} and d_{sm} denotes the axial length of the anti-symmetrical and symmetrical structures, respectively. Note that these lengths are the same as L_{ax} and L_{sx}, respectively, as discussed in Section 5.1. The track lengths of both meander antennas are equal to d of the $\lambda/2$ dipole discussed in Section 2.8.2. The current distribution flowing along these meander arms are also assumed to be approximately sinusoidal, which is very much similar to Fig. 2.13(b). Note that $a_{dm} << d_{am}$, d_{sm} and d_{am} , $d_{sm} << d$.

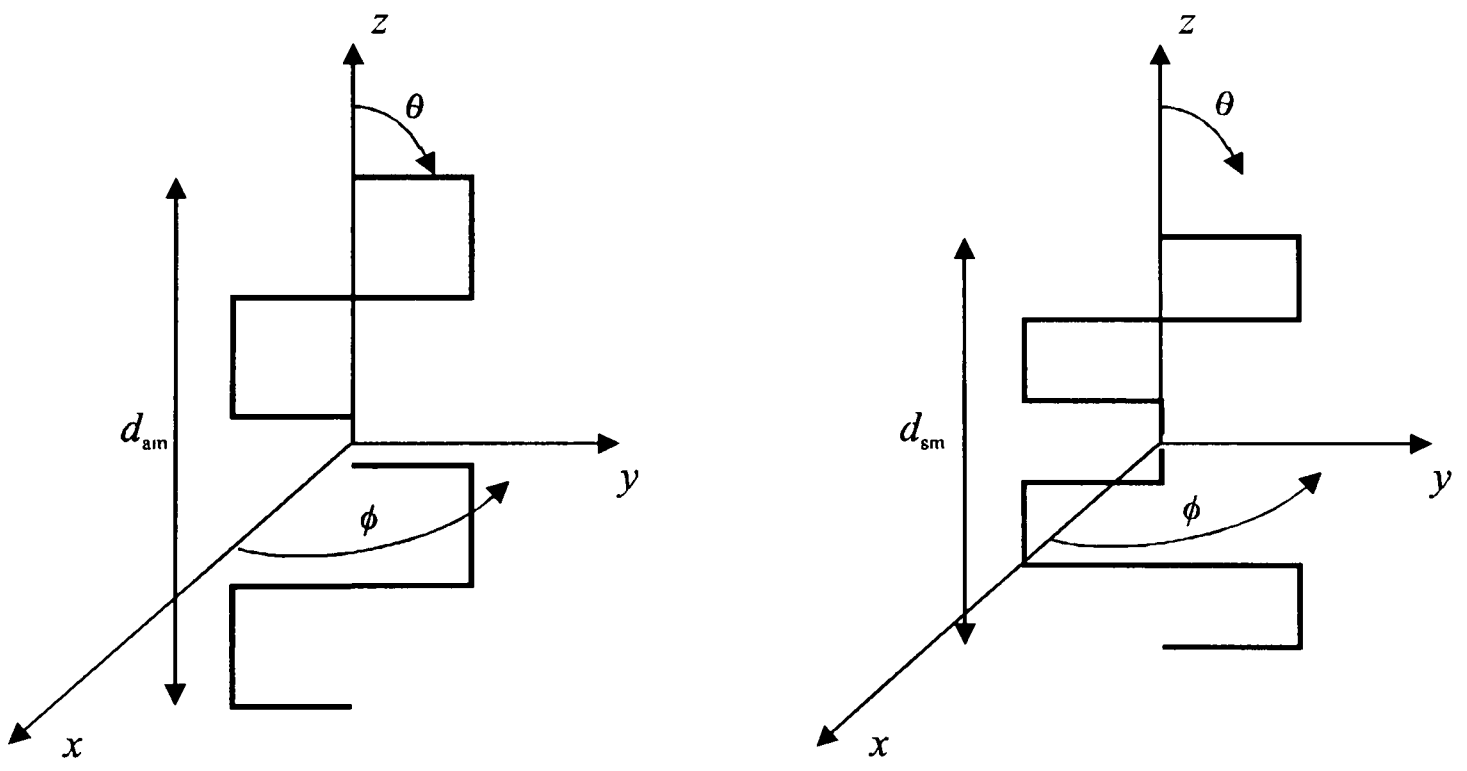

(a) (b)

Fig. 2.15. Meander dipole antennas geometry; (a) anti-symmetrical structure, (b) symmetrical structure.

The expression for the current distribution of eqn. (2.63) leads to the rough approximation expression for the total power radiated as

$$P_{rad} = Z_0 \frac{|I_0|^2}{4\pi} \int_0^{\pi} \left[\cos((k_0 d/2)\cos\theta) - \cos(k_0 d/2)\right]^2 \sin^{-1}\theta \, d\theta \qquad (2.77)$$

Using the expression of eqn. (2.65), the radiation resistance for small lengths of dipoles can be approximated by the expression [1]

$$R_{rad} = Z_0 \left(\frac{\pi}{6}\right) \left|\frac{d}{\lambda_0}\right|^2 \qquad (2.78)$$

Similar to the construction of the short and $\lambda/2$ printed dipole antennas, Z_0 and λ_0 have to be corrected accordingly for the presence of a thin finite dielectric substrate and air medium; using eqns. (2.43) and (2.45), respectively. Hence, eqn. (2.78) becomes

$$R_{rad} = Z_{\text{eff}} \left(\frac{\pi}{6}\right) \left|\frac{d}{\lambda_{\text{eff}}}\right|^2 \qquad (2.79)$$

The axial length of the meander dipole can be regarded as the antenna physical length, d_{phy} , whilst the meander arm length as the antenna resonant length if it were straightened out, d_{res}. Hence, the radiation resistance of meander dipoles of small axial lengths can be written as

$$R_{mrad} = R_{rad} \left(\frac{d_{\text{phy}}}{d_{\text{res}}}\right)^2 \qquad (2.80)$$

The loss resistance is given by [1]

$$R_{loss} = R_s \frac{d_{\text{res}}}{2\pi a_{\text{dm}}} \qquad (2.81)$$

where R_s is the surface resistance as given in eqns. (2.34) and (2.35) for normal conductors and superconductors, respectively, and a_{dm} is the meander dipole arm wire radius or its equivalent radius as given in eqn. (2.37) for printed structures.

The antenna capacitive reactance can be approximated by [1]

$$X = Z_0 \frac{2}{\pi k_0 d} \left[\ln(d / a_{dm}) - 1\right] \tag{2.82}$$

or modified as

$$X_C = Z_{eff} \frac{2}{\pi k_{eff} d} \left[\ln(d / a_{dm}) - 1\right] \tag{2.83}$$

A very close approximation of the meander dipole antenna Q-factor can be obtained from the series equivalent circuit of Fig. 2.10 as

$$Q = \frac{X_C}{R_{mrad} + R_{loss}} \tag{2.84}$$

Substituting eqns. (2.80) and (2.83) into eqn. (2.84) gives

$$Q = \frac{Z_{eff} \frac{2}{\pi k_{eff} d} \left[\ln(d / a_{dm}) - 1\right]}{R_{rad} \left(\frac{d_{phy}}{d_{res}}\right)^2 + R_s \frac{d_{res}}{2 \pi a_{dm}}} \tag{2.85}$$

The meander dipole antenna efficiency can be determined by substituting eqns. (2.80) and (2.81) into eqn. (2.12),

$$\eta_{rad} = \frac{R_{rad} \left(d_{phy} / d_{res}\right)^2}{R_{rad} \left(d_{phy} / d_{res}\right)^2 + \left(R_s \frac{d_{res}}{2\pi a_{dm}}\right)} \tag{2.86}$$

By substituting eqns. (2.80) and (2.83) into eqn. (2.84), Q can be written in terms of η_{rad} as

$$Q = \frac{Z_{\text{eff}} \left(\frac{2}{\pi k_{\text{eff}} d} \right) \left[\ln(d / a_{\text{dm}}) - 1 \right]}{R_{rad} \left(\frac{d_{\text{phy}}}{d_{\text{res}}} \right)^2} \eta_{rad} \qquad (2.87)$$

From the known input impedance, the reflection coefficient can be determined as in eqn. (2.58) or (2.59).

The far-field radiation pattern of the meander dipoles are expected to be of doughnut-shaped. For the anti-symmetrical structure, it is expected to resemble closely that of a linear printed short dipole as in Fig. 2.12. Whilst for the symmetrical structure, it is expected to resemble that of the linear dipole as in Fig. 2.14. Further discussion of the resemblance is discussed in Section 5.1 and further discussed in Section 8.2.

The radiation efficiencies of several printed short dipoles, half-wavelength dipoles and meander dipoles of eqns. (2.53), (2.72) and (2.86), respectively, are compared in Fig. 2.16. All the curves are drawn with respect to their corresponding radius of the smallest sphere that encloses the antenna (r_{small}). The range of r_{small} for the short and meander dipoles is from 0.0075 m to 0.048 m, where the latter is the radianlength. The radianlength of an antenna is $1/2\pi$ of its operating wavelength. This has been discussed in Section 1.1. The range r_{small} for the $\lambda/2$ dipoles is from 0.0075 m to 0.075 m. The meander dipoles are assumed to operate at 1 GHz. All the copper structures have an R_s of ~8 mΩ, whilst the R_s for the HTS meander antennas is 100 μΩ with λ_L of 0.14 μm at 10 GHz [50]. All the tracks of the printed antennas have the equivalent wire radius of 0.25mm. In addition, the physical length of all the meander antennas is 0.15 m. The relative permittivity of the substrates of the copper and the HTS structures are 10.8 and 9.8, respectively. Some of these antennas have been fabricated, experimented and numerically simulated in this study. The designed procedure, fabrication, and numerical simulation and experimental results are discussed in Chapter 5, 7 and 8, respectively.

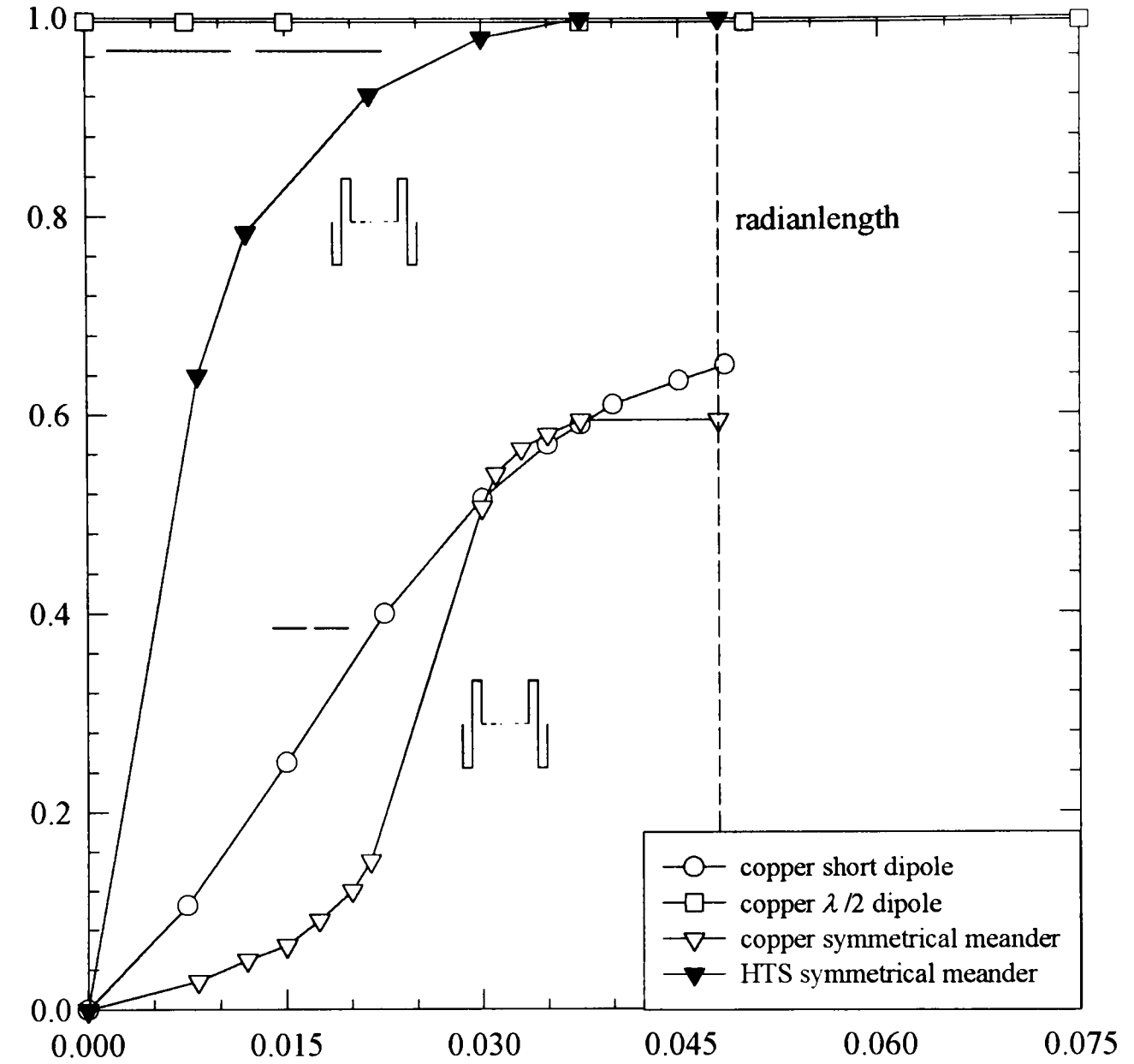

Fig. 2.16. Theoretical radiation efficiency of the short dipoles, linear $\lambda/2$ dipoles and meander dipoles, with respect to their r_{small} .

From Fig. 2.16, the radiation efficiency of the short dipoles increases with increasing r_{small}. All the linear $\lambda/2$ dipoles have almost unity efficiencies. In addition, the normal conducting meander dipoles are inefficient and the curve tends to level off at 0.6 when r_{small} approaches 0.0375 m. On the other hand, the HTS meander dipoles showed significantly higher efficiencies compared to the normal conducting meander dipoles. The HTS antennas tend to achieve constant unity efficiency from similar r_{small} of 0.0375 m.

2.8.4 Meander Dipoles with a Feed Line

In practice, all the printed dipole antennas made from normal conductors can be fed from underneath through the substrate. However, there is great difficulty for the superconducting antennas since the substrate is very brittle and difficult to be drilled. This problem is discussed in Chapter 7. The experimental and numerical simulation results are discussed in detail in Chapter 8. An alternative feeding is by having a length of 50 ohm coplanar strip feed line, which is fabricated at the same time on the same substate as the radiating structure itself. The cross-section of such a line [35] is shown in Fig. 2.17, where w is the strip width, s is the gap between the coplanar strips, t is the strip thickness and h is the substrate height.

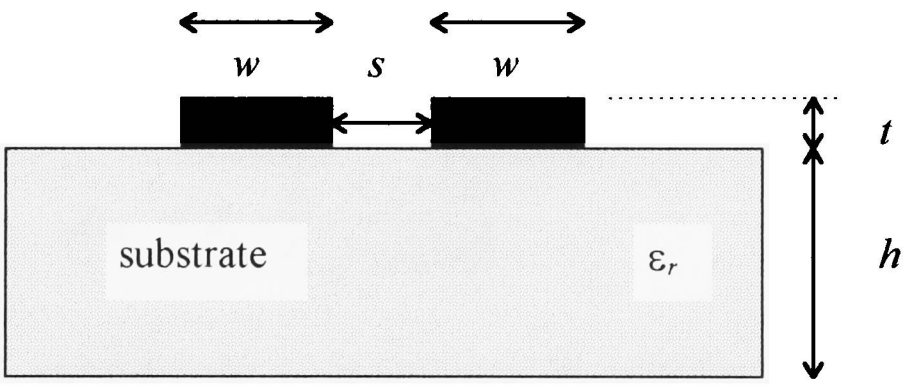

Fig. 2.17. Cross-section of a symmetrical coplanar strip transmission line.

The input impedance of the antenna with the presence of a transmission line of length l as the feed, can be obtained using transmission line theory as [35]

$$Z_{ant} = Z_s \frac{Z_{in} + Z_s \tanh(\gamma l)}{Z_s + Z_{in} \tanh(\gamma l)} \tag{2.88}$$

where Z_s is the characteristic impedance of the coplanar strips, i.e., designed to be 50 ohm, Z_{in} is the antenna input impedance and γ is the line propagation constant. γ is given by

$$\gamma = \alpha + \mathrm{j}k \tag{2.89}$$

where α is the attenuation constant in nepers per meter and k is the phase constant in radians per meter.

For very small values of α, i.e., an almost lossless line, $\gamma = \mathrm{j}k$. Hence, eqn. (2.88) becomes

$$Z_{ant} = Z_s \frac{Z_{in} + Z_s \tanh(\mathrm{j}kl)}{Z_s + Z_{in} \tanh(\mathrm{j}kl)} \tag{2.90}$$

Since $\tanh(\mathrm{j}kl) = \mathrm{j}\tan kl$, eqn. (2.90) can be rewritten as

$$Z_{ant} = Z_s \frac{Z_{in} + Z_s \tan(kl)}{Z_s + Z_{in} \tan(kl)} \tag{2.91}$$

For small values of l, $\tan(kl) \approx kl$. Hence, Z_{ant} approximates to

$$Z_{ant} = Z_s \frac{Z_{in} + \mathrm{j}Z_s(kl)}{Z_s + \mathrm{j}Z_{in}(kl)} \tag{2.92}$$

Exact formulations of Z_s and k for the coplanar strips transmission line can be found in reference [35].

By taking into account the presence of the finite thickness dielectric substrate as in eqns. (2.42) to (2.44), the effective permittivity is

$$\varepsilon_{\mathrm{eff}} = 1.0 + \left(\frac{\varepsilon_r - 1}{2.0} \frac{K(m')}{K(m)} \frac{K(m_1)}{K(m_1')} \right) \tag{2.93}$$

where the terms $K(m')$, $K(m)$, $K(m_1')$ and $K(m_1)$ are known as the complete elliptic integrals of the first kind. Further formulations and definitions related to these terms can be referred to in Appendix 1.

The corresponding Z_s is [35]

$$Z_s = Z_0 \, \varepsilon_{eff}^{-1/2} \, [K(m) / K(m')] \tag{2.94}$$

For better accuracy, however, the effective permittivity of the dielectric substrate has to account for the strip thickness as well. Hence, the effective permittivity and the line characteristic impedance become [35]

$$\varepsilon_{efft} = \varepsilon_{eff1} - \left(\frac{\varepsilon_{efft1} - 1.0}{\left[(w \; / \; 0.7t) \, [K(m) \; / \; K'(m)] \right] + 1.0} \right) \tag{2.95}$$

$$Z_{st} = 30\pi \, \varepsilon_{eff1}^{-1/2} \, [K(m_t') / K(m_t)] \tag{2.96}$$

Derivation of ε_{eff1} and $K(m_t') / K(m_t)$ can also be referred to in Appendix 1.

As for the superconducting coplanar feeding line, the contribution from the London's penetration depth also needs to be accounted. This can be done using the relationship of the line phase velocity by the expression [41]

$$v_{ph} = c \, [\, \varepsilon_{eff} \, (1 + \; 2\lambda_L / s) \,]^{-1/2} \tag{2.97}$$

where s is the gap between the coplanar strips, as illustrated in Fig. 2.17.

From eqn. (2.58), the reflection coefficient of the antenna with the feeding line becomes

$$S_{11} = \frac{Z_{ant} - Z_c}{Z_{ant} + Z_c} \qquad \text{(dimensionless)} \tag{2.98}$$

CHAPTER 3

SUPERCONDUCTING ANTENNAS

3.0 INTRODUCTION

This chapter begins with a review of superconductivity. A discussion of surface impedance and penetration depth; important parameters of a superconducting material, is then given. This is followed by the discussion of the surface impedance of superconducting films with finite thickness. Recent work on small superconducting antennas is discussed in depth in Section 3.4. A brief review of the early application of superconductors in small antenna designs before 1986 has been discussed in Section 1.3. This chapter ends with a short discussion of matching networks for the superconducting antennas.

3.1 SUPERCONDUCTIVITY

In 1911, Onnes discovered the superconductivity phenomenon during a DC resistance measurement with decreasing temperatures [42]. The phenomenon was described as: "below a critical temperature, the material passed into a new state, which on account of its extraordinary electrical properties may be called the superconducting state". In the experiment, the resistance of a mercury wire dropped suddenly to zero at approximately 4K. Such temperature was termed transition or critical temperature, i.e. T_c. Three years later, it was established that such a phenomenon could be destroyed by raising the temperature of the material, applying too strong a current density through the material, or placing the material in too strong a magnetic field.

In 1933, Meissner and Ochsenfeld made a significant discovery of the superconductor's ability to expel flux, known as the Meissner effect [43]. A diamagnetic material is a material that tries to minimise the magnetic flux density, **B**, inside itself, when

placed in a magnetic field. Thus, a superconductor, which seeks to maintain the condition of zero magnetic flux density within itself, is termed a perfect diamagnet. The Meissner effect is an indication that superconductivity is more than merely perfect conductivity.

It can be summarised that the superconducting state possess two independent macroscopic properties. Firstly, it has zero DC electrical resistivity below the critical temperature as shown in Fig. 3.1. Secondly, it has near-perfect diamagnetism in the presence of a weak magnetic field. This property results in the exclusion of magnetic flux from the interior of the superconductor, except within a thin region at the surface. The expulsion is referred to as the Meissner effect, as discussed previously. It is this property that distinguishes a superconductor with zero resistivity (which is only true at DC) from a perfect conductor.

DC Resistivity

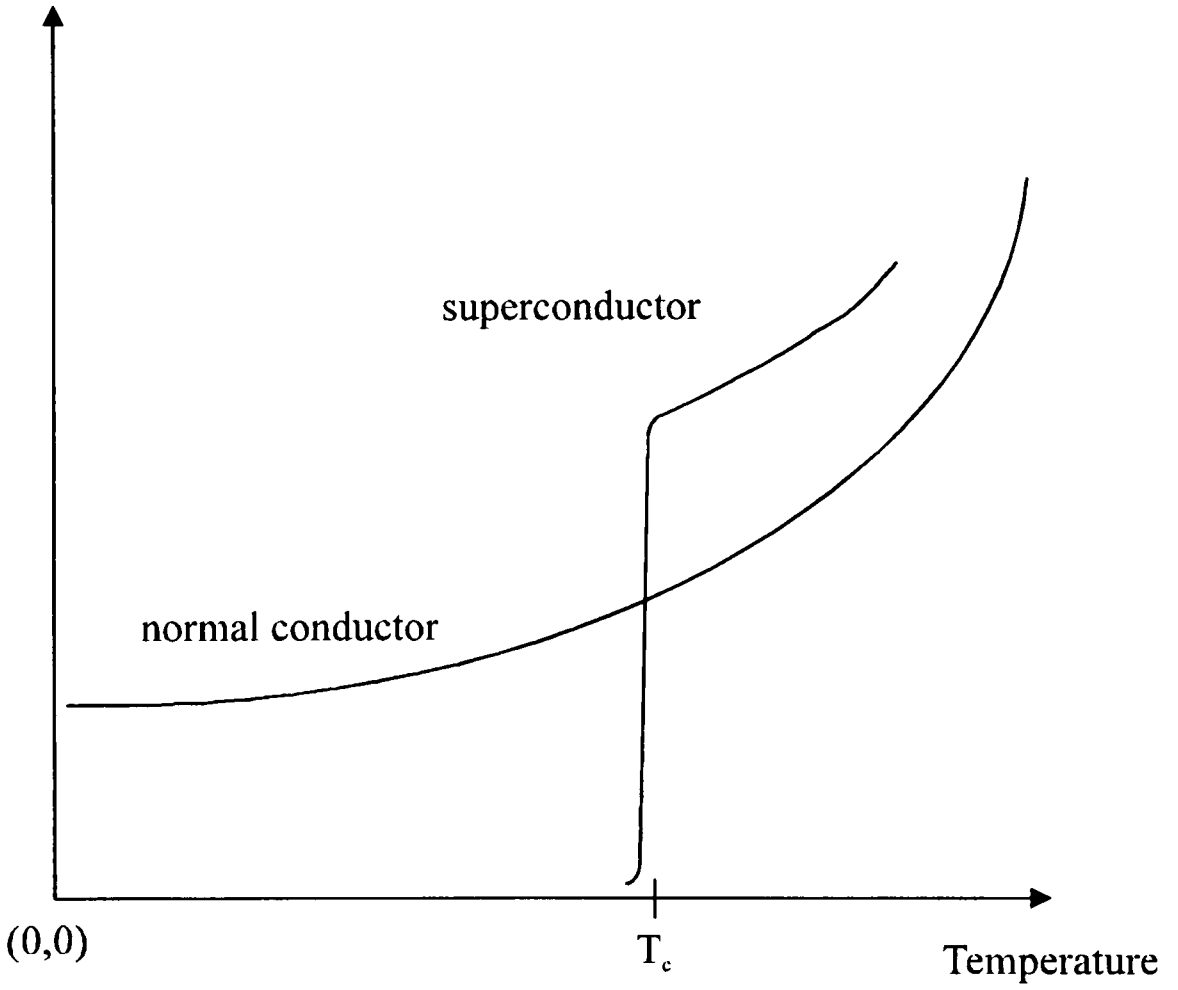

Fig. 3.1. DC resistivity of a superconductor and a normal conductor, as a function of temperature.

In addition, Josephson effects exist in a superconductor device [44]. The junction can be formed when two layers of superconductors are sandwiched with a thin insulator or normal conductor layer between them. The Josephson effect includes the dc effect, the ac effect and the magnetic effect. The dc effect arises when the dc voltage across the junction is zero and there may be a superconducting dc current passing through the junction. The ac effect arises when the superconducting dc current exceeds the critical current and the dc voltage across the junction becomes non-zero. This generates an ac current with a frequency known as Josephson frequency. The magnetic effect arises when the junction zero voltage critical current, which is a function of the magnetic field, is applied to the junction.

A discovery of a material that become superconducting at a critical temperature exceeding 30K was made by Bednorz and Müller in 1986 [45]. The material was a mixture of barium, lanthanum, copper and oxygen, later established as the compound $La_{1.85}Ba_{0.15}CuO_4$. This discovery started a tremendous worldwide effort in discovering superconductors with even higher critical temperatures. Before 1986, liquid helium (boiling temperature of 4.2K) was the usual coolant cold enough for these superconducting experiments. The drawbacks of these low temperature superconductors include impractical low critical temperatures and the associate high cost of liquid helium alternatively the need for a very complicated multistage cryogenic facility. All the available superconductors up to this period are termed low temperature superconductors.

The first superconducting material whose critical temperature was high enough to be cooled by liquid nitrogen (which boils at 77K) was demonstrated by Wu *et al.* in 1987 [46]. This time, the material was a ceramic yttrium-barium-copper-oxide, namely $YBa_2Cu_3O_7$, with a critical temperature of 95K. Such a discovery brightened the prospect of having real superconductors with room temperature critical temperatures. Now, it appears that commercial applications of superconductivity may become more widespread and common.

Since then, several new copper-oxide based material that superconduct at ambient pressure temperatures above 120K were discovered, namely bismuth-strontium-calcium-copper-oxide, thalium-barium-calcium-copper-oxide and mercury-barium-calcium-copper-

oxide. New mechanism for superconductivity is required to explain all high-temperature superconductors. The materials that are commonly studied include $Bi_2Sr_2CaCu_2O_8$ (T_c = 90K), $Bi_2Sr_2Ca_2Cu_3O_{10}$ (T_c = 110K), $Tl_2Ba_2CaCu_2O_8$ (T_c = 110K), $Tl_2Ba_2Ca_2Cu_3O_{10}$ (T_c = 125K) [47] and $HgBa_2Ca_2Cu_3O_8$ (T_c = 133K) [48]. The latter also has a much higher critical temperature of 150K at extremely high pressures [49]. Superconductors with critical temperatures above 30K are copper oxide materials and are termed high-temperature superconductors, or HTS. Detailed discussion of superconductivity is available in references [39], [48], [50] and [51].

3.2 SURFACE IMPEDANCE AND PENETRATION DEPTH [39], [41], [48], [50], [51]

The surface impedance of a superconductor (or in fact any material) is an important parameter which determines the quality of a superconducting material used in practical high frequency applications. It depends on temperature, frequency and surface field. From the measurement of surface impedance, one can obtain valuable information regarding the charge carrier density as well as the conduction mechanism.

The surface impedance is defined as the characteristic impedance seen by a plane wave incident perpendicularly upon a flat surface of the conductor. This can be written as

$$Z_s = \frac{E_t}{\int_{-\infty}^{0} J\,dx} \quad \text{ohms} \tag{3.1}$$

where E_t is the total tangential field, J is the volume current density and x is the direction of wave propagating normally into a planar conductor. Fig. 3.2 illustrates both E_t and J near the surface of a good conductor.

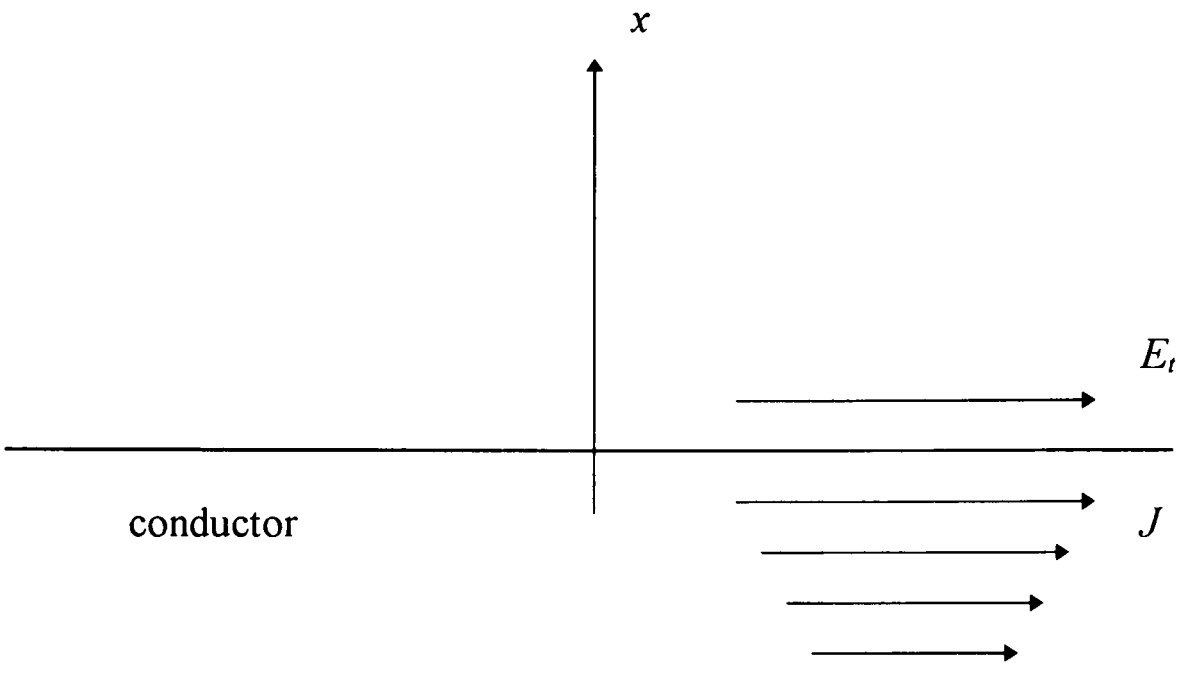

Fig. 3.2. An illustration of E_t and J near the surface of a good conductor [41].

The mathematical discussion of surface impedance for superconductors is similar to that of normal conductors. The impedance consists of a surface resistance (R_s) in series with a surface reactance (X_s), that is,

$$Z_s = R_s + \mathrm{j} X_s \tag{3.2}$$

$$= \left(\sqrt{\frac{\omega\mu_0}{2\sigma_{(sc)}}}\right) + \mathrm{j}\left(\sqrt{\frac{\omega\mu_0}{2\sigma_{(sc)}}}\right) \tag{3.3}$$

$$= (1 + \mathrm{j})\left(\sqrt{\frac{\omega\mu_0}{2\sigma_{(sc)}}}\right) \tag{3.4}$$

$$= \sqrt{(1 + \mathrm{j})^2 \frac{\omega\mu_0}{2\sigma_{(sc)}}} \tag{3.5}$$

$$= \sqrt{\mathrm{j} \frac{\omega\mu_0}{2\sigma_{(sc)}}} \tag{3.6}$$

where $\sigma_{(sc)}$ is the complex conductivity of a superconductor. It is interesting to note that R_s is very small for a superconductor. This is the main reason of using a superconducting material for the antennas.

The surface impedance of a superconductor does not rise as $f^{1/2}$ as with a normal conductor. It in fact rises more rapidly as f^2. The conductivity of a superconductor is complex and is a function of frequency, temperature and material properties. $\sigma_{(sc)}$ can be determined from the two-fluid model as described next.

The concept of the two-fluid theory was developed by Gorter and Casimir [48], [51]. The two fluids consists of a normal current with a carrier density n_n and a superconductive current with a carrier density n_s. Hence, the total carrier density is

$$n = n_n + n_s \tag{3.7}$$

Below T_c, the equilibrium fractions of normal and superconducting electrons, n_n/n and n_s/n, vary with ablsolute temperature T as

$$n_n/n = (T/T_c)^4 \tag{3.8}$$

$$n_s/n = 1 - (T/T_c)^4 \tag{3.9}$$

From eqns. (3.8) and (3.9), it can be seen that at the normal state (T = 0), all of the carriers are superconducting. However, as T approaches T*c*, n_s/n approaches zero.

The two-fluid model correspondingly assumes that the current density **J** consists of two components, namely the supercurrent $\mathbf{J}_{sc}$ and the normal conduction current $\mathbf{J}_{nc}$, that is,

$$\mathbf{J} = \mathbf{J}_{sc} + \mathbf{J}_{nc} \tag{3.10}$$

or,

$$\mathbf{J} = \sigma_{(sc)}\,\mathbf{E} \tag{3.11}$$

where,

$$\sigma_{(sc)} = \sigma_{nc} + \sigma_s \tag{3.12}$$

in which σ_{nc} is the conductivity of the normal current, σ_s is the conductivity of the supercurrent and **E** is the electric field. $\mathbf{J}_{sc}$ has to satisfy London's equations [51]. London's first equation is

$$\frac{\partial \mathbf{J}_{sc}}{\partial t} = \frac{\mathbf{E}}{\mu_0 \lambda_L^2} \tag{3.13}$$

where λ_L is the London's penetration depth and $\partial \mathbf{J}_{sc}/\partial t$ is the time derivative of $\mathbf{J}_{sc}$

London's second equation is

$$\nabla x \, \mathbf{J}_{sc} = - \left(\frac{\mathbf{H}}{\lambda_L} \right) \tag{3.14}$$

in which **H** is the magnetic field and $\nabla x \, \mathbf{J}_{sc}$ is the curl of $\mathbf{J}_{sc}$.

σ_{nc} is a complex quantity defined by

$$\sigma_{nc} = \sigma_{nc1} - j\sigma_{nc2} \tag{3.15}$$

where σ_{nc1} and σ_{nc2} are the real and imaginary components, respectively, of σ_{nc} . The real part contributes to the loss. σ_{nc} can be written as

$$\sigma_{nc} = \left(\frac{n_n \, q_n^2 \, \tau}{m_m} \right) \frac{1 - j\omega\tau}{1 + (\omega\tau)^2} \tag{3.16}$$

where q_n and m_n are the electrical charge, and effective mass of the normal carriers, respectively, and τ is the relaxation time for electron scattering.

On the other hand, σ_s is purely imaginary and does not contribute to the loss. It is given by

$$\sigma_s = 1/(j\omega\mu_0 \lambda_L) \tag{3.17}$$

Substituting eqns. (3.16) and (3.17) into eqn. (3.12) results in

$$\sigma_{(sc)} = \left(\frac{n_n \, q_n^2 \, \tau}{m_m} \right) \frac{1}{1+(\omega\tau)^2} - j \left(\frac{n_n \, q_n^2 \, \tau}{m_m} \right) \frac{\omega\tau}{1 + (\omega\tau)^2} - j \frac{1}{\omega\mu_0\lambda_L} (\omega\tau)^2 \tag{3.18}$$

At microwave frequencies, $(\omega\tau)^2 << 1$, hence eqn. (3.18) can be simplified to

$$\sigma_{(sc)} = \frac{n_n \, q_n^2 \, \tau}{m_m} - j\frac{1}{\omega\mu_0\lambda_L} \tag{3.19}$$

Also,
$$\sigma_{(sc)} = \sigma_1 - j\sigma_2 \tag{3.20}$$

In eqn. (3.19), σ_1 represents the very small loss from the normal carriers, whilst σ_2 is associated with the kinetic energy of the superconductive carriers.

Substituting eqn. (3.20) into eqn. (3.6) gives

$$Z_s = \left(\sqrt{\frac{j\omega\mu_0}{\sigma_1 - j\sigma_2}} \right) \tag{3.21}$$

Since $\sigma_1 << \sigma_2$, eqn. (3.20) can be simplified further using a binomial expansion to [48]

$$Z_s = \sqrt{\frac{\omega\mu_0}{\sigma_2}} \left(\frac{\sigma_1}{2\sigma_2} + j \right) \tag{3.22}$$

Substituting the expressions for σ_1 and σ_2 of eqn. (3.19) into eqn. (3.22) results in

$$Z_s = \frac{\omega \mu_0^{\,2} \lambda_L^3 n_n q_n^2 \tau}{2 m_n} + j \omega \mu_0 \lambda_L \tag{3.23}$$

To account for the temperature dependence of λ_L and σ_n, we have the expressions [48]

$$\lambda_L(T) = \lambda_L(0) [1-(T/T_c)^4]^{-1/2} \tag{3.24}$$

and,

$$\sigma_n = \frac{n_n q_n^2 \tau}{m_m} = \sigma_N (T/T_c)^4 \tag{3.25}$$

where $\lambda_L(T)$ is the London's penetration depth for $T \leq T_c$, $\lambda_L(0)$ is the London's penetration depth as T approaches 0K and σ_N is the normal state conductivity at $T=T_c$. However, for $(\sigma_1 /\sigma_2)^2 << 1$ which is generally true for $T< 0.9T_c$, σ_n approximates to σ_1 . Hence, eqn. (3.23) becomes

$$Z_s = \frac{\omega \mu_0^{\,2} \sigma_1 \lambda_L^{\,3}(T)}{2} + j \omega \mu_0 \lambda_L(T) \tag{3.26}$$

where

$$R_s = \frac{\omega \mu_0^{\,2} \sigma_1 \lambda_L^{\,3}(T)}{2} \tag{3.27}$$

and

$$X_s = \omega \mu_0 \lambda_L(T) \tag{3.28}$$

Eqn. (3.24) can also be written as

$$\lambda_L(T)/ \lambda_L(0) = [1-(T/T_c)^4]^{-1/2} \tag{3.29}$$

The relationship of $\lambda_L(T)/\lambda_L(0)$ with respect to (T/T_c) is illustrated in Fig. 3.3, using $\lambda_L(0)$=1500Å for $YBa_2Cu_3O_{7-x}$ material in microwave devices [48]. T_c is taken as 92K [48]. This material is also used for the fabrication of HTS antennas in this study. From Fig. 3.3, it can be seen that the superconducting state occurs below T_c whilst the normally conducting state occurs above T_c. At $T=T_c$, $\lambda_L(T)/\lambda_L(0)$ gets very large, since the term $[1-(T/T_c)^4]^{-1/2}$ of eqn. (3.29) becomes zero.

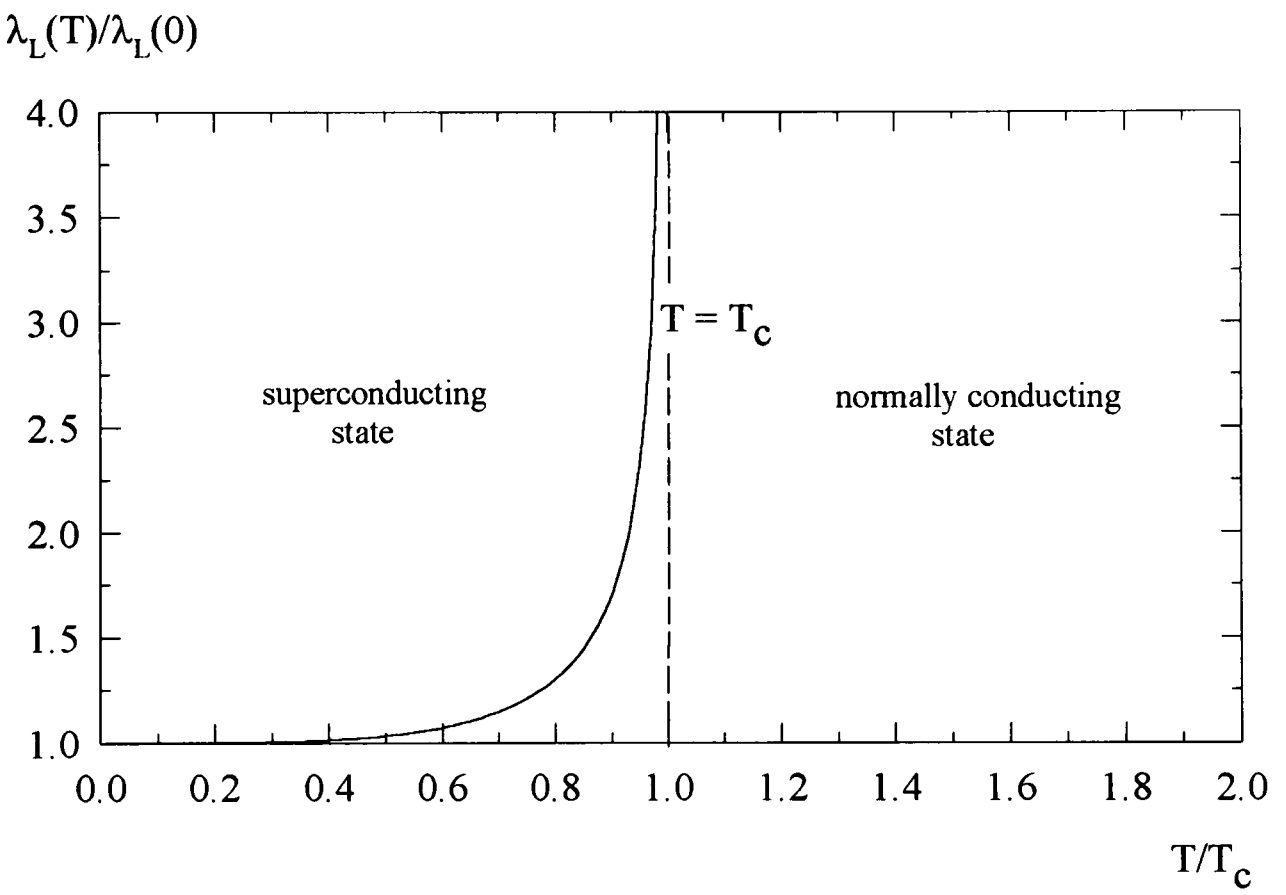

Fig. 3.3. Normalised temperature dependence of penetration depth as a function of temperature normalised to the critical temperature.

The expression for R_s of a superconductor in eqn. (3.27) has been briefly discussed in Section 2.8.1. R_s is proportional to the density of unpaired charge carriers, that is, to the microwave losses. R_s is the quantity that is normally measured with techniques such as resonators [52]. On the other hand, X_s is related to the paired charge carrier density, that is, to the field penetration depth or also known as London's penetration depth. The penetration depth is a measure of the penetration of the fields into a superconductor, similar

to the skin depth in a normal conductor. Notice that X_s of a superconductor is inductive. X_s is independent of frequency, but is dependent of λ_L. λ_L is analogous to the skin depth (δ) of a normal metal. However, unlike δ, λ_L is independent of frequency. It is however dependent of temperature. λ_L is typically on the order of 0.1 μm.

The equivalent inductance in eqn. (3.28) is

$$L_I = \mu_0 \lambda_L(T) \tag{3.30}$$

This is known as the internal inductance. L_I is actually made up of two inductances, namely the magnetic L_m and kinetic inductances L_k. L_m is associated to the penetration of the magnetic field, whilst L_k reflects the kinetic energy of the superconductive carriers, respectively.

The use of the cross-over frequency ($f_{c/o}$) is the usual method of assessing the superconductor loss performance at high frequencies. $f_{c/o}$ is defined as the frequency at which both the HTS material and the normal metal have the same R_s . This occurs because the R_s of the superconductor increases with frequency more rapidly, typically with f^2 , than a normal metal, in which case it increases with $f^{1/2}$ Below $f_{c/o}$, the superconductor has an improved value. For good thick film ceramic materials, $f_{c/o}$ may be as high as 50 GHz at 77K [53] and for good thin film materials above 100 GHz [54]. Hence superconducting antennas will be beneficial when used well below these cross-over frequencies. In addition, a superconductor has a limit on its power handling. For bulk or thick film, the critical current density may be 500 A cm^{-2} ~ 10,000 A cm^{-2} [55].

An effective surface resistance of the thick-film $YBa_2Cu_3O_{7-x}$ at 77K can be approximately expressed in terms of frequency by [56]

$$R_{s\,[f,\,\mathrm{YBCO},\,77\mathrm{K}]} \approx 5.4 \frac{f^2}{f_{c/o}^{3/2}}\ \mathrm{m\Omega} \tag{3.31}$$

where both f and $f_{c/o}$ are given in GHz. The derivation of eqn. (3.31) is given in Appendix 2. Typical measured $f_{c/o}$ values for good quality bulk polycrystalline and unpatterned thick

film $YBa_2Cu_3O_{7-x}$ fall in the 8-10 GHz range [56]. It is lower for patterned films, where edge damage and current accumulation at the edges may cause further degradation.

3.3 SURFACE IMPEDANCE OF SUPERCONDUCTING FILMS WITH FINITE THICKNESS

To account for the finite thickness of a superconducting film deposited on a substrate, the surface impedance discussed in Section 3.2 has to be modified. Consider a plane wave incident upon the film as illustrated in Fig. 3.4.

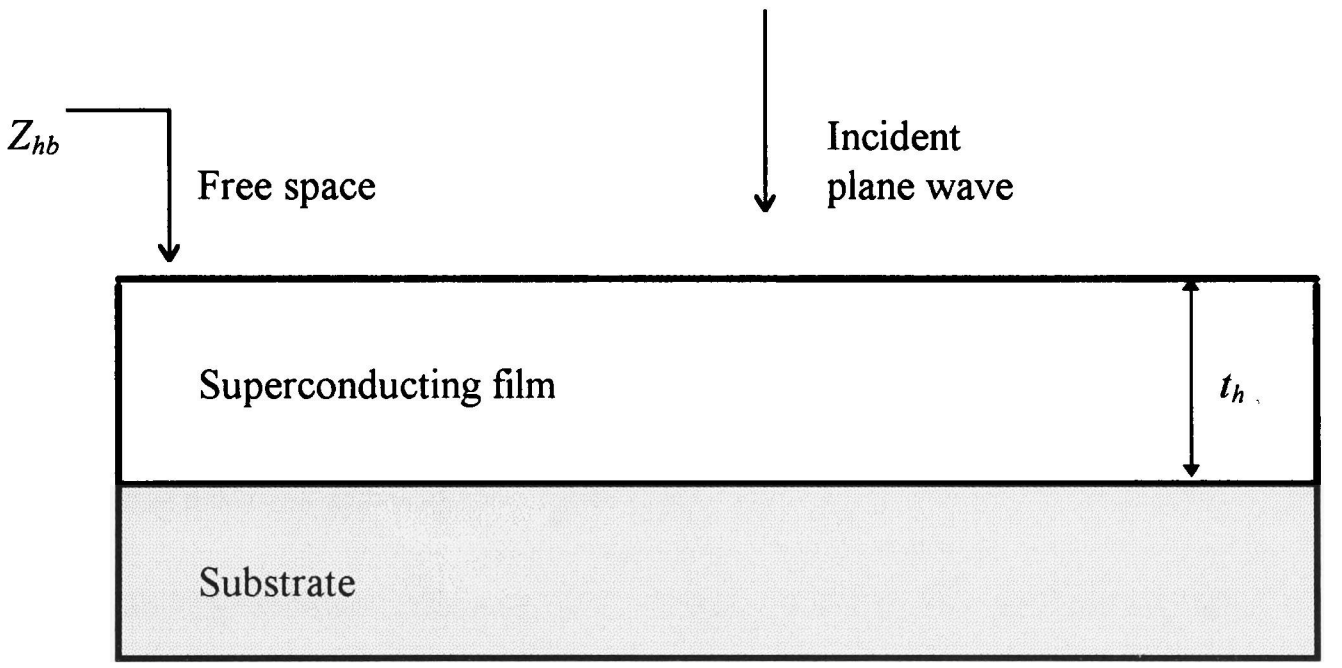

Fig. 3.4. A plane wave incident upon a superconducting film which is deposited on a layer of substrate.

Let the surface or intrinsic impedance and propagation constant of the superconducting material be Z_h and γ_h, respectively, whilst that of the substrate material be Z_b and γ_b, respectively. The thickness of the film is denoted as t_h. Let the impedance of the free space be Z_f. Hence, the impedance looking into the substrate, from the upper surface of the film is similar to eqn. (2.88). Here, it can be written as

$$Z_{hb} = Z_h \frac{Z_b + Z_h \tanh(\gamma_h t_h)}{Z_h + Z_b \tanh(\gamma_h t_h)} \tag{3.32}$$

Considering the approximations [50]

$$Z_b \tanh(\gamma_h t_h) >> Z_h \tag{3.33}$$

and

$$Z_h \tanh(\gamma_h t_h) << Z_b \tag{3.34}$$

Eqn. (3.32) simplifies to

$$Z_{hb} = Z_h \coth(\gamma_h t_h) \tag{3.35}$$

For ultra-thin films, i.e.,

$$\gamma_h t_h << Z_h / Z_b \tag{3.36}$$

eqn. (3.35) can be simplified further to

$$Z_{hb} = Z_h / \gamma_h t_h \tag{3.37}$$

since $\coth(\gamma_h t_h) = 1/\tanh(\gamma_h t_h) \approx 1/\gamma_h t_h$.

However, eqn. (3.35) holds for films of thickness just less than a penetration depth as well as greater than a penetration depth. On the other hand, eqn. (3.37) is not valid for film thickness above a penetration depth [50].

Rewriting the expression for Z_{hb} of eqn. (3.35) as the surface impedance of a finite-thickness superconductor, we have [50]

$$Z_{hb} = R_s \left[\coth\left(\frac{t_h}{\lambda_L(T)} \right) + \frac{t_h}{\lambda_L(T)} \frac{1}{\sinh^2\left(\frac{t_h}{\lambda_L(T)} \right)} \right] - j X_s \coth\left(\frac{t_h}{\lambda_L(T)} \right) \tag{3.38}$$

Eqn. (3.38) applies for $\sigma_1 << \sigma_2$.

However, for thin superconducting films close to T_c, the surface impedance is [50]

$$Z_{hb} = \frac{1}{t_h} \frac{\omega^2 \mu_0^2 \lambda_L^4(T)}{1 + \sigma_1^2 \omega^2 \mu_0^2 \lambda_L^4(T)} (\sigma_1 + j\sigma_2) \tag{3.39}$$

which is not a good approximation for films of the order of a penetration depth thick and above.

If the substrate is lossy, eqn. (3.32) can be written as [50]

$$Z_{hb} = \frac{Z_h}{\tanh(\gamma_h\ t_h)}\left[\frac{1 + \frac{Z_h}{Z_b}\tanh(\gamma_h\ t_h)}{\frac{Z_h}{Z_b}\tanh(\gamma_h\ t_h) + 1}\right] \tag{3.40}$$

Assuming

$$\sqrt{\frac{\omega\mu_0}{\sigma_2}}\left(\frac{\sigma_1}{2\sigma_2} + j\right) >> \sqrt{\frac{\mu_0}{\varepsilon_d}}\left(1 + j\frac{\sigma_d}{2\omega\varepsilon_d}\right) \tag{3.41}$$

eqn. (3.40) can be rewritten as

$$Z_{hb} = Z_h\left[\coth(\gamma_h\ t_h) - \frac{Z_h}{Z_b}\frac{1}{\sinh^2(\gamma_h\ t_h)}\right] \tag{3.42}$$

Notice that eqns. (3.42) and (3.35) are similar but with an additional term $-\frac{Z_h^2}{Z_b}\frac{1}{\sinh^2(\gamma_h\ t_h)}$ whose parameters are associated with the substrate. By splitting eqn. (3.42) into its real and imaginary components while still assuming $\sigma_1 << \sigma_2$, results in [50]

$$Z_{hb} = R_s\left[\coth\left(\frac{t_h}{\lambda_L(T)}\right) + \frac{t_h}{\lambda_L(T)}\frac{1}{\sinh^2\left(\frac{t_h}{\lambda_L(T)}\right)}\right]$$

$$+ X_s^2\sqrt{\frac{\varepsilon_d}{\mu_0}}\left[1 - j\frac{\sigma_d}{2\omega\varepsilon_d}\right]\left[\frac{1}{\sinh^2\left(\frac{t_h}{\lambda_L(T)}\right)}\right] - jX_s\left(\frac{t_h}{\lambda_L(T)}\right) \tag{3.43}$$

where the term $\frac{\sigma_d}{\omega\varepsilon_d}$ is the loss tangent (tan δ) of the substrate. The loss tangent of the substrate is affecting the value of the surface resistance of the superconductor. This term represents penetration of energy through the film into the substrate.

The surface impedance of a superconductor can also be affected by its surface roughness [57]. Although both the surface resistance and surface impedance may increase as the surface roughness approaches the penetration depth, the effect is small. A maximum deterioration of a factor of about 2 may be experienced when the surface roughness increases to several penetration depths. Practically, superconducting films have smooth surfaces of the order of a penetration depth. However, the surface roughness of bulk and thick film materials are not necessarily of that order.

3.4 SMALL HIGH-TEMPERATURE SUPERCONDUCTING ANTENNAS

Miniature superconducting antennas has been the subject of extensive research for the past years. This is reviewed over the recent seven years as follows.

In 1990, Hansen [58] examined the applicability of superconductors to antennas where the roles of external and internal fields are emphasised. He stressed that the use of a superconductor will produce a negligible change in the external fields, resulting in similar impedance, pattern and directivity to normal conductors. A major change is experienced only by the internal fields. This leads mainly to low conduction losses. Hansen concluded further that all antenna properties, except efficiency, depend upon external fields. These are essentially unaffected by superconductors. With thin-film superconductors, internal fields are critical. In this work, electrically small antennas and their matching, two areas where superconductors have been and should be considered, was evaluated quantitatively. The discussion on electrically small antennas was focused in the fundamental limitations on bandwidth, electrically short dipoles, inductively loaded short whips and electrically small loops. Hansen concluded that superconducting materials offer major improvements in matching efficiency, for both superdirective arrays and for electrically small antennas. However, it was claimed that size reduction of antennas will generally not be aided by superconductors.

Hansen [40] re-examined the applicability of superconductors to antennas. He concluded that superdirective arrays and electrically small antennas will not benefit directly

from superconductors, but their tuning/matching networks will. Hence, there will be a significant extension of the useful range of these antennas.

An electrically small antenna of short dipole with twin-lead stub matching network, as shown in Fig. 3.5(a), was theoretically analysed by Dinger and White [59], [60]. It was shown that the antenna ohmic losses actually account for the smallest fraction of the losses. It was further suggested that it is only the matching network that need be made from high-temperature superconducting material. Expressions for the input and radiated powers were derived, from which the antenna efficiency was calculated.

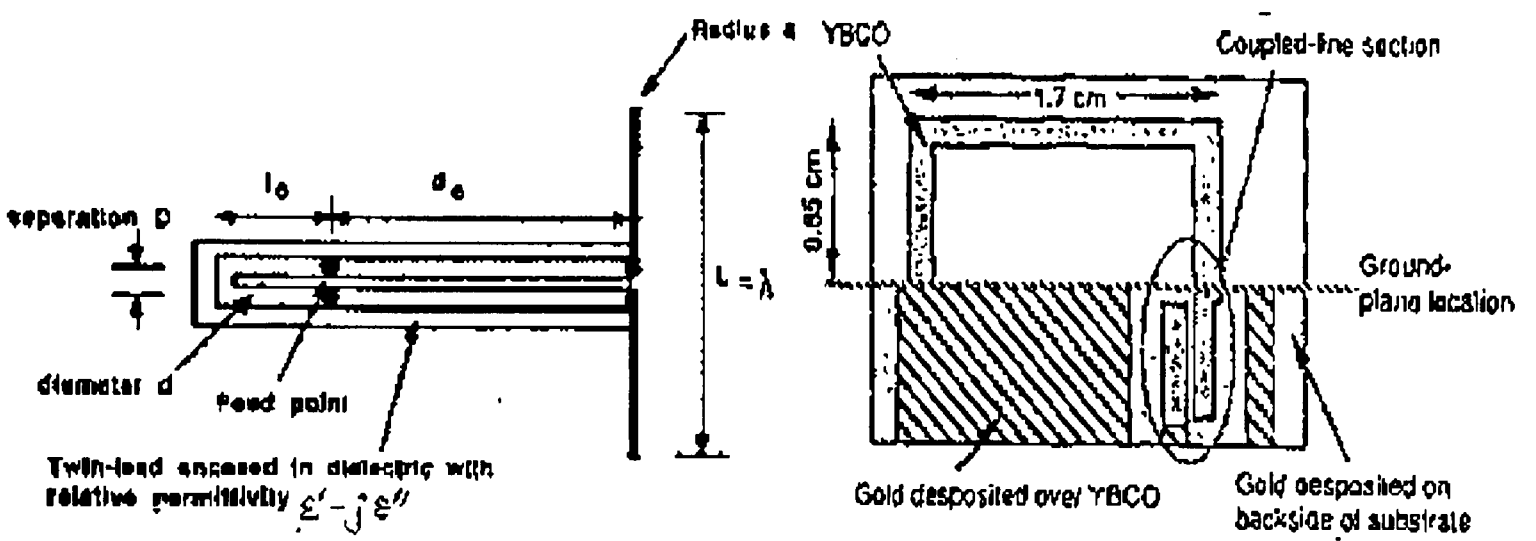

(a) (b)

Fig. 3.5. (a) A short dipole [59], [60], (b) A half-loop antenna [61].

Dinger *et al.* [61] experimentally investigated a 500 MHz half-loop antenna and matching network fabricated from the thin-film high-temperature superconductor, $YBa_2Cu_3O_{7-x}$ or YBCO. This was indeed the first thin-film high-temperature superconductor antenna demonstrated below 2 GHz. Fig. 3.5(b) shows the half-loop antenna structure. Two radiation efficiency formulations were derived. The first was derived from the Friis transmission equation whilst the second is referred as the transfer radiation efficiency. The latter divides out the residual mismatch of the matching network, and permits a more direct comparison of the losses in the YBCO and copper devices. These two definitions are identical at the temperature at which the devices are matched. It was experimentally found that the antenna demonstrates a radiation efficiency of 20 percent, compared to 7 percent for a comparable copper antenna, this was at the lowest temperature (20K) the closed cycle refrigerator was capable of. However, the superconducting antenna

is still inefficient. Nevertheless, if several single elements are combined to form an array structure, much higher efficiency can be achieved. However, this is at the expense of the bandwidth.

In a lengthy discussion of high-temperature superconductors and their application in passive antenna systems; electrically-short dipole antennas, electrically-small loop antennas and superdirective arrays were examined by Williams and Long [41]. The radiation efficiency was defined to account for the ohmic loss associated with the antenna element(s) and that associated with the transmission line feed(s) and matching circuit(s). A trade-off exists between efficiency and Q (or bandwidth) when using superconducting materials for electrically-short dipole antennas. For the small loops, the load matching requirements are more stringent due to very low radiation resistances. Their antenna efficiencies are greatly enhanced by having superconducting matching circuits, but the Q value of the loop will increase even more sharply. These dipoles and loops formed the common elements of superdirective arrays. With dipole elements, superconducting feed and matching networks will contribute to higher gains, at the cost of decreased bandwidths. As Hansen [58] had pointed out, superconducting elements do not offer significant improvement. With loop elements, Williams and Long noted that the individual element efficiency will be increased. When the feed and matching networks are also made from superconducting material, the entire array efficiency is greatly enhanced. However, higher Qs resulted mean impracticably narrow bandwidths.

Another lengthy discussion of the potential of high-temperature superconductors for passive antenna applications were made by Dinger *et al.* [62]. Electrically small antennas and their matching networks; feed and matching networks for compact arrays with enhanced directive gain (superdirective arrays); and feed networks for millimetre-wave arrays; were examined. Preliminary experimental results on a TlBaCaCuO half-loop antenna structure similar to that of Fig. 3.5(b) were presented. The high-temperature superconducting antennas showed a factor of 5 increase in the radiation efficiency over a copper antenna at the same temperature. This is however at the expense of bandwidth.

Electrically small superconducting antennas were highlighted by Chaloupka [63] in 1990 as an example of overcoming the very low efficiency of normally conducting small antennas. For single-resonance devices, electrically small superconducting antennas exhibit a very low frequency bandwidth. However, it was suggested that, in principle, small superconducting antennas which have both a high efficiency and relatively wide bandwidth can be realised by multiresonant structures. These structures may employ either a superconducting matching network or travelling wave structures.

Chaloupka *et al.* [64] presented experimental and computational performance of a miniaturised 2.4 GHz high-temperature superconductor microstrip antenna. The design structure is shown in Fig. 3.6. They claimed that the miniaturisation employs a new stepped impedance patch shape as well as having a relatively high substrate permittivity. However, the shape has been theoretically investigated earlier by Palanisamy and Garg [65] but with a low substrate permittivity. Comparison with a similar copper structure on the same substrate material showed that the superconducting antenna has increased radiation efficiency from 35 % to 65 %, whereas the corresponding copper antenna radiation efficiency is only from 1 % to 6 %. They suggested that considerable improvements could be obtained if a substrate compatible with a high temperature superconductor with a lower loss tangent is available. From experimental investigations, they also observed a non-linear power dependence of the antenna gain at 77K.

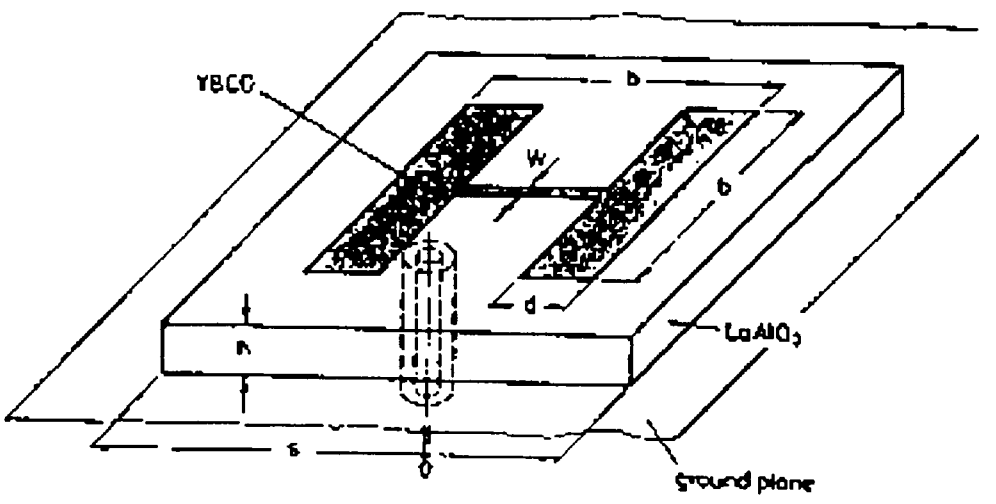

Fig. 3.6. A single patch antenna [64].

An extended version of the single patch antenna, the dual-stacked H-patch antenna, was discussed by Pischke *et al.* [66]. It was demonstrated that this antenna is superior to the single H-patch antenna with respect to bandwidth and radiation efficiency. The bandwidth increased by a factor of about 2, whilst the efficiency by a factor of about 1.5. An optimised design was not accounted for. However, further improvements are expected.

Chaloupka and Müller [67] briefly discussed the microwave properties of presently available thin film high-temperature superconductor. The conditions for applications to planar passive microwave devices was also briefly outlined. A short discussion of the application to electrically small antennas, conventional arrays and superdirective arrays was also made. All these were cases where the efficiencies can become very low when the structures were made from normal conducting materials.

Recently, Chaloupka *et al.* [68] designed and tested a novel type of multiresonant meander structure as depicted in Fig. 3.7. This structure was realised with YBCO thin film deposited on a $LaAl_2O_3$ substrate. It was claimed that a relatively wide half-power bandwidth of 4 %, with respect to the antenna small size was obtained. Furthermore, this structure was capable of achieving a sufficiently high radiation efficiency of more than 60 % at 77K at a resonant frequency of 4.2 GHz. The normal-conducting antenna version was estimated to be only about 5 % efficient. A radiation pattern which follows closely that of a magnetic dipole oriented parallel to the substrate surface and perpendicular to the meander arms was also obtained. In addition, no frequency-response power dependence was observed in the measurement range up to an input power of 20 dBm. This is a very interesting structure with promising performance. However, similar normal-conducting structure operating in free space will resonate at a very much higher frequency of about 18.0 GHz. This means that the antenna is electrically large, though it is physically small. It was the high permittivity $LaAl_2O_3$ substrate that mainly constitutes to the superconducting antenna size reduction. Furthermore, the antenna was not very well-matched throughout the relatively wide bandwidth region achieved.

Fig. 3.7. A multiresonant meander structure [68].

A group from NTT Interdisciplinary Research Laboratories, in Japan, has presented its work on a few designs of superconducting small antennas. One work was basically the helical radiator with different matching circuit designs. Itoh *et al.* [37] aimed to realise the potential of achieving highly-efficient small and/or superdirective antennas. A design of N-element small and superdirective antennas composed of normal-mode helical radiators and quarter-wave matching circuits was proposed. One and two element antennas fabricated with high-temperature superconducting bulk materials was experimented. These structures are depicted in Figs. 3.8(a) and (b). The 500 MHz one-element antenna (Fig. 3.8(a)) consists of $\lambda/40$ helical radiators made of sintered $Bi(Pb)_2Sr_2Ca_2Cu_3O_x$, or BSCCO, bulk material. Its matching circuit consists of linear parallel lines made of copper rods. The matching circuit also serves as a balun since it is directly jointed to the microstrip feed line. It was experimentally found that the absolute maximum actual gain was -1.2 dBi at 80K, which was only 2.7 dB lower than that of a half-wave dipole antenna. The antenna maximum actual gain at 80K was 7.8 and 6.2 dB higher than those of similar copper structure at 300K and 80K, respectively. A 70 % radiation efficiency was estimated, which indicated that this antenna may realise a very high efficiency in spite of its small size. In addition, the antenna was found to be fairly well matched with -9.1 dB input reflection coefficient. The second design shown in Fig. 3.8(b) is a 900 MHz two-element superdirective end-fire antenna with structure similar to the first design. The $\lambda/20$ radiators with $\lambda/11$ element spacing were fabricated from sintered YBCO bulk material. However, the matching circuits were made of YBCO thick films whilst the branch circuit was made of copper foils. It was experimentally found that the absolute maximum actual gain at 80K was -5.2 dBi. This was 4.4 and 3.0 dB higher than those of similar copper antenna at 300K and

80K, respectively. The superconducting antenna unidirectional radiation pattern was found to agree well with their designed 7.5 dB front-to-back lobe ratio value, though the two patterns differed in the rear. This antenna was also found to be fairly well matched with an input reflection coefficient of -10.3 dB. In the third design, parallel meander lines were employed in the design of the matching circuit, whilst the radiator was similar to the first design. The meander lines were fabricated from thin-film $EuBa_2Cu_3O_x$, or EBCO, on an MgO substrate. By meandering the parallel lines, the antenna size was reduced by a factor of 4. In this design, it was experimentally found that the maximum actual gain at 70K was 9.6 and 5.4 dB higher than those of similar copper structure at 300K and 70K, respectively. However, the absolute maximum actual gain was -4.5 dBi, which was lower than that of the first designed antenna. It was claimed that this was due to the unsuitability of the silver paste used for joining the superconducting thin films with the bulk materials. Though all the designs were capable in realising highly-efficient small and superdirective antennas, the use of sintered ceramics poses problems in fabricating small complex structures. Moreover, the loss that occurred at the joint limited the antenna gain. This has to be overcome if the contact resistance is significant.

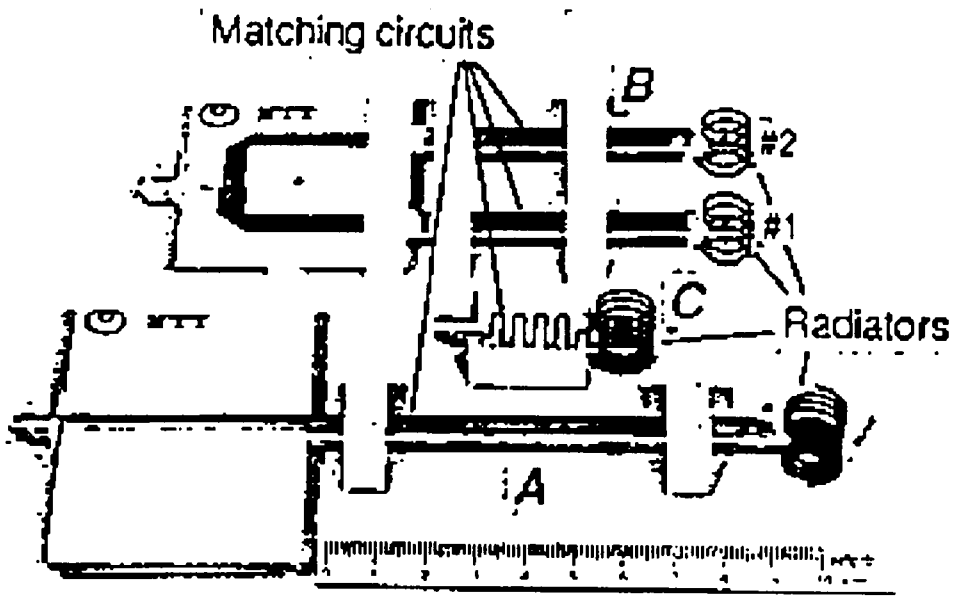

Fig. 3.8. Helical radiators with different matching circuits [37].

Suzuki *et al.* [69] proposed a meander radiator structure with a chip capacitor for impedance matching. The antenna structure is shown in Fig. 3.9(a). The radiator was fabricated from EBCO thin films on MgO substrate. Two other designs were built and

tested for comparing the losses in the radiators and the capacitors. One design is a similarly built copper structure, whilst the other design is an identical EBCO meander radiator but with an $\lambda/4$ impedance matching circuit. The matching circuit was in the form of parallel transmission lines made of copper rods. Experimentally, it was found that the proposed antenna operated properly as a 900 MHz small ($\lambda/42$) antenna. The meander radiator operated as an electrical short dipole with actual gain of -4.8 dBi at 896 MHz and 80K. This was 4.0 dB higher than that of the copper antenna at 80K. However, losses that occured at the capacitor impose limitations to the antenna gain.

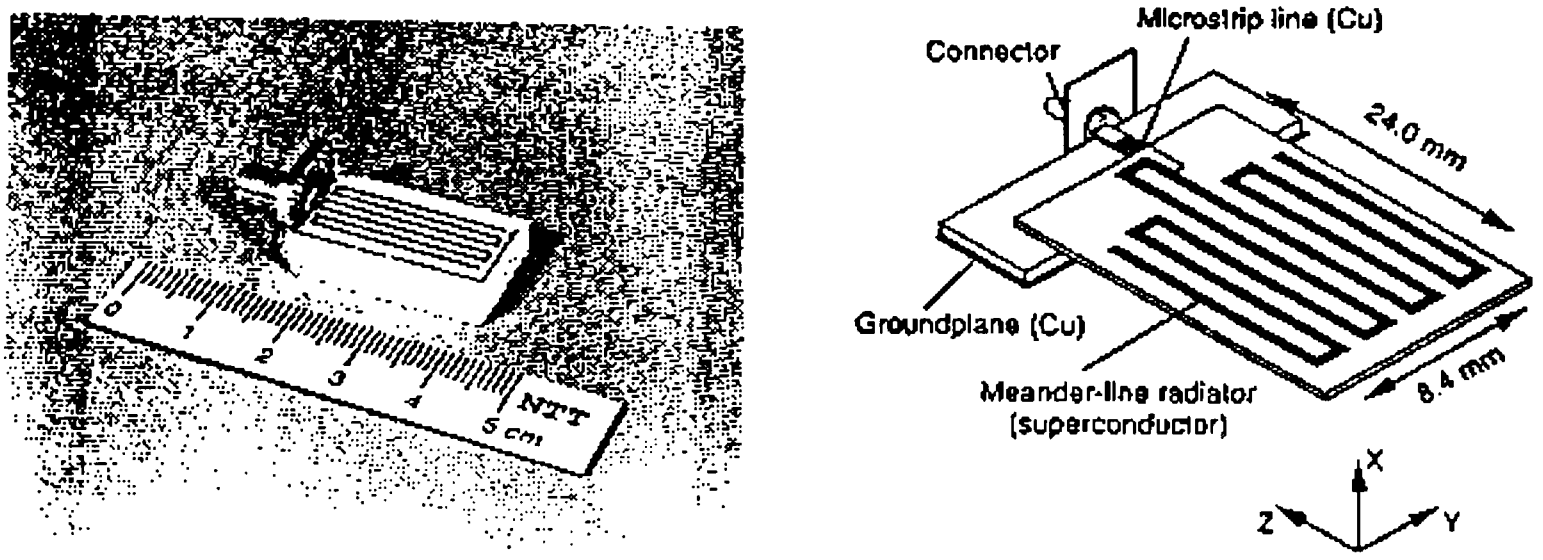

(a) (b)

Fig. 3.9. Meander radiators with different matching circuits [69], [70].

Suzuki *et al.* [70] extended their work by proposing a superconductive thin film antenna, without any joint between the radiator and the feed line, as shown in Fig. 3.9(b). This antenna structure consists of a self-resonant meander-line radiator which was electromagnetically coupled to a 50 Ω microstrip line. It was experimentally found that the antenna actual gain was -2.1 dBi at 950 MHz, that is 14.6 dB higher than that of a similar copper antenna at 953 MHz. The available gain of their superconducting antenna was 1.7 dB higher than that of their previous design [71], although their calculated losses were almost the same. It was concluded that the relatively higher gain is attributed to eliminating the additional matching circuit and contacts. The measured and calculated patterns agreed

well, indicating that the antenna operates as a $\lambda/38$ dipole. Though interesting results were obtained, they did not measure and theoretically calculate the antenna radiation efficiency, which is equally important.

At the University of Birmingham, in the United Kingdom, the world first high-temperature superconducting antenna was practically demonstrated and reported by Khamas *et al.* [72] in 1988. It comprised of a short dipole antenna with matching network made from bulk YBCO ceramic wire, mounted on a Tufnol substrate, as shown in Fig. 3.10. Optimum matching was achieved at 535 MHz. This superconducting antenna exhibited a 6 dB gain enhancement at 77K over a cryogenically cooled similar copper structure. Furthermore, it achieved about 12 dB gain enhancement over the reference copper antenna at room temperature.

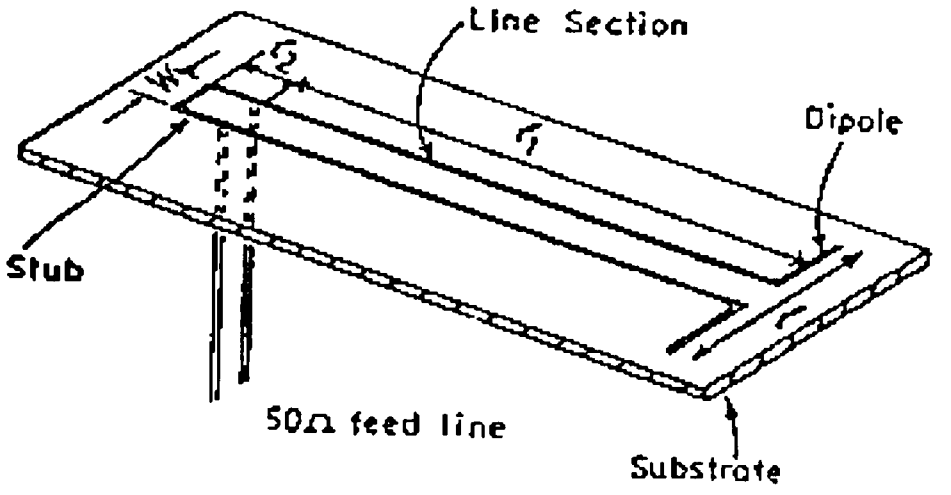

Fig. 3.10. A short dipole antenna [72].

Analysis of the antenna critical currents was discussed by Gough *et al.* [73]. It was found experimentally that linearity of the radiated field strength was maintained up to an input power of almost 20 dBm. At 550 MHz, the rf critical current was calculated to be approximately 1 A. Furthermore, the maximum penetration depth was estimated to be 67 microns. Hence, the critical current density lower bound turned out to be ~500 A cm^{-2}.

Following the successful demonstration of the superconducting small dipole antenna, Wu *et al.* [74] demonstrated a loop antenna made of YBCO superconducting wire loop with a matching network, as depicted in Fig. 3.11, which resonated at 450 MHz. The experimental results showed that the radiated power of the superconducting loop antenna was 9 dB higher than that of the room-temperature copper loop, whilst it was 5 dB higher than that of the supercooled copper structure. In addition, the supercooled and the room-temperature copper loop antenna was 68 % and 87.5 % less efficient, respectively, than the superconducting loop antenna. Both the copper antennas showed low radiation efficiencies, as theoretically expected. It was concluded that the smaller the electrical dimensions, the larger is the potential improvement in efficiency.

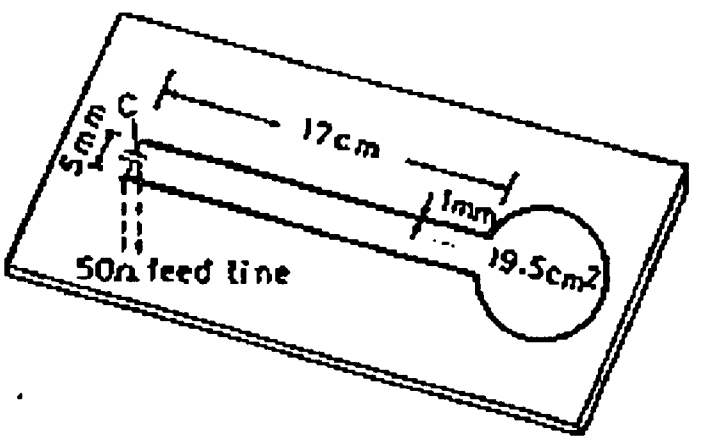

Fig. 3.11. A loop antenna [74].

Wu *et al.* [75] observed a 30 dBm limitation in the maximum output power of the superconducting loop antenna. Similar effect was observed previously with the superconducting dipole antenna [73], showing that the critical current of the superconductor was reached.

Due to difficulty in handling the small wire antennas mechanically, a printed loop version was fabricated and tested by Wu *et al.* [55] in 1990. The 440 MHz printed loop antenna (similar shape as Fig. 3.11) was fabricated on alumina substrate and its performance was compared with those of identical silver antenna. It was found that the printed YBCO loop antenna system showed an improvement on silver system at 77 K. There was a 3.5 dB difference in the radiated field. This could be due to the fact that the YBCO material

used in the fabrication has a low cross-over frequency with copper at 77K as a result of contamination of the material with the alumina substrate. It was claimed that if the YBCO thick film material had a lower surface resistance, the superconducting antenna would perform much better in terms of power gain. Investigation on material with much higher cross-over frequencies in order to improve the antenna performance is being continued.

A closed helix superconducting antenna shown in Fig. 3.12 was briefly discussed by Lancaster *et al.* [76]. The matching circuit consisted of a short length of parallel wire YBCO transmission line with a small capacitor ultrasonically soldered to the end, as with previous loop antenna designs. With this design, they found that the superconducting antenna showed a 5.8 dB gain improvement over the identical copper antenna at 77K, with additional gain enhancement contributed by the superconducting matching network.

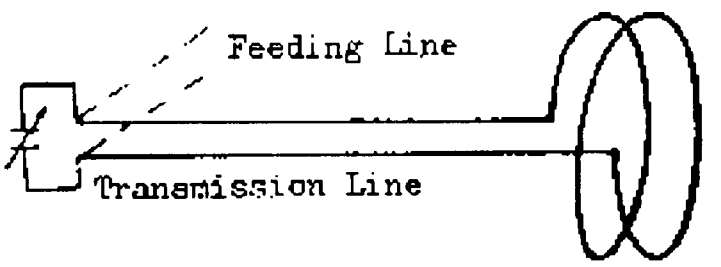

Fig. 3.12. A closed helix antenna [76].

Lancaster *et al.* [77] assessed the performance of previously investigated electrically small superconducting dipole and loop antennas. Various aspects discussed include efficiency, Q-factor, input impedance, power gain, power handling and signal-to-noise ratio, with considerations of the performances when used as both transmitters and receivers. Experimental results of the two antennas were also discussed. The far-field expressions showed that the antennas had the same doughnut-shaped radiation pattern and, hence, the same directivity of 1.5. Efficiency expressions of both antennas indicated that for similar wire diameters, for both copper and superconductors, the dipole efficiency is much larger than the loop. Radiation resistance of the two structures seemed the major factor that caused this difference. It was theoretically showed that the matching network loss is much more important than the ohmic loss in the antennas. Similar conclusion was made earlier by

Khamas *et al.* [73] using the method of moments. Further, Lancaster *et al.* [77] stressed that the shape of the antenna is important in the determination of the lowest Q-factor for a given efficiency, although there is a fundamental limitation to the Q-factor for any given volume occupied by the antenna [58]. However, it was suggested that for medium size antennas and practical surface resistance values, the improvement in efficiency may be quite substantial, with little penalty to be paid in the increase in Q-factor. For receiving antennas, it was pointed out that the signal-to-noise ratio is an important criterion. Above 30 MHz, since the real sky temperature will be significantly reduced, it was argued that there will be significant improvement in using an efficient superconducting antenna in the receiving mode. Finally, for power transmitting antennas, thin film current densities are much more appropriate. However, they are not available with surface areas larger than a few cm^2 and large thicknesses. In contrast, thick film and bulk material sizes are essentially unlimited in size but they have much lower critical current densities. The experimental results indicated that both antennas showed significant improvement in efficiency over their copper counterparts. It was concluded that with careful designs, the theoretical calculations showed that superconducting small antennas can show very considerable improvements over their copper counterparts in all aspects of performance.

Another work which involved an YBCO planar thick film small loop antenna with an integrated superconducting matching network of Fig. 3.13 was reported by Lancaster *et al.* [78]. The whole structure fitted onto a 2 $in.^2$ zirconia substrate, almost 1/20th of a free space wavelength at the operating frequency of 300 MHz. This work was intended to demonstrate the use of thick film material in a practical application in order to assess its potential limitations and to show the improved performance with the available materials. The importance of making both the antenna and the matching network out of superconductor was stressed if maximum efficiency is to be obtained. It was concluded that good quality thick film YBCO has been demonstrated for the first time in an antenna application. Experimental results, which agreed well with theory, showed a significant improvement over a similar silver antenna when operating at the same liquid nitrogen temperature. However, it was found that the material surface resistance appeared to be

degraded in patterned films as oppossed to unpatterned films. This problem is being investigated further. It was also suggested that the trade off between Q and gain need to be considered. Furthermore, antennas need to be designed with integrated matching networks and geometries that can be varied to increase the bandwidth at the expense of gain.

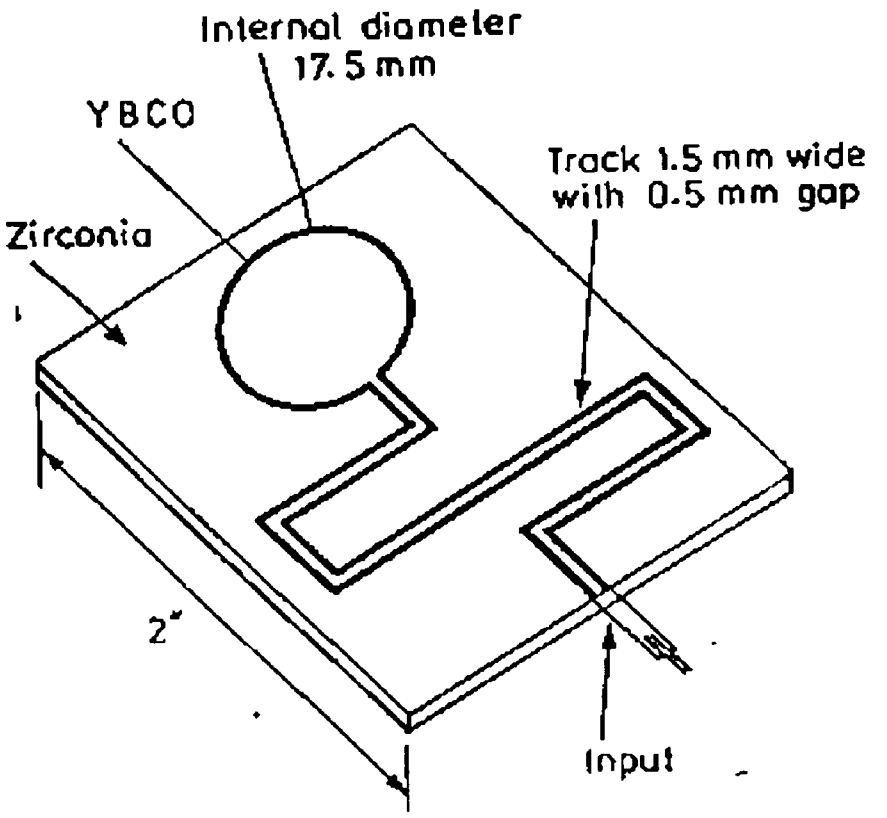

Fig. 3.13. A loop antenna with integrated matching circuit [78].

The investigation of four electrically small thick-film YBCO loop antenna designs with different feeding-matching configurations were recently reported by Ivrissimtzis *et al.* [56]. Two of the antenna structures were previously reported in references [55] and [78]. Fig. 3.14 also shows the other two antenna structures. In this work, the importance of an estimation of the antenna's overall efficiency for a complete characterisation of a high-temperature superconductor antenna was stressed. Microwave network analysis and method of moments were employed for quantitative assessment of the antennas loss mechanisms. The applicability of low frequency efficiency measurement methods for highly efficient high-temperature superconductor antenna systems was outlined and extended for improved accuracy. These methods are further discussed in Section 4.2.2. It was experimentally found that the antennas demonstrated superior gain at the designed resonant frequencies (100 MHz - 500 MHz) over similar supercooled copper and silver structures. This is, however, at the expense of higher Q-factors.

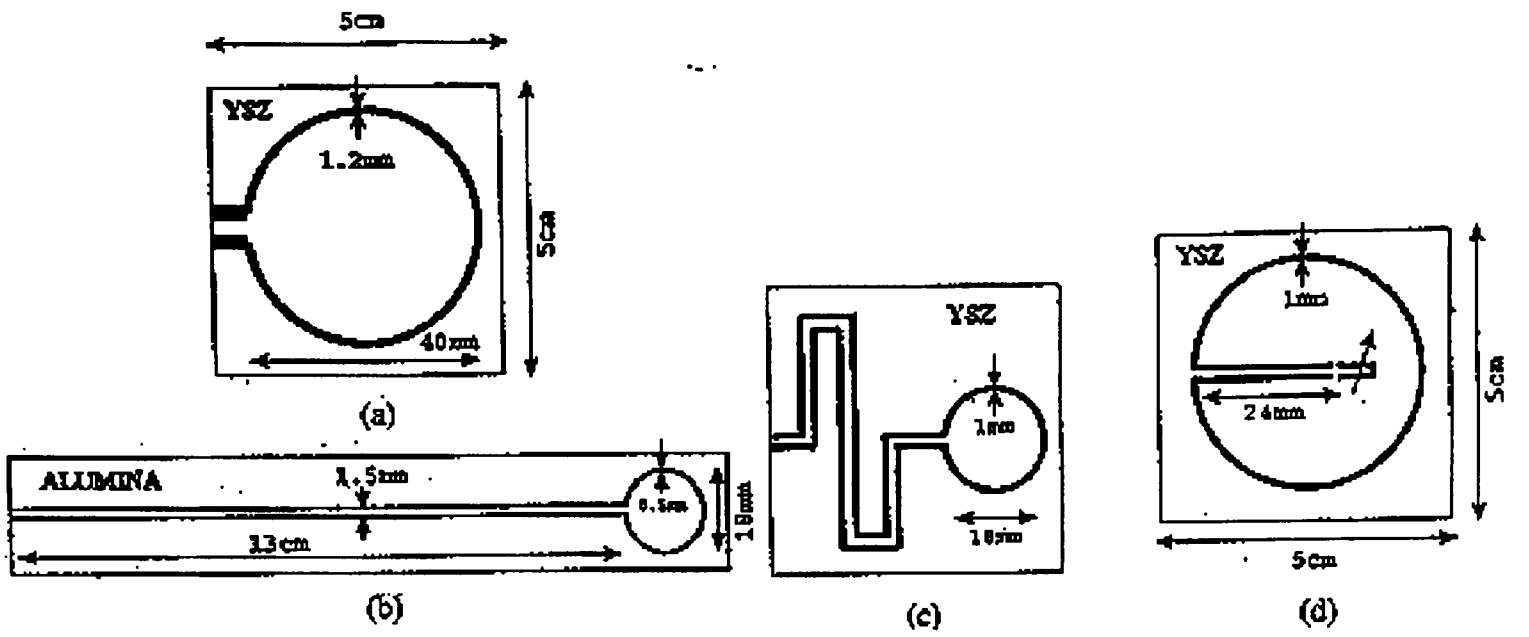

Fig. 3.14. Loop antennas: (a) open loop, (b) loop with stub matching, (b) loop with meander matching, (c) loop with internal stub matching [56].

Recently, Ivrissimmtzis *et al.* [79] discussed the use of high-temperature superconductors in a proposed new class of coplanar radiating structures. These were the folded dipole array and the meander dipole antennas. The geometries of the antennas were as shown in Fig. 3.15. The meander dipole is discussed further in this dissertation. Preliminary experimental results showed that a significant electrical size reduction is achievable while retaining a relatively broadband behaviour. A copy of the published paper can be referred to in Appendix 3.

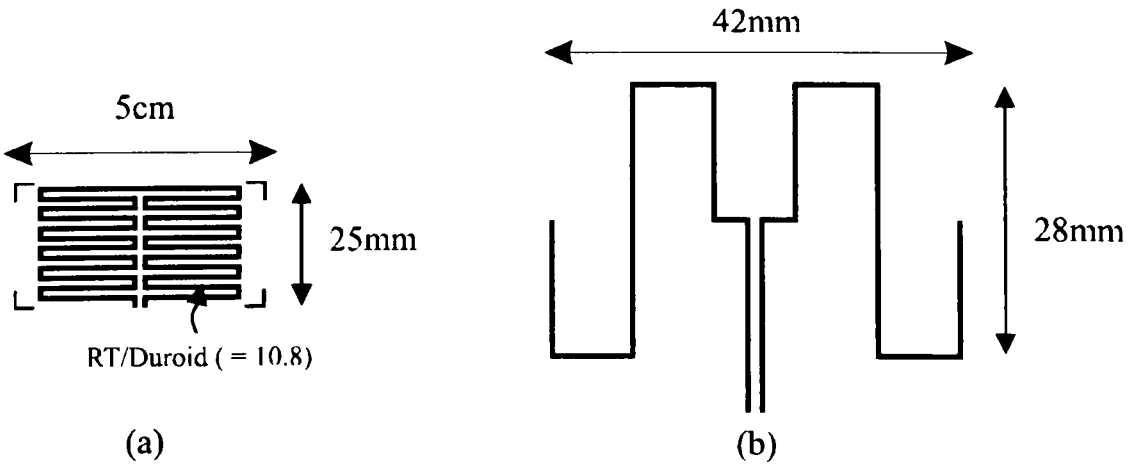

Fig. 3.15. Coplanar radiating structures: (a) folded dipole, (b) meander dipole [79].

The meander structure of Fig. 3.11 is further investigated [80]. Comparison between the performance of the copper structures, with and without the coplanar strip feeding line, is made. This is then compared with an HTS thick-film meander with a feeding line. Fig. 3.16 shows the antennas with and without the feeding line. At 77K, the HTS meander operates at 600 MHz with an improved gain over similar copper structure at 300K. The corresponding copper structure operates at 793.75 MHz. At the operating frequencies of the meander antennas, all the antennas are electrically small. Further discussion of the structures is given in this study. The corresponding published paper can be referred to in Appendix 4.

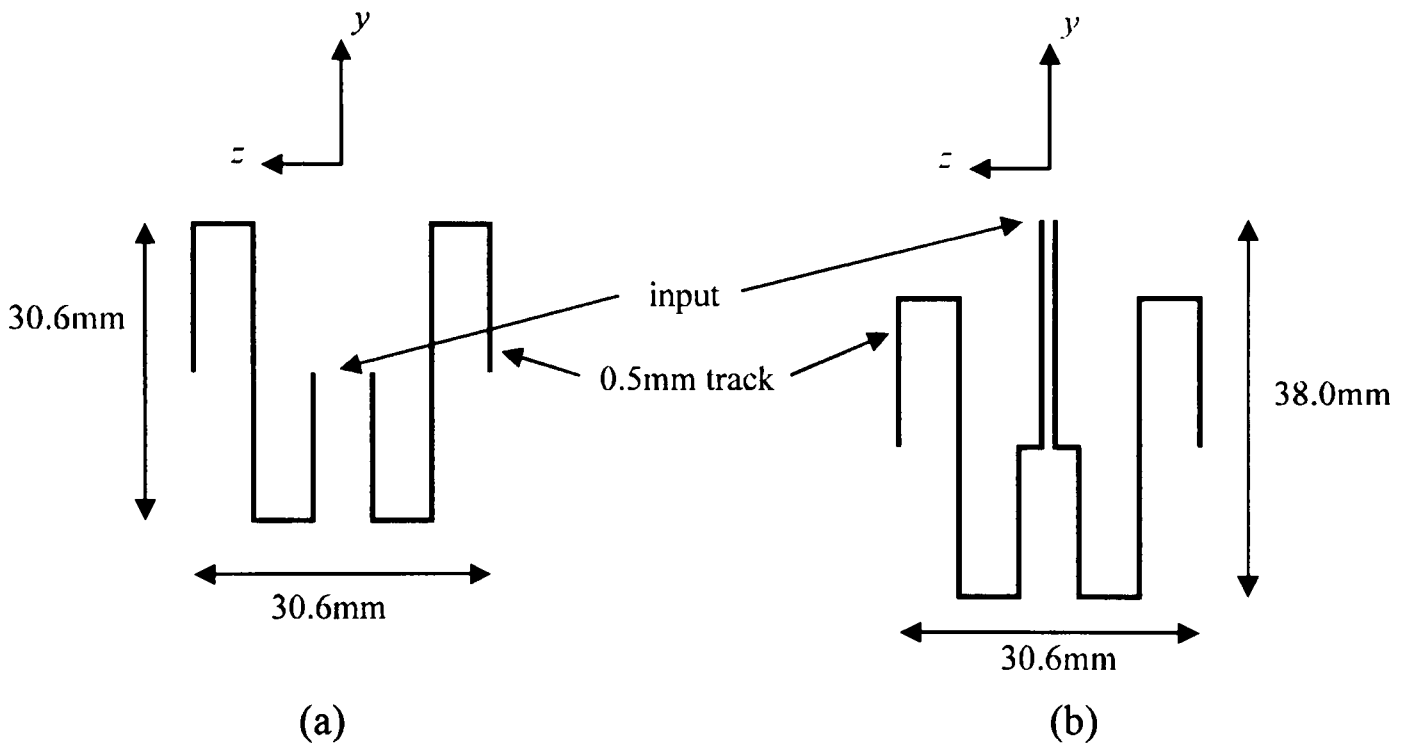

Fig. 3.16. The symmetrical meander antennas: (a) without feed line, (b) with feed line [80].

A further investigation of the symmetrical meander structure is carried out on a thin-film version [81]. Three structures of Fig. 3.17 are numerically simulated and experimented. Interestingly, all the meander antennas are found to operate around the same frequency as the reference linear dipole. In addition, the antennas are electrically smaller. The numerical simulation and experimental results are in good agreement with each other. In this work, the supergain and superdirective properties are not reported. However, detailed discussion of the thin-film symmetrical meander antennas is given in this dissertation. A corresponding paper is given in Appendix 5.

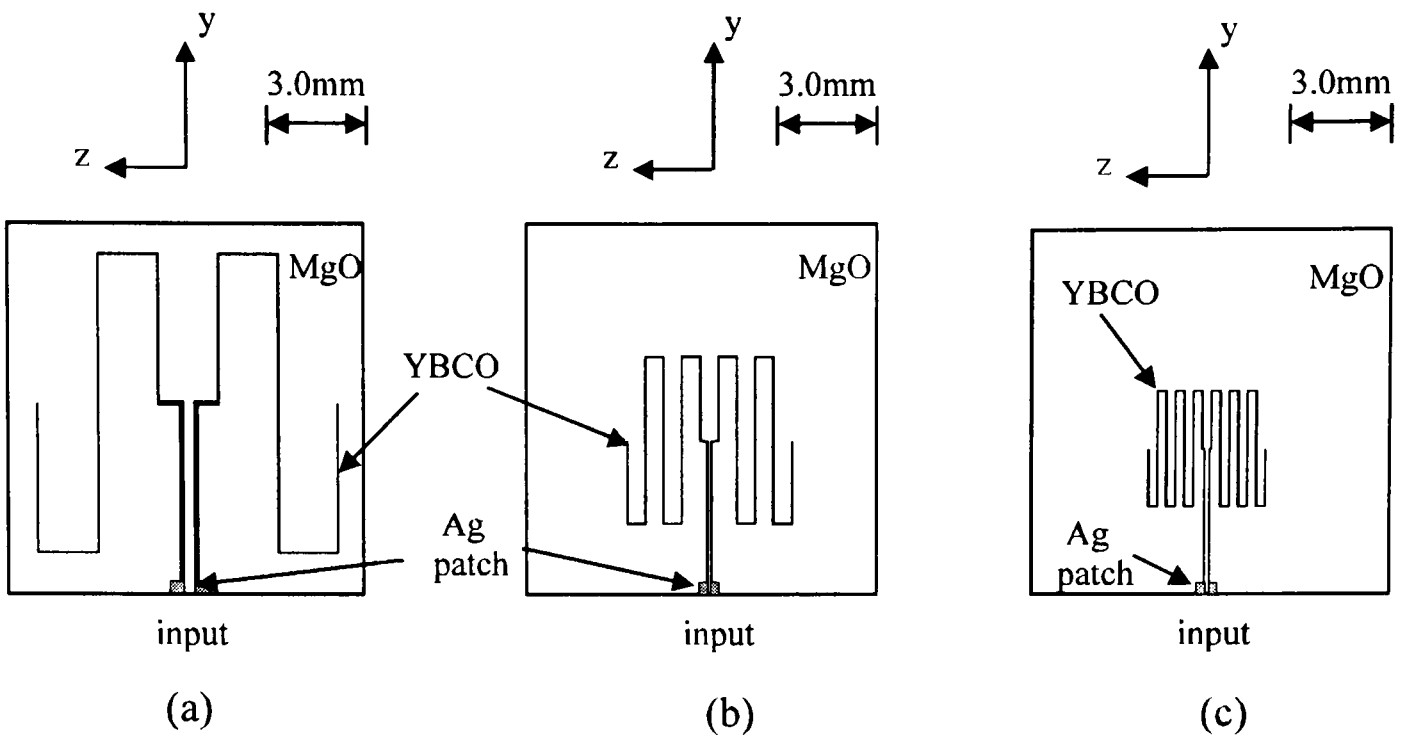

Fig. 3.17. The HTS thin-film symmetrical meander antennas: (a) two meander sections, (b) four meander sections, (c) six meander sections [81].

Recently, the performance of the same H-shaped microstrip structure of Fig. 3.6 [64], [66] has been investigated by G. Drossos *et al.* [82], but operating in the UHF band. The latter is fabricated using a thick-film HTS material with a trimming capacitor for matching to a 50 ohm transmission line. The device is depicted in Fig. 3.18. At 77K, the HTS antenna showed a gain of 10 dB and 5.4 dB above that of the identical siver antenna at 300K and 77K, respectively. However, the bandwidth is reduced by a factor of 3.6 and 1.4, respectively, as would be expected. In addition, two closely spaced H-shaped HTS antennas demonstrate simultaneous operation at two different frequencies. The experimental gains obtained are 10 dB and 8 dB above that of similar silver arrangement at 300K. The bandwidths are reduced by a factor of 3.7 and 3.1, respectively. The difference between the gains is probably partly due to the near field interaction between the two antennas. The range of the operating frequencies of all the antennas is 594.12 MHz to 728.25 MHz.

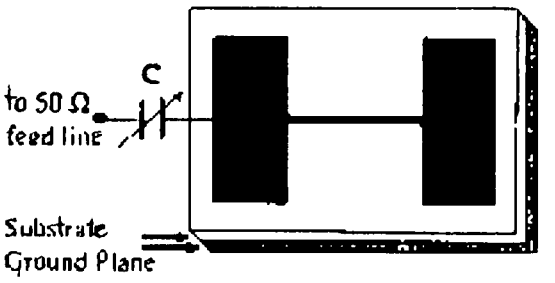

Fig. 3.18. The microstrip antenna [82].

The microstrip patch antenna [82] is then investigated with added capacitive loading [83]. This reduces the operating frequency to the 500 MHz range. A top view of the capacitive loaded antenna is shown in Fig. 3.19. The load is essentially sliding brass mountings. The effect of varying the number of loadings on silver and HTS antennas is investigated. A 15 % operating frequency reduction was obtained without appreciably changing the Q values. The frequency reduction is independent of the antenna material since the only important parameter is the gap between the patch and the ground. The loading technique is simple yet it is useful when one considers the same antenna to operate at a reduced frequency.

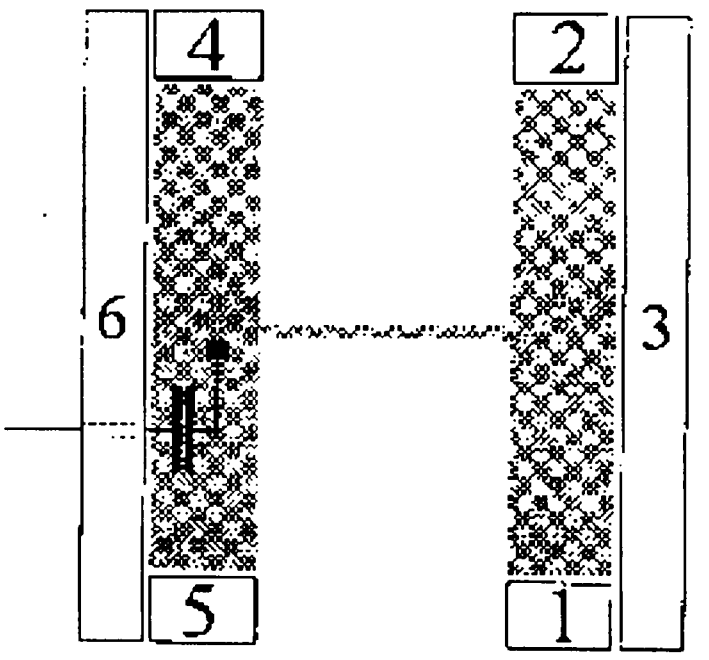

Fig. 3.19. Top view of capacitively loaded microstrip antenna [83].

The possibility of achieving supergain with electrically small thick film HTS array of closely spaced dipoles has been demonstrated by Ivrissimtzis *et al.* [84]. Two structures with alternate polarity of the radiating elements are shown in Fig. 3.20. The structures are serially and corporately fed, respectively. The feeding line for the first structure is approximately 50 ohm. The second structure involves a sectorial power divider and a quarter wavelength impedance transformer, in parallel with a tunable capacitor. The performance of the antennas are compared with that of similar silver versions. As expected, the HTS antennas demonstrate superior performance over similar silver arrays at 77K. All the antennas are electrically small at the corresponding frequency of operation. The series fed arrays are more efficient than the corporate fed arrays. However, the efficiency of the series fed silver array is 2.7 times higher than that of the corporate fed silver array. This is 1.5 times higher than that for the corresponding HTS arrays. In addition, far-field radiation pattern predictions based on the method-of-moments (MM) are also compared with experimental data. It was found that all the antennas showed bidirectional pattern with small discrepancies close to broadside. The principal plane gain patterns of the HTS corporate fed array are shown in Fig. 3.21. The discrepancies is attributed either to inaccurate depiction of the numerical approximation of the current distributions or pattern distortion during the cryogenic measurements.

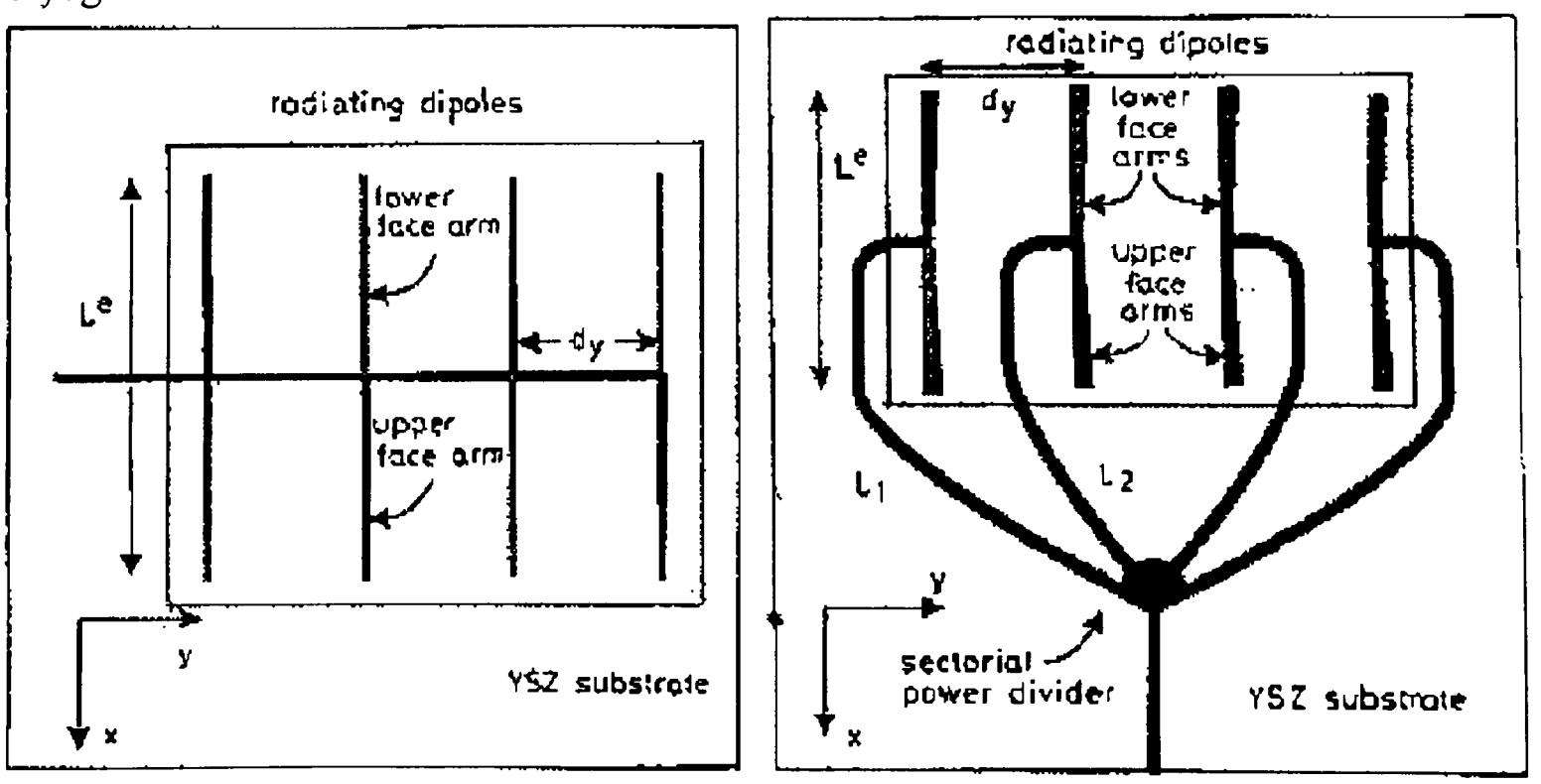

(a) (b)

Fig. 3.20. Closely spaced dipoles array: (a) series fed, (b) corporate fed [84].

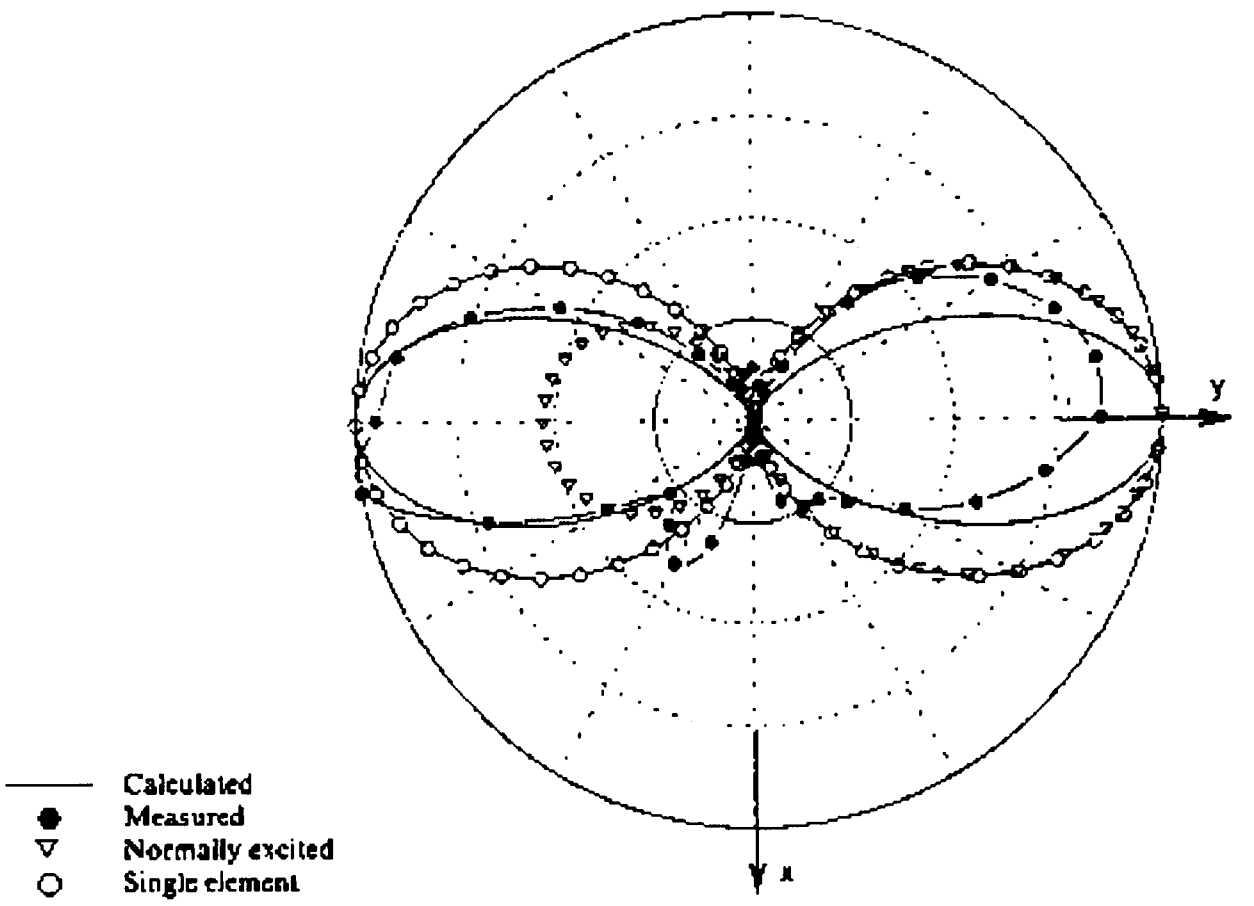

(a)

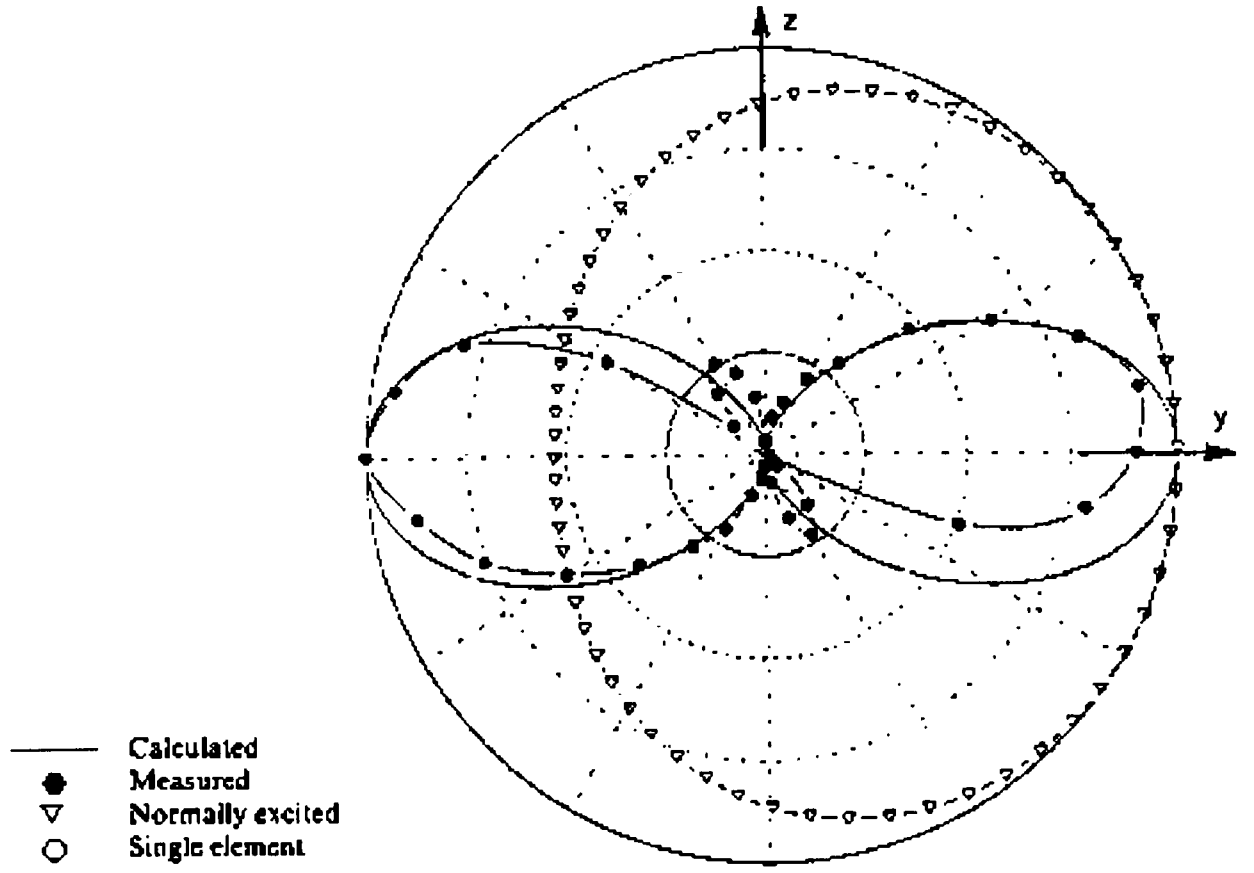

(b)

Fig. 3.21. Far-field principal plane radiation patterns of the HTS corporate fed array: (a) *xy*-plane, (b) *yz*-plane [84].

3.5 MATCHING NETWORKS

Impedance matching is difficult to be achieved for electrically small antennas [40], [58], [85], [86]. Electrically small antennas have small radiation resistances in comparison to large reactances. Hence, the matching of such small resistances to a 50 ohm feed line will result in significant losses. The superconducting matching circuit will have direct benefit, due to the greatly reduced matching losses, and thus will enhance the antenna efficiency [58], [59], [87]. Several matching techniques are discussed in Section 5.2. For example, in a single stub tuner, one may try to tune out the reactance first, followed by an impedance transformer, or vice-versa.

No matching network has been designed for the HTS symmetrical meander dipoles because a reasonably good match is obtained from the intrinsic structure. All the designed antennas are discussed in Chapter 5. Nevertheless, a quarter-wavelength sleeve balun is employed which also serves the purpose of helping matching to the 50 ohm coplanar feeding lines of the superconducting antennas.

CHAPTER 4

ANTENNA MEASUREMENTS

4.0 INTRODUCTION

This chapter presents a discussion of the method of measurements related to the antenna input impedance, reflection coefficient, gain, efficiency and power patterns. A short discussion on the antenna reflection bandwidth and its 3dB beamwidth is also given. The designed antennas in this study were practically experimented as transmitters whilst the corresponding receivers are the resonant $\lambda/2$ dipoles.

4.1 GAIN

There are two well-known methods which can be used for measuring the antenna gain in this study, namely the absolute gain and the gain by comparison (or gain transfer) measurements.

4.1.1 Absolute Gain

The two available absolute gain methods are the two- and the three-antenna methods. These methods are based on the well-known Friis transmission equation.

(a) Two-Antenna Method

Two antennas are arranged in free space as in Fig. 4.1. For polarisation matched antennas oriented for maximum directional radiation and reception, the Friis transmission equation is given by [1]

$$\frac{P_r}{P_t} = \left(\frac{\lambda_0}{4\pi r_a} \right)^2 G_{0r} G_{0t} \qquad (4.1)$$

This equation relates the power P_r (delivered to the receiver load) to the input P_t power of the transmitting antenna. The $(\lambda_0 / 4\pi r_a)^2$ term is known as the free-space loss factor which accounts for the losses due to the spherical spreading of the energy by the antenna. r_a is the antenna separation, which should be greater than $(2 d_m^2 / \lambda_0)$ if the equation is to be valid. d_m is the largest dimension of either antenna and λ_0 is the operating wavelength.

In logarithmic decibel form, eqn. (4.1) can be rewritten as

$$G_{0t} + G_{0r} = 20.0 \log_{10} (4\pi r_a / \lambda_0) + 10.0 \log_{10} (P_r / P_t) \tag{4.2}$$

where both G_{0t} and G_{0t} are in dBs. If the two antennas are identical, eqn. (4.2) simplifies to

$$G_{0t} = G_{0r} = 10.0 \log_{10} (4\pi r_a / \lambda_0) + 5.0 \log_{10} (P_r / P_t) \tag{4.3}$$

or, similar to eqn. (4.1), this is

$$G_{0t} = G_{0r} = (P_r / P_t) / (\lambda_0 / 4\pi r_a)^2 = G_0 \tag{4.4}$$

The network analyser can measure the term $[10.0 \log (P_r / P_t)]$ as $|S_{12}|^2$, where S_{12} is the transmission coefficient.

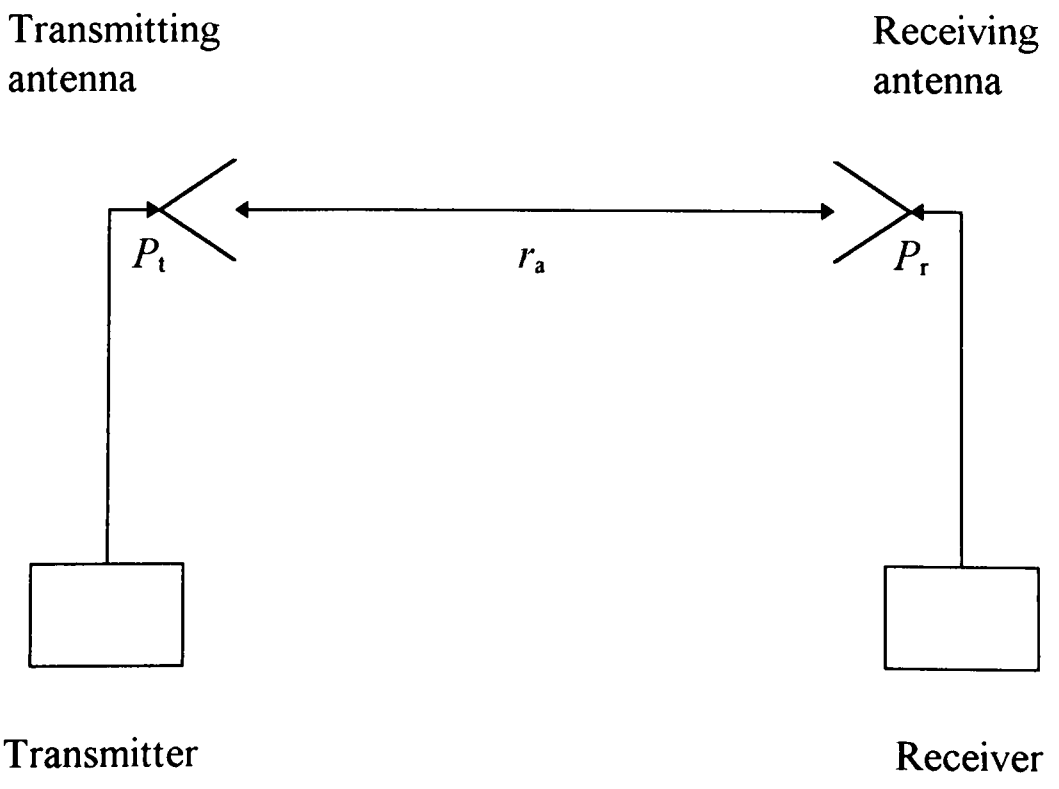

Fig. 4.1. A typical absolute gain measurement set-up.

To account for any impedance mismatches, the measured reflection (S_{11} , S_{22}) coefficients have to be included in eqn. (4.4) [1] - [3]. This is accomplished using [88]

$$G_{0t} = \frac{|S_{12}|^2 \, (4\pi r_a / \lambda_0)^2}{(1 - |S_{11}|^2) (1 - |S_{22}|^2) \, G_{0r}} \tag{4.5}$$

which is rearranged from the Friis transmission equation [1] - [3]. $|S_{12}|$ may be evaluated as the combination of that measured for similarly oriented antennas (principal plane co-polarisations) to account for any significant cross-polarisation component. S_{11} and S_{22} are the reflection coefficient of the transmitting and receiving antenna, respectively. Any unwanted wave reflections in free space that will degrade the measured gain can be minimised by using properly arranged absorbers in a well-designed anaechoic chamber.

In dBi (dB above lossless isotropic antenna),

$$G_{0t} \text{ (dBi)} = 10 \log_{10} G_{0t} \tag{4.6}$$

(b) Three-Antenna Method

If the two antennas described above are not identical, the three-antenna method has to be performed. This method employs three antennas (A, B and C) and three measurements have to be carried out to calculate the gain of each antenna. The set-up for each measurement is similar to Fig. 4.1. Each measurement makes use of one combination of the three antennas. Similar to eqn. (4.2), the three relationships are thus

$$G_{0A} + G_{0B} = 20.0 \log_{10} (4\pi r_a / \lambda_0) + 10.0 \log_{10} (P_{rB} / P_{tA}) \tag{4.7}$$

for the A-B combination, whilst

$$G_{0B} + G_{0C} = 20.0 \log_{10} (4\pi r_a / \lambda_0) + 10.0 \log_{10} (P_{rC} / P_{tB}) \tag{4.8}$$

for the B-C combination, and

$$G_{0A} + G_{0C} = 20.0 \log_{10} (4\pi r_a / \lambda_0) + 10.0 \log_{10} (P_{rC} / P_{tA}) \tag{4.9}$$

for the A-C combination.

Eqns. (4.7) to (4.9) can be solved for each individual antenna gain, with measured values of the power ratios. To account for the losses and mismatches as with the two-antenna method, eqn. (4.5) has to be employed.

Alternatively, two antennas may be made identical where results from the first transmission measurement performed can be used to calculate G_{0r} . The identical antennas could be the gain standards. Hence, another transmission measurement is sufficient for determining the designed antenna gain, G_{0t} .

4.1.2 Gain by Comparison

The gain of the antenna under test is measured with respect to a comparison or reference antenna with predetermined gain as of Fig. 4.2. The two most widely used antennas as gain standards, both possessing linear polarisation, are the resonant $\lambda/2$ dipole and the pyramidal horn antenna. However, any other antenna whose gain is known or can be calculated, may also be employed.

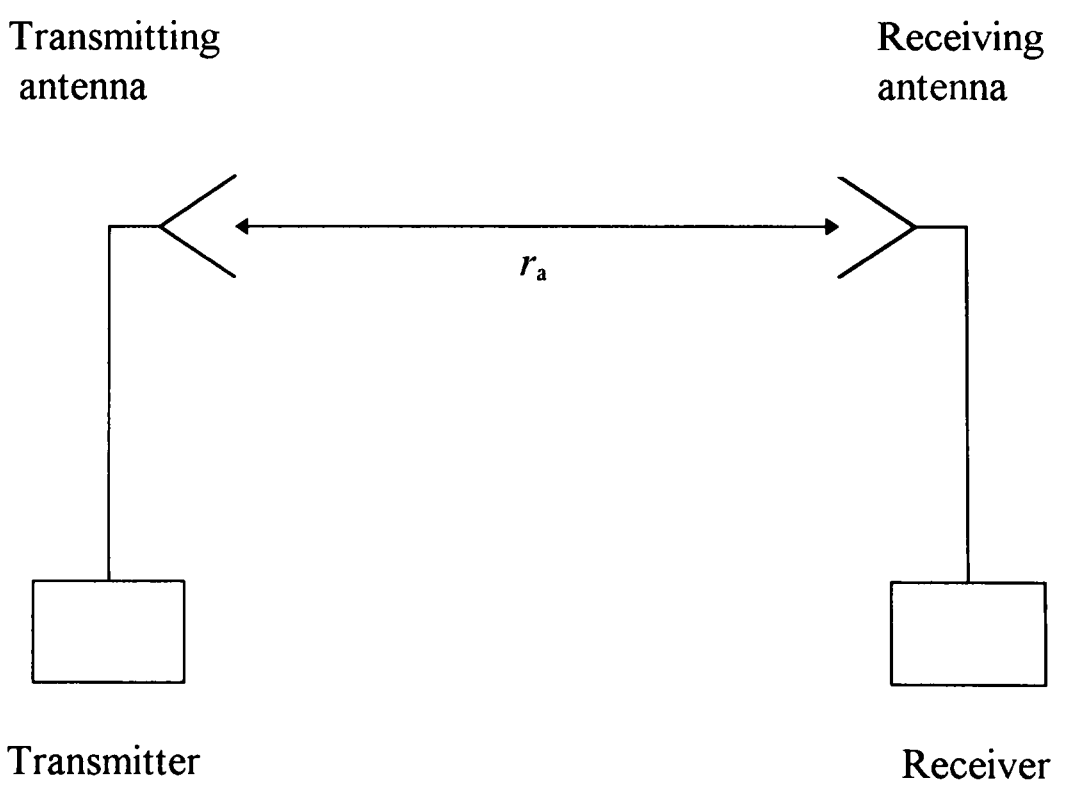

Fig. 4.2. A typical gain by comparison measurement set-up.

There are several methods available. However, a simple procedure requires two sets of measurements. First, the test antenna is operating as a receiver and the power received by a matched load, $P_{\text{aut/load}}$, is recorded. The subscript aut denotes 'antenna under test'. Next, the reference antenna (known gain of G_{ref} dB) replaced the test antenna and the similar power received, $P_{\text{ref/load}}$, is recorded. No other change of geometrical arrangement is to be made. Similar to eqn. (4.2), the measured gain can be calculated as

$$G_{\text{aut}} = G_{\text{ref}} + 10.0 \log_{10} \left(\frac{P_{\text{aut/load}}}{P_{\text{ref/load}}} \right) \tag{4.10}$$

One technique which minimises any system disturbance when changing receiving antennas is to mount both the antenna under test and the reference antenna, back-to-back on either side of an azimuth positioner axis. Connection to the load is via a common reversible switch. Antenna replacement is made through 180° positioner rotation as well as changing the proper switch position.

Another technique is by mounting both antennas side-by-side through a similar switch as shown in Fig. 4.3. The measured gain is given by the ratio of the measured power of the antenna under test, P_{aut}, to that of the reference antenna, P_{ref}. This is also equal to the square of the ratio of the measured voltage of the antenna under test to that of the reference antenna. Comparison is made by switching the receiver from one antenna to another. Mathematically, the measured gain can be written as

$$G = \frac{P_{\text{aut}}}{P_{\text{ref}}} = \left(\frac{V_{\text{aut}}}{V_{\text{ref}}} \right)^2 = 10.0 \log_{10} (G) \text{ dBi} \tag{4.11}$$

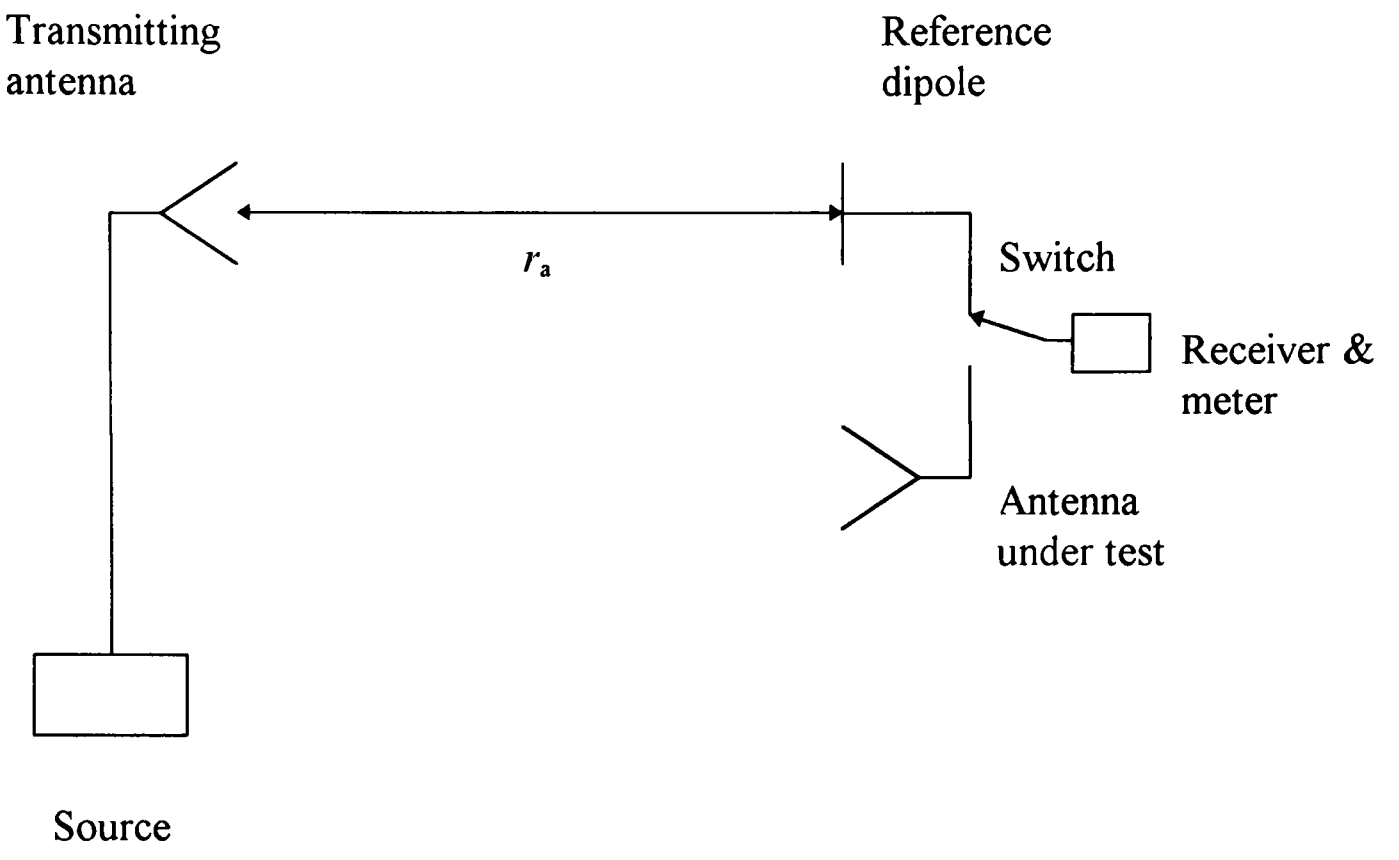

Fig. 4.3. Another type of gain by comparison measurement set-up.

4.1.3 Superdirectivity and Supergain

The electrical size of an antenna is defined as [13]

$$S = k_0 b \tag{4.12}$$

where k_0 is the propagation constant in free space and b is the radius of the smallest sphere that encloses the antenna. For an antenna to be considered electrically small, S has to be very much smaller than unity, i.e.,

$$S << 1 \tag{4.13}$$

Hence, the limit for electrically small antenna is

$$S = 1 \tag{4.14}$$

Note that this smallest sphere is equivalent to that of the radiansphere by Wheeler [15]. In Wheeler's definition, an antenna is considered to be electrically small if b is very much less than its radianlength λ_{rad}, where

$$\lambda_{rad} = \lambda_0 / 2\pi \tag{4.15}$$

Hence, with Wheeler's definition, eqn. (4.13) can be written as

$$b << \lambda_0 / 2\pi \tag{4.16}$$

and the limit of electrically small antenna is

$$b = \lambda_0 / 2\pi \tag{4.17}$$

The maximum attainable gain of a normal antenna can be written as a function of its electrical size as [13]

$$G_n = (k_0 b)^2 + 2 k_0 b \tag{4.18}$$

The measured antenna gain G_{0t} in eqn. (4.5) can be compared to that of G_n. This is termed superdirective ratio or simply [50]

$$s_d = G_{0t} / G_n \tag{4.19}$$

If the antenna efficiency is taken into account, then supergain ratio [50] can also be defined;

$$s_g = \eta_{tot} \; s_d \tag{4.20}$$

where η_{tot} is given in eqn. (2.13).

4.2 EFFICIENCY

4.2.1 General

Practical determination of the antenna radiation efficiency is described in this section.

(a) Wheeler Method

The Wheeler method [15] was used for measuring the efficiency of electrically small multiturn loop antennas [18] and printed antennas [89]. In the latter work, the method was also found to be probably the easiest to implement and gave the most repeatable results, but may be deficient from a theoretical point of view.

The Wheeler method is a simple measurement procedure. The basic assumptions are that the addition of the shield does not change the form of the distribution of current on the antenna, and that there is negligible loss in the shield. In addition, the energy dissipated on the shield is assumed to be negligible. In terms of the components of the input resistance, this means that the resistance due to the loss mechanisms in the antenna is the same with and without the shield, and that the resistance due to the loss in the shield is negligible.

The efficiency can be derived from the relationship

$$\eta = \frac{R_{in} - R_{in}'}{R_{in}} \tag{4.16}$$

where R_{in} and R_{in}' are the antenna input resistances in free space and inside a metallic sphere of radius equivalent to the radianlength, respectively.

Smith [24] suggested that the method can be quite accurate when the dimensions of the shields are a substantial fraction of a wavelength and the antenna is not operated near a critical point like at antiresonance. The shield conductivity does not have to be very high for producing accurate results. However, electrically small shields can result in large errors

since the resistance due to the loss in the shield can be comparable to the antenna radiation resistance.

(b) Resistance-Comparison Method

As discussed in Section 1.1, if the two identically shaped antennas are constructed from different metals of conductivities and permeabilities; σ_1 , μ_1 , and σ_2 , μ_2 , respectively, the ratio of the two antenna surface resistances is equal to that of the two antennas loss resistances. This can be written as [19], [20]

$$\xi = \frac{R_{loss\,2}}{R_{loss\,1}} \approx \frac{R_{s\,2}}{R_{s\,1}} = \left(\frac{\mu_2 \sigma_2}{\mu_1 \sigma_1}\right)^{1/2} \tag{4.17}$$

The difference in the radiation resistances of the two antennas is negligible. The radiation efficiency of either antenna can simply be obtained from the measured values of both the antenna input resistances and the calculated ξ. The first antenna radiation efficiency can be determined using [20], [24]

$$\eta_1 = \frac{R_{in2} - \xi R_{in1}}{1 - \xi} \tag{4.18}$$

(c) *Q*-Method

This method is based on the comparison of measured and ideal Q [18]. The efficiency is termed Q-efficiency. If the Q of a realisable antenna is defined as

$$Q_R = \frac{\omega\,(\text{peak energy stored})}{(\text{average power radiated}) + (\text{average power dissipated})} \tag{4.19}$$

whilst the Q of an ideal antenna is

$$Q_I = \frac{\omega\,(\text{peak energy stored})}{(\text{average power radiated})} \tag{4.20}$$

then the Q-efficiency is given by the ratio

$$\eta_Q = \frac{Q_R}{Q_I} = \frac{(\text{power radiated})}{(\text{power radiated}) + (\text{power dissipated})} \tag{4.21}$$

where the current distribution on both antennas are considered to be the same and hence the stored energies will also be the same. The ideal antenna is identical to the realizable antenna but made from conductors with perfect conductivity and zero dielectric loss. The Q-factor of a high Q antenna at its operating frequency f_0 can be approximated by a measurement of its relative half-power bandwidth Δf_{3dB}:

$$Q_L = \frac{f_0}{\Delta f_{3dB}} \tag{4.22}$$

Q_R can be determined by measuring the real antenna input impedance whilst Q_I can be calculated using the formulation derived in references [11] and [13].

(d) Directivity/Gain Method

This is the most well-known method where the efficiency can be determined from the measured gain and directivity of the test antenna using the formulation from eqn. (2.7):

$$\eta = G_0 / D_0 \tag{4.23}$$

Pozar and Kaufman [89] found that, even though this method is simple in principle and probably the most common method, and essentially requiring only an anaechoic chamber, it is subject to inaccuracies and uncertainties and has poor repeatability.

Nevertheless, the method is sufficiently accurate for electrically small antennas. The efficiency can be calculated by merely measuring the directive gain of the test antenna. The directivity can be taken as 1.5, which equals that of an electrically small antenna.

(e) Formulations by Dinger *et al.* [61]

The transmitting test antenna efficiency can be determined using the formulation

$$\eta = \frac{|S_{12}|^2 \, (4\pi r_a / \lambda_0)^2}{G_{0t} \, G_{0r}} \tag{4.24}$$

A standard $\lambda/2$ dipole of gain 1.64 can be used as the receiving antenna and G_{0t} can be calculated from eqn. (4.5).

4.2.2 HTS Circuits

As defined earlier in Section 2.5, the antenna efficiency is the ratio of the radiation resistance to the antenna input resistance which mainly consists of the radiation resistance and the loss resistance. It is well known that an electrically small normal conducting antenna has low radiation efficiency. This is due to the predominant ohmic losses in the antenna and its matching network. Since the loss resistance is directly proportional to the surface resistance; in eqns. (2.45), (2.80) and (2.93), its value is greatly reduced with the use of a superconducting material. Consequently, this will greatly enhance the superconducting antenna efficiency.

Various practical efficiency measurements have been discussed in the previous section. Three other methods relevant to superconducting antennas were suggested and experimented [56] as follows.

(a) Compensated Wheeler Method

The Wheeler method is the simplest procedure to determine antenna efficiency. However, in the low loss impedance HTS antennas, dissipation on the enclosing radiansphere may deteriorate the accuracy of this technique and predict lower efficiency values. For this purpose, a modified radiansphere method can be used. The method was developed and performed with a compensation for the losses on the radiansphere, by using

two boxes of the same shape but different electrical resistivities of their inner metallic walls. The two boxes serve the purpose of the shield, as with the Wheeler method.

The measured input resistances of the antenna inside the radiansphere becomes

$$R_{in}' \approx R_{loss} + K\,[\rho'(T)]^{1/2} \tag{4.25}$$

where K is a constant which depends on the frequency and the shape of the enclosing box, and $\rho'(T)$ is the electrical resistivity at the temperature T of the experiment. If the measured input resistance for a similar box with resistivity $\rho''(T)$ is R_{in}'', the loss resistance can be found from

$$R_{loss} \approx R_{in}' - \frac{R_{in}' - R_{in}''}{[\rho'(T)]^{1/2} - [\rho''(T)]^{1/2}}\,[\rho'(T)]^{1/2} \tag{4.26}$$

(b) *Q*-Method Upper Efficiency Bound

A good estimate of the upper bound antenna efficiency formulation derived from the Q-method (discussed in Section 4.2.1c above) can be written as

$$\eta_{max} = \frac{2\,f_0}{Q_{min}\,(\Delta f_{3dB})} \tag{4.27}$$

where Q_{min} is the unloaded Q of an antenna.

Assuming equal distribution of transverse electric, or TE, and transverse magnetic, or TM, modes, the unloaded Q equals

$$Q_{min} = 0.5\left(\frac{1}{k_0\,b} + \frac{1}{(k_0\,b)^3}\right) \tag{4.28}$$

(c) Relative Gain Measurements

The efficiency of the antenna under test is related to the efficiency and directivity of the reference antennas by the relationship

$$\eta_t = \frac{\eta_r \ D_r}{D_t} G_{\text{rel}} \tag{4.29}$$

where G_{rel} is the measured relative gain of the test antenna over a reference antenna resonating at the same frequency. The efficiency η_r and the directivity D_r of the reference antenna, and the directivity of the test antenna D_t, are determined analytically.

(d) Transfer Radiation Efficiency

The transfer radiation efficiency divides out the residual mismatch of the existing matching network, and permits a more direct comparison of the losses in the superconducting and normal conductor devices [61].

The transfer radiation efficiency is accomplished by modifying eqn. (4.24) to

$$\eta = \frac{|S_{12}|^2 \ (4\pi r_a / \lambda_0)^2}{(1 - |S_{11}|^2) \ G_{0t} \ G_{0r}} \tag{4.30}$$

where λ_0 is the operating wavelength of the test transmitting antenna.

4.3 RADIATION PATTERN

The radiation patterns of an antenna can be measured in the transmitting or receiving mode, because of reciprocity. As discussed in Section 2.1, the measurements of the orthogonal principal E- and H-plane patterns are sufficient to represent the designed antenna radiation patterns. The measurement set-up for determining the antenna gain can be used. The only difference is, either the test antenna or the reference antenna is rotated

through the elevation and azimuth angles, each at a particular azimuth and elevation angle, respectively. The two principal plane patterns can thus be obtained. From the plot, one can easily determine the beamwidth of the test antenna at the -3 dB level of the major lobe. This is discussed earlier in Section 2.1.

A third pattern measurement may be carried out to check the presence of cross-polarisation component. This value can be accounted for in calculating the antenna gain and efficiency, as discussed in Sections 4.1 and 4.2, respectively. The measurement is done by first orienting the antennas perpendicular to each other. The transmission coefficient (S_{12}) data is taken throughout the transmitting test antenna rotation.

The plotting of the pattern can be done automatically with commercially available workstations. The pattern measurements was done semi-automatically through an HP Basic program, that controls the rotary turn-table through a microprocessor interface, and the network analyser itself that measures the pattern. The process requires only three minutes to measure each pattern and to store the measured data. It is useful to plot the pattern out to ensure that the stored data corresponds with the plot. This will normally need another minute.

However, considerable amount of time is needed for the setting-up of antennas since this has to be done manually. The transmitting and receiving antennas have to be oriented and positioned as accurately as possible, with the help of proper rulers and measuring tapes. Pattern measurements can only be done when the reflection and transmission coefficients over the desired useful frequency range have been successfully and satisfyingly obtained. This requires much time and effort since there are several factors which affect the latter results, as discussed further in Chapter 8 along with the far-field radiation pattern measurements.

CHAPTER 5

ANTENNA DESIGNS

5.0 INTRODUCTION

A description of all the antennas designed is given in this chapter. Design procedures and principles are also described in depth. This is followed by a discussion of matching networks and baluns.

5.1 ANTENNA GEOMETRIES AND DESIGN PROCEDURES

Two different sets of antennas were fabricated, tested and analysed. These were the anti-symmetrical meander dipole antennas and the symmetrical meander dipole antennas. The superconducting versions will be discussed where relevant. In addition, linear $\lambda/2$ dipole antennas were also fabricated for use in the transmission measurements.

5.1.1 Anti-Symmetrical Meander Dipoles

The first set of antennas was in the form of anti-symmetrical meander dipoles. The design was based on the 1.0 GHz linear $\lambda/2$ dipole as shown in Fig. 5.1(a). A basic design which consists of one meander arm on either side of the dipole is shown in Fig. 5.1(b). The geometry of all three generic antenna types in Fig. 5.1 has been altered to produce the performance of a short dipole as the size is miniaturised. These were in the form of four, eight and sixteen meander sections in the half-arms as shown in Figs. 5.1(c), (d) and (e), respectively. The dimensions of the axial length, the total arm length, the track width and the feed gap were kept constant. The design formulations are discussed later in this section. The number of meander sections was varied. Another linear $\lambda/2$ dipole of the same axial length and track width was also built for further comparison, as depicted in Fig. 5.1(f). All

the antennas were fabricated from copper on RT/duroid 5870 glass-fibre reinforced polytetrafluoroethylene (or PTFE) dielectric ($\varepsilon_r = 2.33$, 1.57 mm thick and tan $\delta = 0.0012$), clad in 35.0 μm thick copper electro-deposited on both sides. The antenna structure pattern was etched onto one side of the dielectric using standard photo-lithographic techniques. The tracks were made to be 0.5 mm wide. All the antennas were fed from underneath through the substrate.

The principle behind this design is to determine whether any change in the radiating structure that reduces the physical size, will affect the antenna properties. By keeping the overall track length constant, reducing the antenna size may still maintain the antenna properties. However, due to the position of the opposite current flow in the *y*-direction of the adjacent meander sections, these currents tend to cancel out with each other. Hence, the only current effectively flowing will be that along the sections in the *z*-direction. These lengths, when added together, turned out to be approaching that of a short dipole whose length equals the axial length of the meander antenna. Hence, it is expected that the performance of an anti-symmetrical meander antenna with the highest number of meander sections will resemble more of a short dipole. However, as the meander density increases, capacitive coupling will occur between the meander elements tending to reduce this effect.

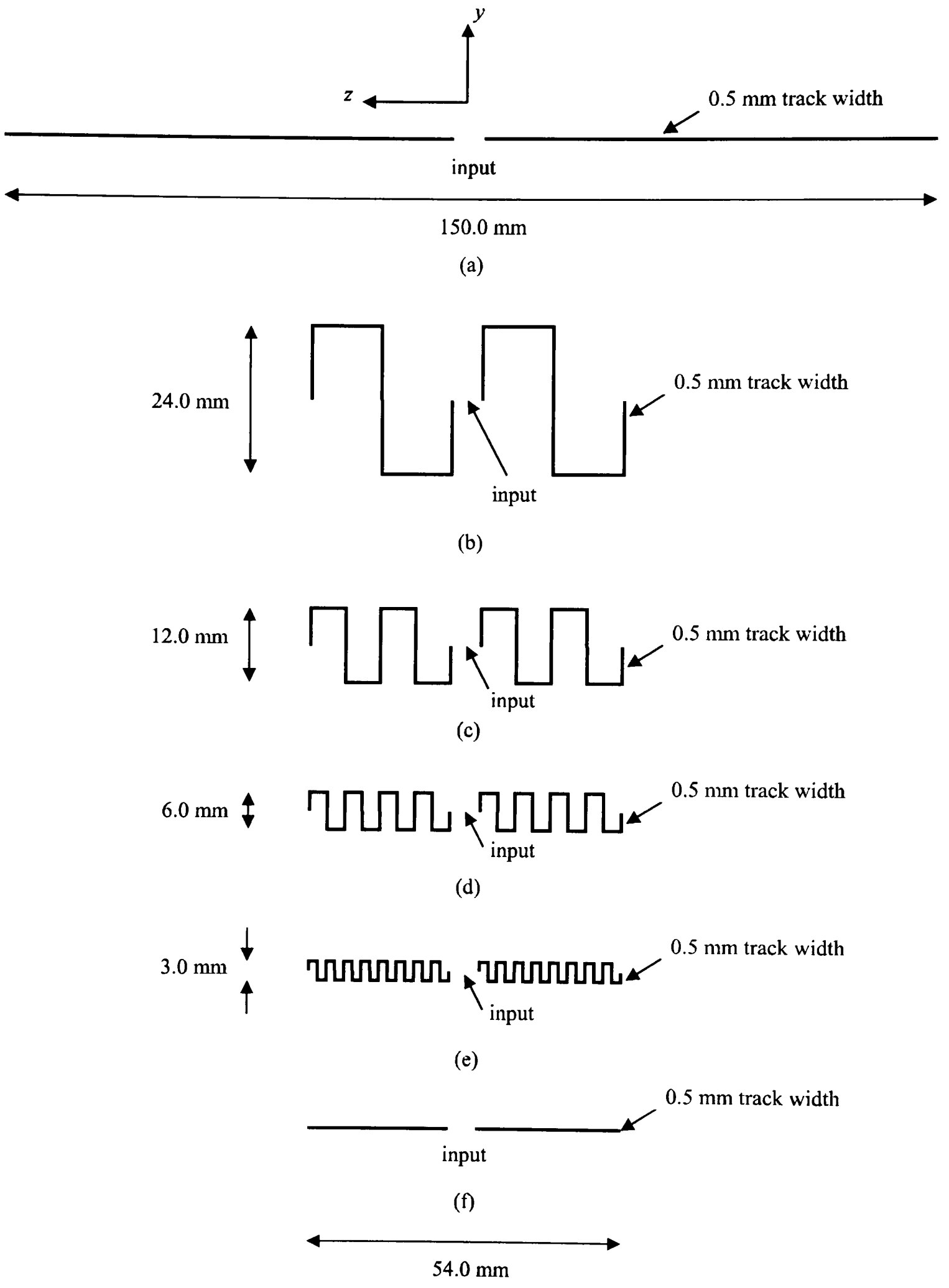

Fig. 5.1. (a) Linear dipole; anti-symmetrical meander dipoles: (b) two, (c) four, (d) eight, (e) sixteen meander sections; (f) short dipole.

The linear $\lambda/2$ dipole of wavelength λ_d was designed to be of 0.5 mm track width. From here, a set of generic anti-symmetrical meander dipoles was designed. Fig. 5.2 shows the geometry of an N-section of such structure. The definition of all the symbols are as follows:

w_a , track width

s_a , feed gap

s_{ag} , total feed gap

w_{am} , mean width of the meander section

W_a , antenna width

W_{am} , mean antenna width

L_{ax} , axial length

L_{at} , total mean arm length

AR_a , aspect ratio

N , number of meander section in the half arm

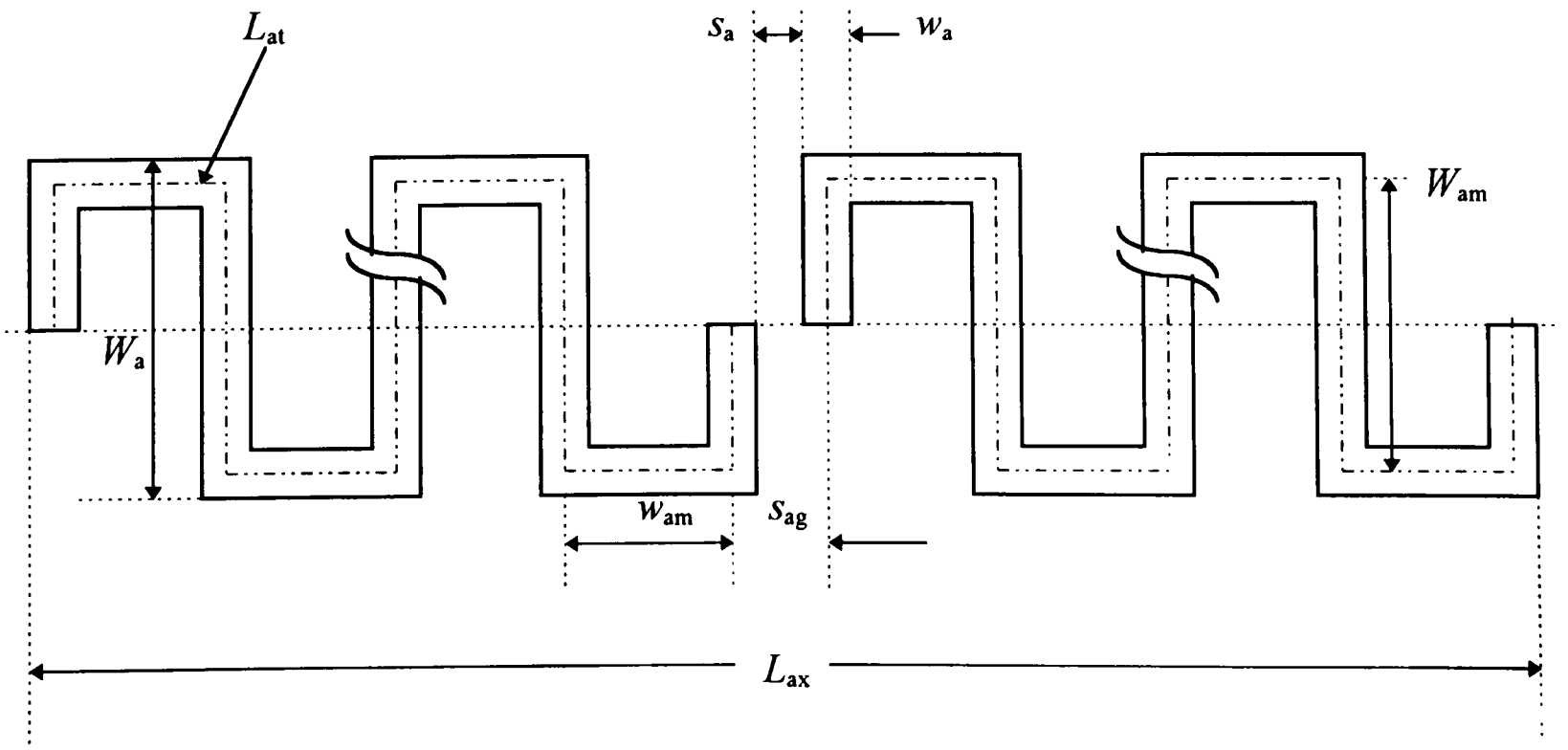

Fig. 5.2. Designed parameters for an N-section anti-symmetrical meander dipole.

The parameters w_a, s_a, s_{ag}, L_{ax} and L_{at} were kept constant. The lengths of w_a and s_{ag} for all structures are 0.5 mm and 5.0 mm, respectively.

$$s_{ag} = 5.0 \quad \text{and} \quad w_a = 0.5 \tag{5.1}$$

The parameter s_{ag} is made up of s_a and w_a, i.e.,

$$s_{ag} = s_a + w_a \tag{5.2}$$

The value of L_{ax} was fixed at 0.18λ or 53.82 mm. This means that the anti-symmetrical meander dipoles were reduced in axial length by 64.0 %.

$$L_{ax} = 0.18\lambda = 53.82 \tag{5.3}$$

In terms of N, w_{am} and s_{ag} ; L_{ax} can be written as

$$L_{ax} = 2(2Nw_{am} + s_{ag}) \tag{5.4}$$

By substituting eqn. (5.2) into eqn. (5.4) gives

$$L_{ax} = 2(2Nw_{am} + s_a + w_a) \tag{5.5}$$

The value of L_{at} was kept constant as 150.0 mm, which is the same as the length of the linear dipole.

$$L_{at} = \lambda_d = \lambda/2 = 150.0 \tag{5.6}$$

L_{at} can also be written as

$$L_{at} = 4N(w_{am} + W_{am}) + s_{ag} \tag{5.7}$$

where w_{am} is obtained from eqn. (5.5) as

$$w_{am} = (0.5L_{ax} - w_a - 0.5s_a)/2N \tag{5.8}$$

Each meander dipole has equal lengths of w_{am}. This width was designed to be halved of W_{am}.

W_{am} can be found from eqn. (5.7) as

$$W_{am} = [(L_{at} - s_a - w_a) / 4N] - w_{am} \tag{5.9}$$

W_a is made up of W_{am} and w_a , i.e.,

$$W_a = W_{am} + w_a \tag{5.10}$$

By substituting eqn. (5.9) into eqn. (5.10) gives

$$W_a = [(L_{at} - s_a - w_a) / 4N] - w_{am} + w_a \tag{5.11}$$

The aspect ratio of the structure is defined as the ratio of the antenna axial length, L_{ax} , to the antenna width, W_a , mathematically written as

$$AR_a = L_{ax} / W_a \tag{5.12}$$

Substituting eqns. (5.5) and (5.11) into eqn. (5.12) gives

$$AR_a = \frac{2(2Nw_{am} + s_a + w_a)}{\{[(L_{at} - s_{ag}) / 4N] - w_{am} + w_a\}} \quad \text{(dimensionless)} \tag{5.13}$$

or,

$$AR_a = \frac{8N(2Nw_{am} + s_a + w_a)}{[(L_{at} - s_{ag}) + 4N(w_a - w_{am})]} \quad \text{(dimensionless)} \tag{5.14}$$

Evaluated values of the designed antenna widths and meander section mean widths, both in mms and in terms of λ_d , and the aspect ratio for different number of meander sections using the above formulations are given in Table 5.1.

Table 5.1. The anti-symmetrical meander dipoles designed dimensions.

N	W_a (mm, λ_d)	w_{am} (mm, λ_d)	AR_a
2	24.67 , 0.164	12.08 , 0.081	2.18
4	12.59 , 0.084	6.04 , 0.040	4.28
8	6.54 , 0.044	3.02 , 0.002	8.23
16	3.52 , 0.024	1.51 , 0.001	15.28

Although further number of meander sections can be designed due to the fairly long axial length, only four antennas were fabricated and tested in this study. This number is considered sufficient to provide an inference. All the meander structures were numerically simulated, using the package discussed in Chapter 6.

5.1.2 Symmetrical Meander Dipoles

This design is an extended version of the anti-symmetrical meander structures. It is still based on the 1.0 GHz linear $\lambda/2$ dipole. However, it is intended to be a more systematic miniaturisation approach. The main principle is to investigate the effect of having symmetrical meander arms on the antenna performance. In addition, different aspect ratios were considered for the structures with the same track widths. The chosen ratios made the physical size of the radiating structure appeared as either a square or a rectangle. Complete sets of copper antennas were fabricated. The next step was the fabrication of the least efficient set of antennas in the thin-film superconducting version. The latter was intended to demonstrate superior performance than its corresponding copper version. All the structures were also numerically simulated, using the package discussed in Chapter 6.

Initially, it was decided to feed the antenna from underneath through the substrate. However, initial measurements showed that the currents on the surface of the SMA connector contributed significantly to the return loss. Consequently, the surface currents caused unwanted stray radiations from the antenna. The high return loss may be reduced by

caused unwanted stray radiations from the antenna. The high return loss may be reduced by incorporating a balun at the feed. Further discussion of the balun is given in Section 5.3. A brief discussion of the experimental and simulated results is given in Chapter 8. An alternative to reduce the high return loss is to feed the antenna with a length of 50 ohm coplanar strip line. The dimensions of appropriate feeding lines were discussed in depth later in this section. The real designed values were also tabulated. Notice that, since it is very difficult to bore the holes through the yttria stabilised zirconia substrate on which the thick-film YBCO was deposited, as well as through the magnesium oxide substrate on which the thin-film YBCO was deposited; the CPS feeding lines were adopted.

A basic design which consists of one meander arm on either side of the dipole is as illustrated in Fig. 5.3(a). The presence of the CPS feeding lines is also illustrated. The geometry of the other two generic antenna types in Fig. 5.3 has been altered to produce similar frequency of operation as size is miniaturised. These were in the form of four and six meander sections in the half-arm as shown in Figs. 5.3(b) and (c), respectively. Only three antennas can be built practically since a higher number of meander sections will end up in meander sections gaps being too close together. This will be discussed further in this section. In these designs, the dimensions of the total arm length, the track width and the meander sections width were kept constant. The meander section width was the same as the feed gap of each antenna. This is because, the overall effect of current cancellation and capacitive coupling between adjacent meander arms on the antenna performance will be similar in all the meander structures.

Three sets of copper meander dipole antennas were actually built; each set with two, four and six meander sections in the half-arm. In total, there were nine antennas. The copper linear dipole and meander dipole antennas were implemented on RT/Duroid 6010 glass-fibre reinforced PTFE dielectric (ε_r = 10.8, 1.27 mm thick and tan δ = 0.001), clad in 17.5 μm thick copper electro-deposited on one side. The pattern of each structure was etched onto the substrate using standard photo-lithographic techniques. The first meander set has 0.5 mm track widths with 3:2 aspect ratio, as shown in Fig. 5.3. The meander sections were separated by gaps of $\lambda/39$, $\lambda/139$ and $\lambda/375$, respectively. The total axial lengths were $\lambda/7$,

$\lambda/12$ and $\lambda/17$, respectively. The tracks were designed to be 0.5 mm wide, similar to the linear $\lambda/2$ dipole.

The second meander set also has 0.5 mm track widths but with an aspect ratio of 1:1. The meander sections gaps were $\lambda/55$, $\lambda/214$ and $\lambda/750$, respectively while the total axial lengths were $\lambda/9.8$, $\lambda/18$ and $\lambda/25$, respectively. The set is as illustrated in Fig. 5.4.

The last meander set has an aspect ratio of 1:1 but with 0.2 mm track widths. The total axial lengths were $\lambda/52$, $\lambda/181$ and $\lambda/428$, respectively, while the meander sections gaps were $\lambda/10$, $\lambda/18$ and $\lambda/25$, respectively. The structure is similar to Fig. 5.4.

All the masks of the designed antennas were drawn using the CORELDRAW package. These masks were sent for fabrication from an enlarged scale printouts to ensure accurate circuit dimensions. The dimensions of the fabricated circuits were then measured under the microscope and compared with the design values.

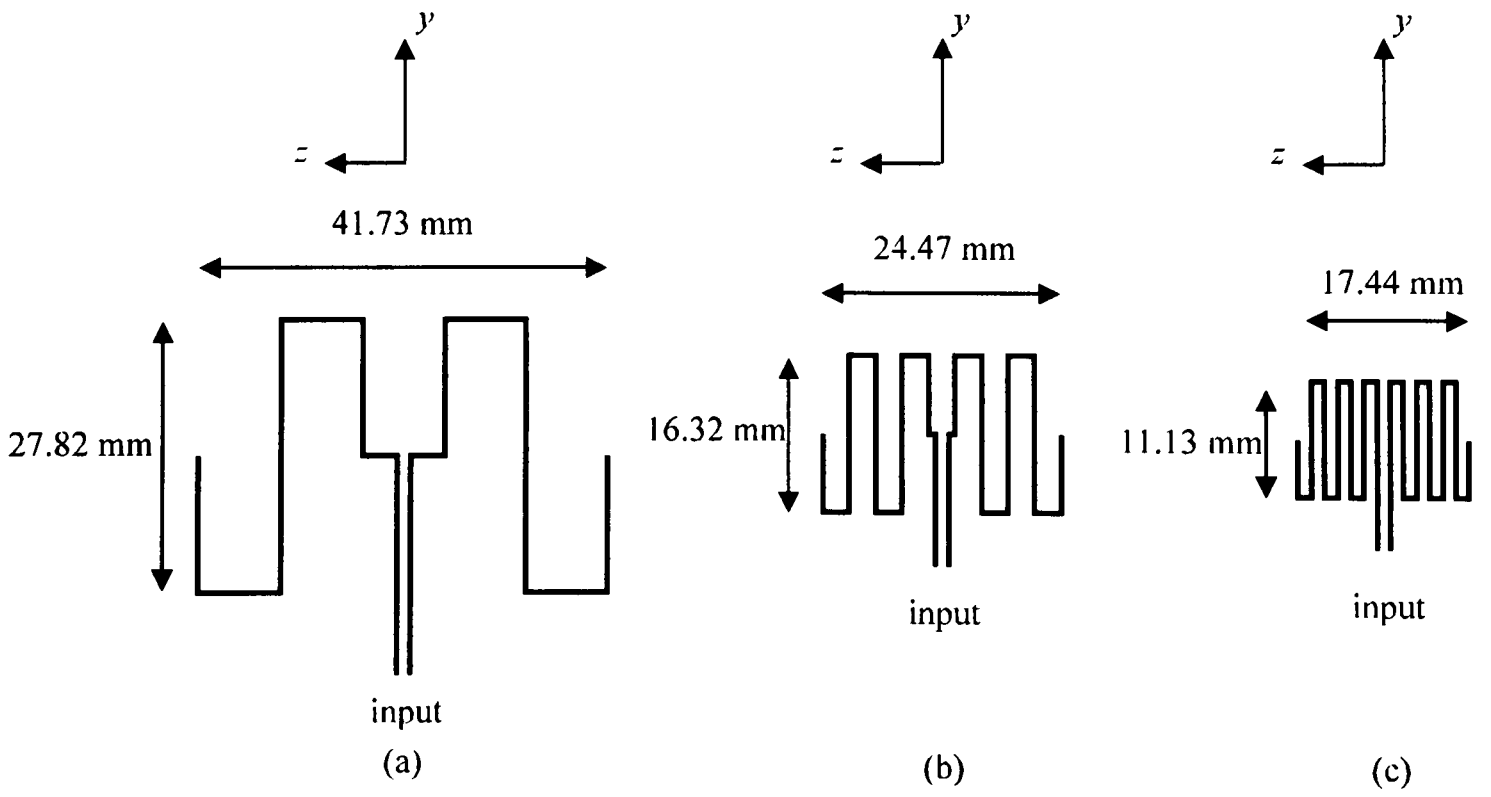

Fig. 5.3. Symmetrical meander dipoles with 3:2 aspect ratio: a) two, b) four, c) six meander sections (1:1 scale). 50 ohm coplanar strip feed lines are also shown.

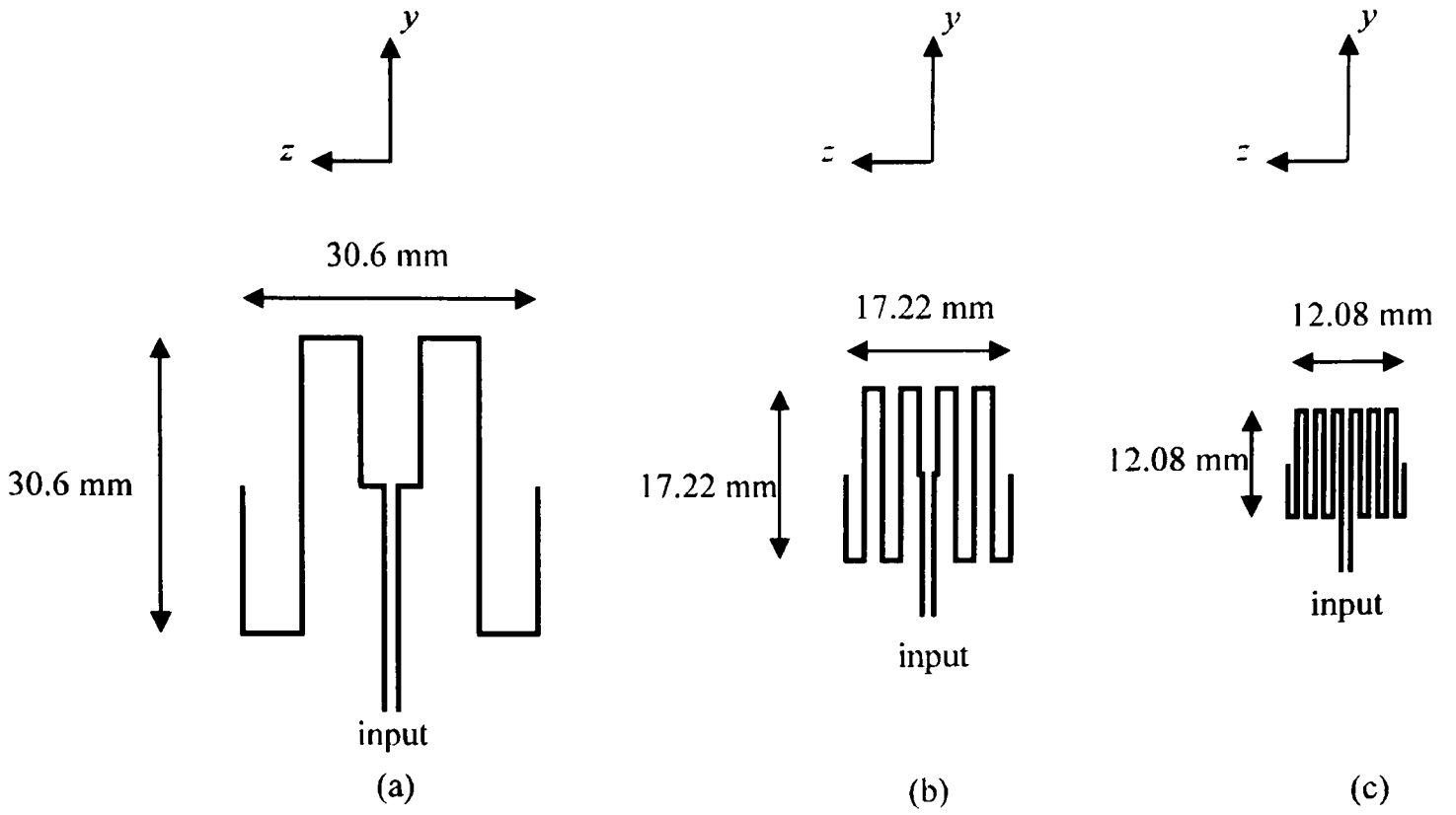

Fig. 5.4. Symmetrical meander dipoles with 1:1 aspect ratio: a) two, b) four, c) six meander sections (1:1 scale). 50 ohm coplanar strip feed lines are also shown.

The linear $\lambda/2$ dipole of wavelength λ_d was designed to be of 0.5 mm track width. From here, a set of generic symmetrical meander dipoles was designed. Fig. 5.5 shows the geometry of an N-section of such structure. The definition of all the symbols are as follows:

w_s , track width

s_s , feed gap

s_{sg} , total feed gap

w_{sm} , mean width of the meander section

w_{si} , internal width of the meander section

w_{sx} , external width of the meander section

W_s , antenna width

W_{sm} , mean antenna width

L_{sx} , axial length

L_{st} , total mean arm length

AR_s , aspect ratio

N , number of meander section in the half-arm

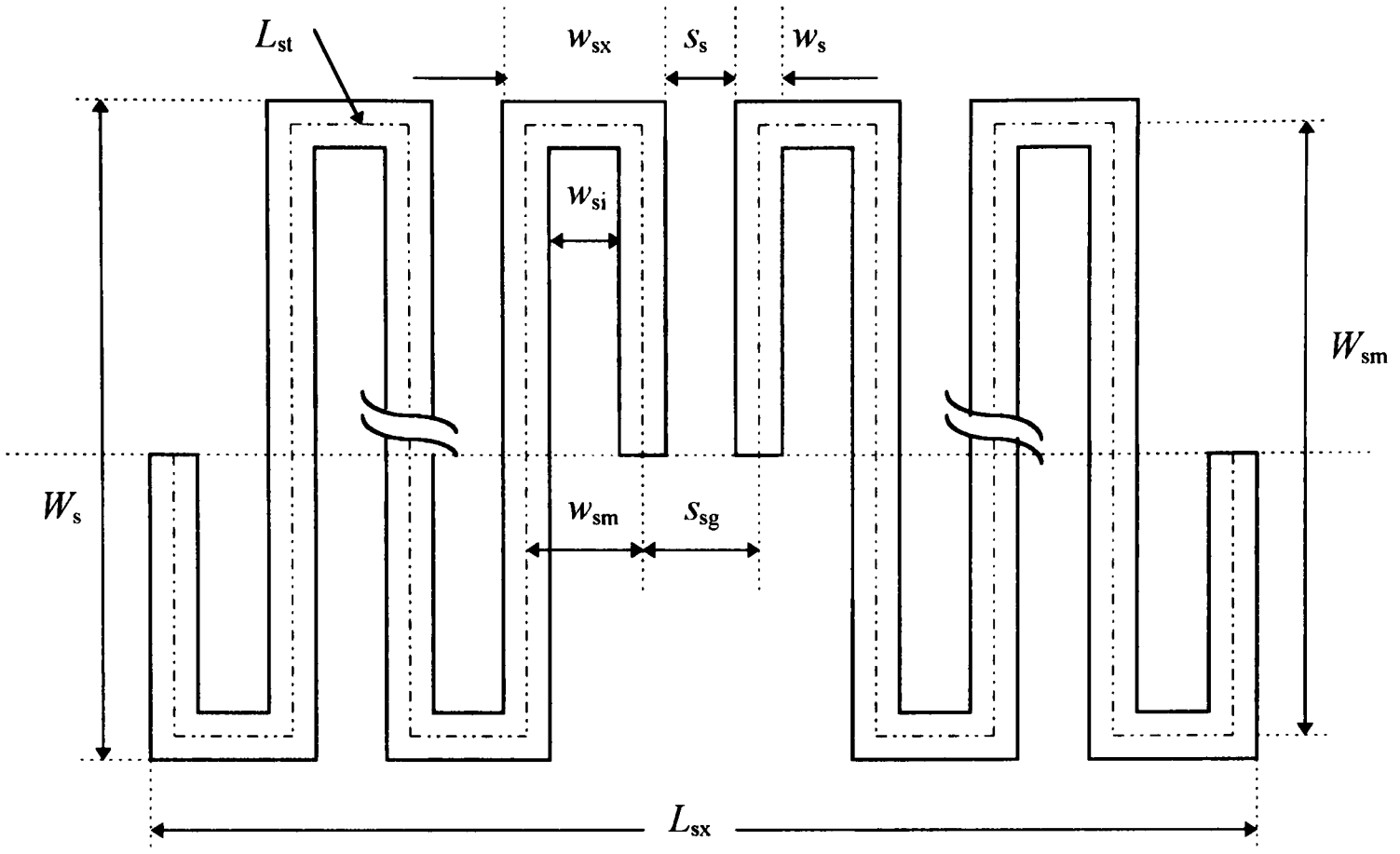

Fig. 5.5. Designed parameters for an N-section symmetrical meander dipole.

The parameters w_s and L_{st} were kept constant. The lengths of s_{sg} and w_{sm} for all structures were designed to be equal.

$$s_{sg} = w_{sm} \tag{5.15}$$

This is to ensure similar effect of adjacent capacitive coupling between adjacent meander bends and that at the feed. Similarly, the lengths of s_s and w_{si} for all structures were designed to be equal.

$$w_{si} = s_s \tag{5.16}$$

The parameter s_{sg} is made up of s_s and w_s, i.e.,

$$s_{sg} = s_s + w_s \tag{5.17}$$

From eqns. (5.15) and (5.17),

$$w_s = w_{sm} - w_s \tag{5.18}$$

The parameter w_{sm} is made up of w_{si} and w_s, i.e.,

$$w_{sm} = w_{si} + w_s \tag{5.19}$$

Rewriting eqn. (5.19) gives

$$w_{si} = w_{sm} - w_s \tag{5.20}$$

The parameter w_{sx} is made up of w_{sm} and w_s, i.e.,

$$w_{sx} = w_{sm} + w_s \tag{5.21}$$

The parameter W_s is made up of W_{sm} and w_s, i.e.,

$$W_s = W_{sm} + w_s \tag{5.22}$$

Rewriting eqn. (5.22) gives

$$W_{sm} = W_s - w_s \tag{5.23}$$

The aspect ratio of the structure is defined as the ratio of the antenna axial length, L_{sx}, to the antenna width, W_s, mathematically written as

$$AR_s = L_{sx} / W_s \qquad \text{(dimensionless)} \tag{5.24}$$

Rewriting eqn. (5.24) gives

$$W_s = L_{sx} / AR_s \tag{5.25}$$

where L_{sx} can be written as

$$L_{sx} = 2[\ 2Nw_{si} + (2N + 1)w_s\ ] + s_s \tag{5.26}$$

Substituting eqn. (5.16) into eqn. (5.26) gives

$$L_{sx} = 2[\ 2Ns_s + (2N + 1)w_s\ ] + s_s \tag{5.27}$$

The length of L_{st} was kept constant as 150.0 mm, which is the same as the length of the linear $\lambda/2$ dipole.

$$L_{st} = \lambda_d = \lambda/2 = 150.0 \tag{5.28}$$

L_{st} can also be written as

$$L_{st} = 2N(W_{sm} + w_{sm}) \tag{5.29}$$

Substituting eqn. (5.23) into eqn. (5.29) gives

$$L_{st} = 2N(W_s - w_s + W_{sm}) \tag{5.30}$$

Substituting eqn. (5.25) into eqn. (5.30) gives

$$L_{st} = 2N[(L_{sx} / AR_s) - w_s + W_{sm}] \tag{5.31}$$

Substituting eqn. (5.27) into eqn. (5.31) gives

$$L_{st} = \frac{8N^2 w_{sm}}{AR_s} + \frac{4Nw_s}{AR_s} + \frac{2Ns_s}{AR_s} - 2Nw_s + 2Nw_{sm} \tag{5.32}$$

Rewriting eqn. (5.32) gives

$$w_{sm} = \frac{L_{st} + 2Nw_s - \frac{2N}{AR_s}(2w_s + 2s_s)}{2N\left(1 + \frac{4N}{AR_s}\right)} \tag{5.33}$$

Tables 5.2-4 show the dimensions of the calculated values of the three sets of designed antenna widths, meander section mean widths and the axial lengths, using the above formulations. The values in the highlighted box were fabricated.

Table 5.2. The first set of symmetrical meander dipoles designed dimensions with aspect ratio = 1.5 and track width = 0.5 mm.

N	W_s (mm, λ_d)	w_{sm} (mm, λ_d)	L_{sx} (mm, λ_d)
2	27.82 , 0.186	8.25 , 0.055	41.73 , 0.278
4	16.32 , 0.109	2.66 , 0.018	24.47 , 0.163
6	11.13 , 0.074	1.30 , 0.009	17.44 , 0.116
8	9.09 , 0.060	0.77 , 0.005	13.63 , 0.091
10	7.49 , 0.050	0.51 , 0.003	11.22 , 0.075
12	6.39 , 0.043	0.36 , 0.0024	9.59 , 0.064

Table 5.3. The second set of symmetrical meander dipoles designed dimensions with aspect ratio = 1.0 and track width = 0.5 mm.

N	W_s (mm, λ_d)	w_{sm} (mm, λ_d)	L_{sx} (mm, λ_d)
2	30.60 , 0.204	6.02 , 0.040	30.60 , 0.204
4	17.22 , 0.115	1.86 , 0.012	17.22 , 0.115
6	12.08 , 0.081	0.89 , 0.006	12.08 , 0.081
8	9.35 , 0.062	0.52 , 0.004	9.35 , 0.062
10	7.67 , 0.051	0.34 , 0.002	7.67 , 0.051
12	6.52 , 0.043	0.24 , 0.0016	6.52 , 0.043

Table 5.4. The third set of symmetrical meander dipoles designed dimensions with aspect ratio = 1.0 and track width = 0.2 mm.

N	W_s (mm, λ_d)	w_{sm} (mm, λ_d)	L_{sx} (mm, λ_d)
2	30.24 , 0.202	6.01 , 0.040	30.24 , 0.202
4	16.89 , 0.113	1.85 , 0.012	16.89 , 0.113
6	11.75 , 0.078	0.89 , 0.006	11.75 , 0.078
8	9.04 , 0.060	0.52 , 0.004	9.04 , 0.060
10	7.35 , 0.049	0.34 , 0.002	7.35 , 0.049
12	6.21 , 0.041	0.24 , 0.0016	6.21 , 0.041

As for the 50 ohm coplanar strip feeding lines, three dimensions were calculated using eqn. (2.96) as discussed in Section 2.8.4. The dimensions were chosen to fit into the antenna appropriate structures. These were tabulated in Table 5.5. CPS type 1 is incorporated in antenna set 1, N = 2, 4; antenna set 2, N = 2, 4 and antenna set 3, N = 2. CPS type 2 is incorporated only in antenna set 1, N = 4. Finally, CPS type 3 is incorporated in antenna set 3, N = 6. For the remaining antennas, that is, antenna set 1, N = 6 and antenna set 2, N = 6, the CPS line extends from the centre of the radiating structure. This was done to ease the connection to the SMA connector. Nevertheless, the line impedances remained approximately 50 ohm.

Table 5.5. 50 ohm coplanar strip feed lines dimensions.

CPS feed line	Type 1	Type 2	Type 3
strip width, *w*, mm	0.50	0.40	0.20
strip gap, *s*, mm	0.90	0.65	0.25
Antenna type	Set 1, N = 2 & 4; Set 2, N = 2 & 4; Set 3, N = 6.	Set 1, N = 4.	Set 3, N = 6.

The 0.5 mm track widths were chosen so that comparison between the anti-symmetrical and symmetrical meander dipoles can be made, based on the same dimension of track widths. It was also decided to design narrower lines (0.2 mm designs), since further comparisons with regards to line track widths can be made. Narrower lines were expected to produce less radiation and hence contribute to less gain. The designs can then be scaled down to the thin-film superconducting structures. This superconducting version, being the smallest in size, is expected to show an improved performance over that of similar copper structures which were of the poorest performance.

The thick-film superconducting structures need no scaling down since the patterns can be fabricated onto a large substrate area. However, the limit of the superconductor line widths has to be observed, in accordance to the available fabrication facilities. The only thick-film superconducting meander antenna fabricated was chosen to be that of the second set symmetrical meander dipole, having two meander sections in the half arm and 0.5 mm track width. This was done while waiting for the thin-film antennas to be fabricated. Efforts undertaken for making successful feeding connections having proper boards for supporting the thin-film antenna without affecting its performance are discussed in Section 8.2.2. Further discussion of the fabrication process of the thick-film superconducting antenna is presented in Section 7.2.2.

The available laser-ablation and patterning facilities enables thin-film superconducting lines as narrow as 10.0 μm to be patterned. This is compared with 0.2 mm line width for the copper structures which is also the limit of the available photo-lithography facilities. From Tables 5.2 to 5.4, designs with more than six meander bends in the half-arm appeared impossible to be fabricated, since the gaps were too small. This problem may be solved using lines which are narrower than 0.2 mm. However, this is beyond the capability of the available photo-lithography facilities. A brief discussion of the standard etching process is presented in Section 7.1.3.

The configuration of the thin-film superconducting structures can be obtained from the corresponding designed copper antennas, by a simple scaling down. This is because, the whole superconducting structure has to fit onto a 1x1 cm^2 magnesium oxide, or MgO,

substrate ($\varepsilon_r = 9.8$, 0.5 mm thick). The fabrication is possible through the laser ablation and patterning facilities available in the school. These techniques are briefly discussed in Section 7.3 whilst the problem related to making feeding connections is discussed in Section 7.4.

Three parameters have to be considered in the scaling down procedure; the reduction factor, the constant ratio of the track width to substrate height and the operational frequency. The substrates for both copper and superconductor have the same permittivities.

The physical size of the copper and superconducting antennas, respectively, are given by

$$A_{(sc)} = L_{sx(sc)}\ W_{s(sc)} \tag{5.17}$$

$$A_{(nc)} = L_{sx(nc)}\ W_{s(nc)} \tag{5.18}$$

where A is the antenna area, L_{sx} is the antenna axial length, and W_s is the mean antenna width. The subscripts (sc) and (nc) refer to the thin-film superconductor and normal conductor, respectively.

If the physical size of the copper antenna (track width $w_{(nc)}$ and substrate height $h_{(nc)}$) is reduced by a factor of p, then the corresponding size of the thin-film superconducting antenna of eqn. (5.17) is also given by

$$A_{(sc)} = A_{(nc)} / p \tag{5.19}$$

Hence, the track width, $w_{(sc)}$, of the corresponding thin-film structure on the MgO substrate becomes

$$w_{(sc)} = \frac{w_{(nc)}}{p\, h_{(nc)}\, h_{(sc)}} \tag{5.20}$$

Eqn. (5.20) is also valid for the strip width, w, and the strip gap, s , of the corresponding thin-film CPS feed line on the same MgO substrate.

The operational frequency of the thin-film structure will thus be increased by a factor of p. A very slight shift in this frequency may be experienced due to the permittivity of liquid nitrogen which is slightly higher that unity, that is, 1.44 [50]. However, this effect is not very critical to the antenna performance.

As the available facilities only allow the use of 1x1 cm^2 MgO substrate, the value of p was chosen to be 3.31. The dimensions of the thin-film HTS symmetrical meander dipoles, including their CPS feed lines, which were fabricated and tested are tabulated in Table 5.6.

Table 5.6. Thin-film HTS symmetrical meander dipoles designed dimensions with aspect ratio = 1.0 and track width = 78.0 μm.

N	W_s (mm, λ_d)	w_{sm} (μm, λ_d)	L_{sx} (μm, λ_d)	w (μm)	s (μm)
2	913.6, 0.061	181.6, 0.0121	913.6, 0.061	151.0	270.0
4	510.3, 0.034	55.9, 0.0036	510.3, 0.034	120.0	196.0
6	355.0, 0.024	26.9, 0.0018	355.0, 0.024	60.0	75.7

5.2 MATCHING NETWORKS

No matching network was designed for all the designed antennas. The reason being, all the experimental antennas showed reasonably good matching at their corresponding frequencies of operation. However, this is only accomplished after problems related to the measurement was solved. Further reduction in the return loss is provided by the incorporated balun. The simulated results did not include any balun, but gave good matching and figure-of-eight far-field radiation patterns. These results and the related measurement problems were discussed further in Section 8.2.

However, there is still some space available in the thin-film HTS device, for the design of a matching network. This is especially true for the antennas with four and six meander sections in the half arm because the radiating structures occupy a small area.

5.3 BALUNS

As discussed earlier in Section 5.1.2, a balun was incorporated to reduce the feeding loss and stray radiation. In addition, the balun also behaves as a matching network. The CPS feeding of the symmetrical meander antenna is essentially a transmission line which is in a balanced state. The input is connected through a length of coaxial cable which is inherently unbalanced, via the SMA connector at the feed. The inner and outer conductors of the coaxial cable are separated by a PTFE dielectric tube. The antenna ground is connected to this outer conductor. These conductors do not couple well to the antenna which is in a balanced state. This uncoupling causes a net current flow to ground on the outside part of the outer conductor. The existing currents on the cable and in the equivalent circuit are as illustrated in Fig. 5.6(a) and (b), respectively. Z_L is the input impedance of the antenna at the terminals 1-2.

The current, I_1 , flowing in the inner conductor of the coaxial cable is also flowing in the connected one arm of the antenna. The voltages in each side of the radiating structure and the ground are equal in magnitude but 180° out of phase. This produces a current flow, I_4 , on the outside surface of the coaxial cable. However, this current does not exist if the current flowing in the inside surface of the coaxial cable, I_3 , equals I_1 . The current flowing in the other arm of the antenna, I_2 , is made up of the currents I_3 and I_4 . One arm of the antenna is connected directly to the outer conductor of the coaxial cable at terminal 2 for the ground. The other arm is merely weakly coupled to it at terminal 1. This connection produces a much larger current I_3 . Hence, there is no possibility for the current I_4 to be removed. The amount of I_4 is determined by the impedance, Z_g , from the outer conductor to ground. This current can be significantly reduced if Z_g is made large enough by incorporating a suitable balun at the antenna feed. A balun (balance to unbalance converter)

is a device that is used to balance inherently unbalanced system. This is done by cancelling or choking the outside unwanted current I_4.

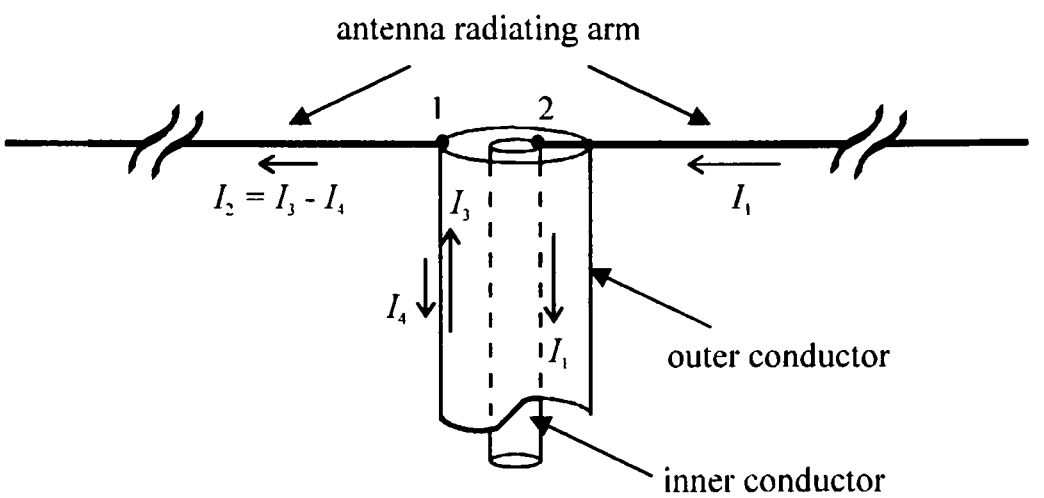

(a)

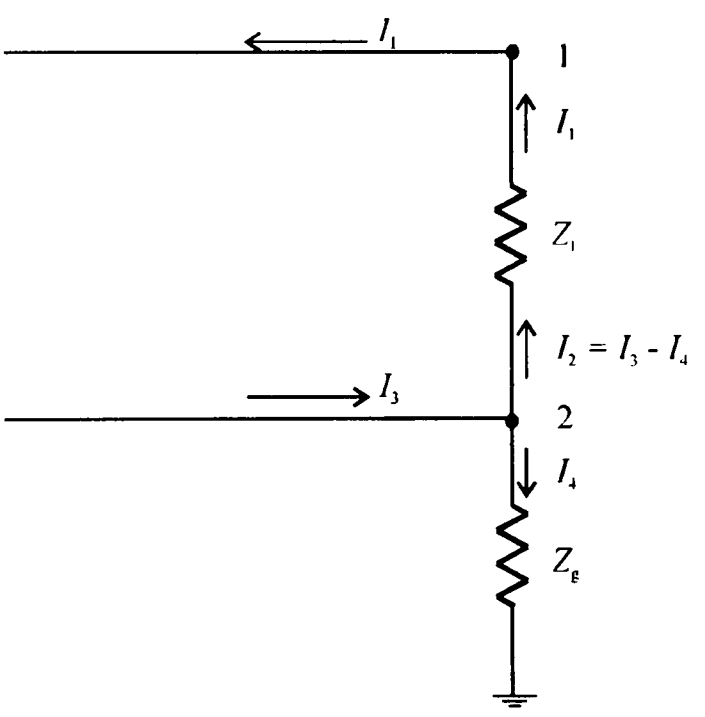

(b)

Fig. 5.6. (a) Unbalanced coaxial line, (b) the equivalent circuit.

The designed balun that was used in this study is an adjustable bazooka balun. The basic structure of the bazooka balun can be found in references [1] and [3]. The designed structure of the adjustable balun is depicted in Fig. 5.7. It is formed by a length (B_{L1}) of good conductor metallic sleeve (T_1), made of brass, that enclosed part of a thicker inner brass tube (T_2) of length B_{L4}. This brass tube can be adjusted so that the coxial cable length B_L is quarter-wavelength. Brass was chosen over other good conductor metals such as copper and aluminium because it has a softer texture which makes it easily machined. Although brass is a soft material, the balun does not bend easily during the experimental work.

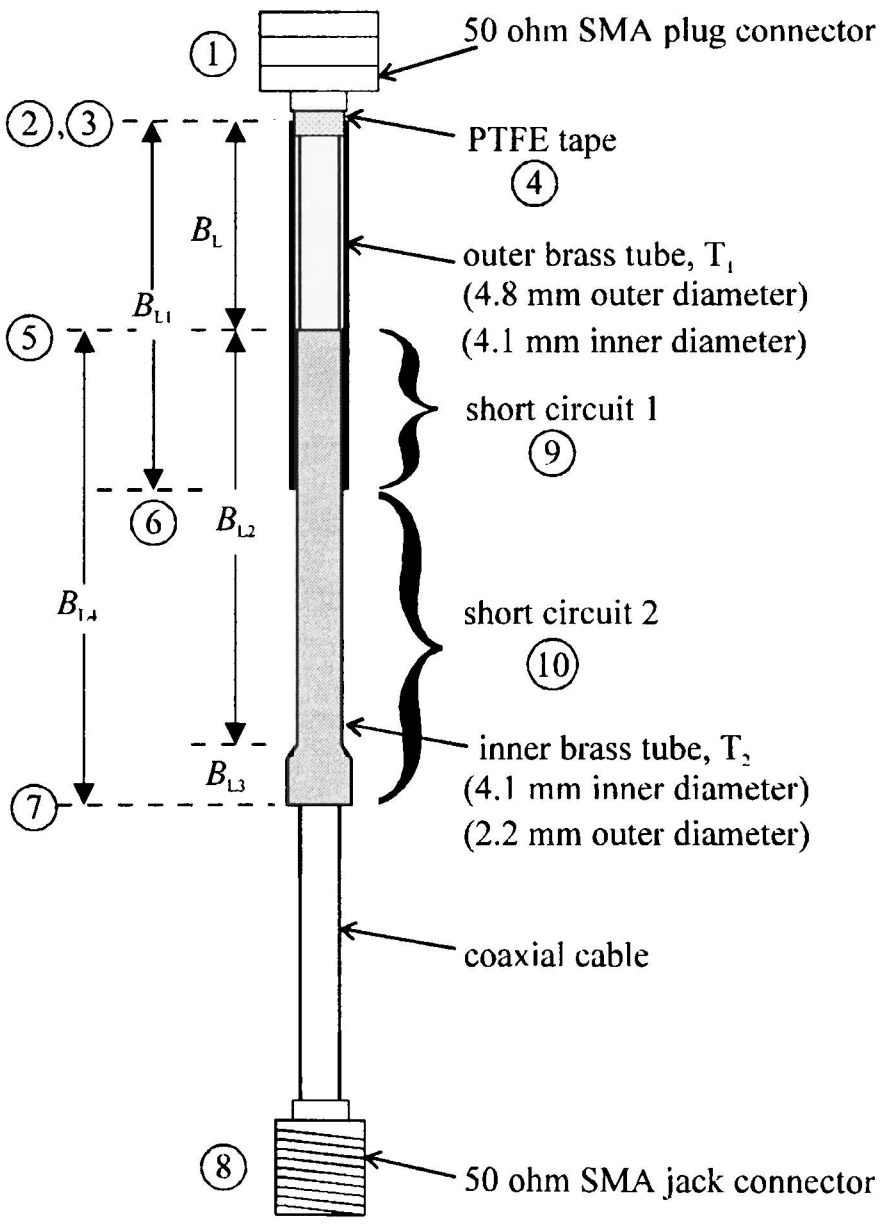

Fig. 5.7. The designed adjustable bazooka balun.

One end of T_1 was left as an open circuit, very closely positioned to the 50 ohm SMA connector at position 2. This can be done by having several turns of PTFE tape around the outer conductor of the coaxial cable. The very low relative permittivity of PTFE [90] makes it an ideal material for this purpose. One may also use a very small length of PTFE tube. Position 3 is where the connector is soldered onto the coaxial cable. At position 5, T_1 was short-circuited to one end of T_2 and the outer conductor of the coaxial cable. The contact between these three components extends along position 9. At position 6, the other end of T_1 touches T_2. Along position 10, T_2 touches the outer conductor of the coaxial cable. This ends at position 7. This end of T_2 was made thicker to ease its adjustment during the experiments. The length of B_{L3} is 10 mm, with an outer diameter of 6.4 mm. The other end of the coaxial cable is connected to a 50 ohm SMA connector. The test antennas are connected to connector 1. Connector 8 was connected to the network analyser through a connecting semi-rigid cable. The experimental work is discussed further in Section 8.2.

In this study, two similar baluns were constructed. The first balun has the adjustable length B_L between 73 mm and 125 mm. This was used for all the copper and thick-film symmetrical meander dipoles, which operate around 1.0 GHz. The adjustable length B_L of the second balun is between 5.0 mm and 35.0 mm. This balun was incorporated in the thin-film HTS antennas, which operate around 3.0 GHz. The dimensions of T1 and T2 are given in Table 5.7.

Table 5.7. Dimensions of the designed balun.

Balun/Dimensions	B_{L1} , mm	B_{L2} , mm	B_{L4} , mm
Balun 1	75.0	70.0	82.0
Balun 2	40.0	35.0	47.0

The electrical operation of the balun is thus described. The shorted B_L is essentially a transmission line. Hence, the input impedance at the open end of this line is very large [35]. Ideally, the value is infinity This input impedance is equal to Z_g . Hence, the current is choked, if not completely removed, and the system is balanced.

CHAPTER 6

NUMERICAL SIMULATIONS

6.0 INTRODUCTION

A full-wave electromagnetic simulation software produced by Sonnet Software [91] has been employed in this study. This chapter describes the numerical simulations used for all the designed and tested antennas. Some examples of program listings and outputs are presented where appropriate. Further results are presented in Chapter 8.

6.1 DESCRIPTION

There are five tools of Sonnet which are used throughout the numerical work; namely ***xgeom***, ***em***, ***emvu***, ***patgen*** and ***patvu***. The relationship is as illustrated in Fig. 6.1. A brief explanation then follows.

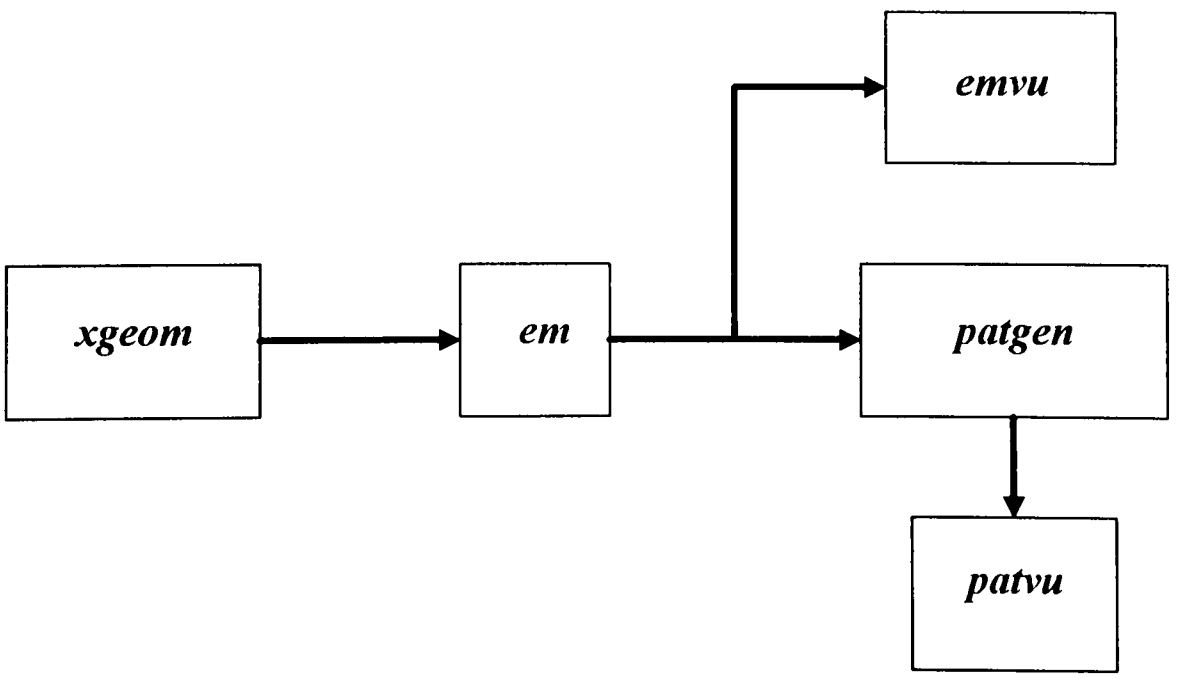

Fig. 6.1. Relationship between Sonnet programs.

Xgeom enables the drawing of the layout of the antenna structure in a rectangular metallic box. The size of the box is very important. It must not interfere with the surface current distribution and far-field radiation pattern of the antenna. A distance of half-wavelength between each cover of the box and the antenna is sufficient for this purpose. In addition, a distance of at least the antenna axial length from the sides of the box is sufficient for accurate simulations. A lossy air layer above and below the antenna which acts as absorbers are also needed. Design specifications which closely approximate that of the actual device can be given. This include specifying the metallisation loss for the copper circuits and the surface reactance for the superconducting circuits. The former is modelled by [91]

$$R_{DC} = \frac{1}{\sigma a_h} \tag{6.1}$$

and

$$R_{RF} = \sqrt{\pi \frac{\mu_0}{\sigma}} \tag{6.2}$$

where R_{DC} and R_{RF} determine the loss at low and high frequency, respectively. The parameter a_h is the metallisation thickness, as discussed in Section 2.8. The value of the surface reactance (also known as the kinetic inductance) can be found using eqn. (3.28) of Section 3.2. For example, if the experimental operating frequency obtained for the HTS device is 3 GHz, then at 77K, R_{RF} approximately equals 4.55 mΩ.

The substrate thickness can also be considered. Two types of antenna feeding has been used in the measurements. These are modelled as simple internal port for the direct SMA connector feed and balanced or push-pull port for the CPS feed. For the first type, the port is labelled by "1" whilst for the second type, the signal port is labelled "1" and the ground port as "-1".

The circuit specified by ***xgeom*** can then be electromagnetically analysed by ***em***. This is done by solving the current distribution in the circuit metallisation using the Method of Moments. A surface meshing technique is employed. This full-wave or complete

electromagnetic analysis calculates *S*-parameters for arbitrary 3-D planar radiating geometries. It accounts all possible coupling mechanisms and includes metallisation loss and dielectric loss related to an antenna. The analysis uses the open waveguide simulator technique. The resistance of the top and bottom covers of the metallic box were set to be that of free space. The bottom cover was left open since all the antennas designed do not have any ground plane. The air layer above and below the antenna are at least half the operational wavelength. This is sufficient for accurate radiation pattern generation simulated by ***patgen***. Subsectioning the metallisation and invoking a single precision matrix may be employed to increase the execution speed while maintaining full accuracy at all microwave frequencies. As an antenna circuit only has one input port, the only parameter data calculated by ***em*** is the return loss; both magnitude and phase, at the specified single frequency or over the specified range of frequencies.

The surface current distribution generated by ***em*** can then be viewed using ***emvu***; the current density visualisation tool. Half-wave approximately sinusoidal current distribution was observed on all the simulated designed antennas. This will be discussed further in Chapter 8. Two examples are discussed in Section 6.2.

Patgen is the radiation pattern analysis tool. It uses the current density information that ***em*** generates to compute the far-field radiation of the antennas above the horizon. The spherical co-ordinate system used is as shown in Fig. 6.3. XY-plane is the plane of the ***xgeom*** window. One can choose to have either earth, spherical or top co-ordinates for the display. An example of the earth co-ordinate control program listing used in this study is given in Appendix 6. The co-ordinate was used to obtain the E-plane, which is equivalent to the experimental horizontal plane, pattern. No H-plane, or the equivalent experimental vertical plane, pattern can be obtained in this study. This is because, Sonnet is unable to simulate any pattern which is normal to the sidewalls of the simulation box.

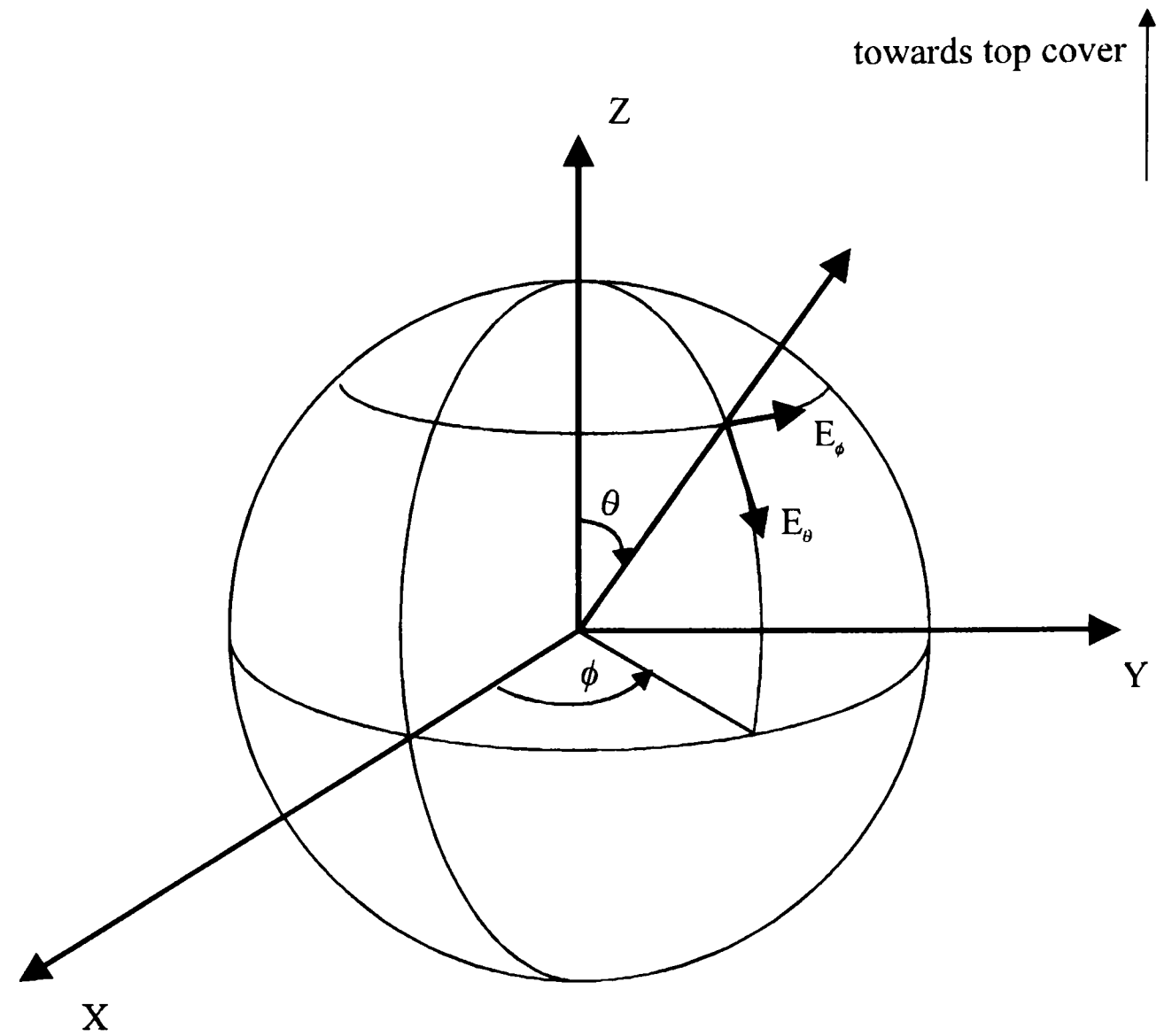

Fig. 6.2. The spherical co-ordinate system of ***em*** and ***xgeom***.

However, Sonnet is unable to simulate accurately the radiation pattern of antenna circuits with direct coaxial feed lines. Such effects can be observed in the experiments, as described in Section 8.3, particularly for very small antennas.

Patvu is an X Window System and is the visualisation tool for the radiation pattern computed by *patgen*. It has the capability to display either the Cartesian or polar plot. A 3D plot may also be generated. However, only Cartesian plots are used throughout the data presentation in this thesis since direct comparison with the measured results can be made. ***Patvu*** also enables the display over its absolute value, normalised over its maximum, normalised over a dipole or normalised over an isotropic antenna. An example of the display is discussed in Section 6.2. If the presence of cross-polarisation component is of interest, one can choose either the right hand/left hand, circular or Ludwig definitions.

6.2 EXAMPLES OF RESULTS

Two examples of the current distribution viewed using ***emvu*** are depicted in Fig. 6.2. Fig. 6.2(a) is the surface current distribution of an anti-symmetrical printed meander dipole antenna. The coaxial feed is represented by port "1". The current is maximum at port "1", which is the input of the antenna. This is shown in red colour. The current decreases approximately sinusoidally until it becomes null at the both ends of the antenna. This is shown in blue colour. The scale of the current density is not shown here. Fig. 6.2(b) shows the surface current distribution of a symmetrical printed meander dipole antenna. Ports "1" and "-1" represent the input to the CPS line, where "-1" is the ground.

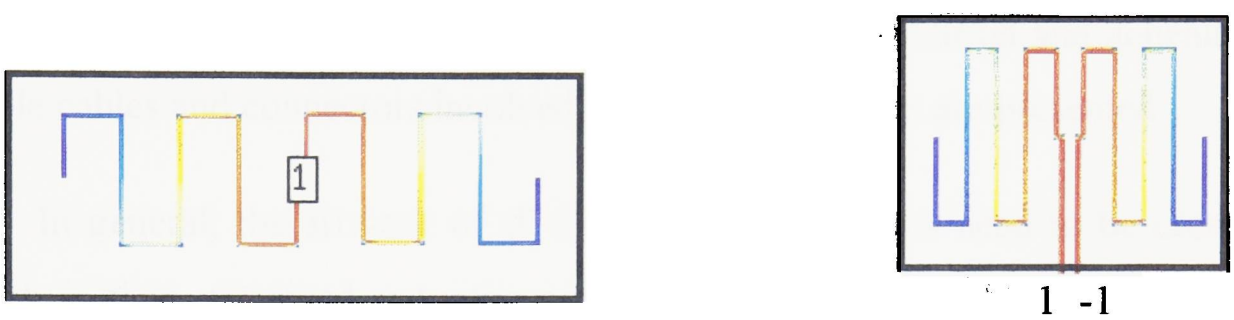

(a) (b)

Fig. 6.3. Examples of ***emvu*** display: (a) direct feed, (b) CPS line feed.

An example of the E-plane far-field radiation pattern of the anti symmetrical meander dipole antenna, viewed using ***patvu***, is shown in Fig. 6.4. This pattern is normalised over its maximum. The pattern is in the top hemisphere of the antenna. The other half can be predicted as having similar pattern. The data is read into standard spreadsheet software to produce similar plot. More results will be discussed in Chapter 8.

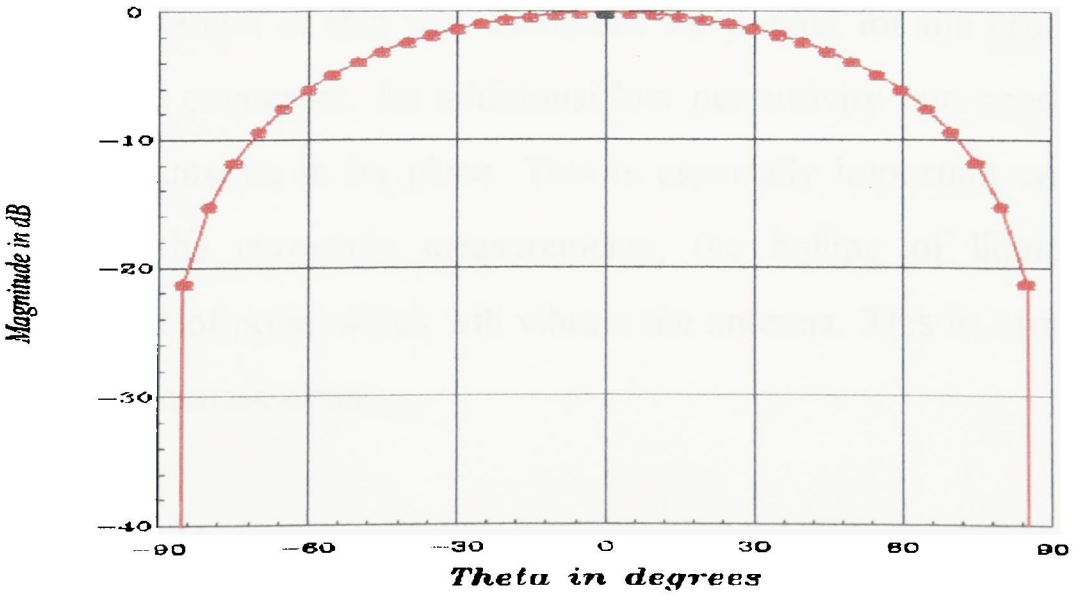

Fig. 6.4. An example of ***patvu*** display.

CHAPTER 7 MATERIALS AND FABRICATION TECHNIQUES

7.0 INTRODUCTION

In this chapter, different materials involved and their related fabrication techniques carried out are discussed. A brief discussion of patterning and etching techniques are also given. This is followed by a short discussion of silver evaporation and annealing processes. Suitable cables and connectors involved in the measurements are presented.

In general, the artwork of all the radiating structures need to be created first. The artwork is then patterned onto the corresponding substrate. After patterning, etching is carried out to remove the unwanted conductor, leaving the radiating structure on the substrate. Finally, connection is made for the input ports of the device. As for the superconducting structures, direct soldering to the YBCO is not possible for making electrical contact. A small patch of silver need to be applied for making contact between the SMA connector and the YBCO feed line. For the thick-film devices, direct soldering on this silver patch may be made. However, due to the very thin feeding lines of the thin-film structures, a minute quantity of silver-epoxy is applied to bond the connector to the antenna. A very short length of thin wire facilitates the joining for the ground of the CPS feed line to that of the connector. An additional low permittivity non-conducting board is needed to hold each antenna in its place. This is especially important when performing experiments. As for the cryogenic measurements, the boiling of liquid nitrogen can introduce small amount of noise which will vibrate the antenna. This in turn may cause the connection to break in certain cases.

7.1 COPPER CIRCUITS

7.1.1 RT/Duroid

All the copper devices were implemented on RT/Duroid glass-fibre reinforced polytetrafluoroethylene (or PTFE) dielectric clad. The RT/Duroid 5870 dielectric clad for the anti-symmetrical meander dipoles, short dipole and the corresponding linear reference dipole was 1.57 mm thick and has relative permittivity of 2.33 and loss tangent of 0.0012. These devices were in 35 μm thick copper electro-deposited on both sides. However, the artwork was etched onto one side of the dielectric using standard photographic technique for printed circuit board as described in the next section. The data sheet of the board can be referred to in Appendix 7.

As for the symmetrical meander dipoles, it was decided to implement on a much higher relative permittivity dielectric clad to ease direct comparison with the superconducting thin-film structures. Hence, RT/Duroid 6010 was chosen. It was 1.27 mm thick and has relative permittivity of 10.8 and loss tangent of 0.001. These devices and the corresponding linear reference dipole were in 17.5 μm thick copper electro-deposited on one side. The data sheet can also be referred to in Appendix 7. Similar etching procedure was employed as described in Section 7.1.1.

7.1.2 Fabrication Process

The artwork need to be first prepared. This can be done using commercially available drawing packages and the final artwork is printed onto a laminate using a very high resolution printer. The standard etching technique for printed circuit board is employed. The simple procedure is listed as follows:

1. Clean the board in de-oxidised bath.
2. Coat the board with photo-resist.
3. Bake the coated board in a preheated oven for 15 minutes.

4. Attach the artwork onto the baked board.
5. Expose the board with the attached artwork to ultra-violet bed for 5 minutes.
6. After the exposure, remove the artwork and dipped the board into an etching tank of ferric chloride solution for 10 minutes.
7. Give the board a good wash under running tap water to completely remove the layer of etching solution which is still covering the board.
8. Leave the board to dry naturally. This usually takes a very short time.

7.2 THICK-FILM HTS CIRCUITS

7.2.1 YBCO/YSZ

The thick-film superconducting antennas were fabricated from YBCO material deposited on YSZ which has relative permittivity of about 30.0 and loss tangent of 0.001. YSZ was chosen due to its high strength, toughness and compatability with YBCO [92], [93]. Tolerance to shock and vibration is excellent thus avoiding a key concern with regard to some applications. Altough there is a reaction between YSZ and YBCO which forms mainly barium zirconate, this reaction layer does not impair the superconducting properties. In fact, the reaction layer provide an excellent adhesive bond. For the only thick-film superconducting symmetrical meander antenna, the thicknesses of the YBCO and YSZ were 0.1 mm and 1.0 mm, respectively.

YSZ properties can be referred to in Appendix 8.

7.2.2 **Fabrication Process** [93] - [95]

The preparation of the antenna artwork is similar to Section 7.1 1. Next, the thick-film YBCO ink is prepared. This is done by mixing $BaCO_3$, CuO and Y_2O_3 together and heating to ~900 °C. The yttria content is 3 mol%. The mixture is then grinded to form a fine powder. The powder is made into the required viscosity ink by mixing with standard polymers and solvents on a three roll mill. The ink is deposited onto the YSZ substrate by doctor-blading technique. After drying, the coated substrate is fired in an oxygen

atmosphere at temperatures of around 1030 °C to 1050 °C. After firing, the thick-film YBCO is patterned using the screen-printing technique. In this technique, the mask is placed on the sample via a nylon-steel mesh. The sample is coated with emulsion and exposed to ultra-violet light. When the emulsion has cured, the unwanted YBCO area is removed using an air-abrasion technique. This technique preserve the required antenna pattern definition, since the melt-processing destroys any circuit patterns produced at the coating stage. Silver contact patches at the end of the CPS feed line are added subsequently. This is done using a proprietary Ag thick-film ink sintered at 850 °C.

When the antenna has cooled down to room temperature, it is placed onto a supporting board as discussed further in Section 7.4. Direct soldering onto the sintered silver patch is applied to the feed point. The device is then coated with a thin layer of polyurethane, to protect it against humidity and film degradation [48]. Finally, the device may be placed in a dessicator to prevent accidental breakage.

7.3 THIN-FILM HTS CIRCUITS

The first step is to get the artwork developed by commercial drawing package onto a glass plate. When the YBCO film on MgO substrate has been deposited, patterning and etching of the sample are made. These are then followed by evaporating silver patches onto the ends of the CPS feeding line for making electrical contact with the SMA connector. The silver has to be annealed to prevent it from dropping off. Finally, soldering is applied at the feed contact. The device has to be kept in a dessicator to protect it against humidity and film degradation. Extreme care is needed when handling the device as it is very brittle.

7.3.1 YBCO/MgO

Superconducting thin films need to be grown on a substrate which satisfy microwave requirements [50]. It has to be inert, compatible with both the growth of a good quality film and has appropriate microwave properties for application purposes. It is

convenient if the dielectric constant does not vary with temperature as this will improve the temperature stability of the antenna. It need also be reproducible and should be compatible with good film growth. Some substrates can react chemically with the superconductor which cause impurity in the grown films and consequently reduce the performance of the final device. The substrate should also meet mechanical requirements such as smooth surface and free from any defects. It has to be strong and capable of being thinned to a certain extent for corresponding application. Good environmental stability is an advantage with sizes available in large dimensions such as above 6x6 mm^2.

Ideally, such a substrate is not yet available. However, 0.5 mm thick MgO is used in this study onto which YBCO is deposited. It has a low ε_r of 9.8 and a very low loss tangent ($\tan \delta \sim 10^{-15}$) . The properties of MgO are given in Appendix 8. Single-sided films of YBCO on MgO which were deposited by Pulsed Laser Deposition (or PLD) technique were used for all the superconducting thin-film antennas. The thickness of the laser ablated YBCO film for all the antennas is about 350 nm. The deposition technique is described in the next section. YBCO was chosen as the superconductor material for all the HTS antennas as it is by far the most popular material. It has a transition temperature of 92 K. Although there other HTS materials available, the surface impedance of any of them does not improve significantly over YBCO, even though the transition temperature may be higher.

7.3.2 **Pulse Laser Deposition** [96] - [98]

All the thin films were deposited using a KrF filled Questek 2720 pulsed excimer laser at a wavelength of 248 nm. The set-up of the pulsed laser deposition is depicted in Fig. 7.1. The laser was operated at 500 mJ and 10 Hz. It was focussed with a beam area of 5x2 mm^2 onto a rotating stoichiometric sintered YBCO target (Seattle Speciality Ceramics, 99.9% purity) with a fluence of ~1.5 Jcm^{-2}. The distance between the target and substrate was 7 cm. The substrates used were polished on an inconel heater at a temperature of 780 °C. The films were deposited in an atmosphere of 400 mTorr of O_2 for 10 minutes before cooling. The transition temperature (T_c) is typically 92 K.

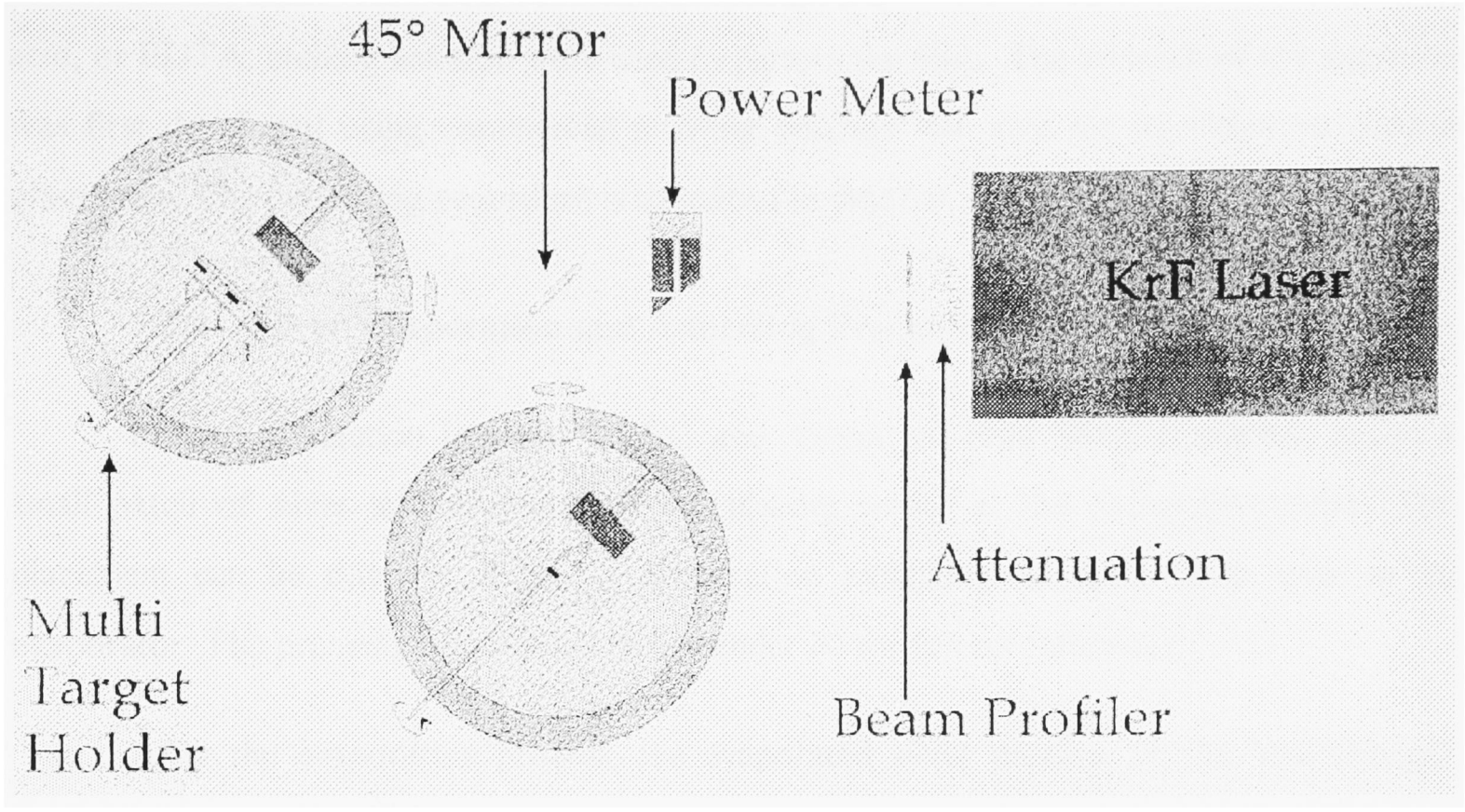

Fig. 7.1. Pulsed laser ablation set-up.

The surface morphology of the YBCO thin films was examined using a Jeol 6300 Scanning Electron Microscope and a Digital Instruments Nanoscope (II) Scanning Probe Microscope. The thickness of the films was determined by Rutherford Backscattering Spectrometry (or RBS) using a beam of He^+ ions at 2 MeV Dynamitron accelerator. The crystallinity of the thin films was monitored by X-ray FWHM rocking curve measurements and RBS channelling experiments. The critical temperature was measured by ac susceptibility.

Other depositing techniques include sputtering, electron beam co-evaporation and metalorganic chemical-vapour deposition (or MOCVD), which are equally well in producing good quality epitaxial thin films with low surface resistance values [50].

7.3.3 Patterning and Etching Techniques

It is important that patterning process does not deteriorate the superconducting thin films which will form the superconducting antennas. The method employed for the HTS thin-film antennas is wet etching. This method is preferable due to its convenience and is

economical to run. Standard positive photolithography and an ethylenediaminetetraacetic acid; or EDTA, etching solution were used to pattern the films. The artwork of the antennas was first developed using commercial drawing package and sent for development onto a glass plate. The patterning procedure is described in depth in Appendix 9.

7.3.4 Silver Evaporation and Annealing Processes

Proper connection between YBCO and normal 50 ohm SMA connector needs a small patch of silver sufficient enough for placing solder at the connection point. The placement can be done by a simple evaporation technique of clean silver wire in an evaporator. The procedure is detailed in Appendix 10 for further reference.

After the evaporation process, the evaporated silver patches on the YBCO/MgO need to be annealed. This is to give the silver greater adhesion. Annealing is done in a furnace tube, which has been temperature programmed, under a constant flow of oxygen gas. An Euroterm 818 controller programmed the temperature of the annealing process.

The annealing procedure is listed as follows:

1. Slide down the glass tube of the furnace. Put the sample (using a plastic tweezer) in the small ceramic cup (facing up) and position the cup to be at the centre of the tube. Close this end with a rubber bunk. Slowly slide back and position the glass tube in the furnace. Check that the other end is connected to the oxygen tank.
2. Program the temperature controller as listed in Table 7.1.
3. Switch on the oxygen tank. Set the level to be at 100 cm^3/min.
4. Press RUN on the controller to start the annealing process.
5. When the process has ended, switch off the oxygen tank. Slide out the cup as before. Store the device in a dessicator. Put back the cup and the glass tube into the glass furnace, ready for the next annealing process.

The next process is to add on the connector onto the feed end. This is as explained in the next section.

Table 7.1 Program for Euroterm 818 temperature controller.

Step	Parameter	Value
1	P_{ramp} 1	300 ^{0}C/h
2	P_{level} 1	450 ^{0}C
3	P_d 1	60.0 min
4	P_{ramp} 2	120 ^{0}C/h
5	P_{level} 2	15 ^{0}C
6	P_d 2	END

7.4 CABLES AND CONNECTORS

Standard RG402 microwave semi-rigid cables have been used to provide extra length of feeding connection to the antennas. These lengths are accounted for in the calibration procedure as the reference plane was set at the actual feed of the device, hence any associated errors will be removed. The two ends of the connecting cable are fitted with proper microwave connectors. One end of the cable is to mate with the connector to the antenna feed, whilst the other end is to mate with the available cable to the network analyser. The 50 ohm female SMA connector is used on all the antennas.

Each antenna with the CPS feeding line need to be placed on a non-conducting board, using non-conducting double sided tape, as support. The connector is held in place using plastic screws which are screwed into the board. The screws are expected not to interfere with the performance of the antenna. The board also helps to keep the feeding connection stable and from breaking off during far-field radiation pattern measurements. Perspex glass has been chosen for this purpose. In addition, due to the very narrow widths of the CPS feeding lines, minute amount of silver epoxy has been used as the bonding material for the SMA connectors. The data sheet of the epoxy used is available in Appendix 11. As for curing the epoxy, one needs to let the epoxy dry naturally at room temperature or it may be blow dry from a hot air blower at a distance. The latter is extremely important for the thin-film devices so as not to destroy any part that are not heat resistant.

CHAPTER 8

RESULTS AND DISCUSSION

8.0 INTRODUCTION

This section begins with a discussion of the experimental set-up. Considerations prior to measurement are also discussed in this section. All the experimental and theoretical results associated with the designed antennas are given and discussed in this chapter. Relevant tables and graphs are also given for a clear picture of the tested antenna performance.

8.1 EXPERIMENTAL SET-UP

All the experimental measurements were performed using the HP8510C automatic network analyser [99], placed outside an anaechoic chamber. Basic measured performance characteristics include reflection coefficient (and hence the input impedance and the return loss), reflection bandwidth, directive gain and radiation patterns. The experimental set-up for the reflection coefficient and gain measurements of the copper antennas is illustrated in Fig. 8.1, whilst that of the superconducting antennas is as shown in Fig. 8.2. The test antenna is immersed in a polystyrene container filled with liquid nitrogen, for the 77K environment. The container has negligible effect on the antenna performance [50], [56], [88] due to its relative permittivity of almost unity [90]. With the reference plane calibrated at the connection of the antenna feed, any losses associated with the feed are minimised (if not completely removed).

Prior to making any *S*-parameter measurements, the experimental set-up has to be calibrated. This is a standard procedure which ensure precise measurements. Simple impedance measurements require only one-port calibration whilst gain, efficiency and

pattern measurements require full two-port calibration. The connectors used have to be tested using a connector gauge, to ensure that they are perfectly matched and do not damage the cables to the HP8510C. The experimental data was stored on a floppy disk and analysed using the personal computer at a later date.

Prior to the symmetrical meander antenna transmission measurements, the far-field radiation pattern measurements on the anti-symmetrical meander antennas were performed manually. An antenna positioner was used to position the transmitting test antenna. The rotation of the positioner was controlled by a positioner control unit which has speed controller. Appropriate speed has to be chosen so as not to vibrate the test antenna as well as the set-up of the support structure. Such vibrations, if occurred, will result in measurement inaccuracies. The rotation was carried out at 15° intervals over the full 360° rotation. Measured $|S_{12}|$ data at each angle was then noted down individually. Appropriate care and attention were given to ensure accurate data reading. The positioner control unit also has forward and reverse switches. After a complete rotation, the positioner was rotated back to its original position. Since the process was very time-consuming, only 15° intervals were used. A satisfactory measurement might take several days. For the transmission and pattern measurements of the other principal plane, the transmitting test antenna was manually turned 90°.

When the semi-automatic pattern measurement set-up was ready, the transmitting test antennas still need to be positioned and oriented manually for each principal plane. A computer program written on HP Basic 5.0/5.1 language [100] was developed. The listing is given in Appendix 12. The first part of the program controls the HP8510C Network Analyser and the PDX15 Indexer for anaechoic chamber pattern measurements. An input of frequency value is prompted for. After a complete 360° rotation, the turn-table is then rotated back to its original position. This section has been previously created. The measured data is then saved on DOS format onto a 3.5 inch floppy disk which is placed in the network analyser set-up. Finally, the program enables the hard-copy plotting of the measured radiation pattern Cartesian plot over a full rotation of 360°. However, for the

purpose of presentation in this thesis, the saved data is processed using commercial PC data-processing software.

Several considerations need to be given prior to measurement since the determination of the characteristics or performance of very small size antennas has related difficult problems [86]. It was first decided to test only the radiating structures made from copper material. The antenna is fed directly from a 50 ohm SMA connector. This method is used for the anti-symmetrical meander dipoles and the linear dipoles. The discussion of the antennas has been given in Section 5.1.1. Since the antennas matched well at their corresponding frequency of operations, the method is employed for the symmetrical meander dipoles. However, it has to be borne in mind that although the anti-symmetrical meander dipoles are electrically small, they are nearer to the upper size limit. Numerically simulated results also showed well matched antennas with figure-of-eight far-field radiation patterns. In addition, the measured far-field radiation patterns showed almost figure-of-eight shapes. Further discussion of the experimental and numerically simulated results are given in Section 8.2.1.

In the design of the symmetrical meander dipoles, the copper versions were first tested. The antennas were physically smaller than the first designs. The discussion of the designs has been given in Section 5.1.2. Direct connection to the semi-rigid coaxial cable is made with a 50 ohm SMA connector. This causes the existing unbalanced current on the outside surface of the cable to flow on the surface of the SMA connector. Hence, a variable quarter-wavelength sleeve balun is employed so that the antenna remains in a balanced state. The detailed discussion of the balun has been addressed in Section 5.3. However, difficulty arises when much smaller size antennas need to be connected to a 50 ohm connector from underneath through the substrate, even for the copper structures. This is because, in addition to drilling smaller holes, it is much more difficult to connect tiny length of very thin wire or tiny strip of copper tape from the ground arm of the radiating structure to the connector ground. There is also high possibility of damaging the ends of the radiating structures when heat is applied during direct soldering. In addition, the smaller gaps at the centre of the radiating structure do not correspond with the larger gap between the centre

pin and the nearest ground of the connector. This problem increases the capacitance at the feeding point. Consequently, the performance of the test antennas will be affected, even though the balun is used.

The next step is to test the copper radiating structures with 50 ohm coplanar feeding lines. The feeding line is added to enable direct connection with the 50 ohm SMA connector, to avoid drilling feeding holes in the circuit area. This problem is recognised since the both the substrates for the thick and thin film superconducting antennas are brittle and difficult to be drilled. In addition, when a balun is incorporated, each test antenna will always be positioned in parallel to the balun length. This ensures that there is no disturbance from the metallic surface of the balun. In addition, the connecting feeding semi-rigid cable is further away than the radiating structures. The part which is out of the liquid nitrogen remains covered with the absorber, thus reducing any unwanted disturbance to the measurement.

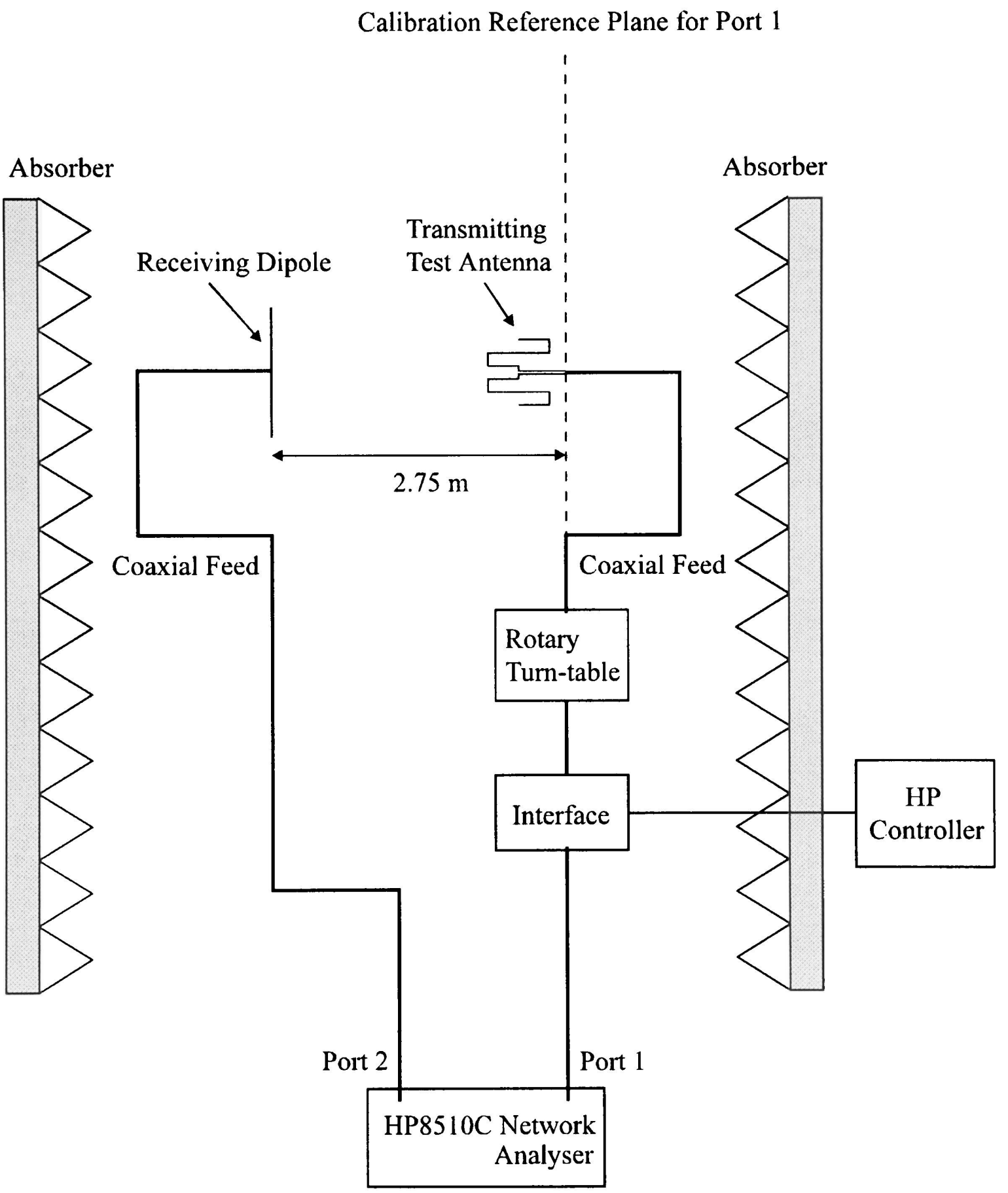

Fig. 8.1. Experimental configuration for the copper test antennas.

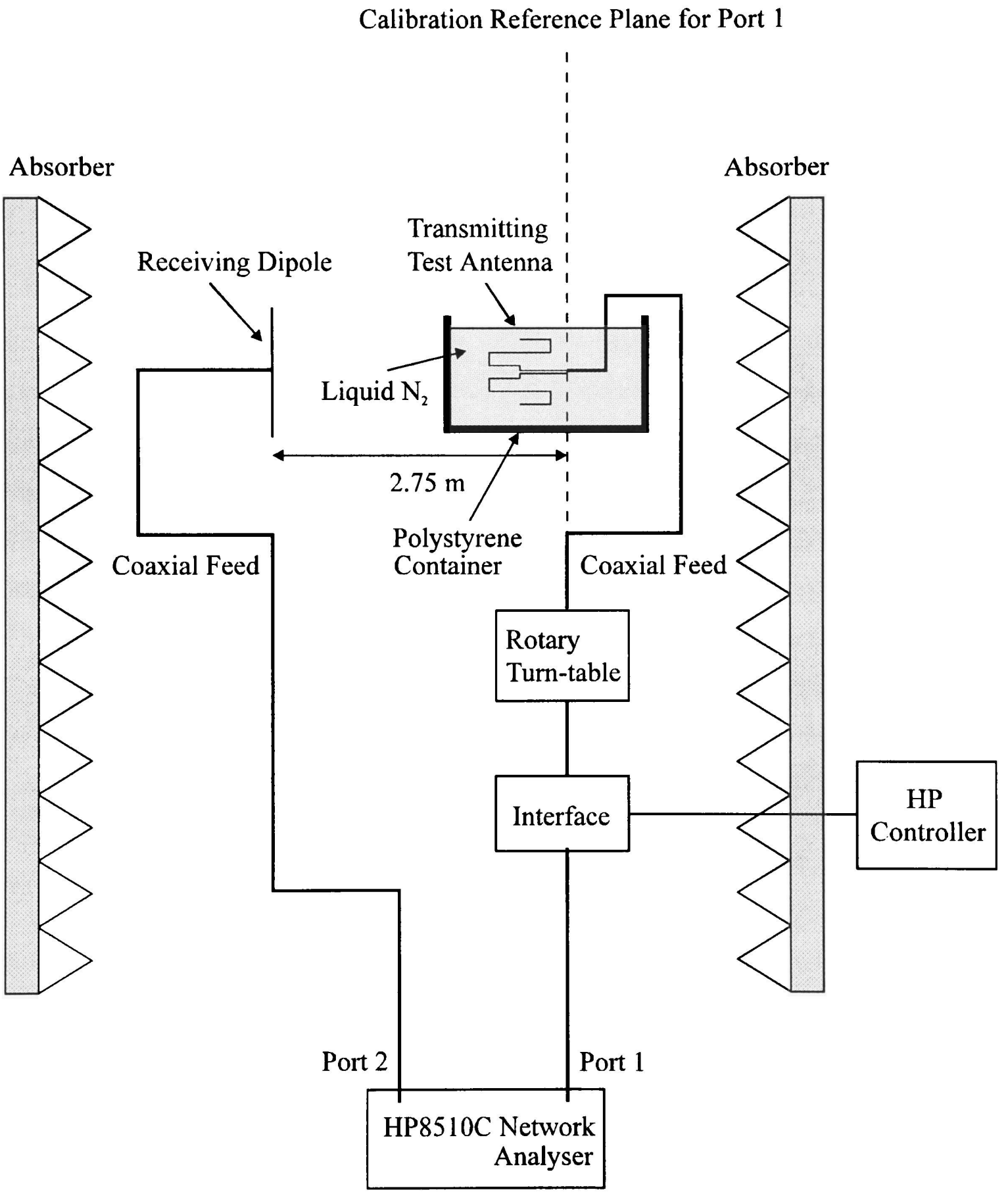

Fig. 8.2. Experimental configuration for the superconducting test antennas.

8.2 MEANDER DIPOLE ANTENNAS

This section discusses both the performances of the copper and superconducting meander dipole antennas. Both the experimental and simulated results are presented and discussed in depth.

8.2.1 Anti-Symmetrical Structure

For the anti-symmetrical meander dipole antennas of Fig. 5.1, redrawn here for convenience in Fig. 8.3, the full *S*-parameter measurements at 300K have been carried out. The respective abbreviations are also given. For simplicity, the following abbreviations were used for all the dipoles: mda for anti-symmetrical meander dipole, hwd for the linear half-wavelength dipole and dax for the short dipole. Information on each antenna input impedance, reflection coefficient, operating frequency, bandwidth, directive gain and efficiency have been obtained. In addition, pattern measurements were also performed. Comparisons between the four meander dipoles will been made. In addition, these dipoles are compared to the linear half-wavelength dipole as well as the linear dipole of the same axial length (whose length was 35.0% of the linear half-wavelength dipole). The latter is a very short dipole.

From the reflection measurements of all the six dipoles performed, the measured results at each corresponding resonant frequency are tabulated in Table 8.1. The measurements were performed over the frequency range 50.0 MHz to 4.0 GHz. The measured $|S_{11}|$ curves for all the four anti-symmetrical meander dipoles over the frequency range are shown in Fig. 8.4. The corresponding measured reflection bandwidths are also shown. The values are taken at -10.0 dB $|S_{11}|$ level, as given in Section 2.6. In addition, the measured $|S_{11}|$ of the two linear dipoles are also displayed for further comparisons. The simulated resonances for all the dipoles, as described in Chapter 6, are illustrated in Fig. 8.5.

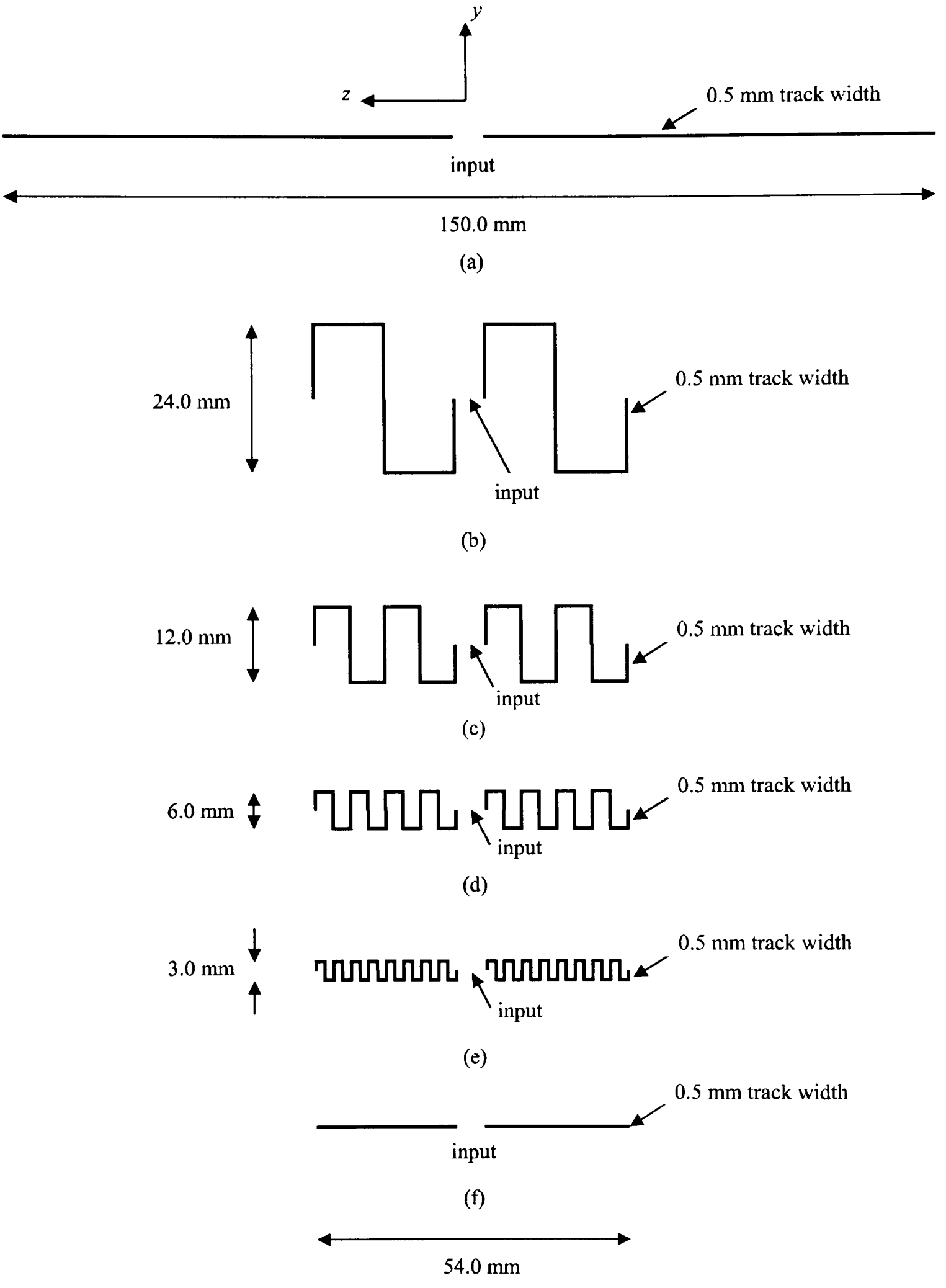

Fig. 8.3. (a) Linear dipole (hwd) ; anti-symmetrical meander dipoles: (b) two (mda1), (c) four (mda2), (d) eight (mda3), (e) sixteen meander (mda4) sections; (f) short dipole (dax).

The operating frequencies (f_0) and corresponding return losses are tabulated in Table 8.1.

Table 8.1. Experimental and simulated results for the linear half-wavelength dipole, the anti-symmetrical meander dipoles, and the short dipole.

antenna	**Measured**		**Simulated**	
	f_0 GHz	$\|S_{11}\|$ dB	f_0 GHz	$\|S_{11}\|$ dB
hwd	0.867	-19.40	0.95	-34.14
mda1	1.16	-10.02	1.10	-11.37
mda2	1.49	-10.44	1.20	-13.66
mda3	1.54	-11.68	1.30	-16.02
mda4	1.92	-14.45	1.45	-19.87
dax	2.48	-20.46	2.65	-14.58

From Figs. 8.4 to 8.5 and Table 8.1, it can be seen that the measured return losses of the meander dipoles decreases as the number of meander sections increases. The resonant frequency shifted upwards from that of the half-wavelength dipole, with more meander sections. This shifting approaches that of the short dipole. The operating frequency shifting is suspected to be due to the coupling between the meander bends. This is also probably true for the decrease in the measured return loss. The percentage of the measured resonant frequency shifting are 34.0%, 72.0%, 78.0% and 122.0% for the first, second, third and fourth meander dipoles, respectively. On the other hand, that of the numerical simulation are 16.0%, 26.0%, 37.0% and 53.0%, respectively. These were a factor of 2 less than the measured values. However, all the simulated return losses showed reasonably well-matched

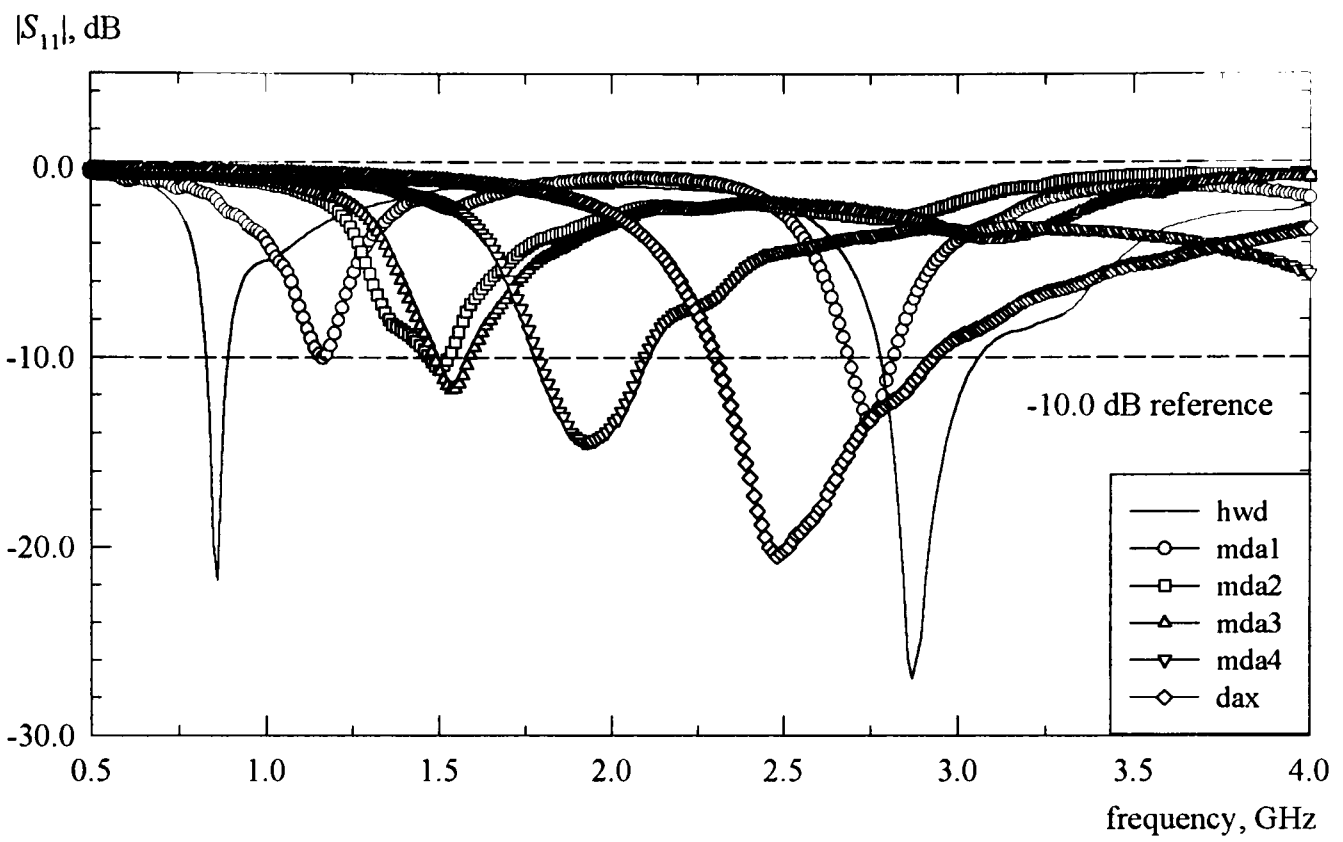

Fig. 8.4. Measured return losses of all the dipoles.

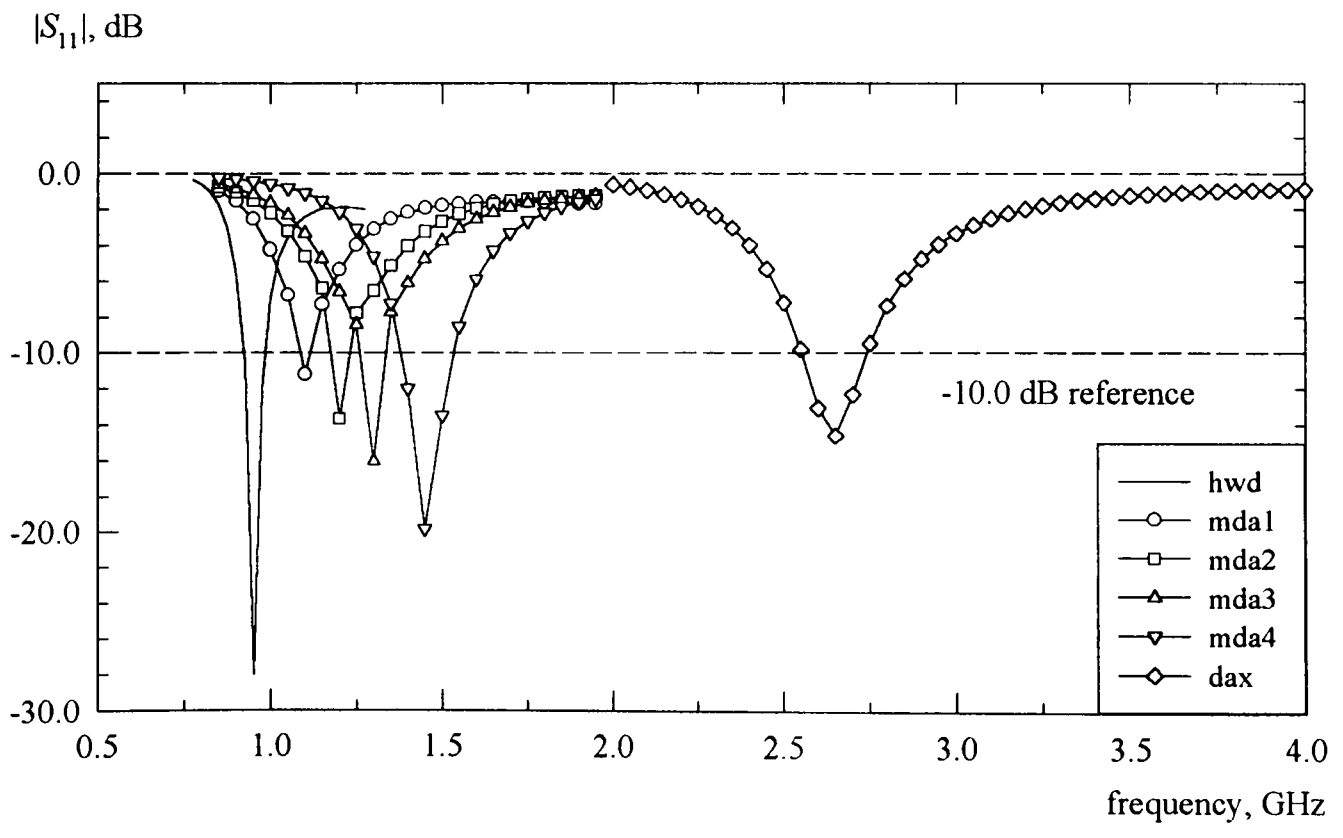

Fig. 8.5. Simulated return losses of all the dipoles.

to the dipoles, since the unbalanced state of the coaxial feed is not accounted for. As for the reflection bandwidths, it gets wider with increasing number of meander sections. This is probably due to the increase in the loss resistance as the antenna shrinks in size.

The transmission and pattern measurements of all the meander dipoles are relative to the half-wavelength dipole. The measurements are taken with both the transmitting test antenna and the receiving dipole (i) (a) oriented horizontally ($|S_{12}|_H$), or the E-plane co-polarisation, and (b) oriented vertically ($|S_{12}|_V$), or the H-plane co-polarisation, and (ii) oriented normal to each other ($|S_{12}|_X$) with the test antenna oriented horizontally, the E-plane cross-polarisation. $|S_{12}|_H$ (which is equivalent to $|S_{21}|_H$, due to reciprocity) is measured at the meander dipoles maximum direction of radiation, at the resonant frequencies of the meander dipoles. The measured radiation patterns of all the meander dipoles are drawn as linear plots in Figs. 8.6 to 8.9, respectively. Finally, the measured co-polar horizontal and co-polar vertical radiation patterns for all the four meander dipoles are grouped together with that of the short and linear $\lambda/2$ dipoles in Fig. 8.10 and 8.11, respectively. The corresponding simulated co-polar horizontal radiation patterns are shown next in Fig. 8.12. The co-polar vertical radiation pattern, however, cannot be simulated.

The measured radiation patterns showed that all the meander dipoles closely resemble that of the short dipole. A considerable amount of cross-polarisation component exists in the radiation pattern. In the co-polar horizontal radiation pattern, the two nulls are not the same. This is probably due to spurious currents on the 50 ohm SMA connector. The supporting structure in the measurements might have also contributed to the distortion. However, the contribution is small. An acceptable variation of 1 to 4 dB was observed in all the co-polar vertical radiation patterns. On the other hand, the numerically simulated results are almost ideal figure-of-eight patterns. No disturbance due to the antenna support structure and the unbalanced state of the semi-rigid coaxial cable feed can be seen. This unbalanced state has been discussed in Section 7.4. It can be concluded that both the measured and numerically simulated results are in good agreement with each other.

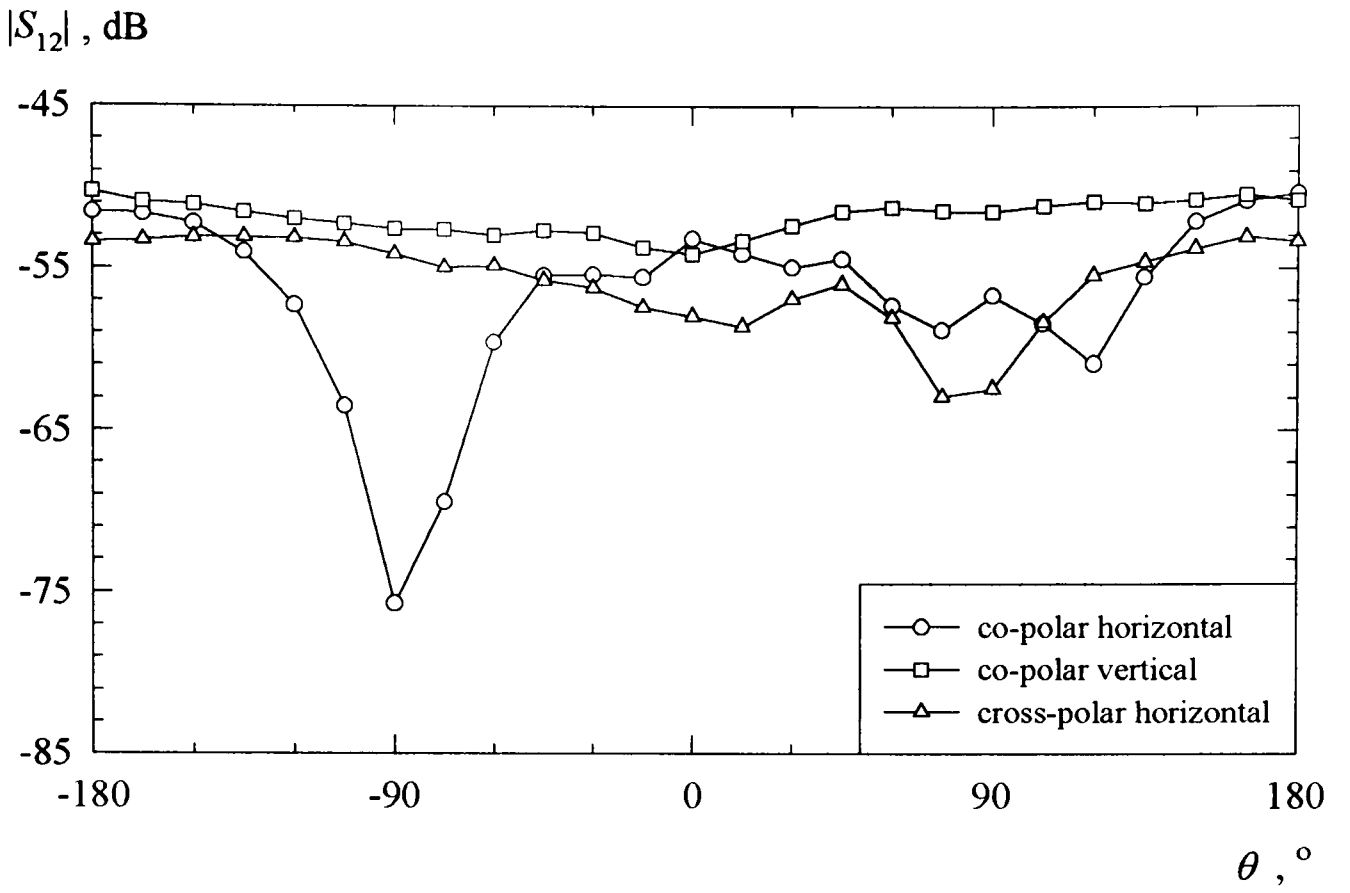

Fig. 8.6. Measured radiation patterns of the first anti-symmetrical meander dipole; mda1.

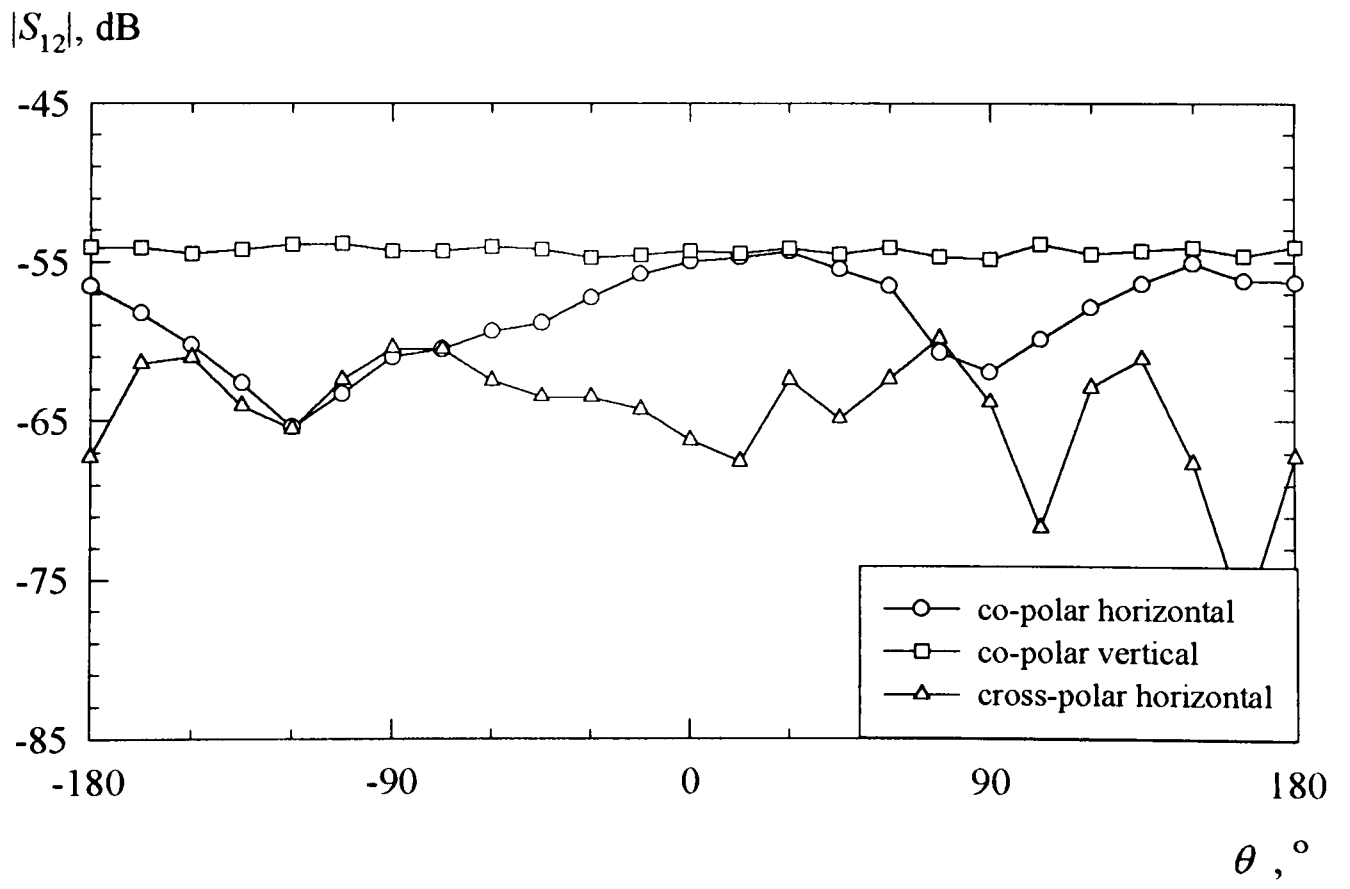

Fig. 8.7. Measured radiation patterns of the second anti-symmetrical meander dipole; mda2.

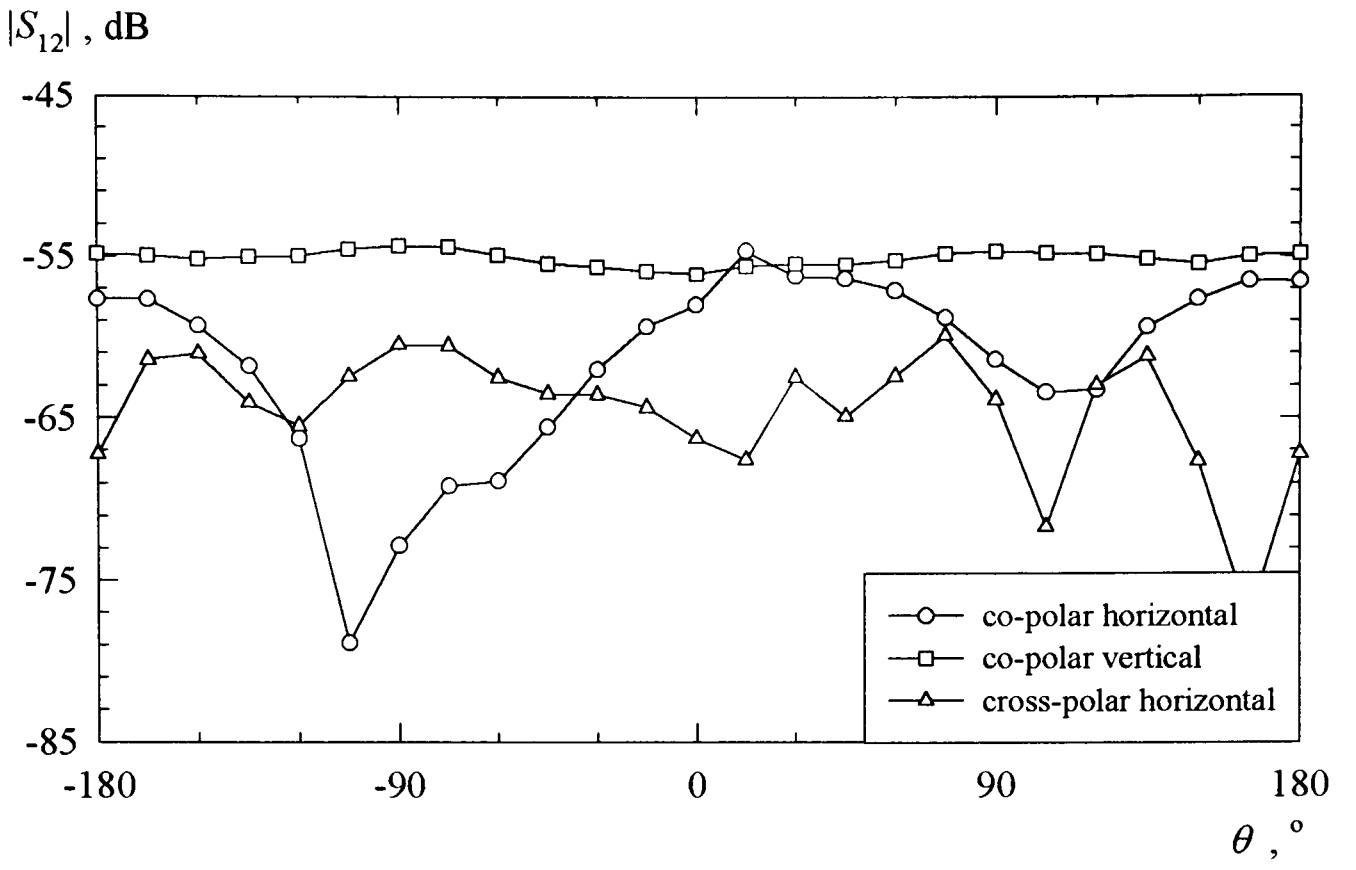

Fig. 8.8. Measured radiation patterns of the third anti-symmetrical meander dipole; mda3.

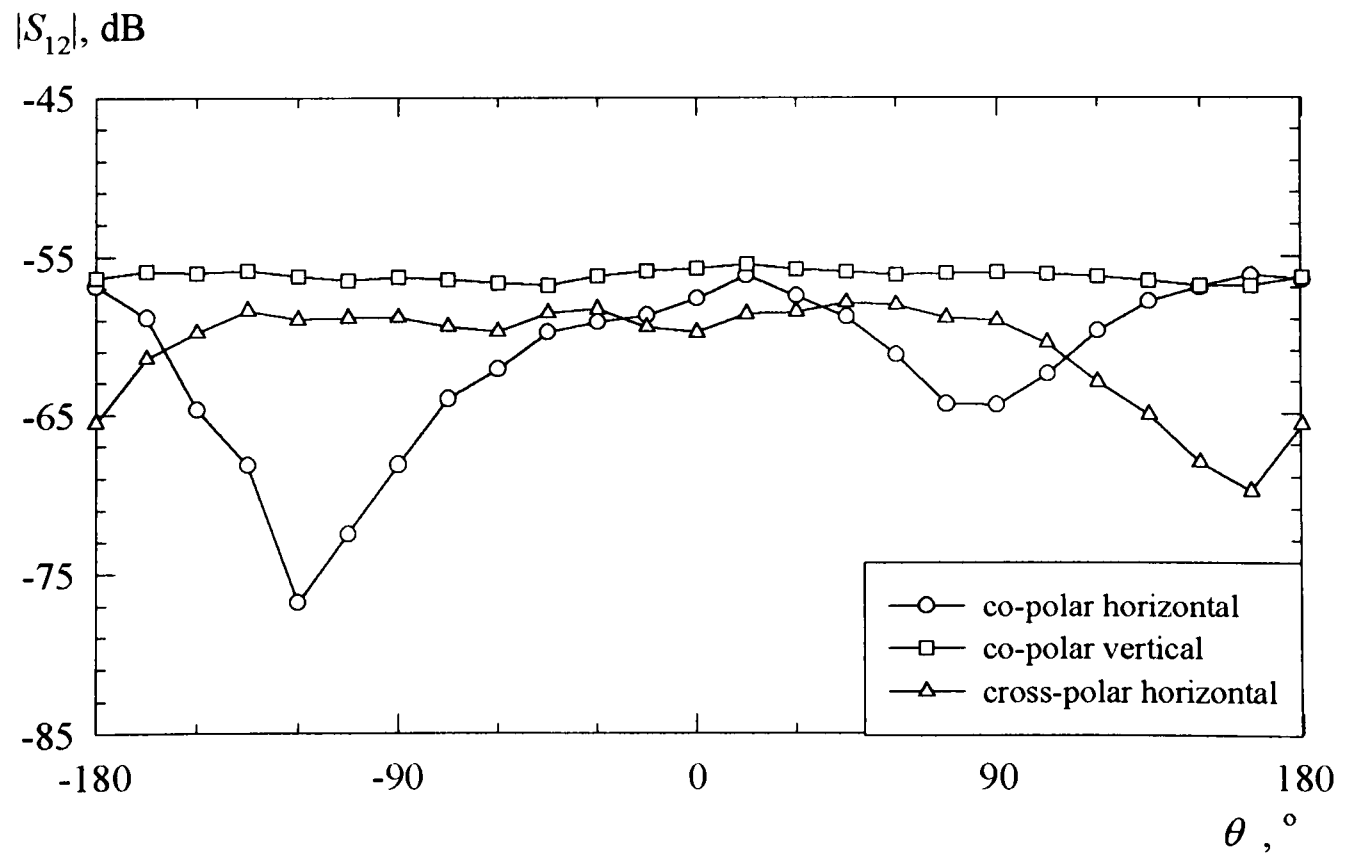

Fig. 8.9. Measured radiation patterns of the fourth anti-symmetrical meander dipole; mda4.

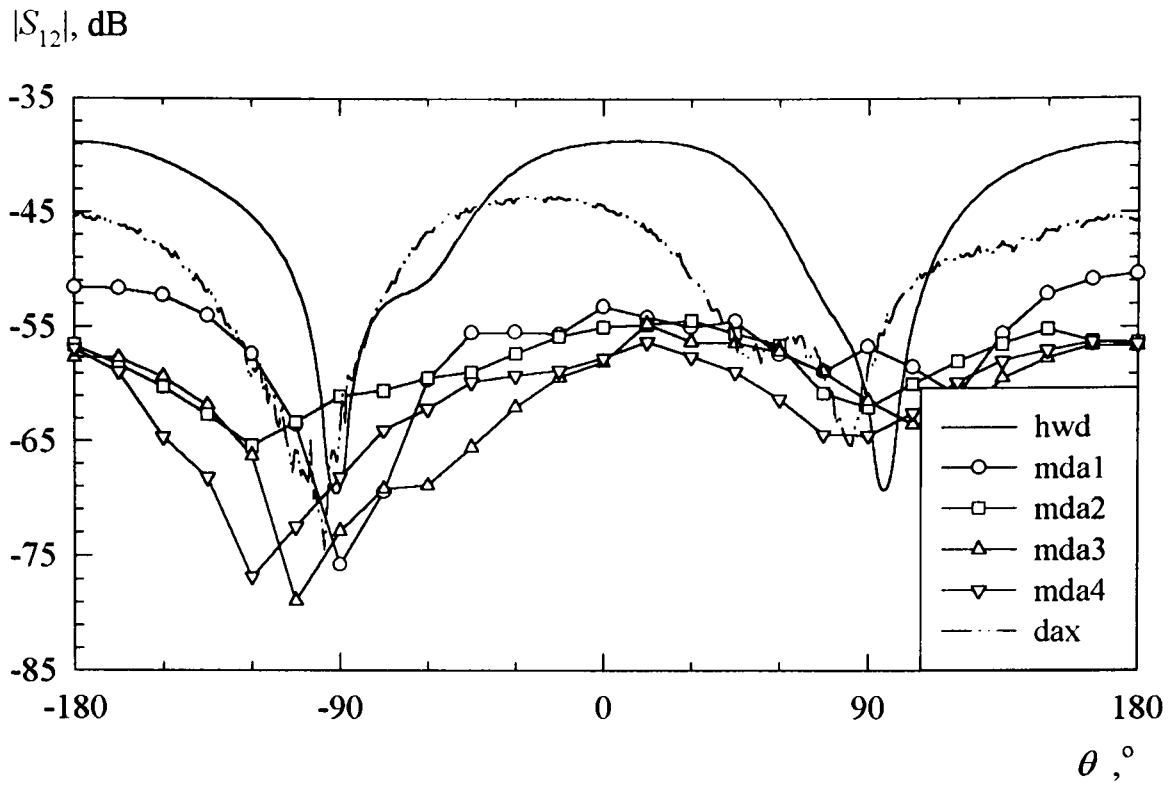

Fig. 8.10. Measured co-polar horizontal radiation patterns of the anti-symmetrical meander dipoles, in comparison with that of linear $\lambda/2$ and short dipoles.

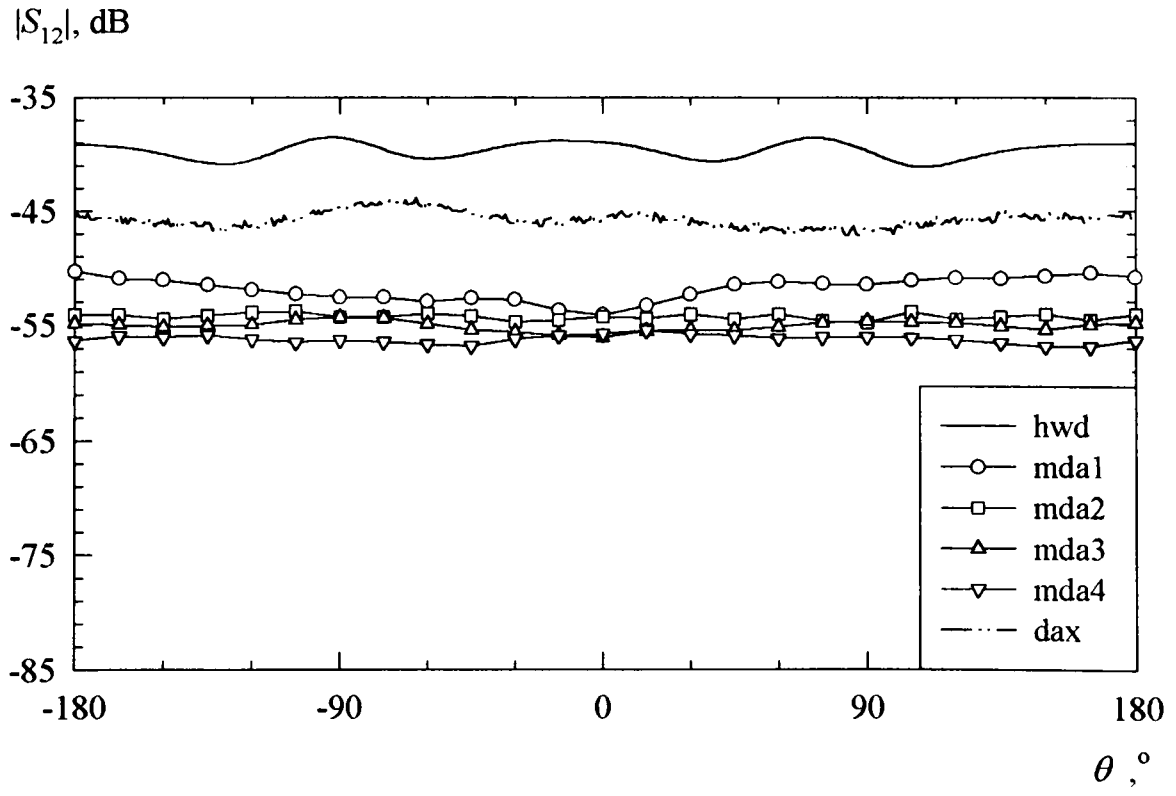

Fig. 8.11. Measured co-polar vertical radiation patterns of the anti-symmetrical meander dipoles, in comparison with that of linear $\lambda/2$ and short dipoles.

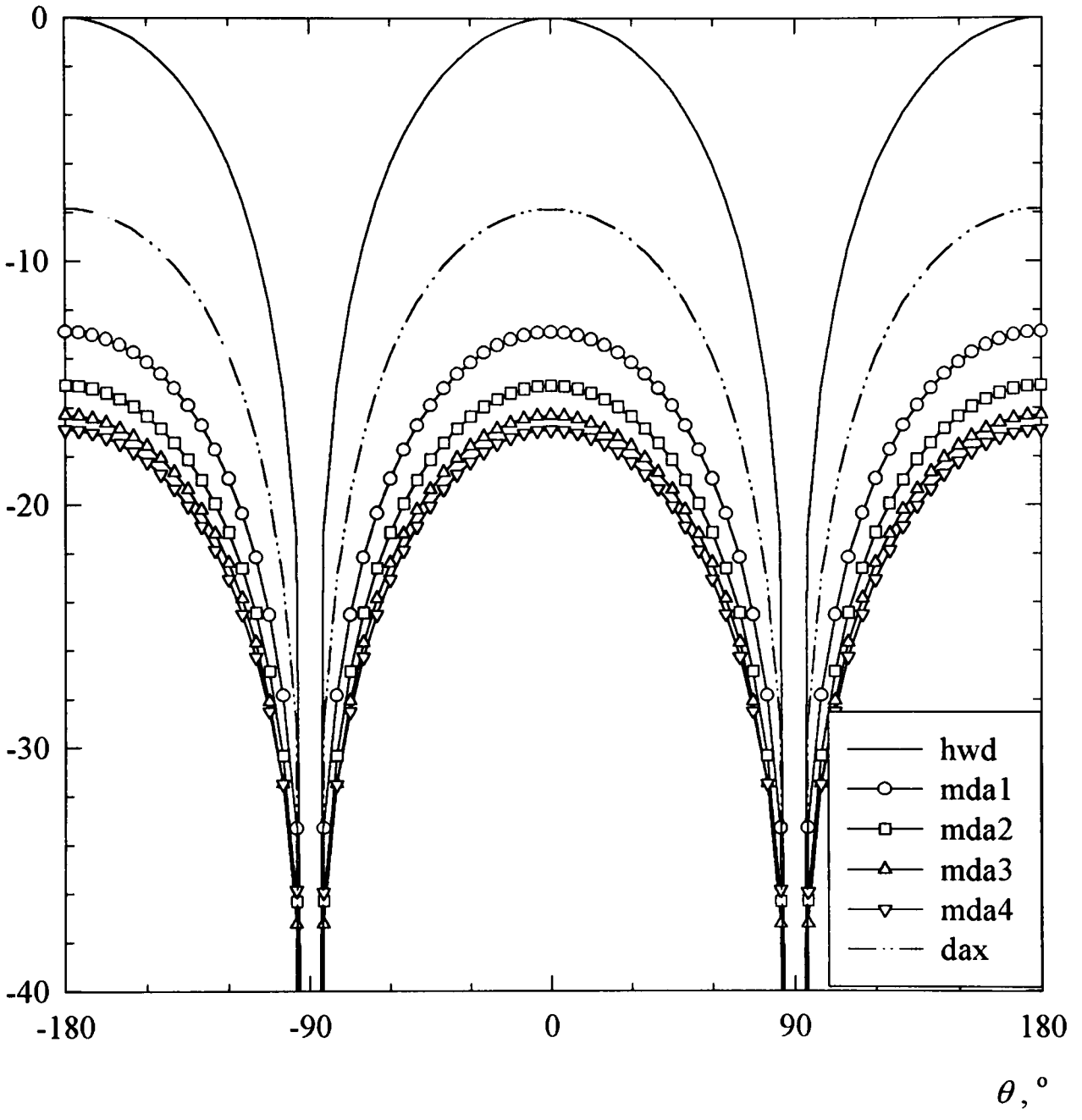

Fig. 8.12. Normalised simulated co-polar horizontal radiation patterns of the anti-symmetrical meander and short dipoles, relative to that of the linear $\lambda/2$ dipole.

The measured overall directive gain, G_0 (in dB) and percentage efficiency, η, of each antenna using eqns. (4.5) and (4.24) of Sections 4.1.1 and 4.1.2, respectively, are tabulated in Table 8.2. G_0 was calculated by subtracting that of the vertically oriented antennas, G_{0V} dB, from that of the horizontally oriented antennas, G_{0H} dB. This accounts for the significant amount of cross-polarisation component. However, this method cannot be employed for the numerical simulation. An alternative is to obtain the difference G_{0D} between the $|S_{12}|$ maximums of the horizontal plane radiation patterns of the antennas and the linear $\lambda/2$ reference dipole. This method enables direct comparison with the numerical simulation. The corresponding η_D, HPBW and numerically simulated G_{0D}, η_D, and HPBW, where η_D was calculated using eqn. (4.23) of Section 4.1.2, are also tabulated in Table 8.2. Since the HPBW of the mda antennas are equal to that of a short dipole, their directivities are approximately 1.5 [1] - [3]. G_0, G_{0D}, η and η_D are relative to the linear $\lambda/2$ dipole.

Table 8.2. Measured and simulated relative gains, efficiencies and beamwidths of the anti-symmetrical meander dipoles and the short dipoles, relative to that of the linear $\lambda/2$ dipole.

	Measured					**Simulated**		
antenna	G_0, dB	G_{0D}, dB	η, %	η_D, %	HPBW,°	G_{0D}, dB	η_D, %	HPBW, °
mda1	-7.6	-11.6	32	26	91	-12.9	40	88
mda2	-8.2	-14.8	29	19	93	-15.1	25	89
mda3	-13.0	-15.4	24	17	94	-16.3	19	90
mda4	-18.0	-17.2	18	14	90	-16.9	16	90
dax	-1.2	-6.5	60	32	90	-7.8	47	90

G_0 : gain, obtained using eqn. (4.5). η : efficiency, obtained using G_0 in eqn. (4.24).

G_{0D} : gain; difference in $|S_{12}|$ maximums. η_D : efficiency, obtained using G_{0D} in eqn. (4.23).

All the measured and simulated results are in good agreement with each other. The relative gain of the antenna reduces from the hwd, to the dax and through the mda antennas. Consequently, the efficiency decreases with decreasing electrical size of the antenna, as will be investigated. All the meander antennas have measured and numerically simulated 3 dB beamwidths of the short dipole, as discussed in Section 2.8.1.

The relationship between the antenna size (both physical and electrical), the number of meander sections and the operating frequency is investigated. The sizes of the four meander dipoles are compared based on the measured operating frequencies, directive gain and efficiency. Similar trend can be seen for the simulated results.

The physical size is considered equivalent to the maximum dimension of the antenna, which equals twice the radius b of the antenna. An antenna is considered to be physically small if this maximum dimension $2b$ is very much less than its operating wavelength [1]. The value of $2b = 0.25\lambda_0$ is taken as the limit of the physical size, where λ_0 is the operating wavelength. Each radius is normalised to that of the $\lambda/2$ dipole, λ_d. The relationship of both the measured and simulated results are shown in Fig. 8.13, together with the theoretical operating frequency curve of multiples of half-wavelength dipoles. It can be seen that the meander and short dipole antennas are physically small at their corresponding operating frequencies. The physical size decreases as the number of meander sections increases. This occurs from the linear $\lambda/2$ dipole, through the meander dipoles and the short dipole. Correspondingly, being smaller in size, the antennas exhibit lesser gain and are inefficient. On the other hand, the linear $\lambda/2$ dipole is physically large at its operating frequency. The measured and simulated results are in good agreement. The operating frequencies of the meander dipole antennas are well below the curve of multiples of half-wavelength dipoles. All the meander dipoles did not operate close to the linear half-wavelength dipole. Instead, all appeared to approach that of a short dipole.

The electrical size S is calculated using $k_0 b$ of eqn. (4.12), where k_0 is taken as $2\pi/\lambda_0$. The electrical size limit is at $k_0 b = 1$, that is the limit indicating if the antenna is 'small' or 'large'. This corresponds to the limit defined by Wheeler [15], and has been discussed in Section 4.1.3. The relationship of both the measured and simulated results are shown in Fig. 8.14, and they are in good agreement with each other. All the meander dipole antennas are electrically small. Although the operating frequency of the meander dipoles approach that of the short dipole, the short and the $\lambda/2$ dipoles are electrically large. The meander dipole antenna gets electrically larger as the number of meander sections increases.

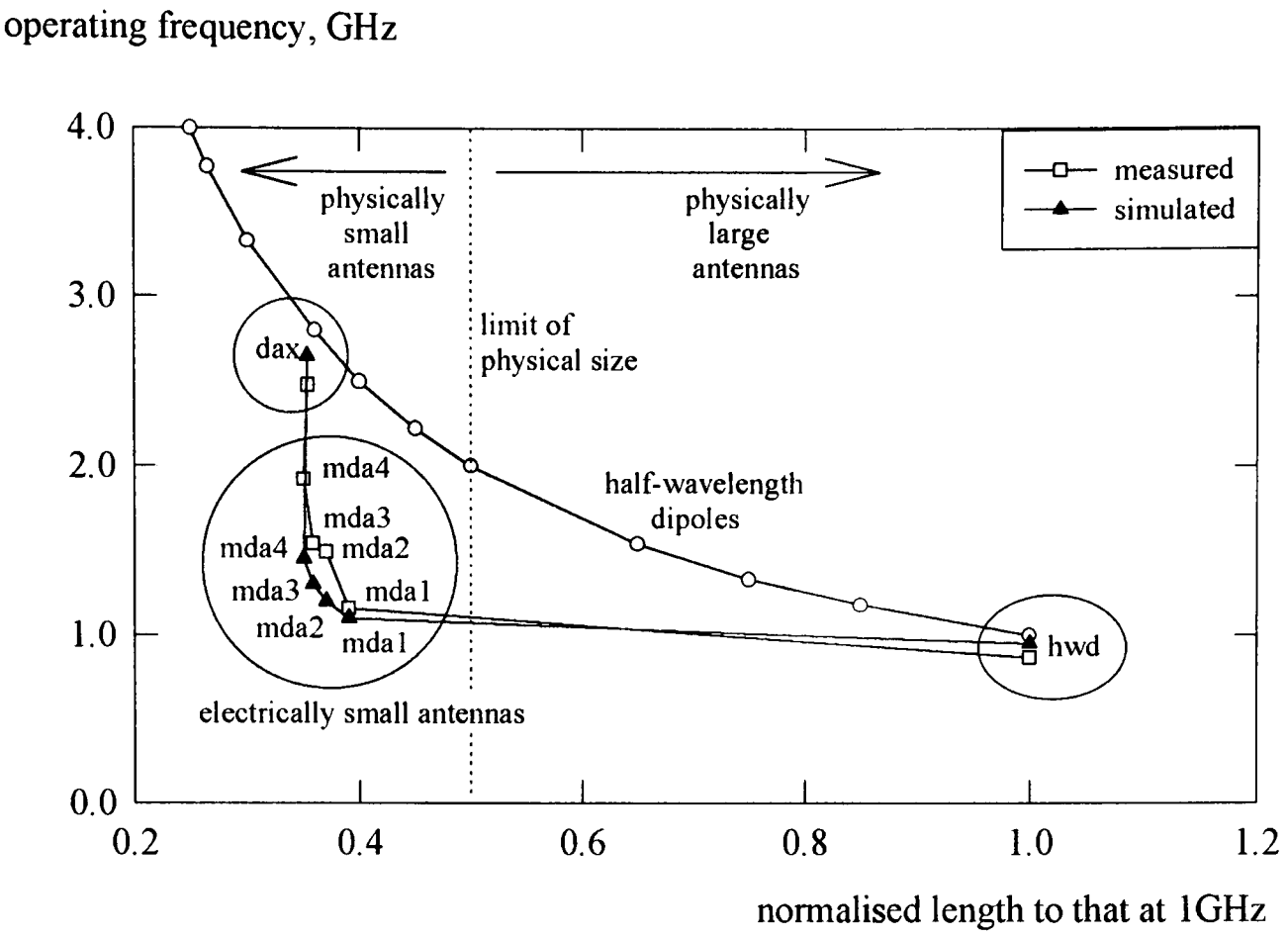

Fig. 8.13. Measured and simulated operating frequencies with respect to the antenna radius and theoretical operating frequency of several linear half-wavelength dipoles.

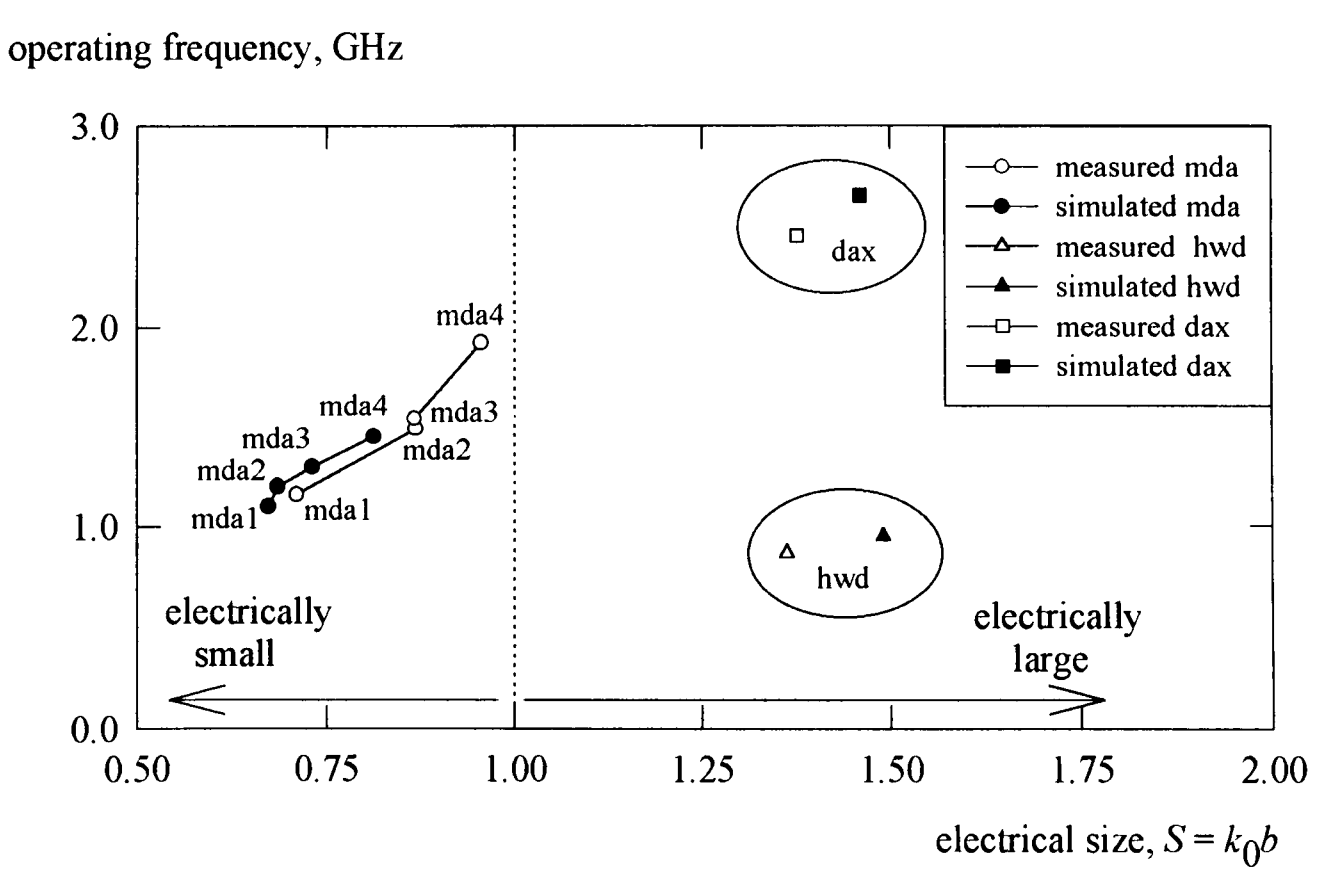

Fig. 8.14. Measured and simulated operating frequencies with respect to the electrical size.

The simulated surface current distribution on all the dipoles are shown in Fig. 8.15. Each distribution showed an approximate half-wave sinusoidal variation, with peaks at the feed (centre of antenna) and nulls at the radiating ends. Comparison of the current levels along the antenna track length and along the antenna axial length are now discussed.

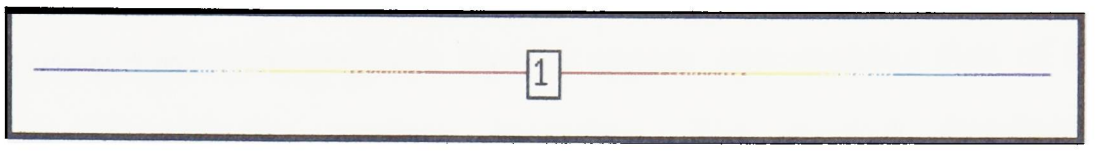

(a) linear half-wavelength dipole

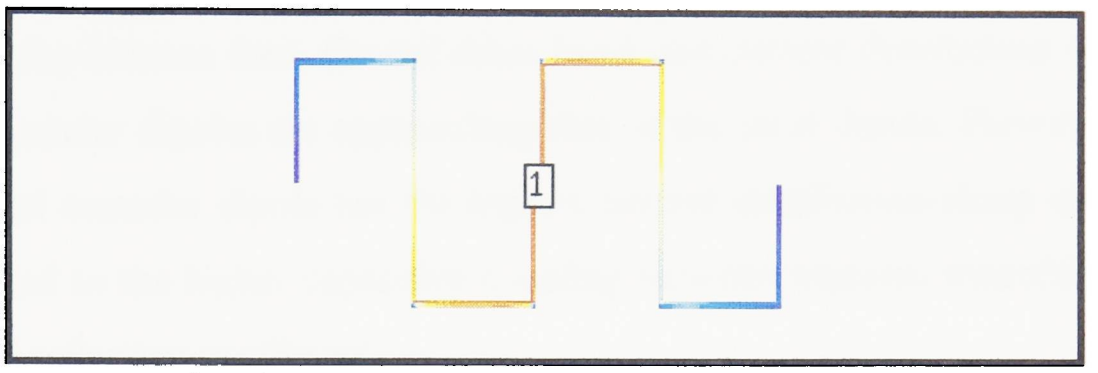

(b) first anti-symmetrical meander dipole

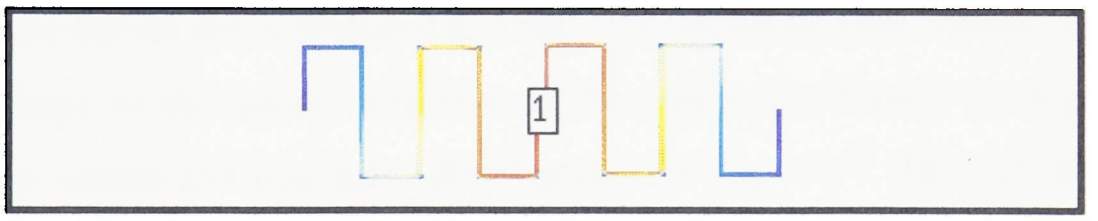

(c) second anti-symmetrical meander dipole

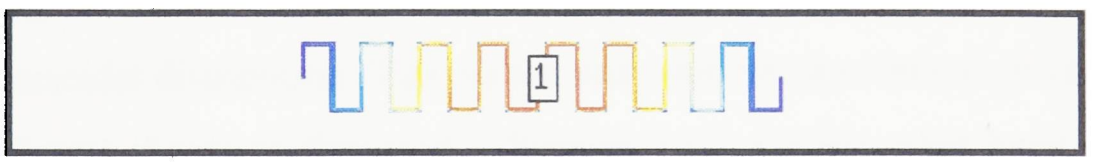

(d) third anti-symmetrical meander dipole

(e) fourth anti-symmetrical meander dipole

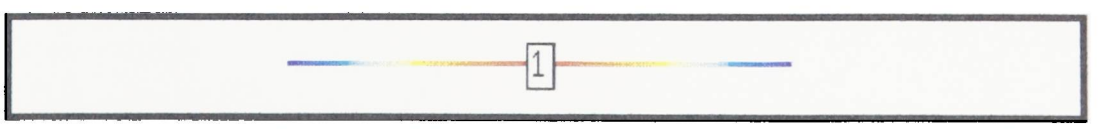

(f) short dipole

Fig. 8.15. Simulated surface current distribution along the dipoles arm.

The simulated surface current distribution of each antenna is plotted against the corresponding track length and axial length in Figs. 8.16 and 8.17, respectively. In Fig. 8.16, the current distribution of the $\lambda/2$ dipole is compared to that of the anti-symmetrical meander dipoles. Whilst in Fig. 8.17, the current distribution of the short dipole is compared to that of the anti-symmetrical meander dipoles. In both figures, each curve shows a peak at the antenna feed and nulls at both ends of the radiating arms. However, in Fig. 8.16, the curves of the anti-symmetrical meander dipoles appear approaching that of the $\lambda/2$ dipole, as the number of meander sections increases. The current distribution curve is approximately sinusoidal. The dominant peaks indicated that the current tends to concentrate at the antenna feed. On the other hand, the current distribution of all the anti-symmetrical meander dipoles are approaching that of the short dipole. However, the fourth anti-symmetrical meander dipole has the highest current distribution along its axial length. This is attributed to the higher capacitive coupling between adjacent meander sections and better matched reflection coefficient.

The same curves are normalised to their corresponding peak values. This is done to compare the shape of the curves with that of the cosine distribution for Fig. 8.16, whilst with that of the cosine and triangular distributions for Fig. 8.17. The corresponding plots are shown in Figs. 8.18 and 8.19, respectively. In Fig. 8.16, all the curves overlap with each other, indicating that the current distribution along the antenna $\lambda/2$ track length are of half-wavelength sinusoidal distribution. This agrees well with the theoretical current distribution of a half-wavelength dipole as discussed in Section 2.8.2. On the other hand, all the curves of Fig. 8.17 which overlap with other in Fig. 8.19, do not approach the triangular distribution. Instead, all agrees with the cosine distribution. This does not agree with the triangular shaped current distribution of a short dipole as discussed in Section 2.8.1.

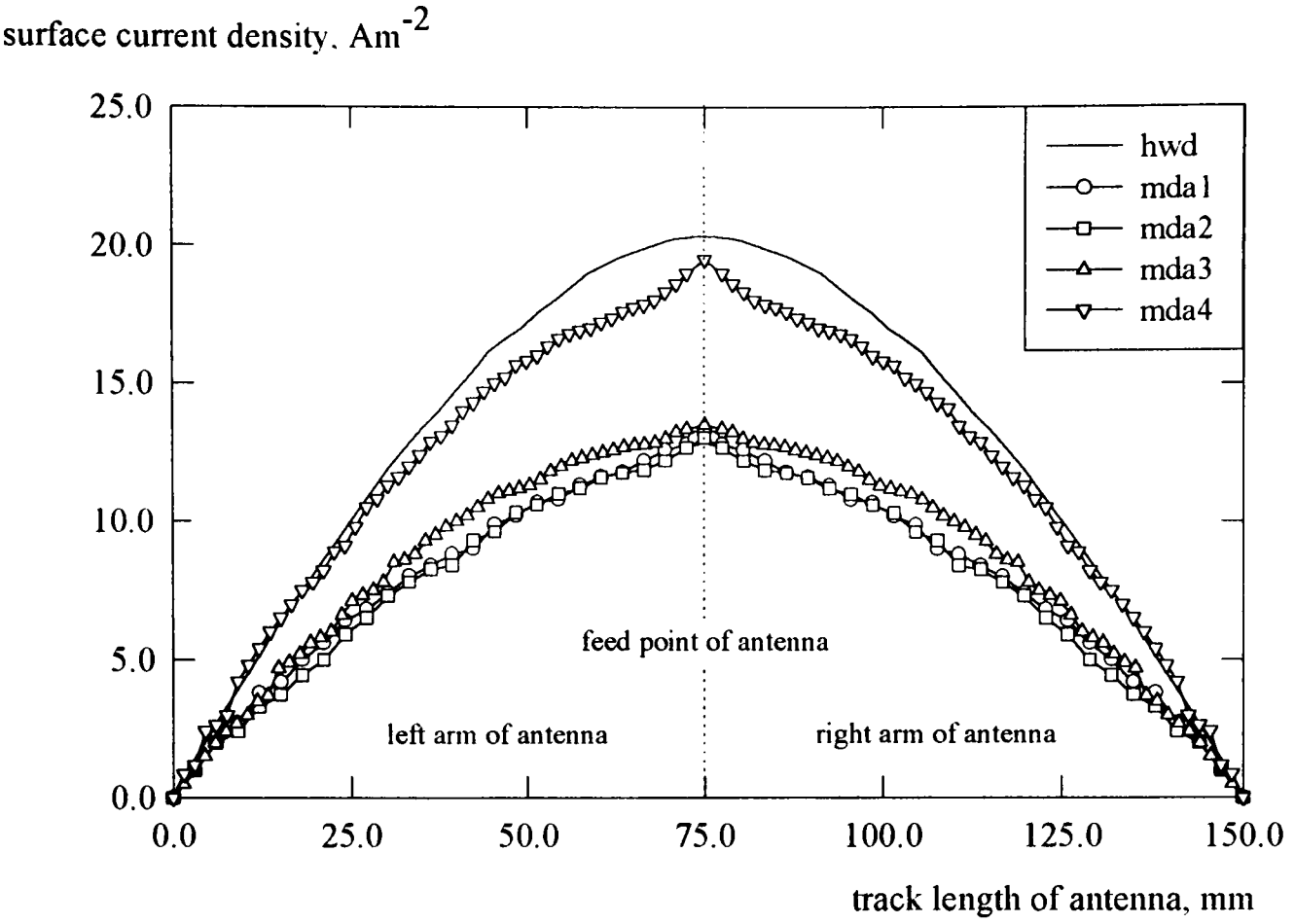

Fig. 8.16. Current distribution along the track length of the antenna.

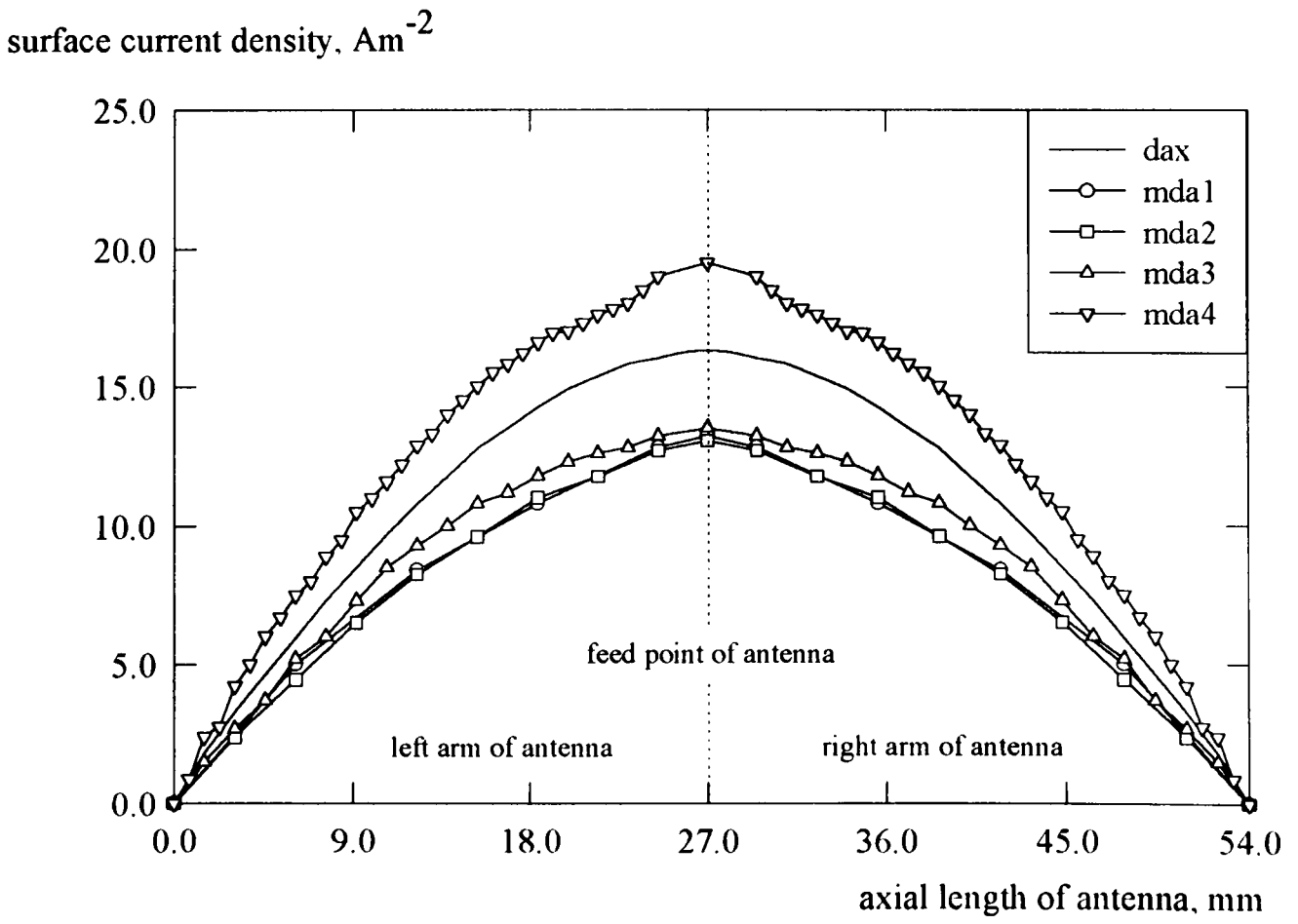

Fig. 8.17. Current distribution along the axial length of the antenna.

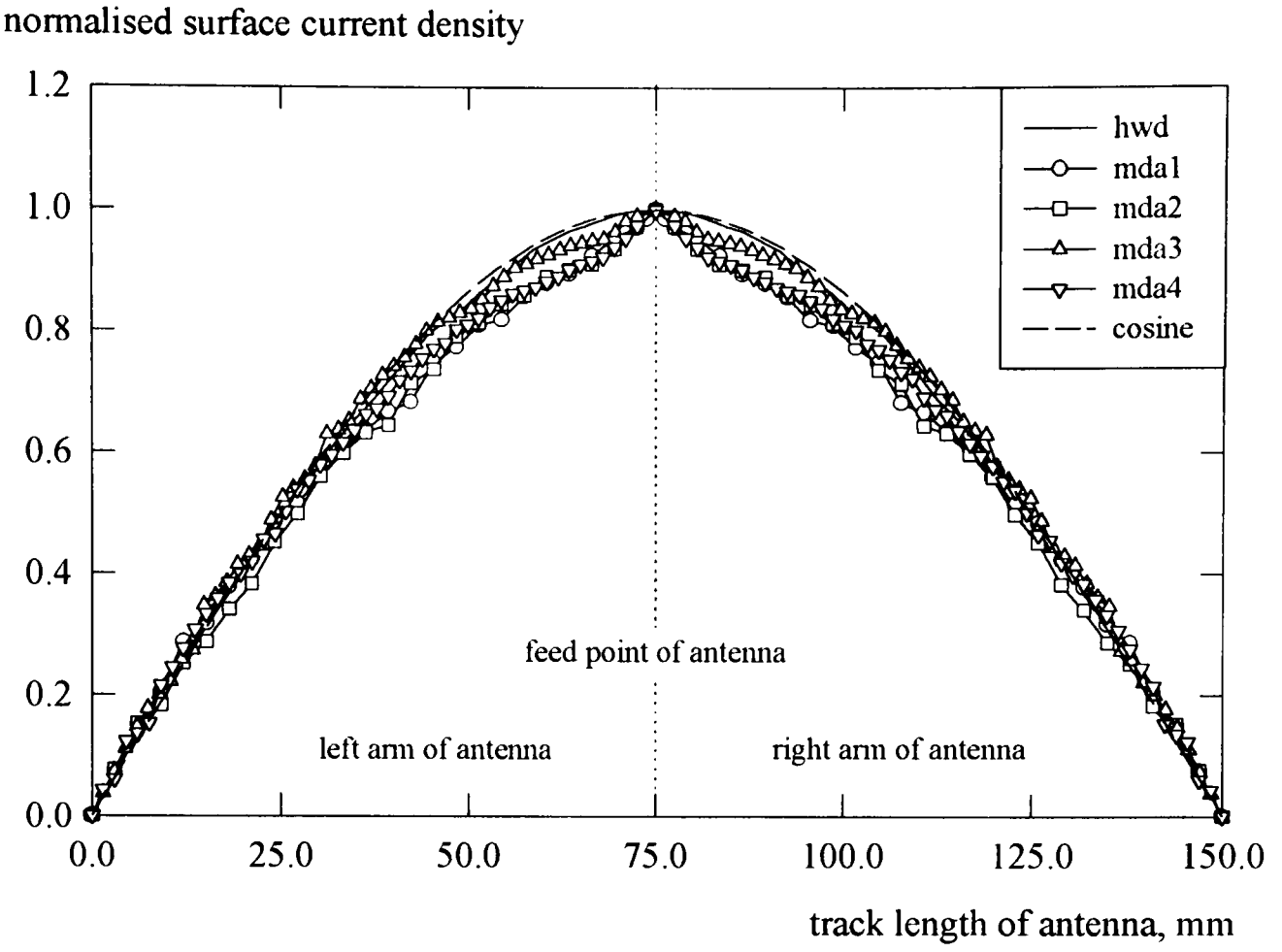

Fig. 8.18. Normalised current distribution along the track length of the antenna.

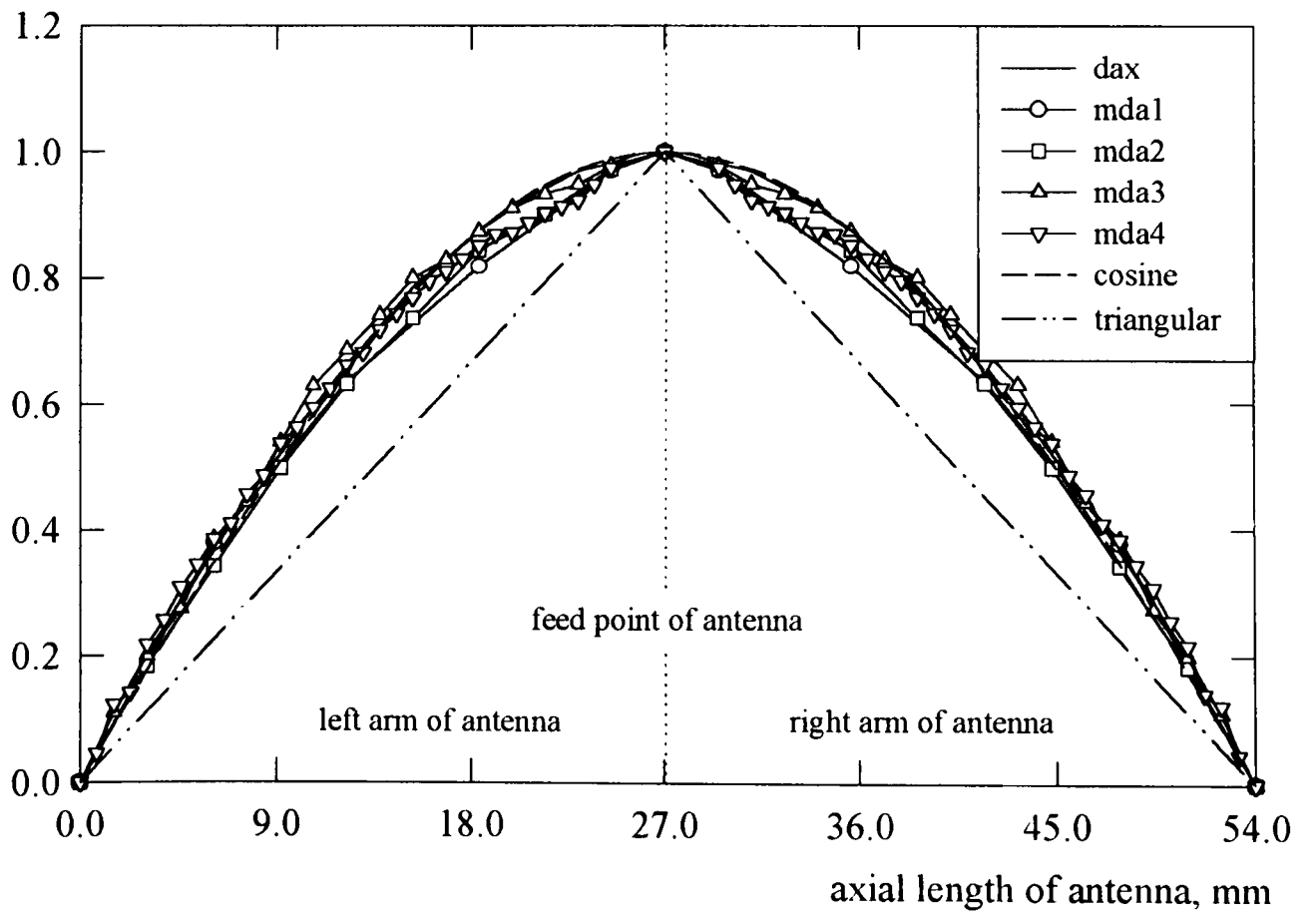

Fig. 8.19. Normalised current distribution along the axial length of the antenna.

8.2.2 Symmmetrical Structures

The design procedure of the symmetrical meander structures has been discussed in Section 5.1.2. The first and second sets copper symmetrical meander dipole antennas of Figs. 5.3 and 5.4, redrawn here for convenience in Figs. 8.20 and 8.21, respectively. The third set is shown in Fig. 8.22. Another similar three sets of copper antennas were also fabricated, but without the CPS feeding lines. Only the third set without the feeding line is shown in Fig. 8.23. Two identical linear copper $\lambda/2$ dipoles were also fabricated for further comparison. These have the same track length as the copper symmetrical meander dipoles. In addition, the fabricated thick and thin film HTS antennas are also shown in Figs. 8.24 and 8.25, respectively. Each HTS antenna has CPS feed line. The thin film HTS antennas are a factor of 3.31 smaller than the corresponding set 3 copper antennas. The respective abbreviations are also given in Figs. 8.20 to 8.25. For simplicity, the following abbreviations are used for all the dipoles: Rk for symmetrical meander dipole set 1, Sk for symmetrical meander dipole set 2, Sn for symmetrical meander dipole set 3 and dip for the linear half-wavelength dipole. Prefix Cu, Hk and Hn will be added to denote copper antennas, thick-film HTS antenna and thin-film HTS antennas, respectively. Postfix F will be added for antennas with the CPS feeding line. In addition, the number that follows the abbreviation denotes the number of meander sections.

Full *S*-parameter and pattern measurements have been carried out. Comparisons between all the meander dipoles on various aspects will be discussed. Further comparisons with the numerical simulations will also be made. In addition, these dipoles will be compared to the linear $\lambda/2$ dipole. The discussion starts with the performance of the directly fed copper meander dipoles. After discussing the relevant problems encountered during the experimental work and comparing with the numerical simulations results, the discussion proceeds to the copper meander dipoles with the CPS feed lines. The discussion is followed by the HTS antennas. Finally, comparison between all the meander dipoles with the CPS feeding lines will be made.

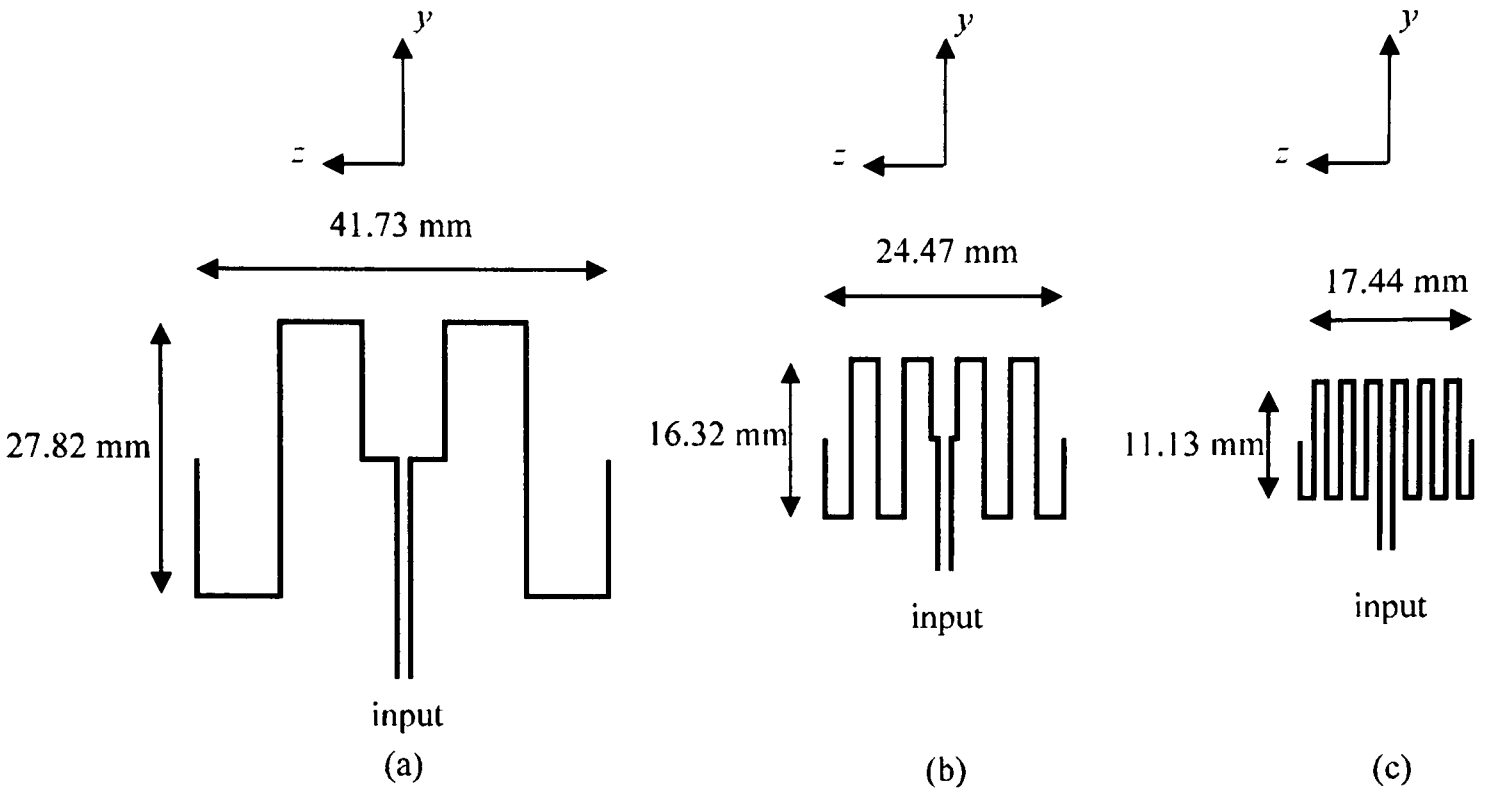

Fig. 8.20. 50 ohm CPS fed copper symmetrical meander dipoles (0.5 mm track width) with 3:2 aspect ratio: a) two, b) four, c) six meander sections (1:1 scale); CuRkF.

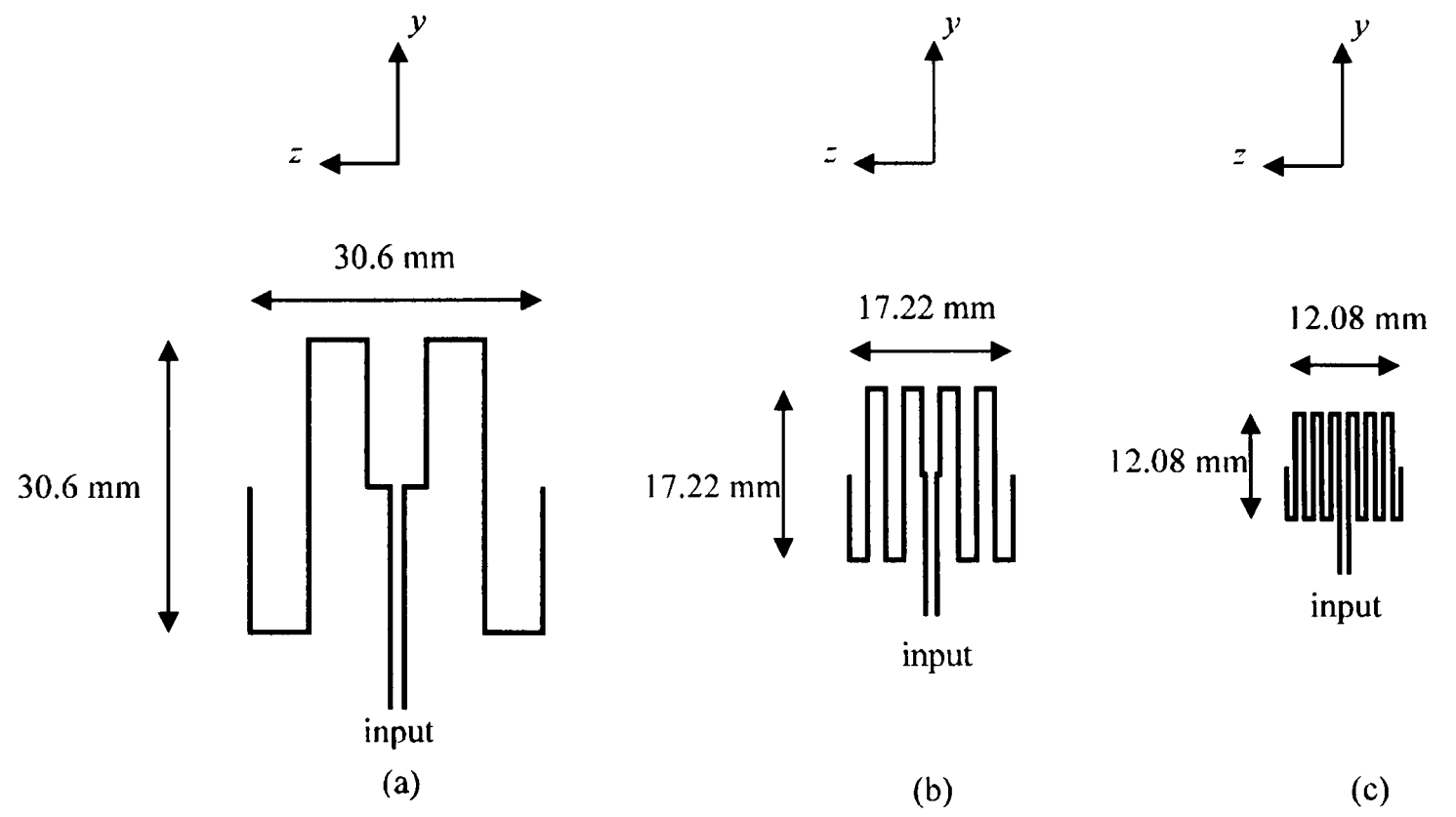

Fig. 8.21. 50 ohm CPS fed copper symmetrical meander dipoles (0.5 mm track width) with 1:1 aspect ratio: a) two, b) four, c) six meander sections (1:1 scale), CuSkF.

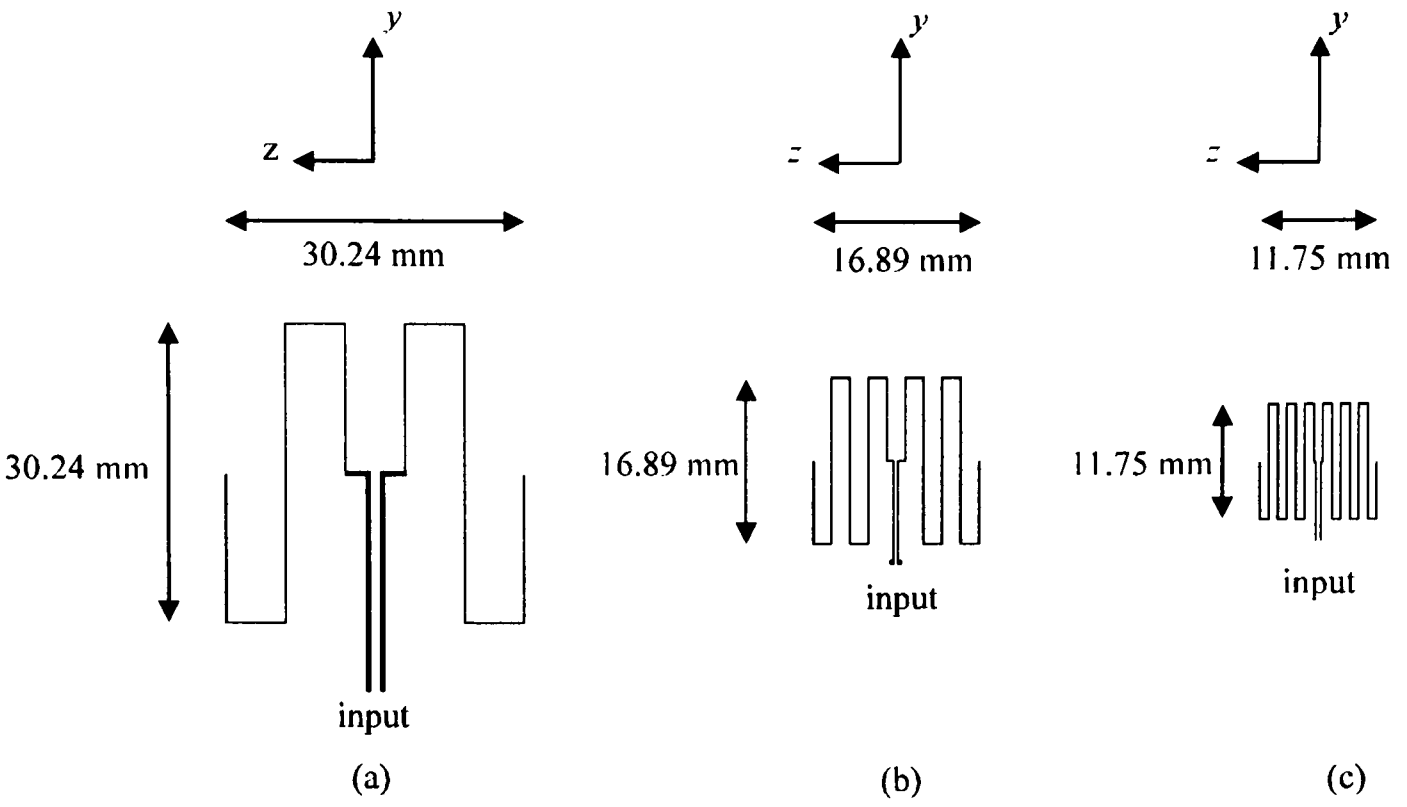

Fig. 8.22. 50 ohm CPS fed copper symmetrical meander dipoles (0.2 mm track width) with 1:1 aspect ratio: a) two, b) four, c) six meander sections (1:1 scale); CuSnF.

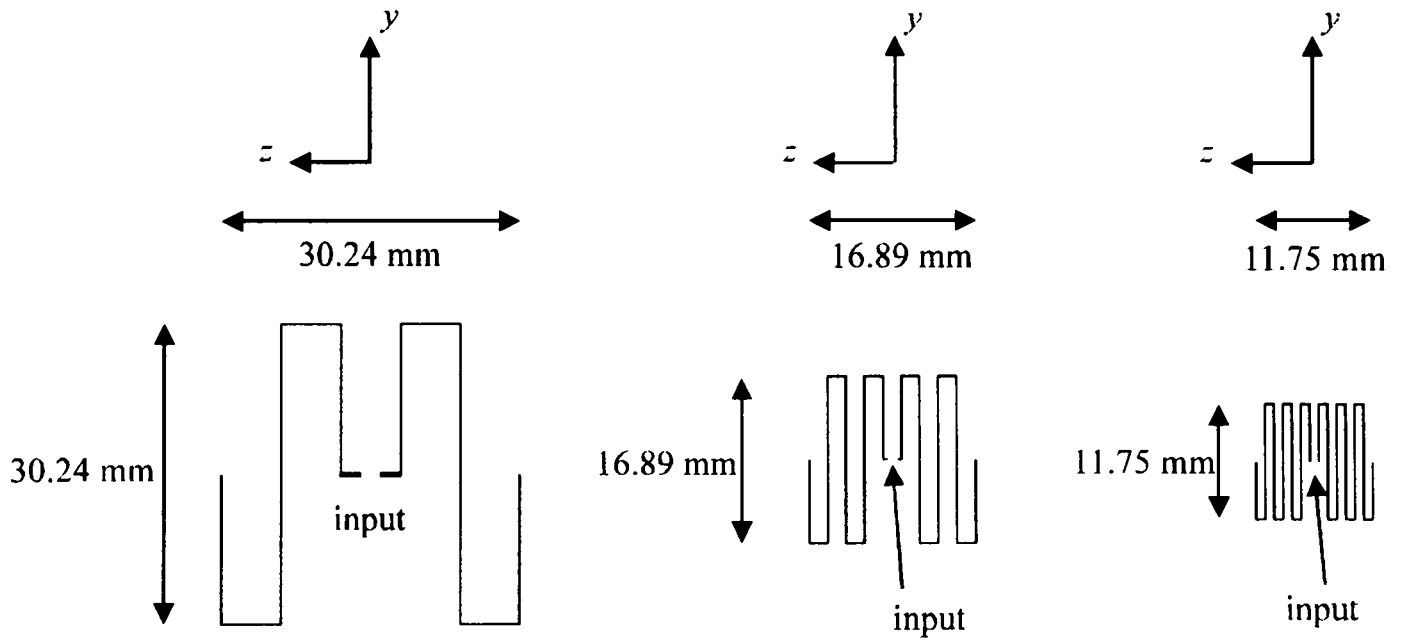

Fig. 8.23. Direct 50 ohm SMA connector fed copper symmetrical meander dipoles (0.2 mm track width) with 1:1 aspect ratio: a) two, b) four, c) six meander sections (1.1 scale); CuSn.

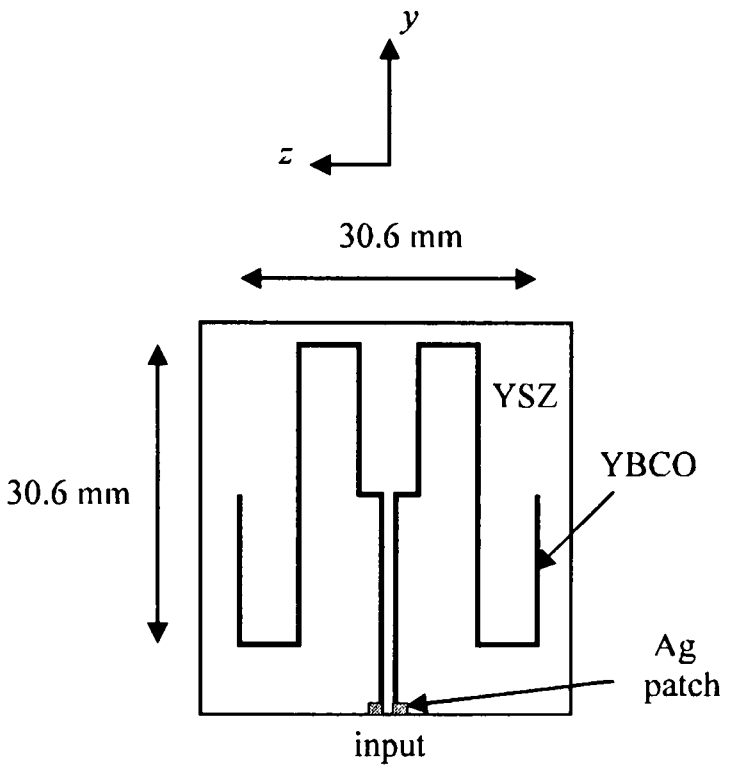

Fig. 8.24. 50 ohm CPS fed thick film HTS symmetrical meander dipole (0.5 mm track width) with 1:1 aspect ratio: two meander sections (1:1 scale); HkSkF.

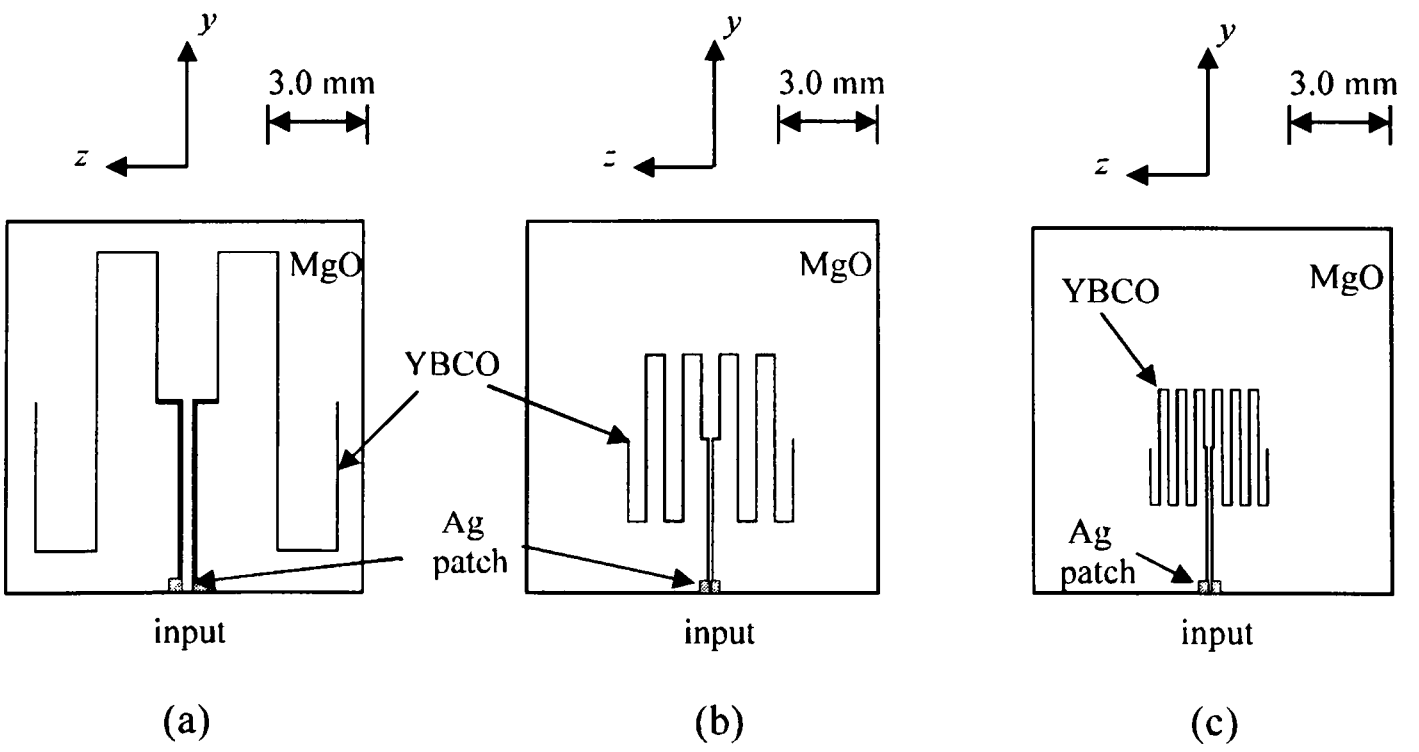

Fig. 8.25. 50 ohm CPS fed thin film HTS symmetrical meander dipoles (78.0 μm track width) with 1:1 aspect ratio: a) two, b) four, c) six meander sections; HnSnF

Initially, the reflection measurements of the directly fed copper symmetrical meander dipoles at 300K are performed without using the $\lambda/4$ sleeve balun. The measured resonant frequencies are tabulated in Table 8.3. The measurements are performed over the frequency range 50.0 MHz to 4.0 GHz. The simulated results are also tabulated in Table 8.3. An example of the measured and simulated $|S_{11}|$ curves for the CuSn antennas over a smaller frequency range are shown in Figs. 8.26 to 8.27, respectively. The corresponding measured reflection bandwidths are also shown. The values are taken at -10.0 dB $|S_{11}|$ level, as given in Section 2.6. In addition, the measured and simulated $|S_{11}|$ of the linear copper $\lambda/2$ dipole are also displayed in relevant figures for further comparison.

Table 8.3. Measured and simulated results for the directly fed copper symmetrical meander dipoles and the linear copper $\lambda/2$ dipole.

antenna	Measured		Simulated	
	f_0 GHz	$\|S_{11}\|$ dB	f_0 GHz	$\|S_{11}\|$ dB
dip	0.981	-19.40	1.0	-20.06
CuRk2	0.981	-11.00	1.0	-15.81
CuRk4	1.031	-7.03	1.1	-17.53
CuRk6	1.181	-6.10	1.2	-20.04
CuSk2	0.888	-15.55	0.95	-16.10
CuSk4	0.969	-5.27	1.05	-17.40
CuSk6	1.219	-12.76	1.2	-15.63
CuSn2	0.844	-9.29	1.0	-17.02
CuSn4	0.95	-10.09	1.1	-16.10
CuSn6	1.10	-8.52	1.15	-15.11

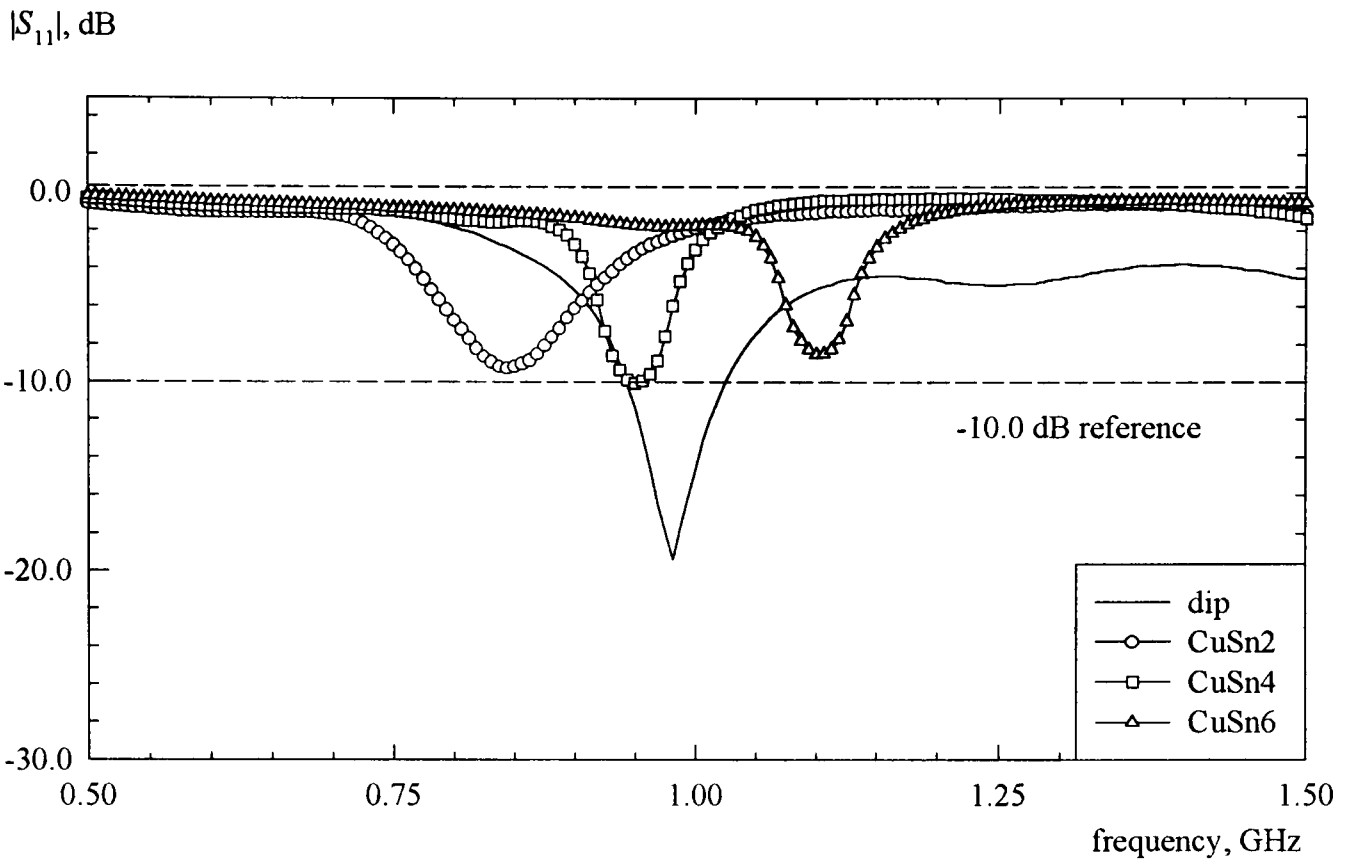

Fig. 8.26. Measured return losses of the CuSn and dip antennas. No balun was used.

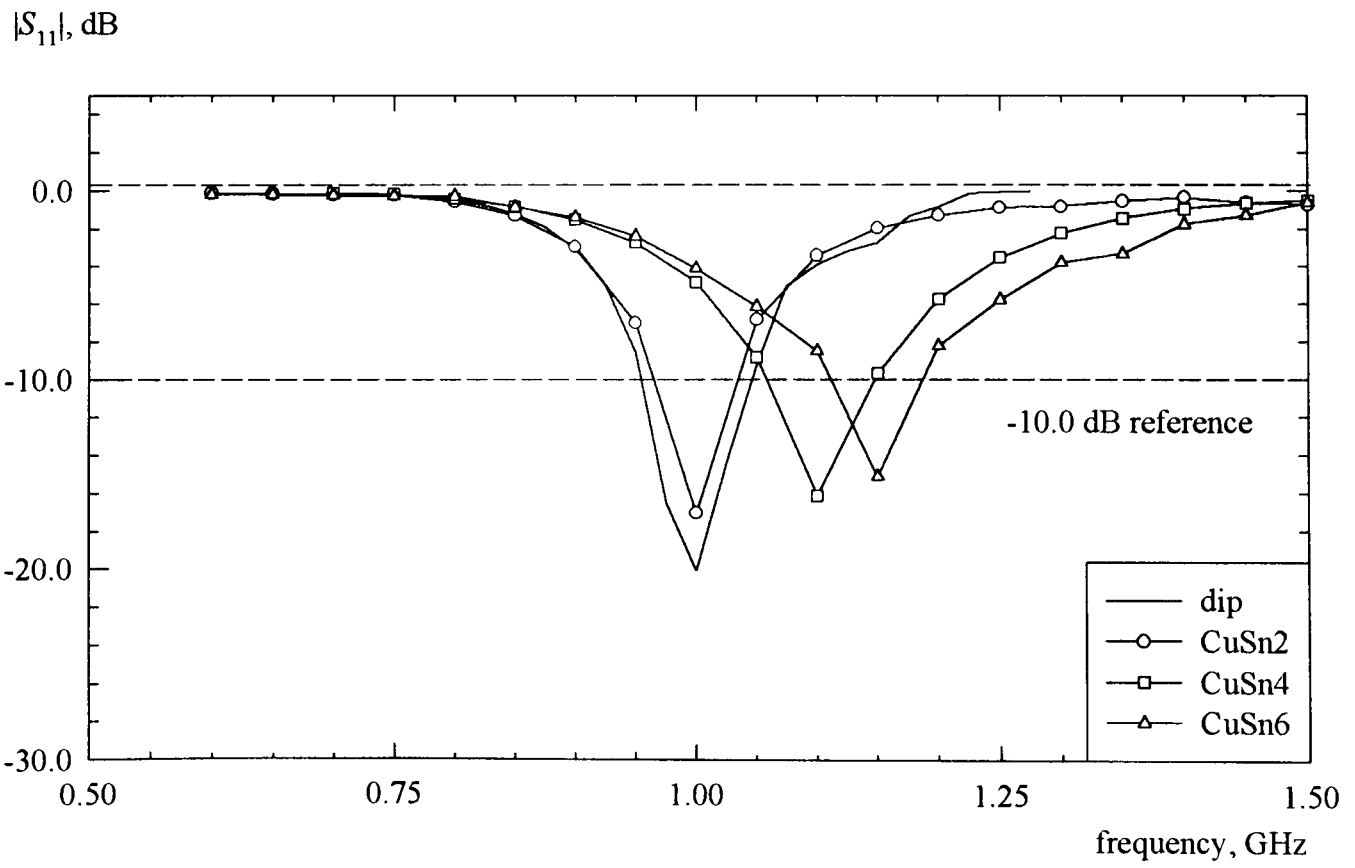

Fig. 8.27. Simulated return losses of the CuSn and dip antennas. No balun was used.

From Table 8.3 and Fig. 8.26, it can be seen that all the measured meander antennas have resonant frequencies around 1 GHz, indicating no change in the operating frequencies with respect to the linear $\lambda/2$ dipole. However, only four out of nine meander antennas are well-matched to the input. Hence, the reflection bandwidths of the poorly-matched antennas are not available. The problem is probably due to the unbalanced state of the semi-rigid feeding cable. The measurements are then repeated, but with the feeding cable covered with absorbing material. However, the results are similar. The poor matching problem will probably be solved if a $\lambda/4$ sleeve balun is employed. The linear $\lambda/2$ dipole has been shortened by 10%, in order to achieve the frequency of operation of 1 GHz.

From the simulated results in Table 8.3 and Fig. 8.27, the effect of the feeding cable is not seen. However, all the meander dipole antennas showed similar behaviour in terms of the frequency of operation, with the measured results. Nevertheless, all the antennas are well-matched relative to the input. The relatively wide reflection bandwidths and low Q_L remain approximately constant in each set of meander antenna. The measured and simulated results for the linear $\lambda/2$ dipole are in good agreement.

The reflection measurements of the meander dipole antennas are repeated with the incorporation of a $\lambda/4$ sleeve balun. The measured results are tabulated in Table 8.4. However, the incorporation of the balun is not simulated. Hence, the measured results are compared with the previously obtained simulated results.

Table 8.4. Measured and simulated results for the directly fed copper symmetrical meander dipoles and the linear copper $\lambda/2$ dipole. A $\lambda/4$ sleeve balun is incorporated with the meander dipoles during the measurements.

antenna	**Measured**		**Simulated**	
	f_0 GHz	$\|S_{11}\|$ dB	f_0 GHz	$\|S_{11}\|$ dB
dip	0.981	-19.40	1.0	-20.06
CuRk2	1.013	-27.73	1.0	-15.81
CuRk4	1.031	-14.30	1.1	-17.53
CuRk6	1.169	-20.04	1.2	-20.04
CuSk2	0.894	-17.50	0.95	-16.10
CuSk4	1.063	-16.84	1.05	-17.40
CuSk6	1.213	-19.53	1.2	-15.63
CuSn2	0.919	-17.64	1.0	-17.02
CuSn4	0.981	-14.91	1.1	-16.10
CuSn6	1.125	-18.50	1.15	-15.11

From Tables 8.3 and 8.4, it can be seen that the balun has helped in matching the antennas. Slight shiftings of the frequency of operation of some meander antennas can be observed. However, the measured and simulated frequency of operation shown in Table 8.4 are in good agreement. An example of the measured $|S_{11}|$ curve for the CuSn antennas with the incorporation of the balun is illustrated in Fig. 8.28. Due to the difference in the matching of the antennas to the input, no correlation between the reflection bandwidth can be made.

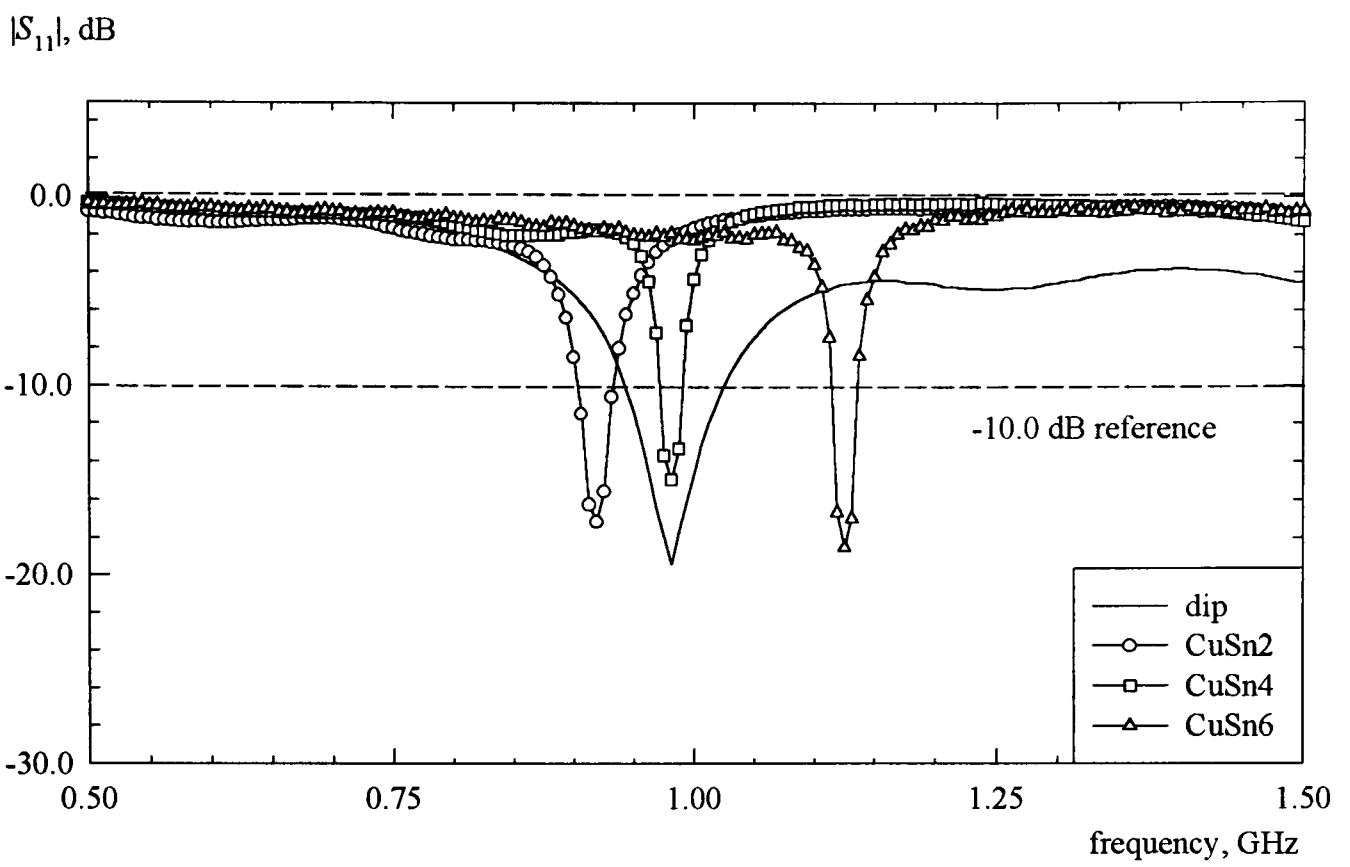

Fig. 8.28. Measured return losses of the CuSn and dip antennas. A $\lambda/4$ sleeve balun is incorporated with the CuSn antennas.

Further measurements of the far-field radiation patterns of all the three sets of directly fed copper meander antennas clearly showed that there is pattern distortion. An example of the co-polarisation principal plane radiation patterns of the CuSn antennas, in comparison with that of the linear dipole, are shown in Figs. 8.29 and 8.30. The radiation patterns of the CuSn antennas do not agree with that of the linear $\lambda/2$ dipole. This suggests the need of the $\lambda/4$ sleeve balun to be incorporated in the experiments. On the other hand, the simulated meander dipoles showed ideal figure-of-eight normalised far-field radiation patterns. These patterns have similar shapes to that of the simulated linear $\lambda/2$ dipole. The corresponding normalised simulated co-polar horizontal radiation patterns for the CuSn antennas are shown in Fig. 8.31. The co-polar vertical radiation pattern cannot be simulated.

Due to the problems mentioned above, the antennas with CPS feeding lines were fabricated and tested. The $\lambda/4$ sleeve balun is also incorporated in the measurements.

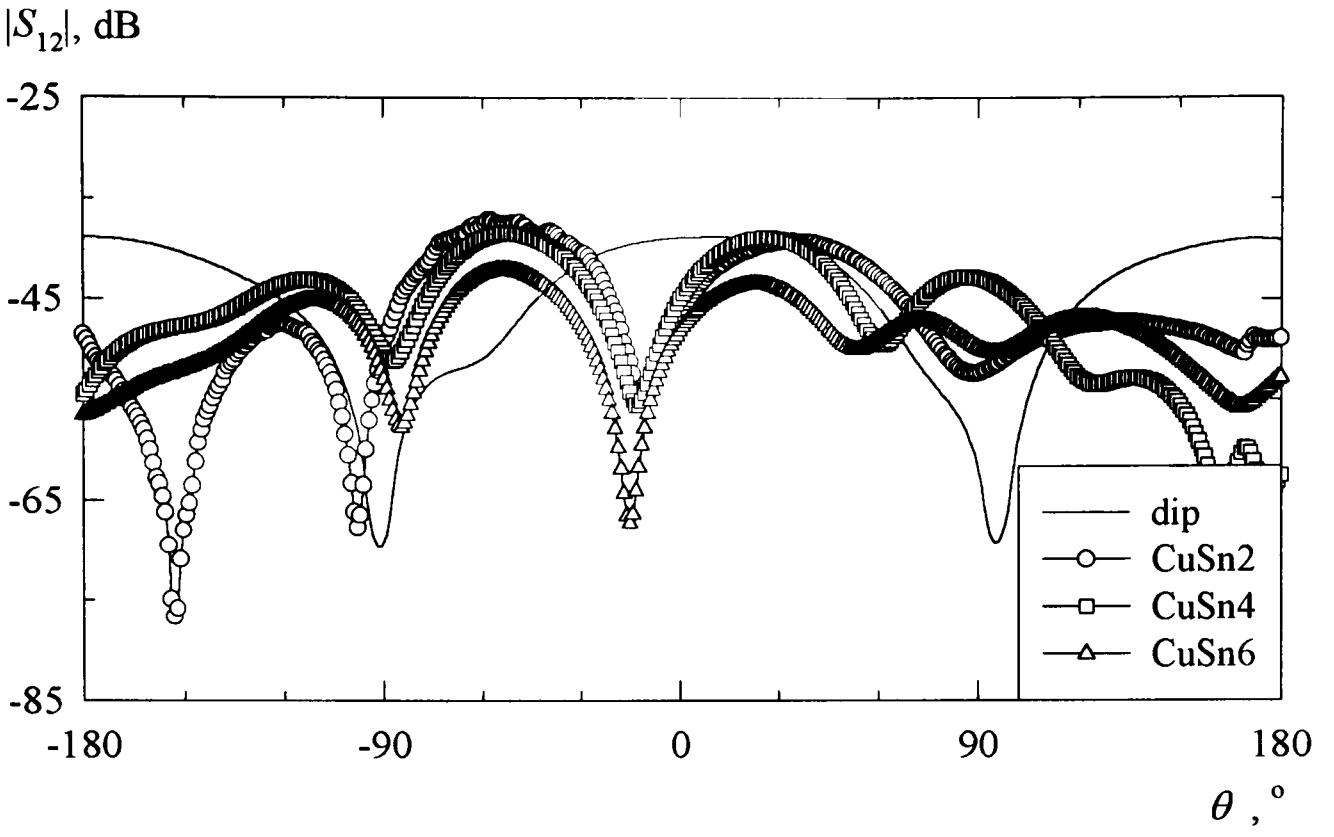

Fig. 8.29. Measured co-polar horizontal radiation patterns of CuSn and dip antennas.

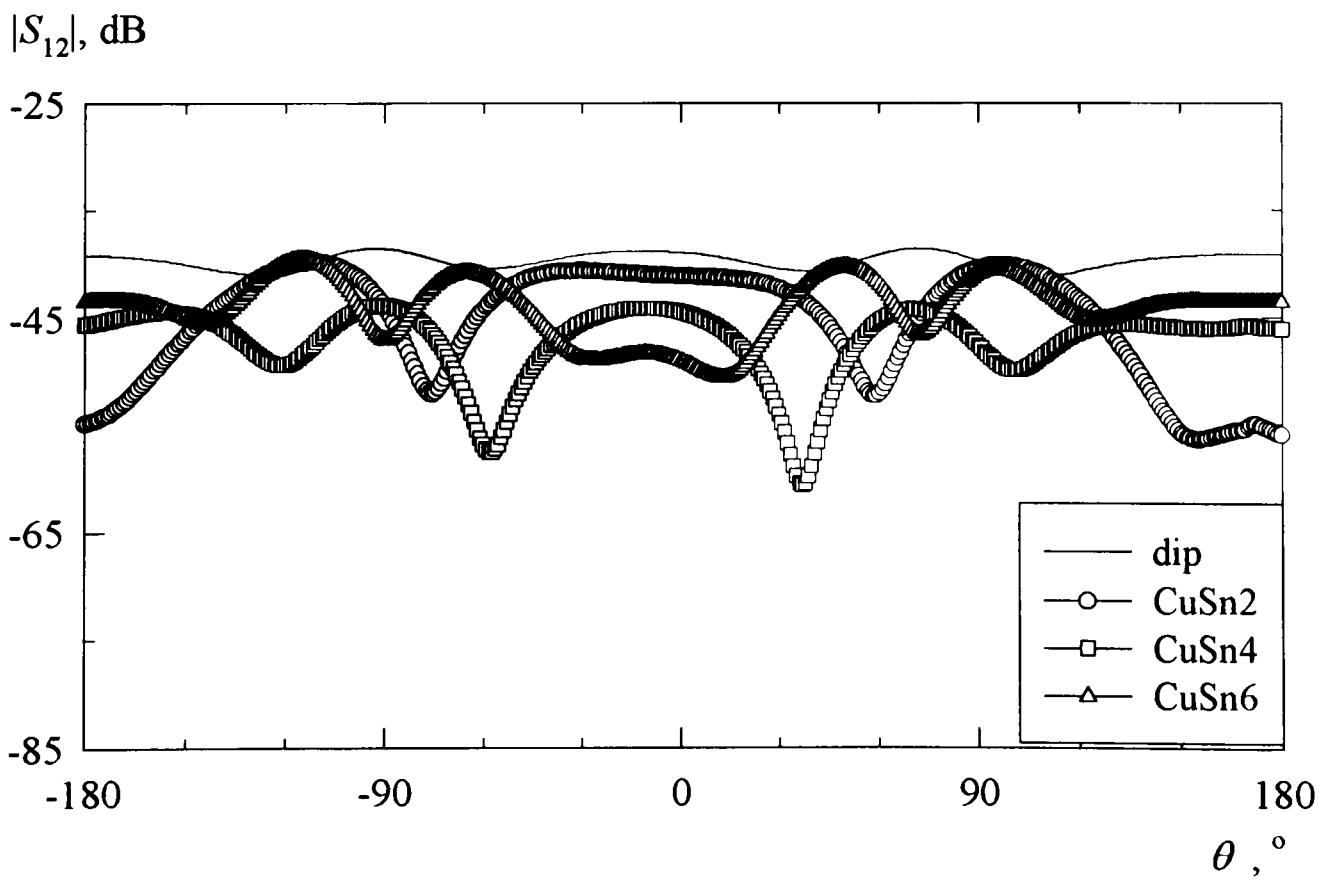

Fig. 8.30. Measured co-polar vertical radiation patterns of CuSn and dip antennas.

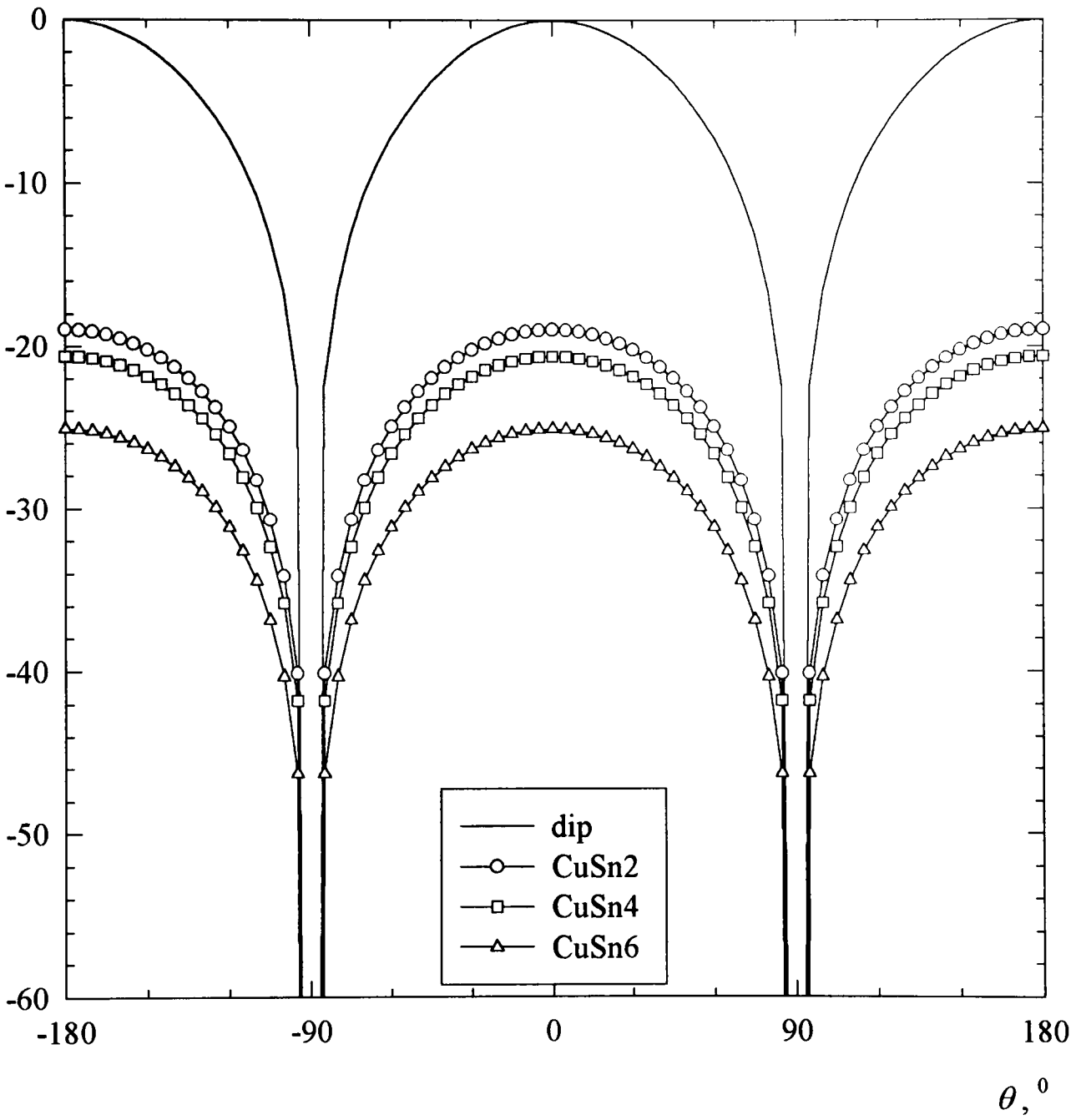

Fig. 8.31. Normalised simulated co-polar horizontal radiation patterns of CuSn antennas, relative to that of the dip antenna.

The measured resonant frequencies of all the CPS fed copper symmetrical meander antennas are tabulated in Table 8.5. The simulated results are tabulated in Table 8.5, for comparison. An example of the measured and simulated $|S_{11}|$ curves for the CuSnF antennas are shown in Figs. 8.33 and 8.34, respectively. The corresponding measured reflection bandwidths are also shown. The values are taken at -10.0 dB $|S_{11}|$ level, as given in Section 2.6. In addition, the measured and simulated $|S_{11}|$ of the linear copper $\lambda/2$ dipole are also displayed in relevant figures for further comparison.

Table 8.5. Measured and simulated results for the CPS fed copper symmetrical meander dipoles and the linear copper $\lambda/2$ dipole.

antenna	**Measured**		**Simulated**	
	f_0 GHz	$\|S_{11}\|$ dB	f_0 GHz	$\|S_{11}\|$ dB
dip	0.981	-19.40	1.0	-20.06
CuRkF2	0.781	-12.80	1.0	-15.78
CuRkF4	0.925	-15.27	1.05	-13.56
CuRkF6	0.981	-17.66	1.15	-13.94
CuSkF2	0.794	-19.36	0.90	-16.18
CuSkF4	0.956	-23.88	0.95	-17.80
CuSkF6	1.20	-17.90	1.0	-18.81
CuSnF2	0.732	-12.68	0.93	-17.76
CuSnF4	0.9	-15.42	1.1	-14.80
CuSnF6	1.031	-15.56	1.1	-16.10

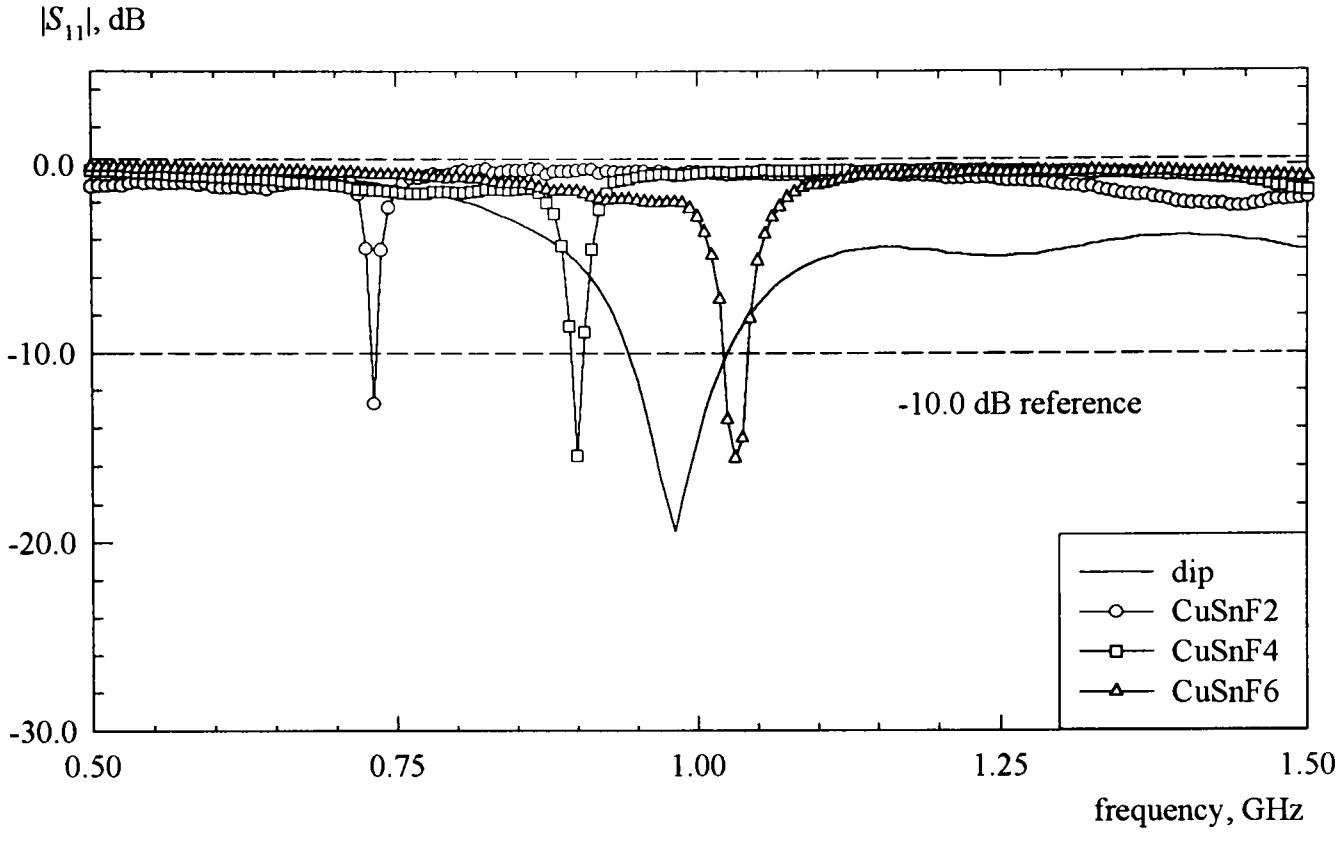

Fig. 8.33. Measured return losses of the CuSnF and dip antennas.

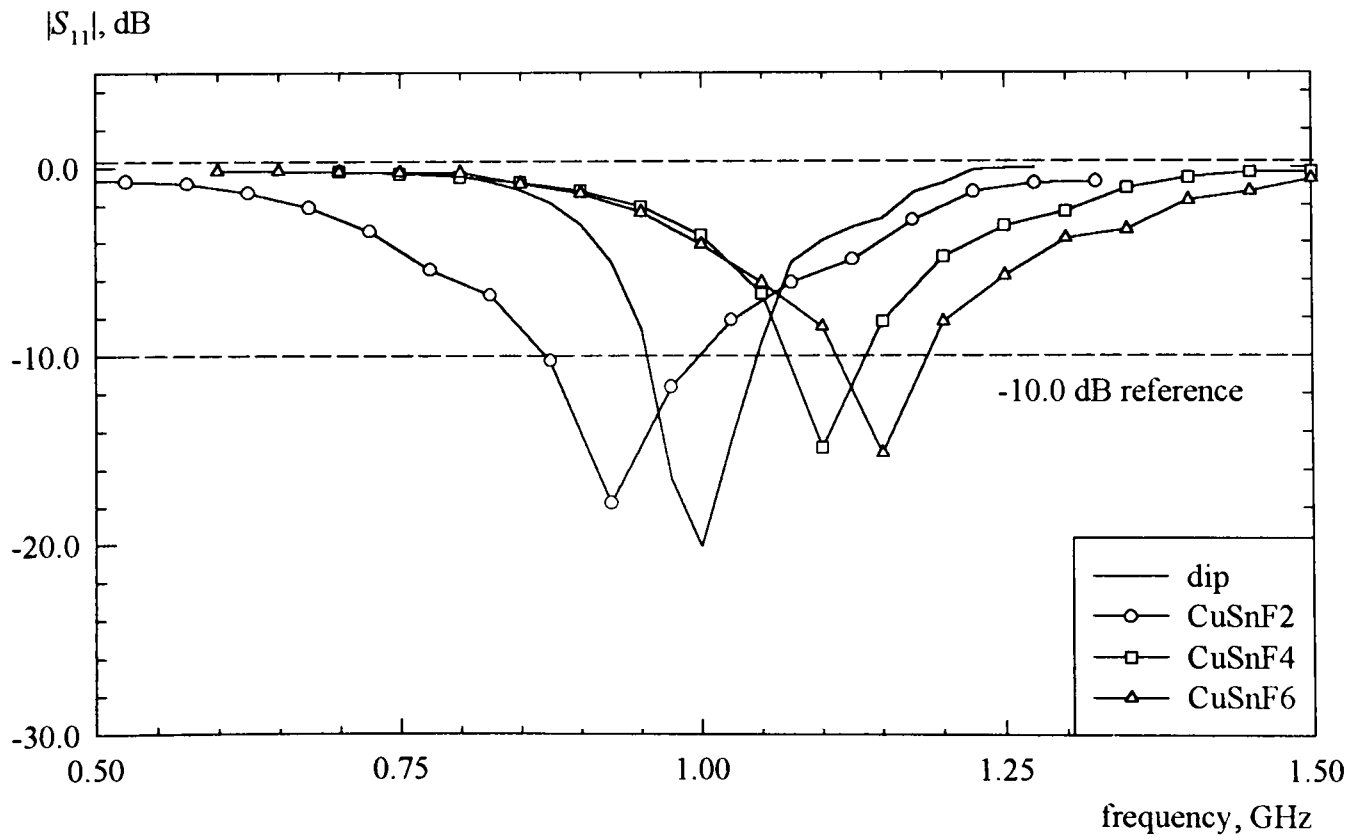

Fig. 8.34. Simulated return losses of the CuSnF and dip antennas.

From Table 8.5 and Fig. 8.33, it can be seen that all the measured CPS fed meander antennas have resonant frequencies around 1 GHz, indicating very little change in the operating frequencies with respect to the linear $\lambda/2$ dipole. Almost all the CPS fed meander antennas have narrower reflection bandwidths compared with the directly fed structures.

From the simulated results in Table 8.5 and Fig. 8.34, all the CPS fed meander dipole antennas showed similar almost constant behaviour of the frequency of operation with the measured results. However, due to the difference in the matching of the antennas to the input, no correlation can be made between the reflection bandwidth and the size of the antennas.

The measured far-field radiation patterns of all the meander antennas are similar. In addition, the simulated far-field radiation patterns are also similar. An example of the measured and simulated co-polarisation principal plane radiation patterns of the CuSnF antennas, in comparison with that of the linear dipole, are shown in Figs. 8.35 to 8.36 and 8.37, respectively. Both the shape of the measured and simulated radiation patterns of each set of antennas are in good agreement with each other. An acceptable variation of 3 dB in the vertical plane pattern is observed. The small discrepancy observed in the measured horizontal plane pattern near to broadside is probably due to pattern distortion by the polystyrene container. Nevertheless, the patterns resemble that of the linear $\lambda/2$ dipole. This proves the need of the $\lambda/4$ sleeve balun to be incorporated in the experiments, as well as feeding the antennas with the CPS lines.

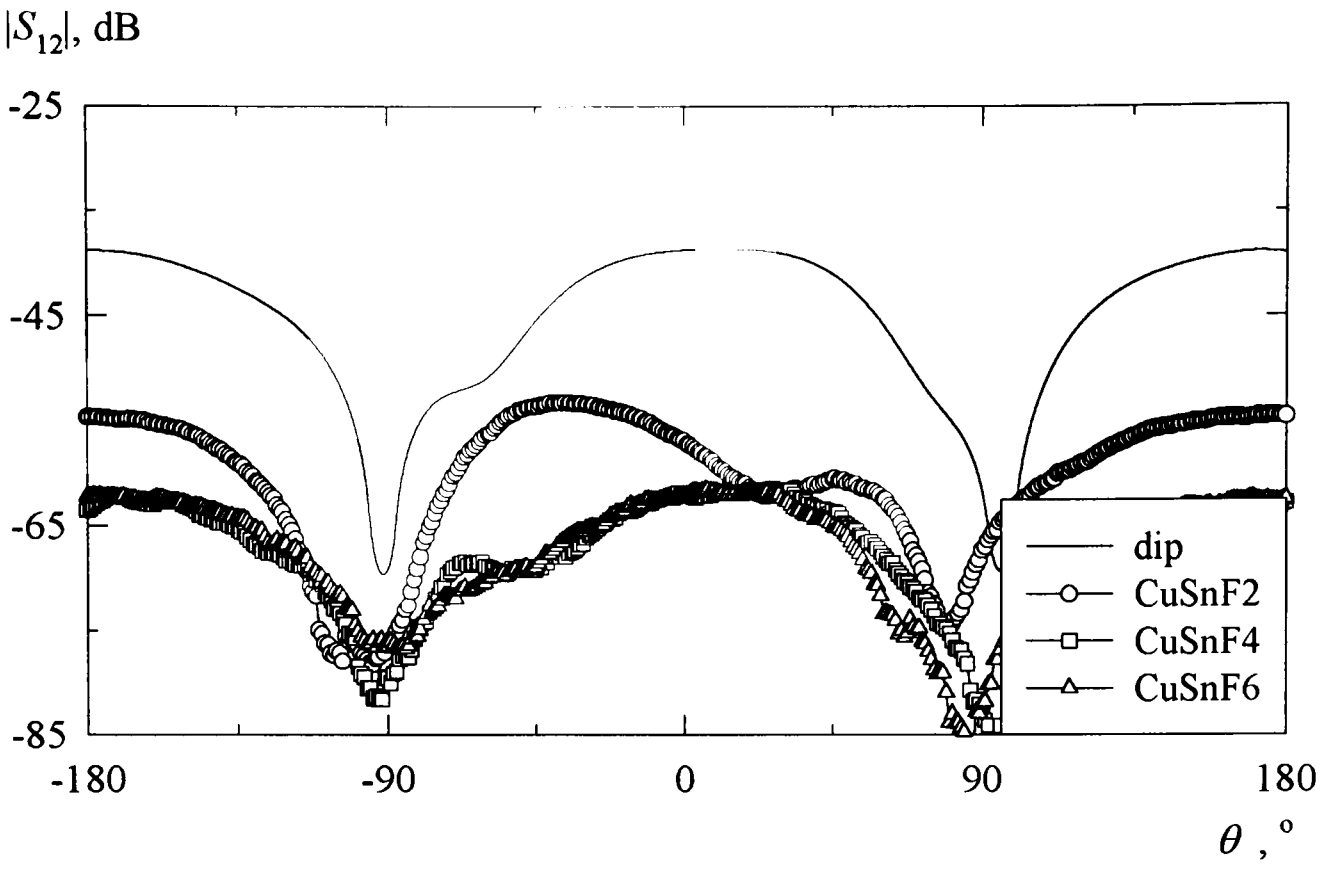

Fig. 8.35. Measured co-polar horizontal radiation patterns of CuSnF and dip.

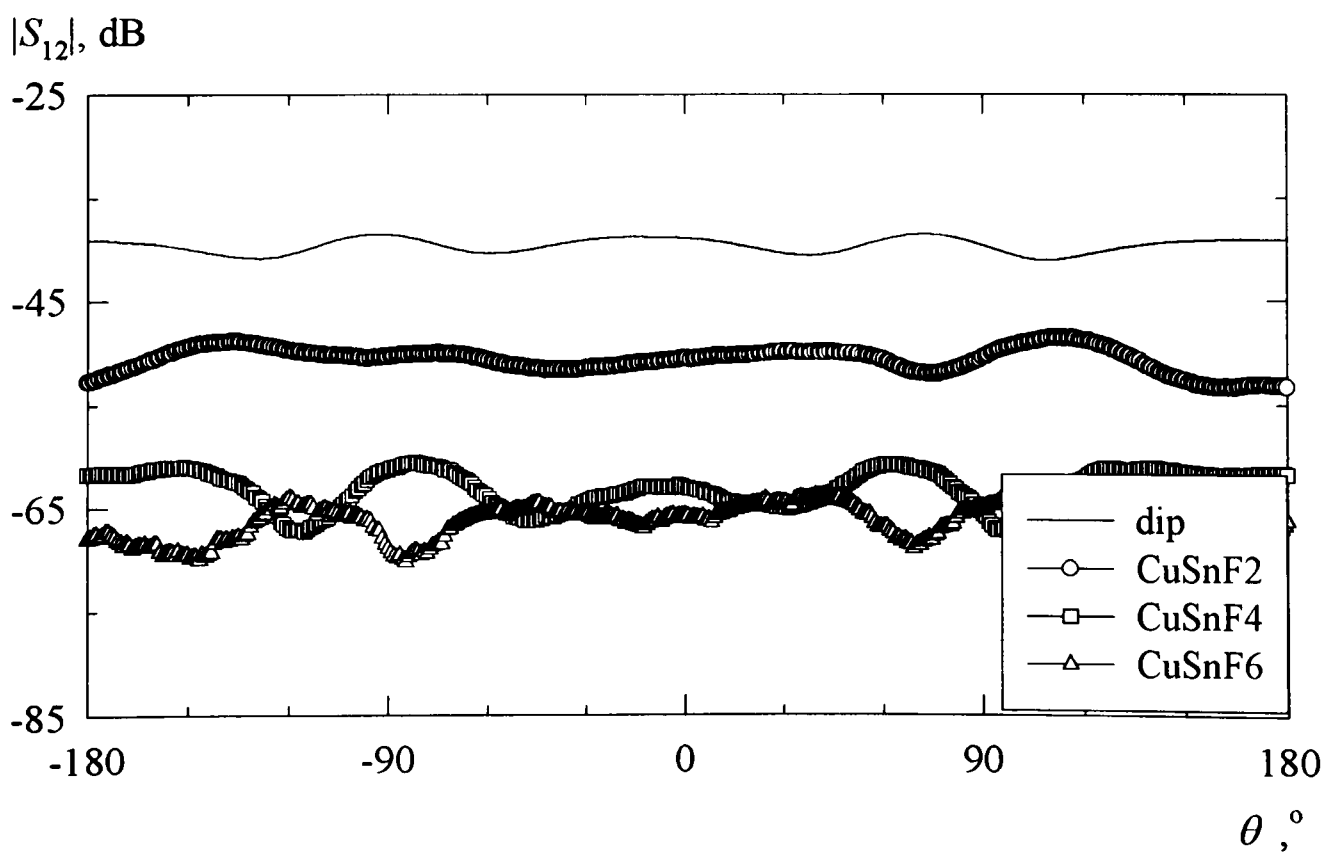

Fig. 8.36. Measured co-polar vertical radiation patterns of CuSnF and dip.

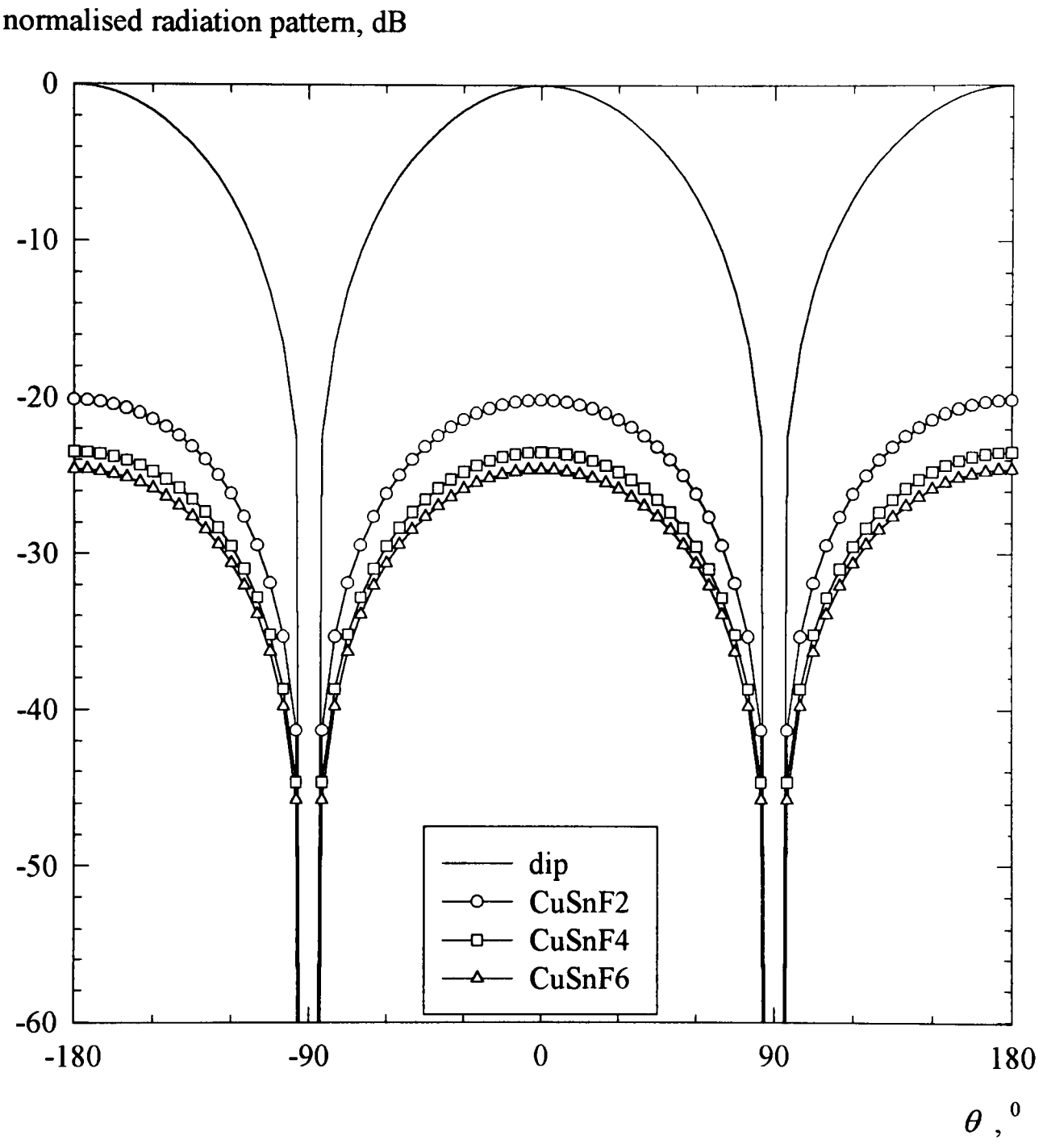

Fig. 8.37. Normalised simulated co-polar horizontal radiation patterns of CuSnF antennas, relative to that of the dip antenna.

Similar to the discussion of the anti-symmetrical meander dipole antennas, the measured and numerically simulated observations from the radiation patterns are tabulated in Table 8.6. G_0, G_{0D}, η and η_D are relative to the linear $\lambda/2$ dipole.

Table 8.6. Measured and simulated gains, efficiencies and beamwidths of the 50 ohm CPS fed symmetrical meander dipoles, relative to the linear $\lambda/2$ dipole.

	Measured					**Simulated**		
antenna	G_0 , dB	G_{0D} , dB	η , %	η_D , %	HPBW, °	G_{0D} , dB	η_D , %	HPBW,°
CuRkF2	-1.2	-13.1	46	22	79	-18.3	25	88
CuRkF4	-3.1	-16.3	30	15	86	-20.8	14	89
CuRkF6	-4.8	-24.7	20	6	70	-23.0	8	89
CuSkF2	-1.6	-12.7	42	23	78	-21.0	13	88
CuSkF4	-4.5	-21.1	22	9	71	-21.7	11	90
CuSkF6	-4.6	-24.1	21	6	90	-25.4	5	89
CuSnF2	-1.5	-16.0	43	15	85	-20.2	16	92
CuSnF4	-1.7	-22.9	41	8	76	-23.5	7	88
CuSnF6	-7.0	-24.8	12	7	75	-24.6	6	89

G_0 : gain, obtained using eqn. (4.5). η : efficiency, obtained using G_0 in eqn. (4.24).

G_{0D} : gain; difference in $|S_{12}|$ maximums. η_D : efficiency, obtained using G_{0D} in eqn. (4.23).

Although, the measured relative gains, G_0 and G_{0D}, and efficiencies, η and η_D, differ by a factor of 10 and 2, respectively, the trend associated with decreasing number of meander sections agrees well. The relative gain of the meander antennas reduces with increasing number of meander sections. Consequently, the efficiency decreases. This is due to the decrease in the antenna size, as will be investigated. However, the measured and numerically simulated G_{0D} and η_D appear consistent. In addition, all the antennas have approximately similar measured HPBWs with that of the linear $\lambda/2$ dipole. However, the

simulated HPBWs appear consistent with a short dipole, indicating lower directivities. All the meander antennas are inefficient as expected due to their small size, however, CuSnF antennas have the least relative gains and efficiencies. This is attributed to the smaller size and thinner radiating structure which contribute to less radiation and more conductor loss.

The sizes of the 50 ohm CPS fed meander dipoles are also compared based on the measured operating frequencies, directive gain and efficiency. The relationship of both the measured and simulated operating frequencies with respect to the antenna radius are shown in Fig. 8.38. The theoretical operating frequency curve of multiples of half-wavelength dipoles is also shown. It can be seen that all the 50 ohm CPS fed meander antennas are physically small at their corresponding operating frequencies. The physical size decreases as the number of meander sections increases. This occurs from the linear $\lambda/2$ dipole to the meander dipoles. Correspondingly, being smaller in size, the antennas exhibit lesser gain and are inefficient, as previously discussed. On the other hand, the linear $\lambda/2$ dipole is physically large at its operating frequency. The measured and simulated results are in good agreement. The operating frequencies of the meander dipole antennas are well below the curve of multiples of half-wavelength dipoles. All the meander dipoles operate close to the linear $\lambda/2$ dipole which has the same radiating track length, indicating that the symmetrical meander structures maintain the frequency of operation.

The relationship of both the measured and simulated operating frequencies with the electrical size S of the antenna are shown in Fig. 8.39. They are in good agreement with each other. All the meander dipole antennas are electrically small. The meander dipole antenna gets electrically smaller as the number of meander sections increases. On the other hand, the linear $\lambda/2$ dipole is electrically large. It can be inferred that the linear $\lambda/2$ dipole can be electrically miniaturised whilst maintaining its frequency of operation, by symmetrically meandering the radiating structure.

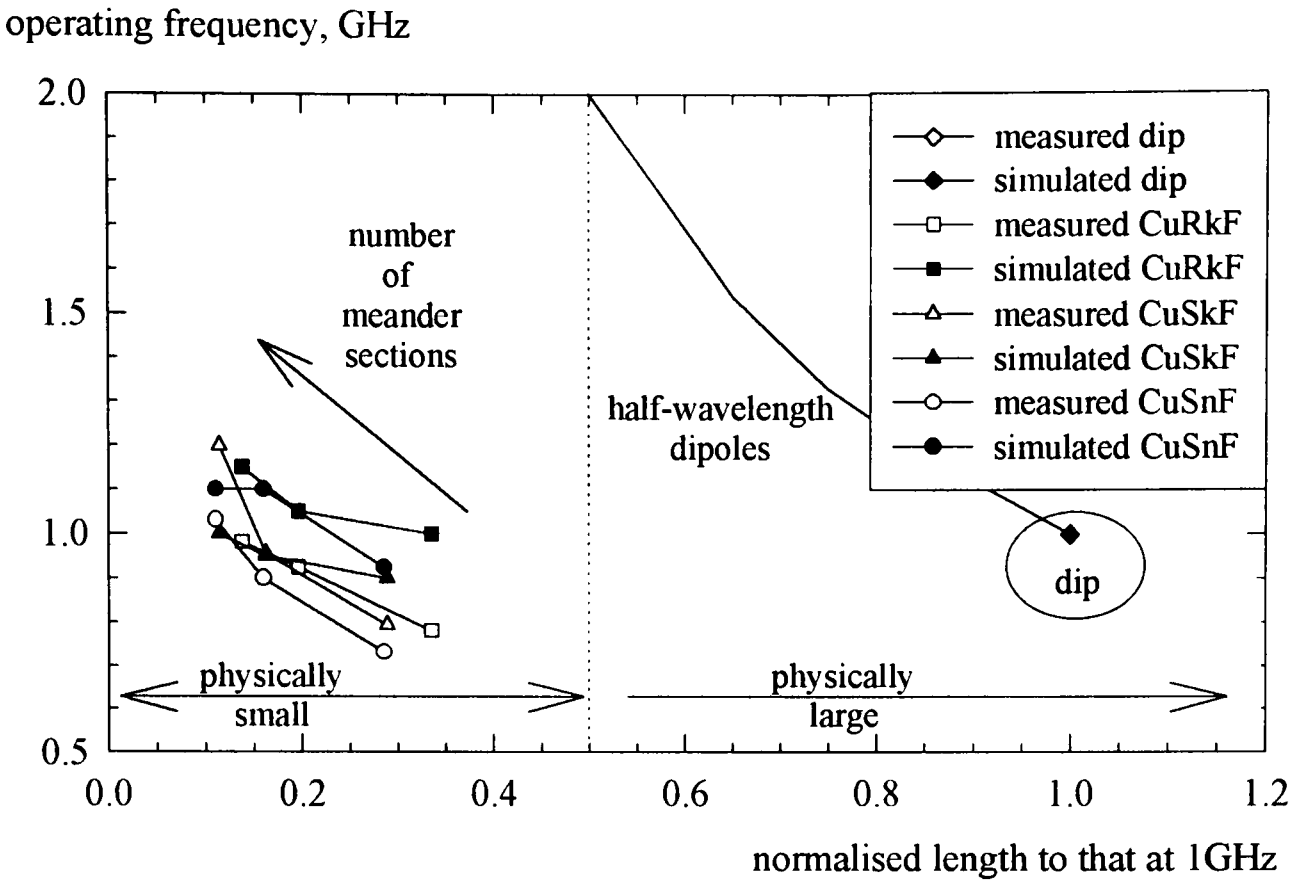

Fig. 8.38. Measured and simulated operating frequencies with respect to the antenna radius and theoretical operating frequency of several linear half-wavelength dipoles.

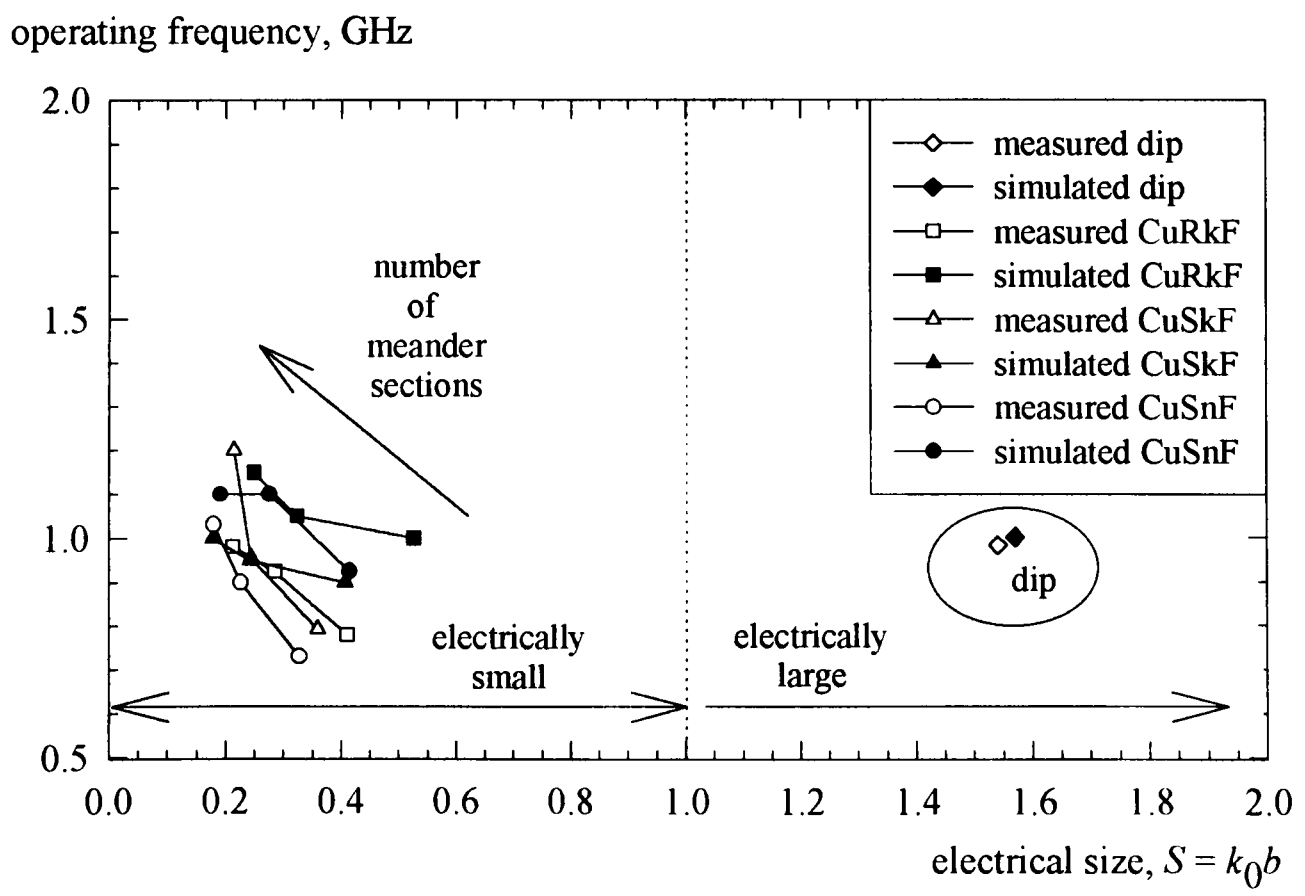

Fig. 8.39. Measured and simulated operating frequencies with respect to the electrical size.

The simulated surface current distribution on all the CPS fed antennas showed an approximate half-wave sinusoidal variation along the track length of the antenna. The distributions are nulls at the radiating structure ends whilst they are peaks at the centre. The distributions are depicted in Fig. 8.40, in comparison with that of the $\lambda/2$ dipole.

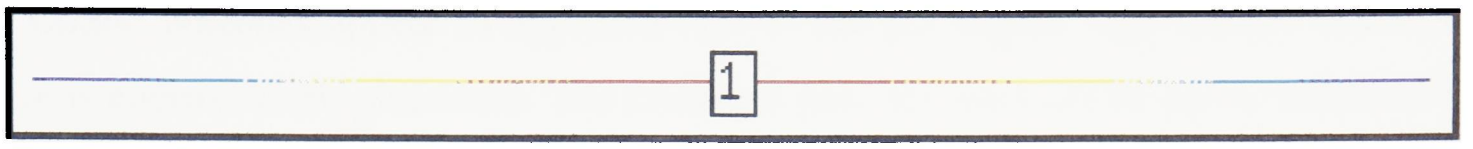

(a) half-wavelength dipole

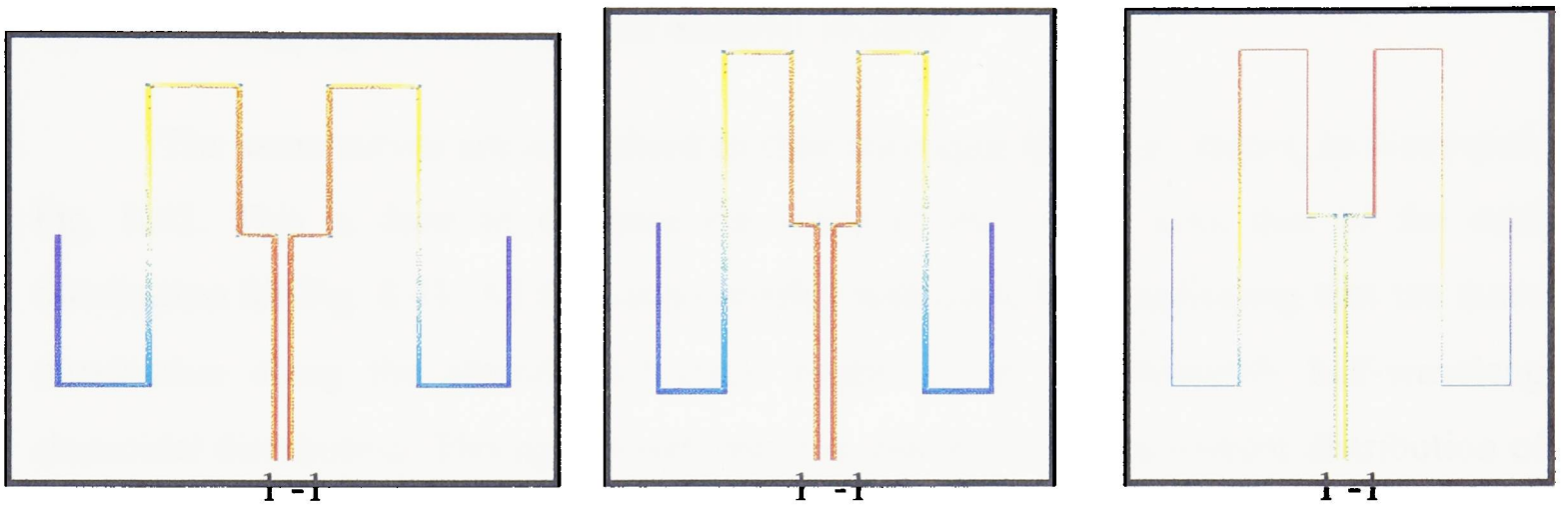

(b) CuRkF2 (e) CuSkF2 (h) CuSnF2

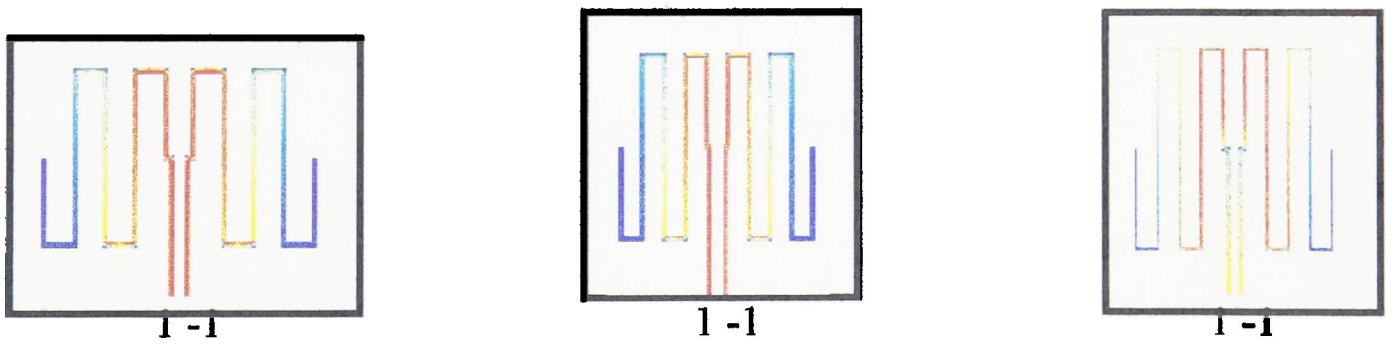

(c) CuRkF4 (f) CuSkF4 (i) CuSnF4

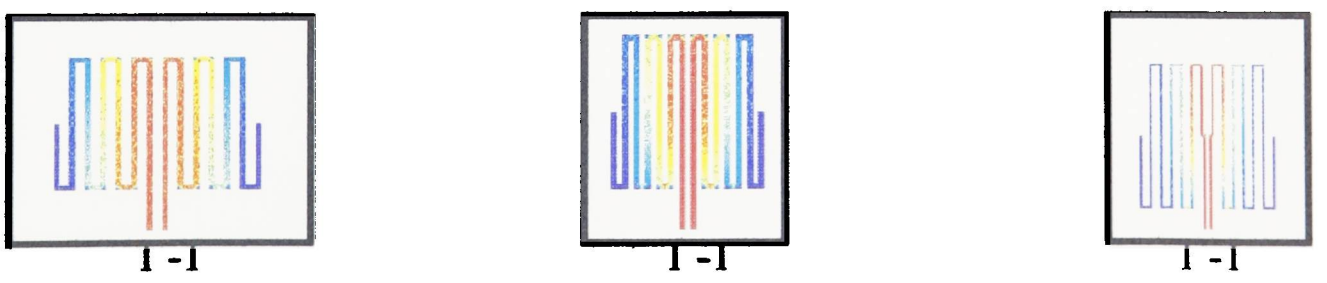

(d) CuRkF6 (g) CuSkF6 (j) CuSnF6

Fig. 8.40. Simulated current distribution along the arm of the antennas.

The simulated surface current distribution along the track length of the antennas is now discussed. An example will be given for the CuSnF antennas. The simulated surface current distribution on each CuSnF is plotted against the corresponding track length in Fig. 8.41. Each current distribution is compared to that of the $\lambda/2$ dipole. Each curve shows a near peak at the antenna feed and nulls at both ends of the radiating arms. All the curves of the CuSnF antennas appear to approach that of the $\lambda/2$ dipole. The current distribution curve is approximately sinusoidal. The dominant peak for the CuSnF6 curve indicated that the current tends to concentrate at the antenna feed. The CuSnF6 meander dipole also has the highest current distribution along its axial length. This is attributed to the higher capacitive coupling between adjacent meander sections.

The same curves are normalised to their corresponding peak values, as illustrated in Fig. 8.42. This is done to compare the shape of the curves with that of the cosine distribution for Fig. 8.41. All the curves overlap with each other, indicating that the current distribution along the antenna $\lambda/2$ track length are of approximately half-wavelength sinusoidal distribution. This agrees well with the theoretical cosine current distribution of a half-wavelength dipole as discussed in Section 2.8.2.

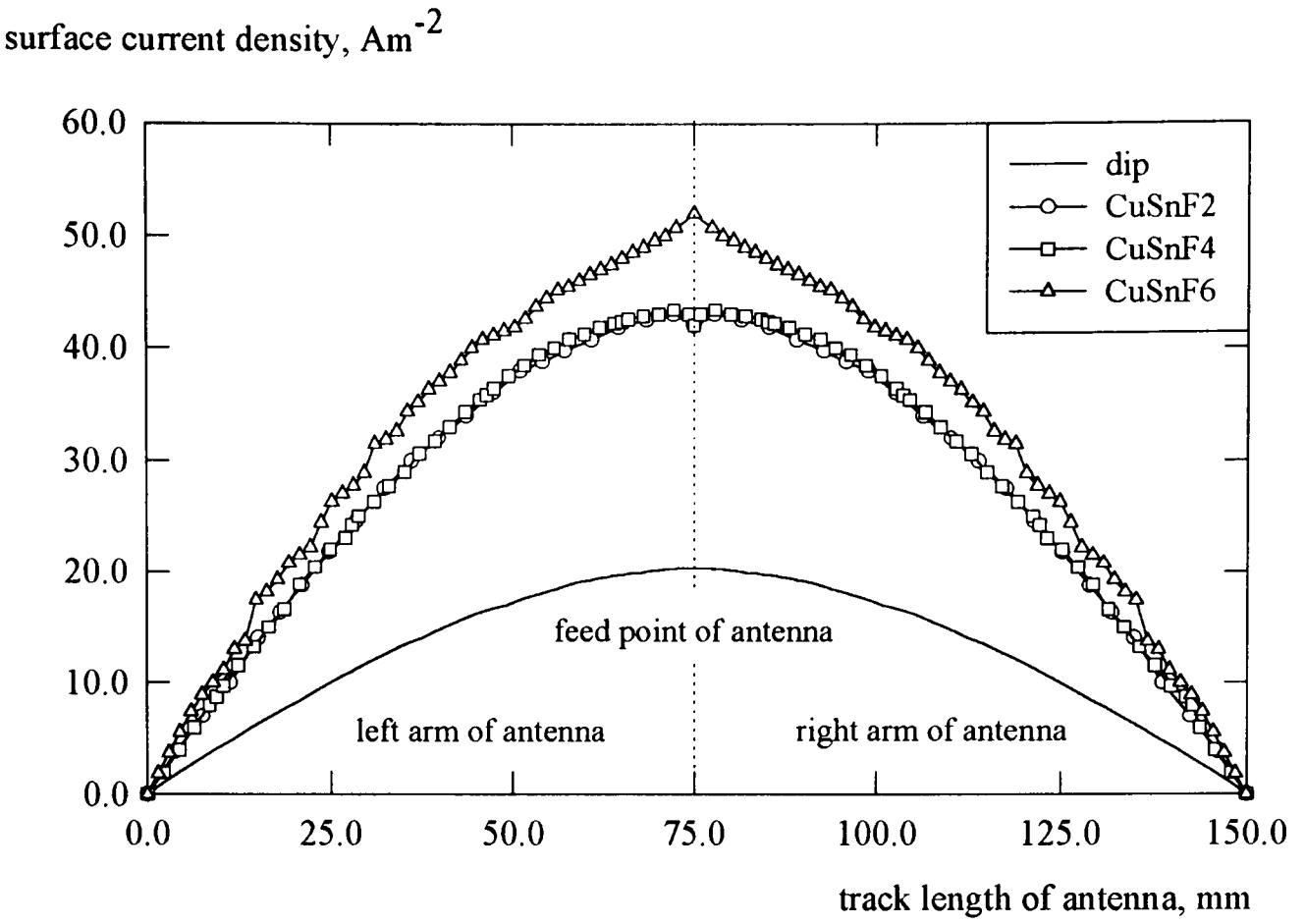

Fig. 8.41. Current distribution along the track length of the CuSnF and dip antennas.

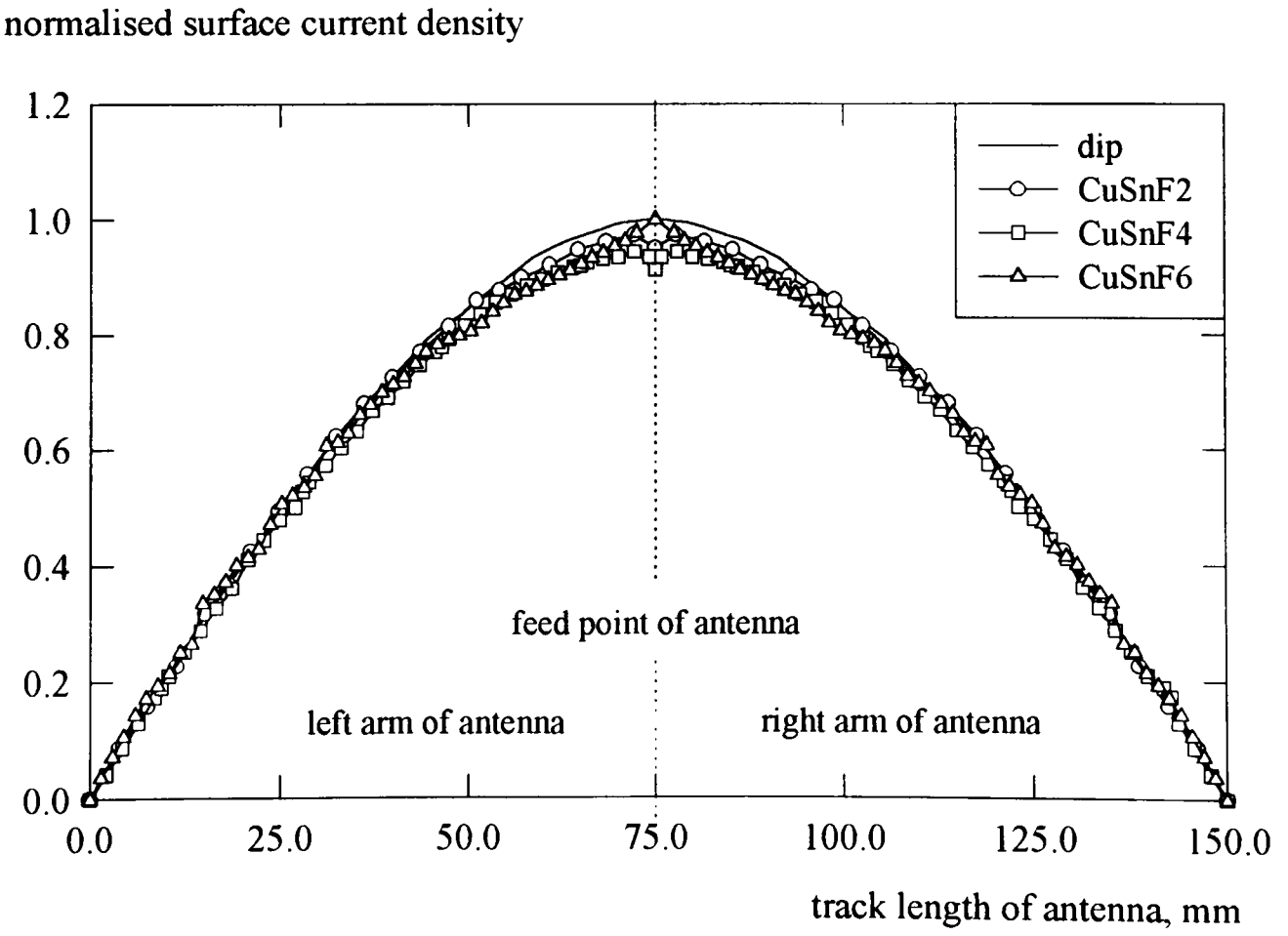

Fig. 8.42. Normalised current distribution along the track length of the antennas.

For the reflection measurements of the HTS antennas at 77K, the results obtained are tabulated in Table 8.7, together with the corresponding numerically simulated results. In addition, the results for the corresponding copper structures at 300K are also presented. The measured and simulated $|S_{11}|$ curves for the thick- and thin-film HTS antennas are shown in Figs. 8.43 to 8.44 and 8.45 to 8.46, respectively. The corresponding reflection bandwidths, taken at the -10.0 dB $|S_{11}|$ level, are also shown. The measured and simulated $|S_{11}|$ of the linear copper $\lambda/2$ dipole and the corresponding copper structures are also displayed in relevant figures for further comparison. The second resonance of the linear dipole (dip2) is included for reference to the HnSnF antennas. The abbreviation dip1 refers to the fundamental resonance of dip.

Table 8.7. Measured and simulated results for the directly fed copper symmetrical meander dipoles and the linear copper $\lambda/2$ dipole.

antenna	**Measured**		**Simulated**	
	f_0 GHz	$\|S_{11}\|$ dB	f_0 GHz	$\|S_{11}\|$ dB
dip1	0.981	-19.40	1.0	-20.06
dip2	3.07	-30.82	3.0	-26.94
CuSkF2	0.794	-19.36	0.90	-16.18
HkSkF4	0.6	-17.03	0.78	-17.86
CuSnF2	0.732	-12.68	0.93	-17.76
CuSnF4	0.9	-15.42	1.1	-14.80
CuSnF6	1.031	-15.56	1.1	-16.10
HnSnF2	1.963	-12.28	3.00	-15.95
HnSnF4	2.769	-14.58	3.10	-14.22
HnSnF6	2.738	-17.57	3.20	-15.19

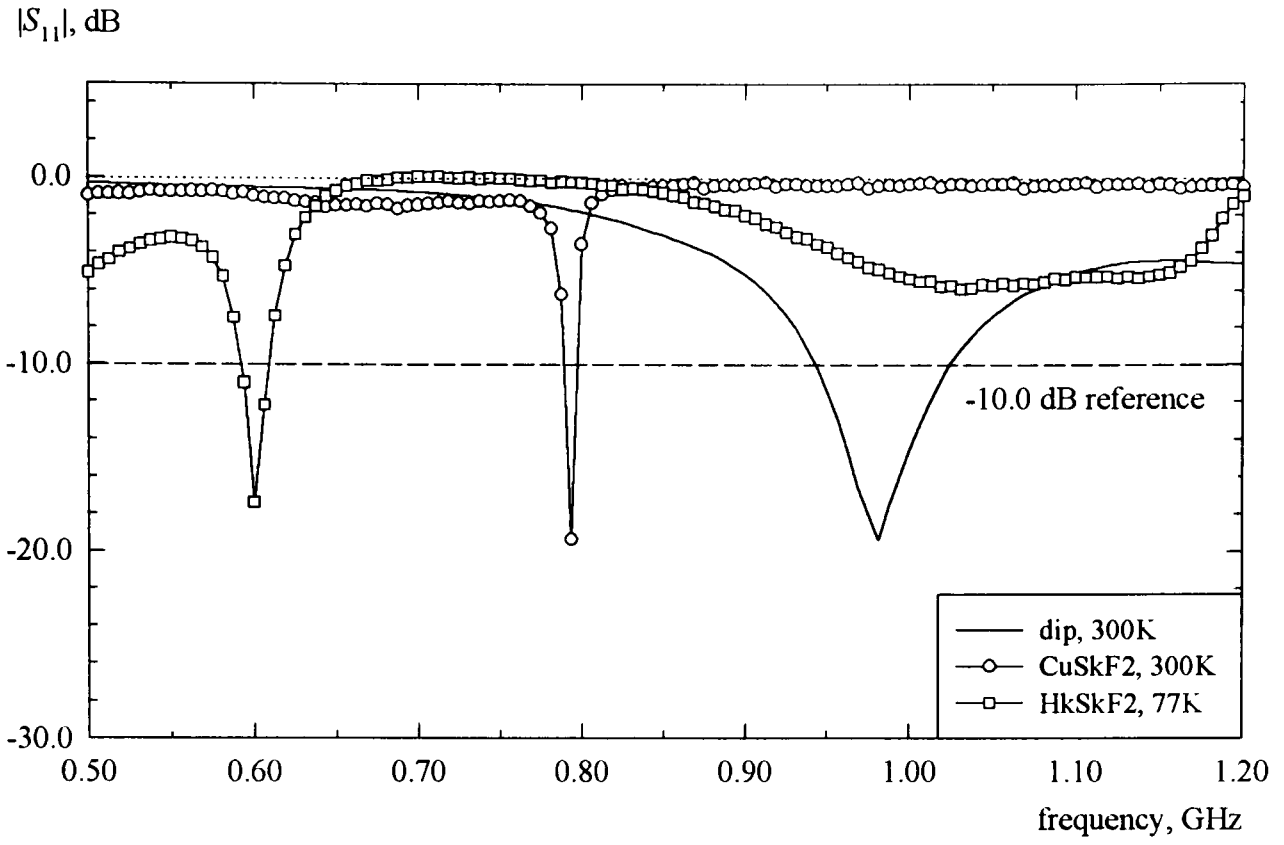

Fig. 8.43. Measured return losses of the CuSkF2, HkSkF2 and dip antennas.

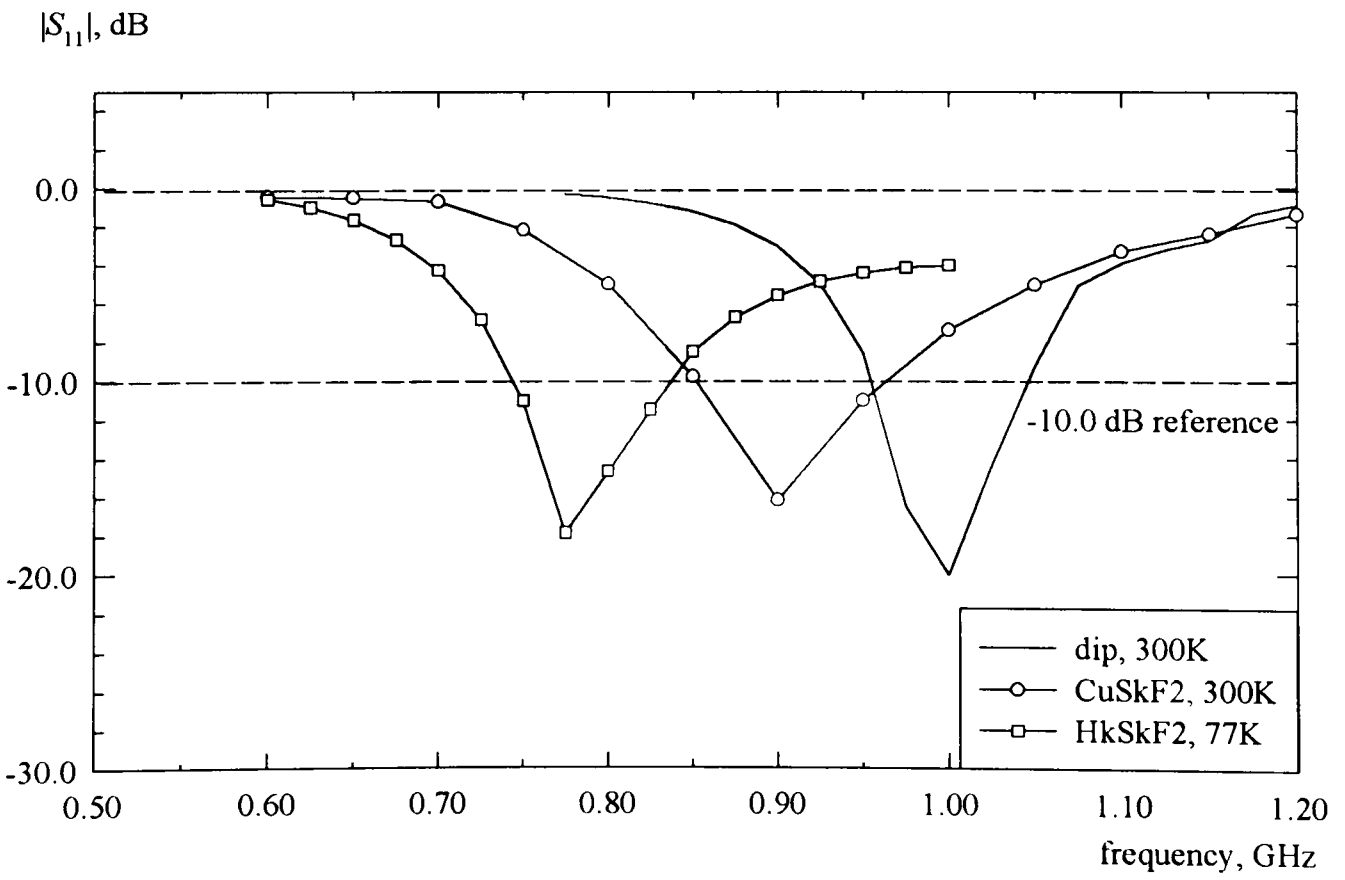

Fig. 8.44. Simulated return losses of the CuSkF2, HkSkF2 and dip antennas.

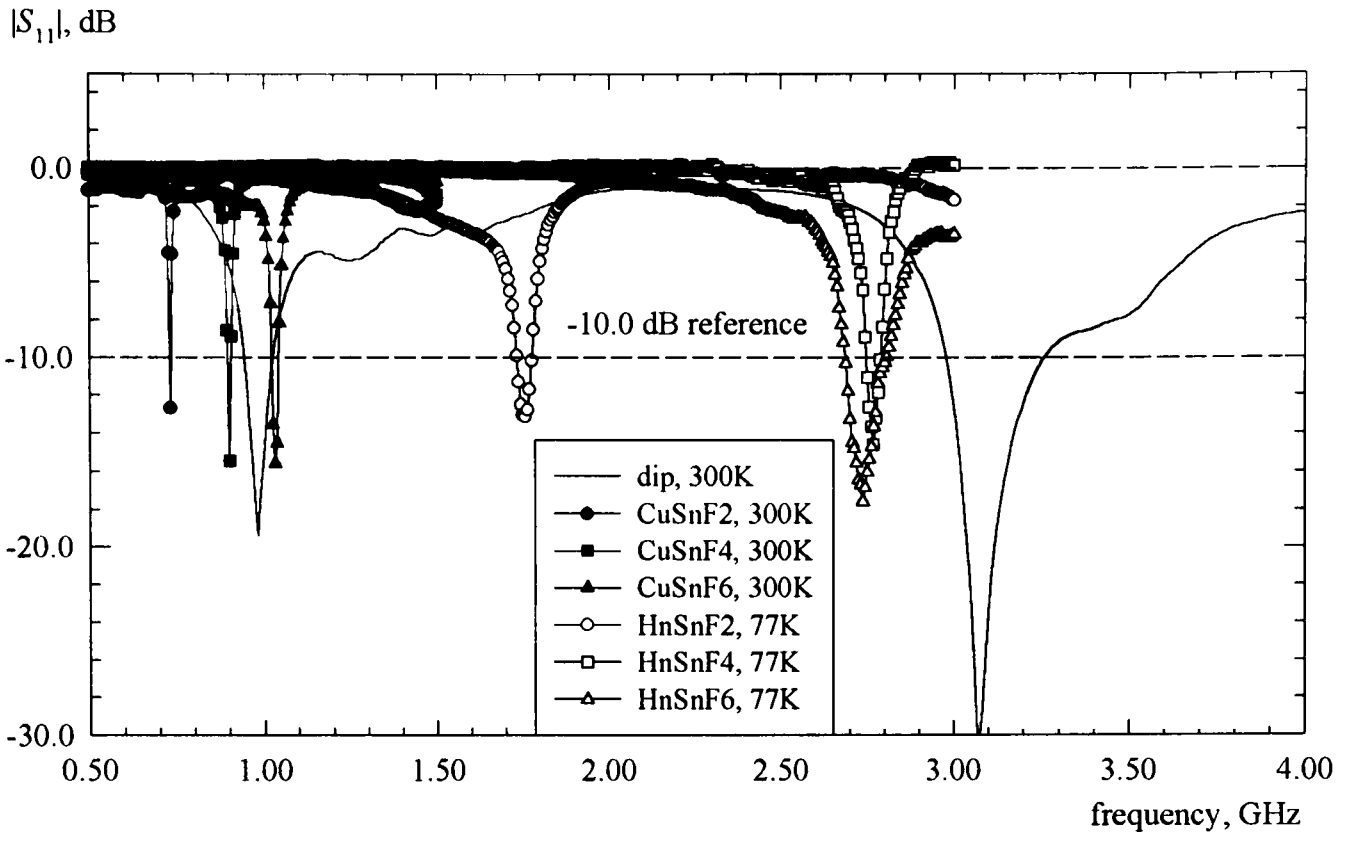

Fig. 8.45. Measured return losses of the CuSnF, HnSnF and dip antennas.

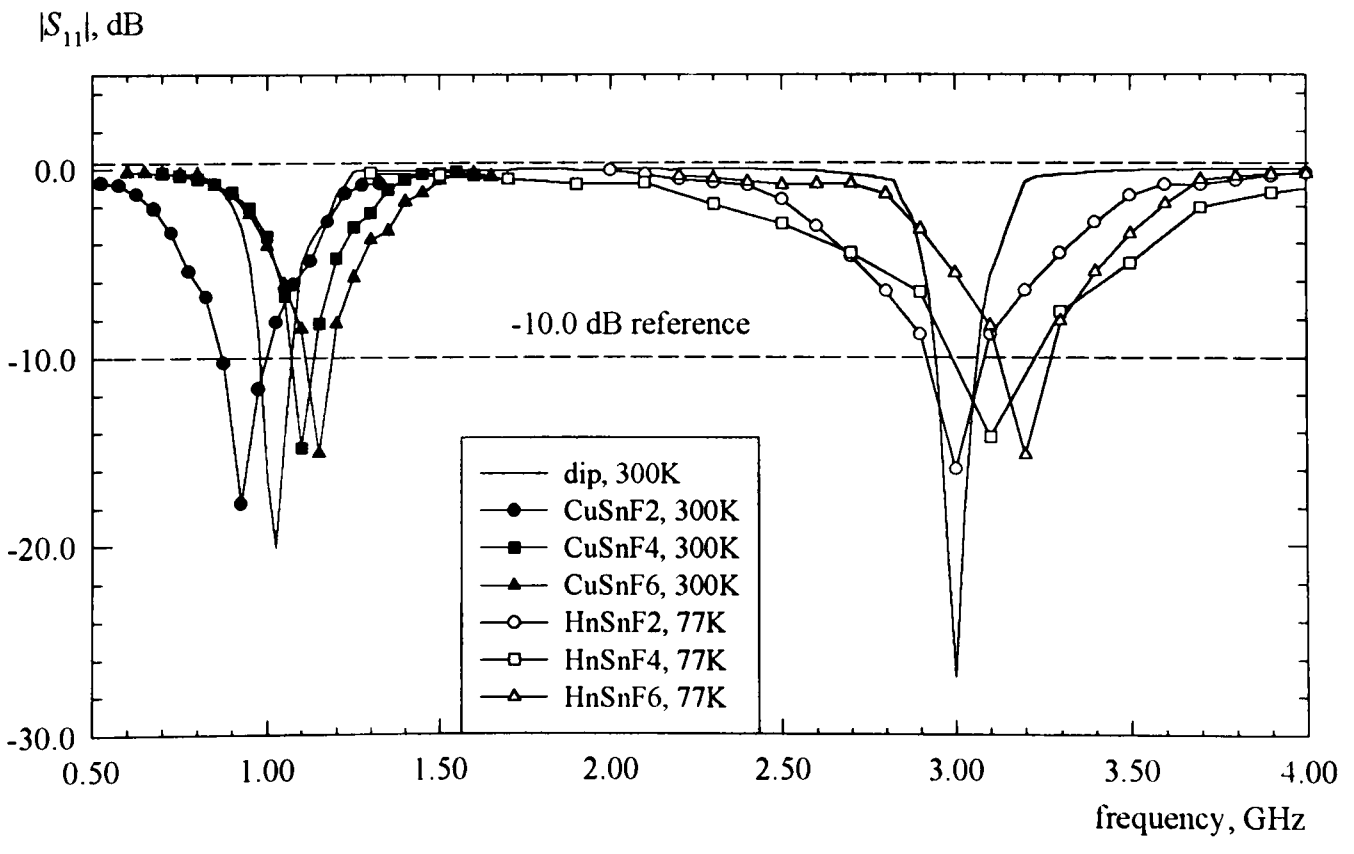

Fig. 8.46. Simulated return losses of the CuSnF, HnSnF and dip antennas.

From Table 8.7 and Fig. 8.43, it can be seen that the measured operating frequency of HkSkF2 shifted down by about 24 % from that of CuSkF2, due to the 1.44 relative permittivity of liquid nitrogen [39], kinetic inductance of the YBCO material and the relative permittivity of the YSZ substrate. The contribution from the latter is quite significant because it is almost a factor of 3 higher than that of RT/duroid substrate. The kinetic inductance has been discussed in Section 3.2. Similar frequency shifting from that of the corresponding normal conductor antenna structure has been observed by other researchers such as in references [37], [55], [61], [64], [70], [82] and [88]. The frequency shiftings from that of dip1 are about 20 % and 40 %, for CuSkF2 and HkSkF2, respectively. The HkSkF2 antenna has been reasonably matched to the input.

From the simulated results in Table 8.7 and Fig. 8.44, HkSkF2 showed similar behaviour of the frequency of operation with the measured results. The shift in frequency from the corresponding copper structure is about 13 %. Both results agree well with each other.

Since the HnSnF antennas are designed to be a factor of 3.31 physically smaller than the corresponding CuSnF antennas, it can be seen from Table 8.7 and Figs. 8.45 to 8.46 that similar factor of shiftings in the frequency of operation are observed. Although the HnSnF2 resonates at a lower measured frequency of operation, all the thin film antennas operate quite close to that of dip2. The lower measured frequency of operation of HnSnF2 is probably due to the slightly longer CPS feeding line as a result of the patterning procedure. Comparison with dip2 is also made because its frequency of operation is equivalent to that of a linear $\lambda/2$ dipole which has the same track length with the HnSnF antennas. Due to the difference in the matching of the meander antennas to the input, the bandwidth does not correlate with the size of the meander antenna. All the HnSnF antennas are reasonably well-matched to the input.

The measured far-field radiation patterns of all the superconducting meander antennas are similar to the figure-of-eight shape. In addition, the simulated far-field radiation patterns are also similar.

The measured principal plane radiation patterns of HkSkF2, in comparison with dip1 and CuSkF2 antennas, are shown in Figs. 8.47 and 8.48. The corresponding simulated co-polarisation horizontal plane radiation patterns, normalised to the corresponding maximum, are shown next in Fig. 8.49. Both the shape of the measured and simulated radiation patterns of the meander antenna are in good agreement with each other and with that of dip1. The measured and simulated HPBW of HkSkF2 are slightly larger than that of CuSkF2, indicating slightly less directive radiation patterns. In addition, both antennas are less directive than dip1.

For the HnSnF antennas, the measured principal plane radiation patterns are shown in Figs. 8.50 and 8.51, together with that of dip2 antenna. The simulated co-polar horizontal plane patterns, normalised to the corresponding maximum, are shown in Fig. 8.52. All patterns have similar shape. The corresponding radiation patterns for CuSnF antennas are given earlier in Figs. 8.35 to 8.37. The measured and simulated HPBW of HnSnF antennas are slightly larger than that of CuSnF antennas, indicating less directive radiation patterns. In addition, HnSnF and CuSnF antennas are less directive than dip2 and dip1, respectively. Further comparison of all the meander antennas is discussed in Section 8.2.3.

In relation to the far-field radiation patterns, the discussion proceeds to the performance of the HTS antennas in terms of the absolute gain, supergain and efficiency over that of the corresponding copper structures. The measured and numerically simulated HPBW of the thick- and thin-film HTS antennas, are given in Tables 8.8 and 8.9, respectively.

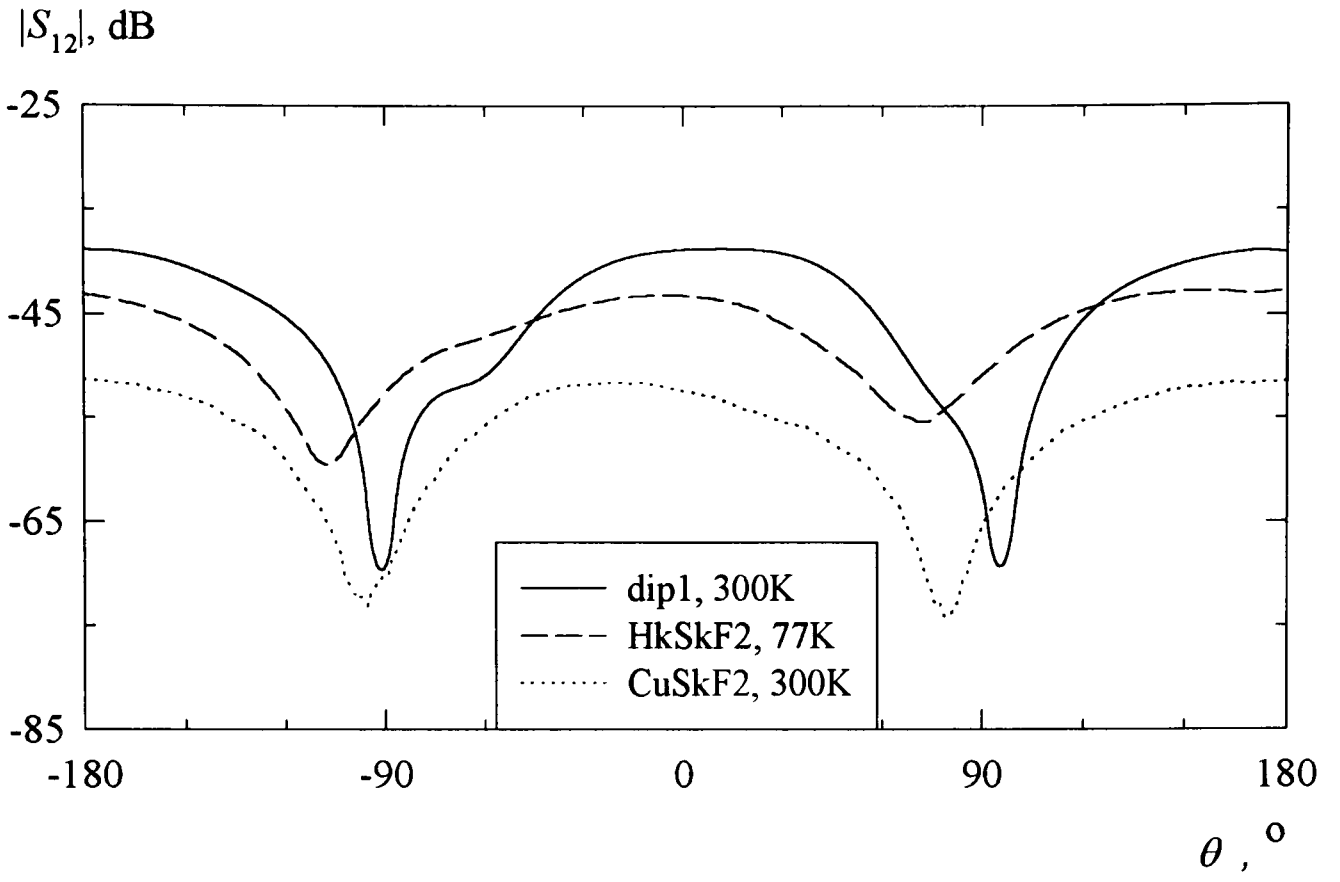

Fig. 8.47. Measured co-polar horizontal radiation patterns of HkSkF2, CuSkF2 and dip1.

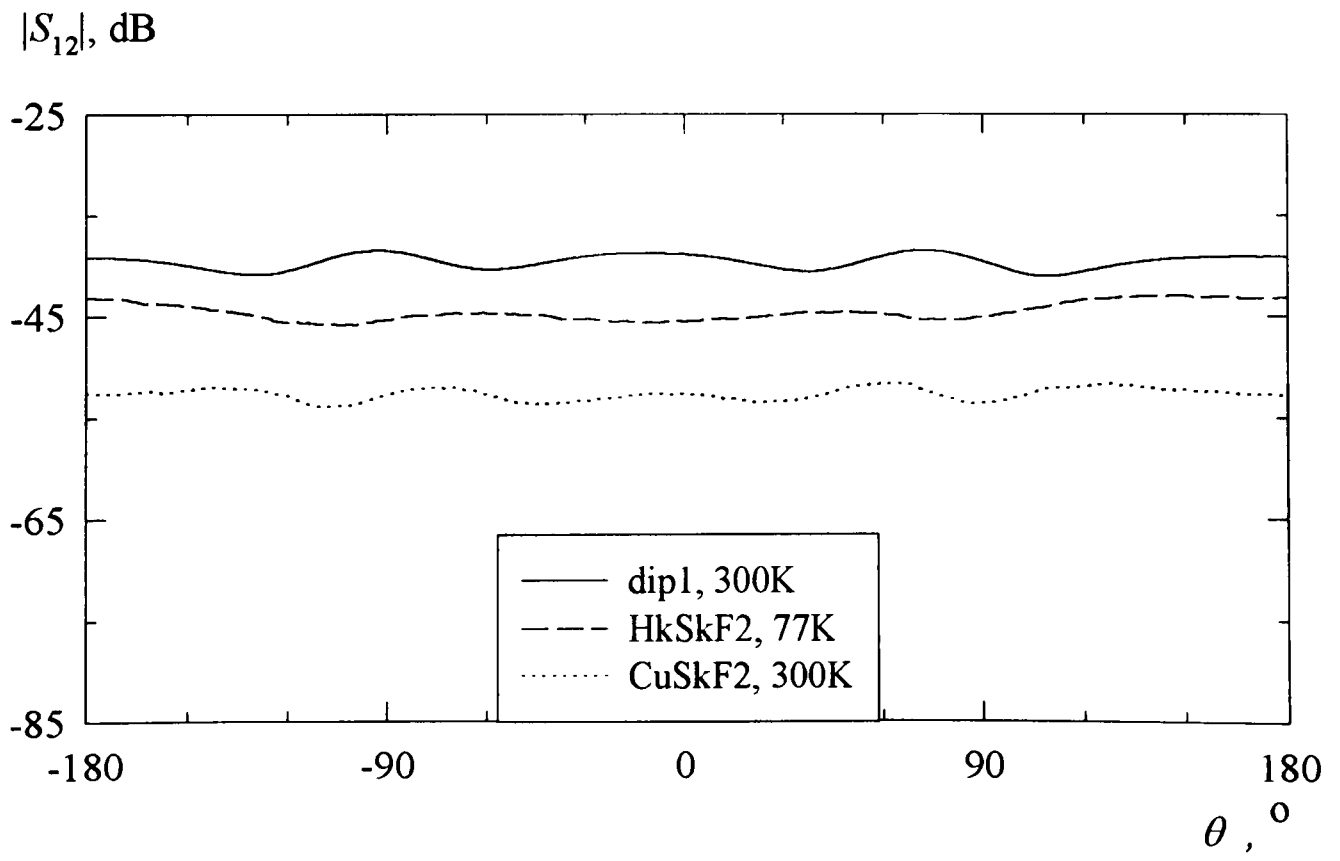

Fig. 8.48. Measured co-polar vertical radiation patterns of HkSkF, CuSkF2 and dip1.

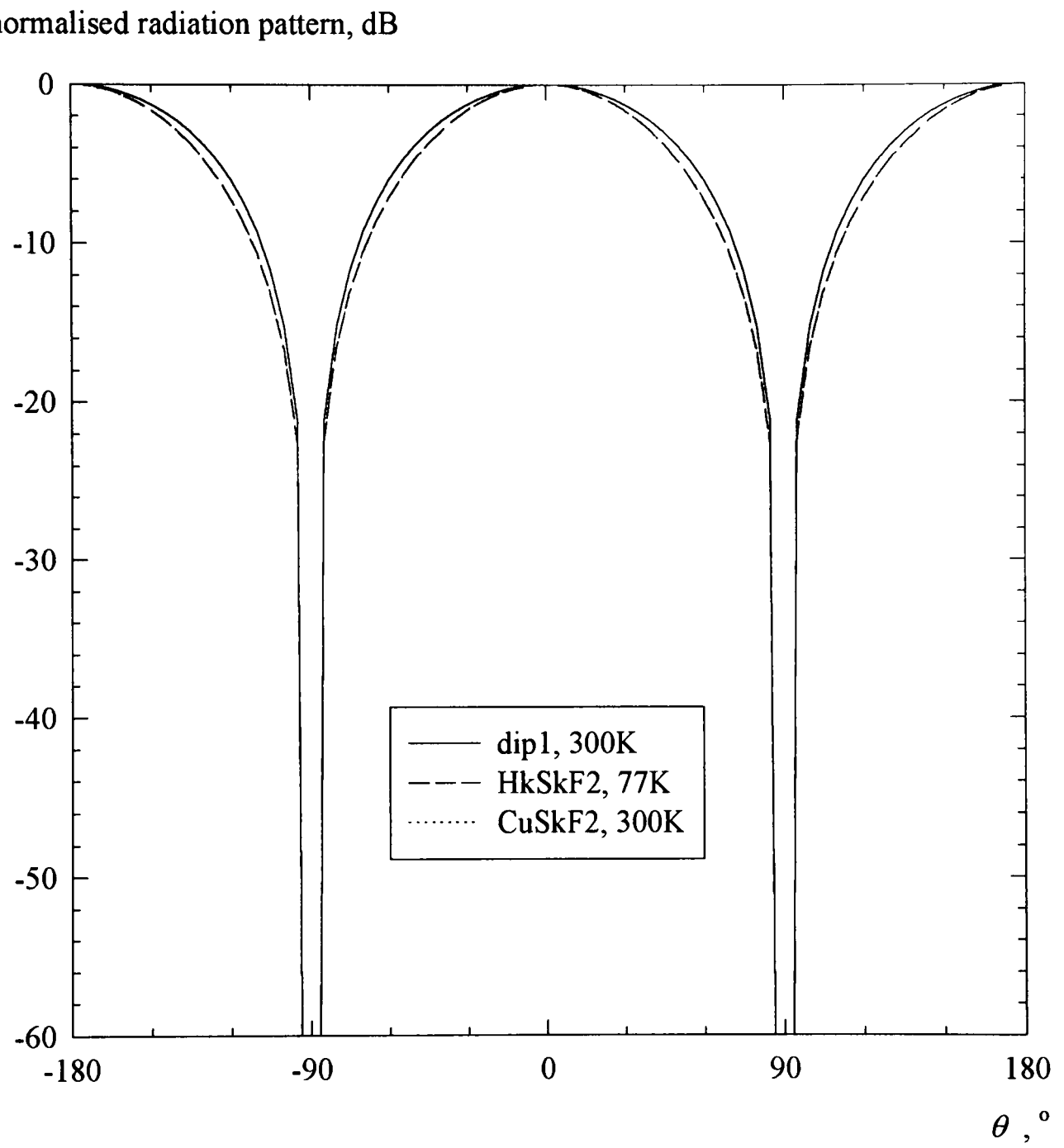

Fig. 8.49. Simulated co-polar horizontal radiation patterns of the dip1, HkSkF2 and CuSkF2 antennas, normalised to the corresponding maximum.

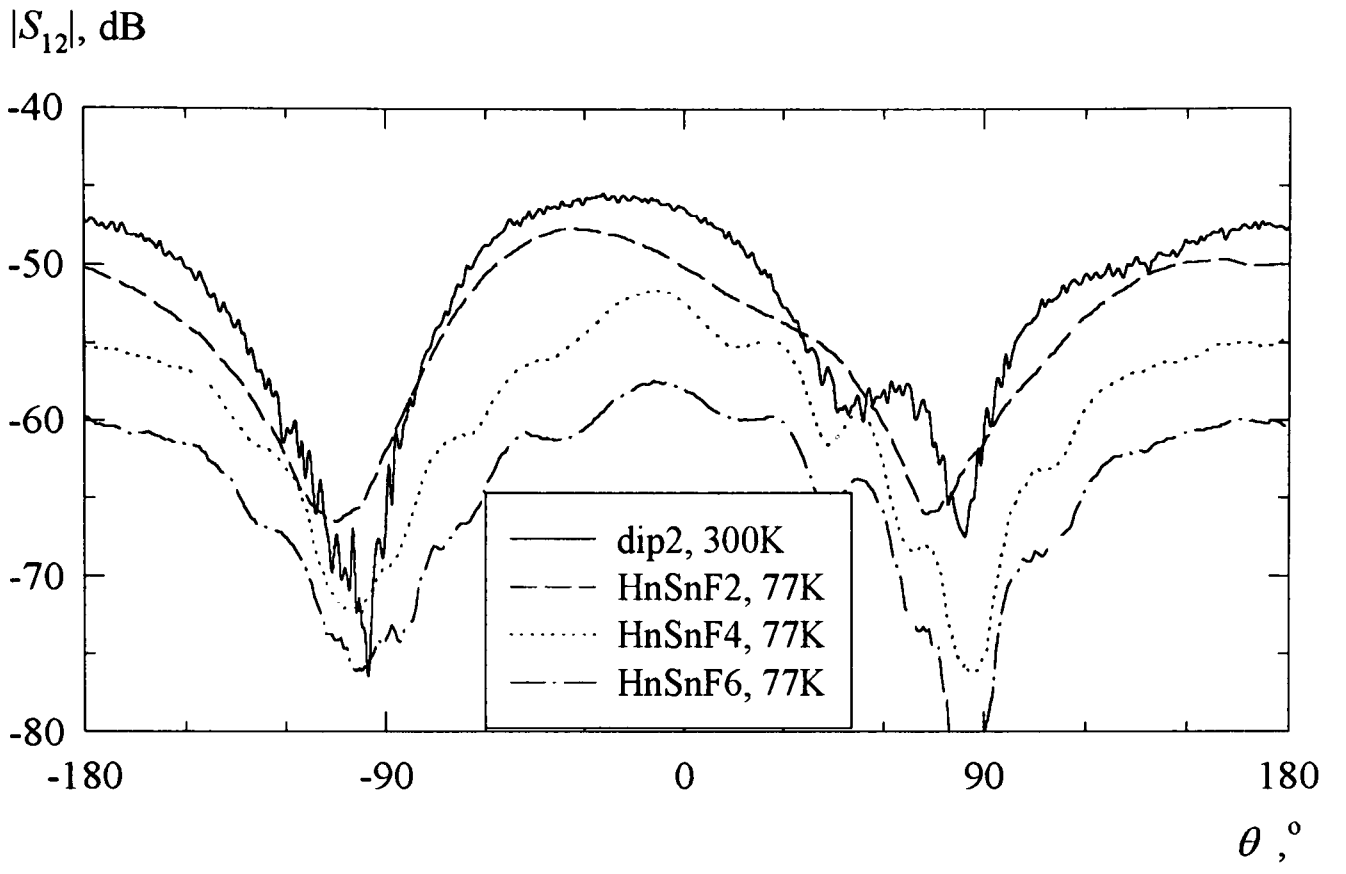

Fig. 8.50. Measured co-polar horizontal radiation patterns of HnSnF and dip2 antennas.

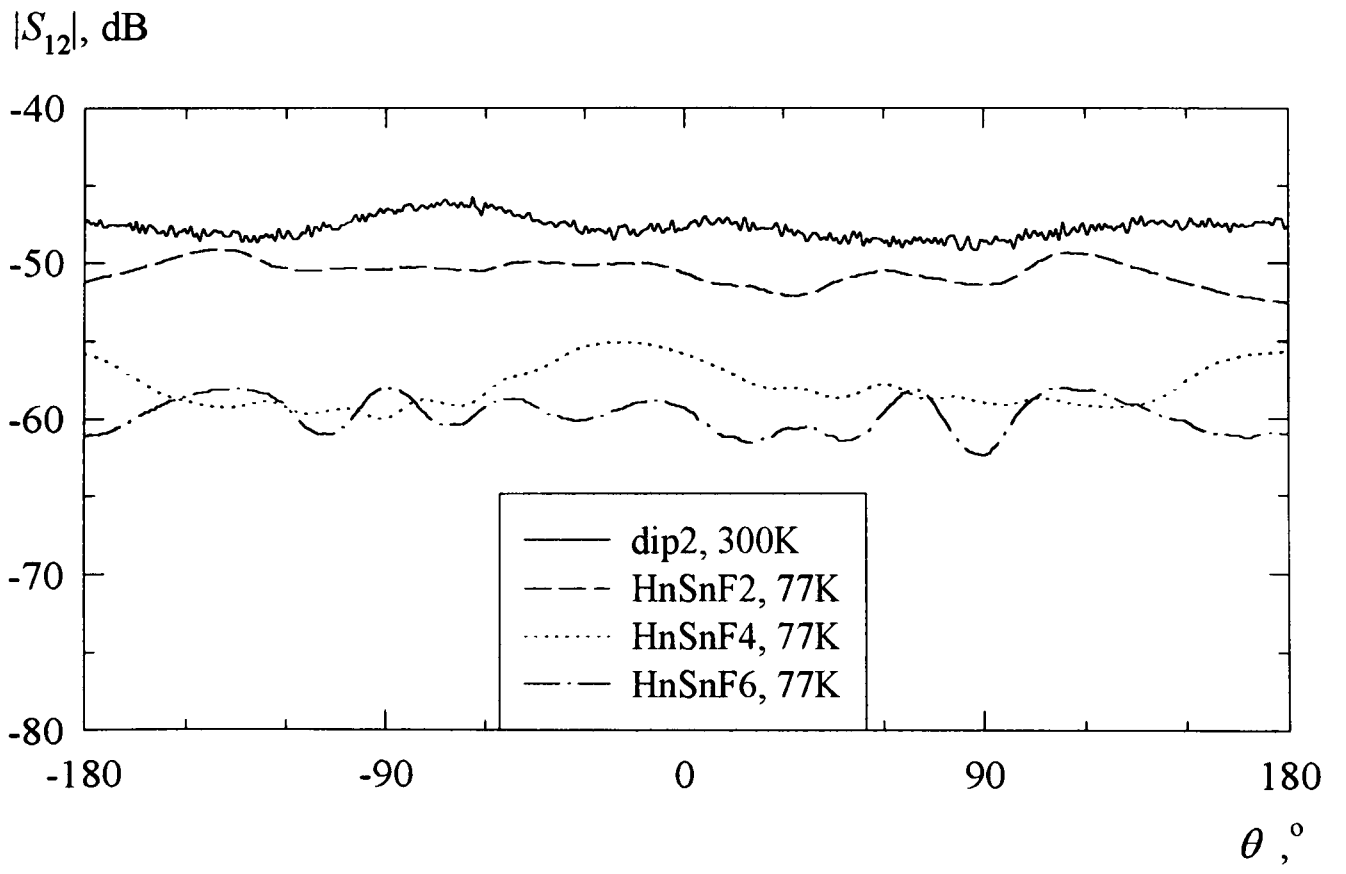

Fig. 8.51. Measured co-polar vertical radiation patterns of HnSnF and dip2 antennas.

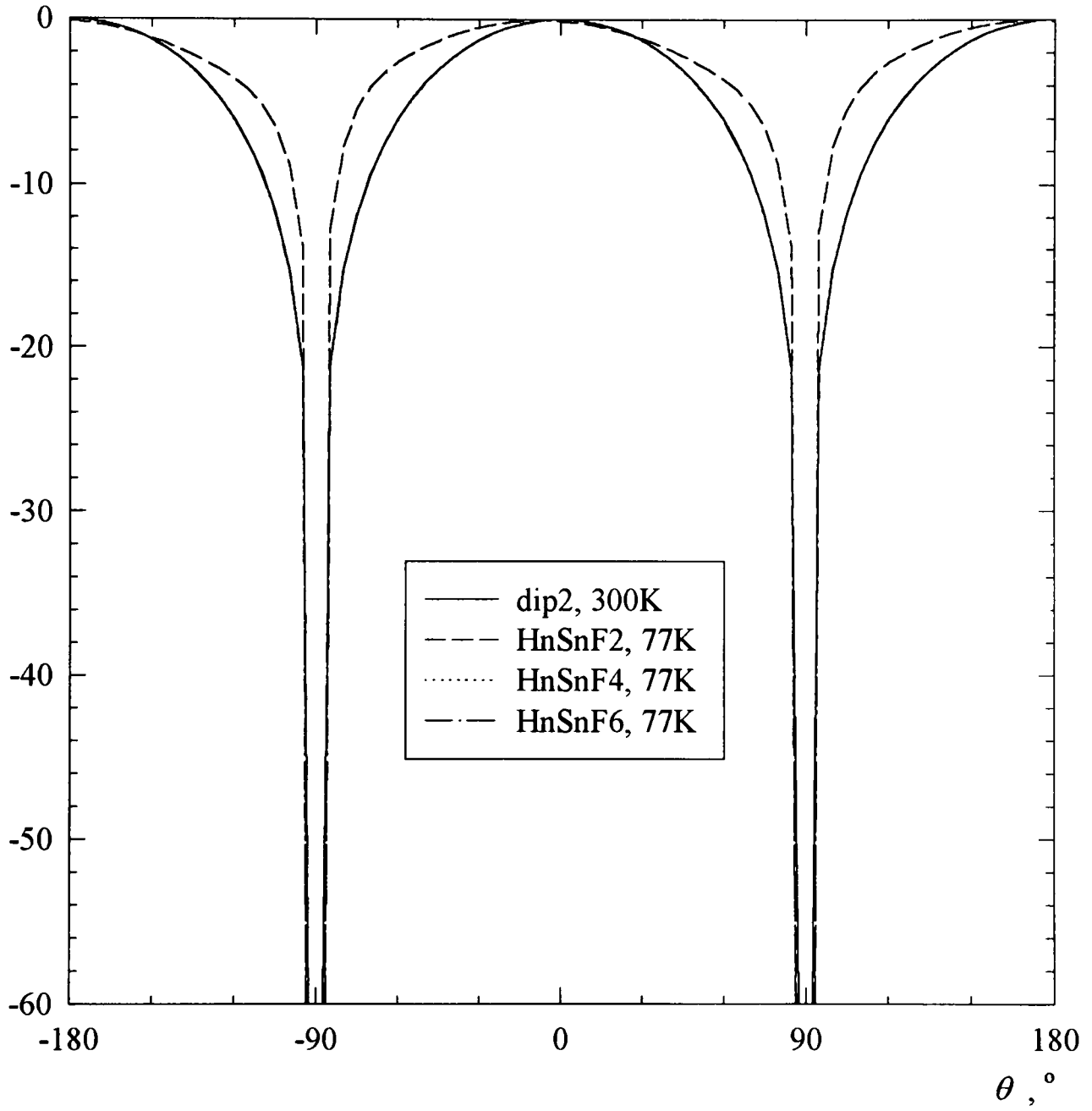

Fig. 8.52. Simulated co-polar horizontal radiation patterns of the dip2 and HnSnF antennas, normalised to the corresponding maximum.

The measured and numerically simulated observations from the far-field radiation patterns of the thick- and thin-film HTS meander antennas are tabulated in Tables 8.8 and 8.9, respectively. The corresponding observations of the copper versions are also given. Here, G_{0D} is the absolute gain obtained as the difference in the observed $|S_{12}|$ at maximum radiation of the frequency of operation in the horizontal plane. The corresponding efficiency η_D is obtained using eqn. (4.23) of Section 4.2.1. G_{0D} and η_D of the HTS antennas are evaluated relative to the corresponding copper meander structures, because direct comparison between similar structures can be made.

Table 8.8. Observations from the measured and simulated radiation patterns of the thick-film HTS symmetrical meander dipole, relative to the CuSkF2 antenna. HPBW values are also given.

	Measured			**Simulated**		
antenna	G_{0D} , dB	η_D	HPBW, °	G_{0D} , dB	η_D	HPBW, °
CuSkF2	0	1.0	78	0	1.0	88
HkSkF2	9.1	5.0	80	2.8	1.3	99

G_{0D} : gain; difference in $|S_{12}|$ maximums. η_D : efficiency, obtained using G_{0D} in eqn. (4.23).

Inconsistencies appear in the measured and corresponding simulated results because Sonnet was unable to predict the gain for the HTS antennas. However, the HTS antennas outperformed the corresponding copper structures in terms of gains and efficiencies. The HPBW of HkSkF2 is slightly wider than CuSkF2 by a factor of 0.025, indicating that its radiation pattern is only slightly less directive. Although there is no correlation in the measured HPBW of the CuSnF and HnSnF antennas with the number of meander sections, the values indicated that both antennas have almost similar directive patterns. The observation is in good agreement with the simulated HPBWs. It can be deduced that the HTS and the corresponding copper antennas have similar directive radiation patterns.

Table 8.9. Observations from the measured and simulated radiation patterns of the thin-film HTS symmetrical meander dipoles, relative to the CuSnF2 antenna. HPBW values are also given.

antenna	Measured			Simulated		
	G_{0D} , dB	η_D	HPBW, °	G_{0D} , dB	η_D	HPBW, °
CuSnF2	0	1.0	85	0	1.0	92
CuSnF4	-7.5	0.11	76	-3.6	0.3	88
CuSnF6	-8.5	0.08	75	-9.7	0.07	89
HnSnF2	4.8	2.0	92	3.8	1.6	108
HnSnF4	-0.5	0.59	88	-0.3	0.62	90
HnSnF6	-4.7	0.23	89	-4.6	0.23	90

G_{0D} : gain; difference in $|S_{12}|$ maximums. η_D : efficiency, obtained using G_{0D} in eqn. (4.23).

Even though the CuSnF antennas showed the worst performance in comparison with CuSkF and CuRkF antennas, the thin film versions are capable of producing more radiation with very little conductor loss associated with the YBCO material. Similar observation has been seen with the thick film HkSkF2 antenna, which performs better than the corresponding CuSkF2 antenna. The ablity of the HTS meander antennas to radiate more energy whilst having much less conductor loss has thus enhanced its efficiencies. This agrees well with the theoretical radiation efficiency of eqn. (2.12) discussed in Section 2.5.

The discussion proceeds to the behaviour of the frequency of operation of the HTS antennas in relation to the electrical size of the antenna. The performance of the antenna with respect to the physical size is similar. The relationship of the measured and simulated results are illustrated in Fig. 8.53. From Fig. 8.53, it can be seen that the HTS meander antennas are electrically small at their corresponding operating frequencies. These are in fact much smaller than the corresponding copper structures discussed earlier. The size decreases as the number of meander sections increases. Although the HTS antennas are smaller in size than the corresponding copper structures, the antennas exhibit better gain

and are more efficient, in consistent with Tables 8.8 and 8.9. On the other hand, the corresponding linear $\lambda/2$ receiving dipole is electrically large at its operating frequency for both the HTS antennas. The measured and simulated results are in good agreement with the exception of the measured HnSnF2. The inconsistency of the latter is probably due to the quality of the YBCO film slight degradation after the patterning and etching processes. The HTS meander dipoles operate quite close to the corresponding linear receiving $\lambda/2$ dipole which has the same radiating track length. This shows that the symmetrical meander structure maintains the frequency of operation. The discussion of the HnSnF antennas is also given in Appendix 5, but with simulated dip2 of 50.0 mm long and the measured dip2 was evaluated as a factor of 3 larger than the measured dip1.

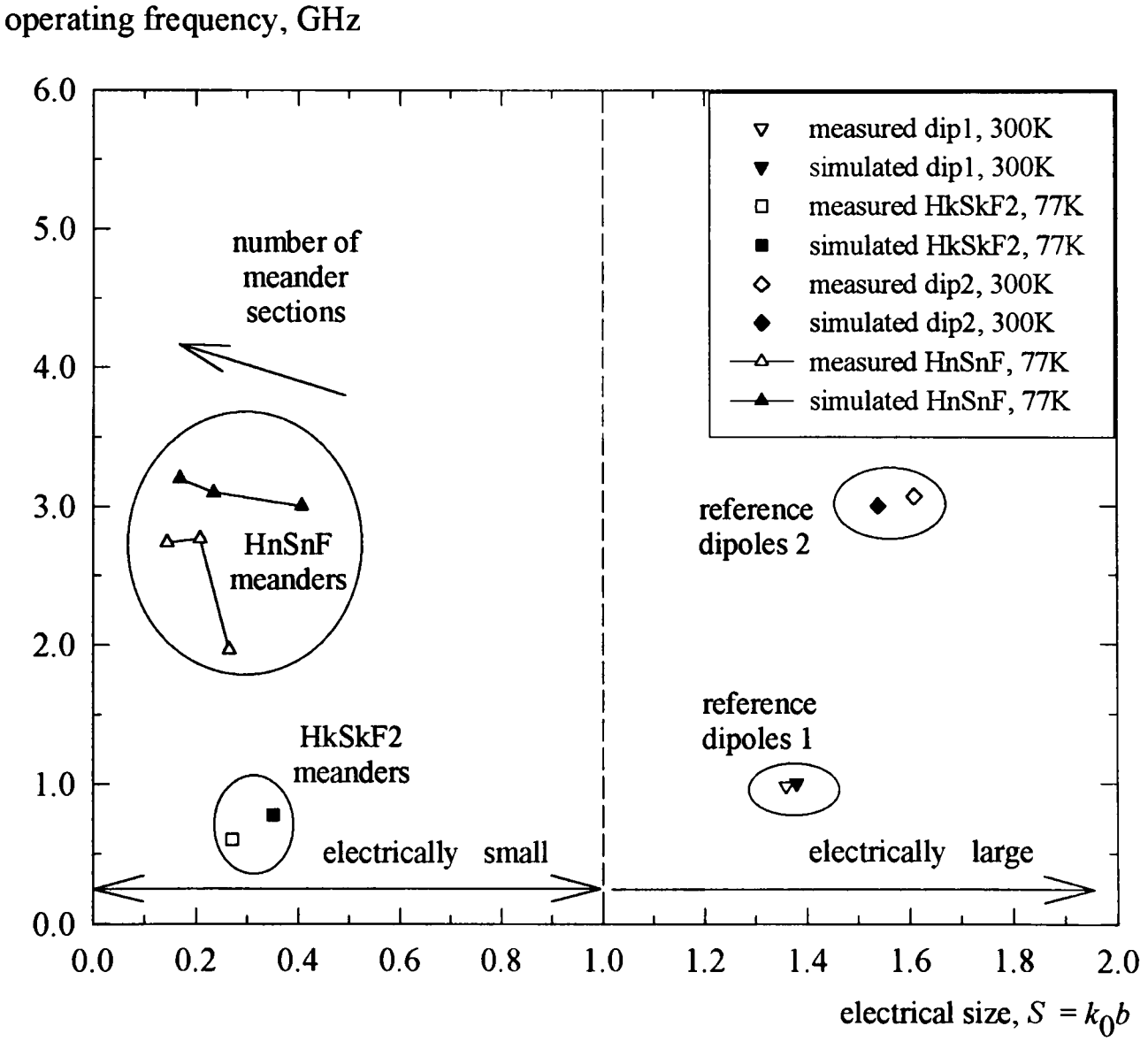

Fig. 8.53. Measured and simulated operating frequencies with respect to the antenna size.

The HTS antennas can also be accessed in terms of superdirective, s_d, and supergain, s_g, ratios. The ratios are obtained using eqns. (4.19) and (4.20) of Section 4.1.3. Tables 8.10 and 8.11 show the measured and simulated ratios of the thick- and thin-film HTS antennas, relative to the CuSkF2 and CuSnF2 antennas, respectively.

Table 8.10. Measured and simulated superdirective and supergain ratios of the thick-film HTS meander antenna, relative to the CuSkF2 antenna.

antenna	Measured		Simulated	
	s_d	s_g	s_d	s_g
CuSkF2	1	1	1	1
HkSkF2	8.85	44.3	1.54	2.0

s_d : superdirective ratio, obtained using eqn. (4.19). s_g : supergain ratio, obtained using eqn. (4.20).

Table 8.11. Measured and simulated superdirective and supergain ratios of the thin-film HTS meander antennas, relative to the CuSnF2 antenna.

antenna	Measured		Simulated	
	s_d	s_g	s_d	s_g
CuSnF2	1	1	1	1
CuSnF4	0.32	0.04	0.70	0.21
CuSnF6	0.33	0.03	0.26	0.02
HnSnF2	5.0	10.1	2.5	4.0
HnSnF4	1.94	1.15	1.8	1.12
HnSnF6	1.1	0.25	0.97	0.22

s_d : superdirective ratio, obtained using eqn. (4.19). s_g : supergain ratio, obtained using eqn. (4.20).

It can be inferred from Tables 8.10 and 8.11 that the HTS antennas exhibit far greater superdirective and supergain ratio than the corresponding copper structures. The

inconsistencies between the measured and numerically simulated results are due to the incorrect gain prediction by the Sonnet numerical software.

Similar to the CPS fed copper antennas, the simulated surface current distribution on all the HTS antennas showed an approximate half-wave sinusoidal variation along the track length of the antenna. The distributions are nulls at the radiating structure ends whilst they are peaks at the centre. The distributions are depicted in Fig. 8.54, in comparison with the corresponding reference dipoles.

The simulated surface current distribution on each HTS antenna is plotted against the corresponding normalised track length in Fig. 8.55. Similar to the discussion of the CPS fed antennas, each current distribution is compared to that of the corresponding linear $\lambda/2$ dipole. Here, each curve shows a near peak at the antenna feed and nulls at both ends of the radiating arms. However, all the curves of the HTS antennas appear to approach that of the linear $\lambda/2$ dipole. The current distribution curve is approximately sinusoidal. The HnSnF6 meander dipole also has the highest current distribution along its axial length. This is attributed to the higher capacitive coupling between adjacent meander sections.

The same curves are also normalised to their corresponding peak values, as illustrated in Fig. 8.56, for comparison with that of the cosine distribution for Fig. 8.55. The results are similar to the CPS fed antennas.

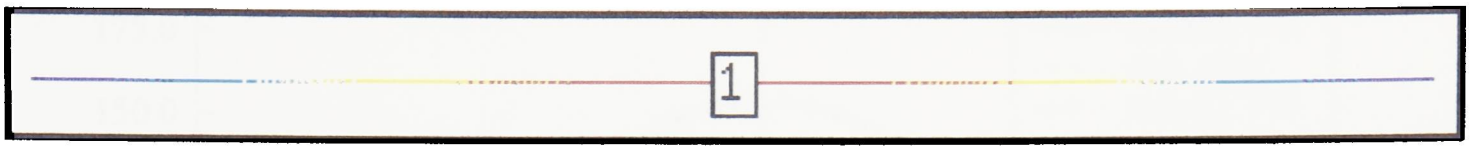

(a) half-wavelength reference dipole 1 (to scale)

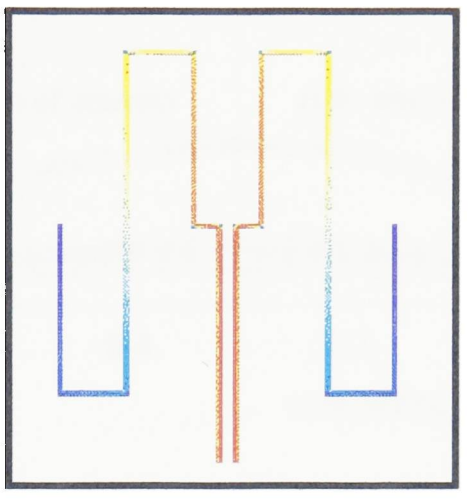

1 -1

(b) HkSkF2 (to scale)

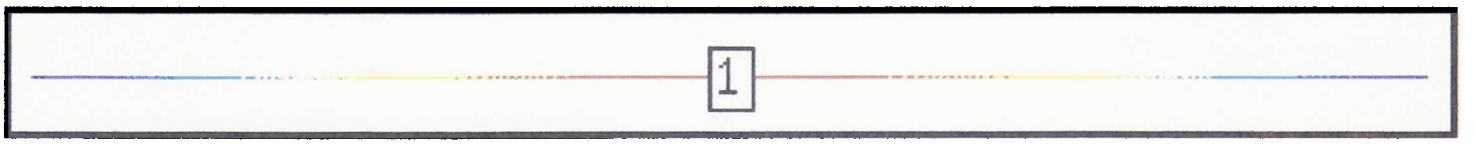

(c) half-wavelength reference dipole 2 (scale 3:1)

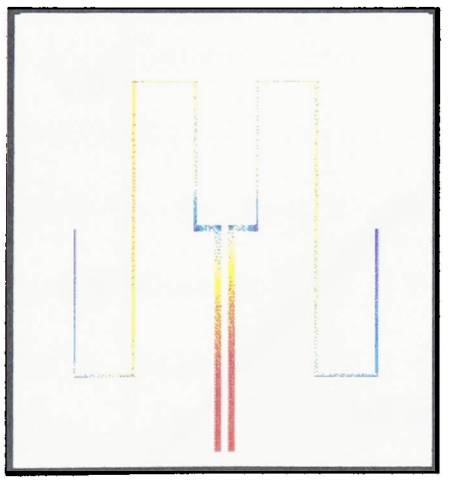

1 -1

(d) HnSnF2 (scale 3:1)

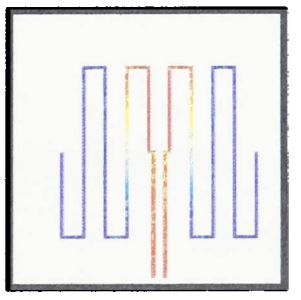

1 -1

(e) HnSnF4 (scale 3:1)

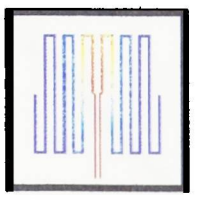

1 -1

(f) HnSnF6 (scale 3:1)

Fig. 8.54. Simulated current distribution along the arm of the HTS meander antennas, in comparison with the corresponding reference linear $\lambda/2$ dipoles.

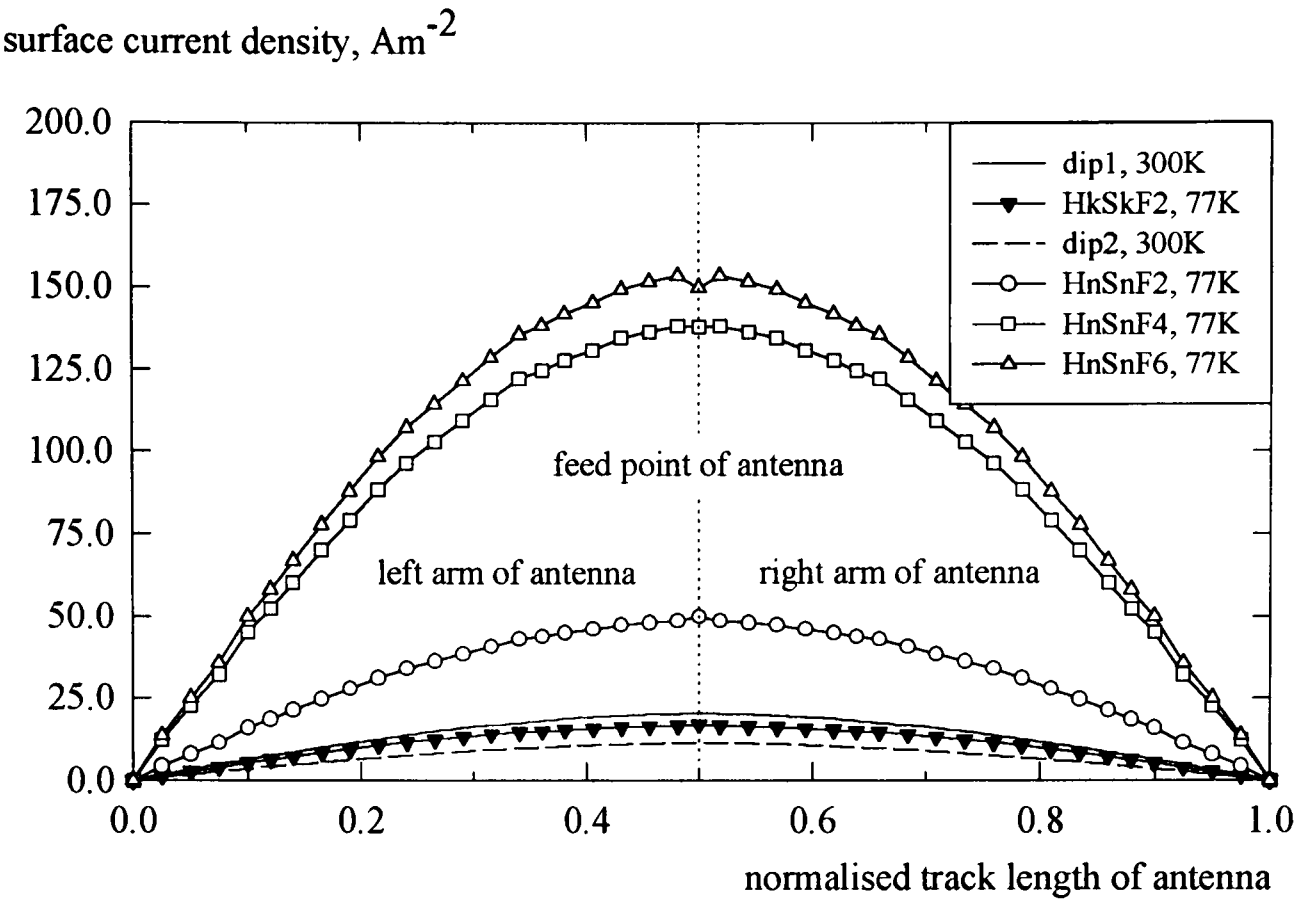

Fig. 8.55. Current distribution along the track length of the HTS and dip antennas, versus the corresponding normalised track length of antenna.

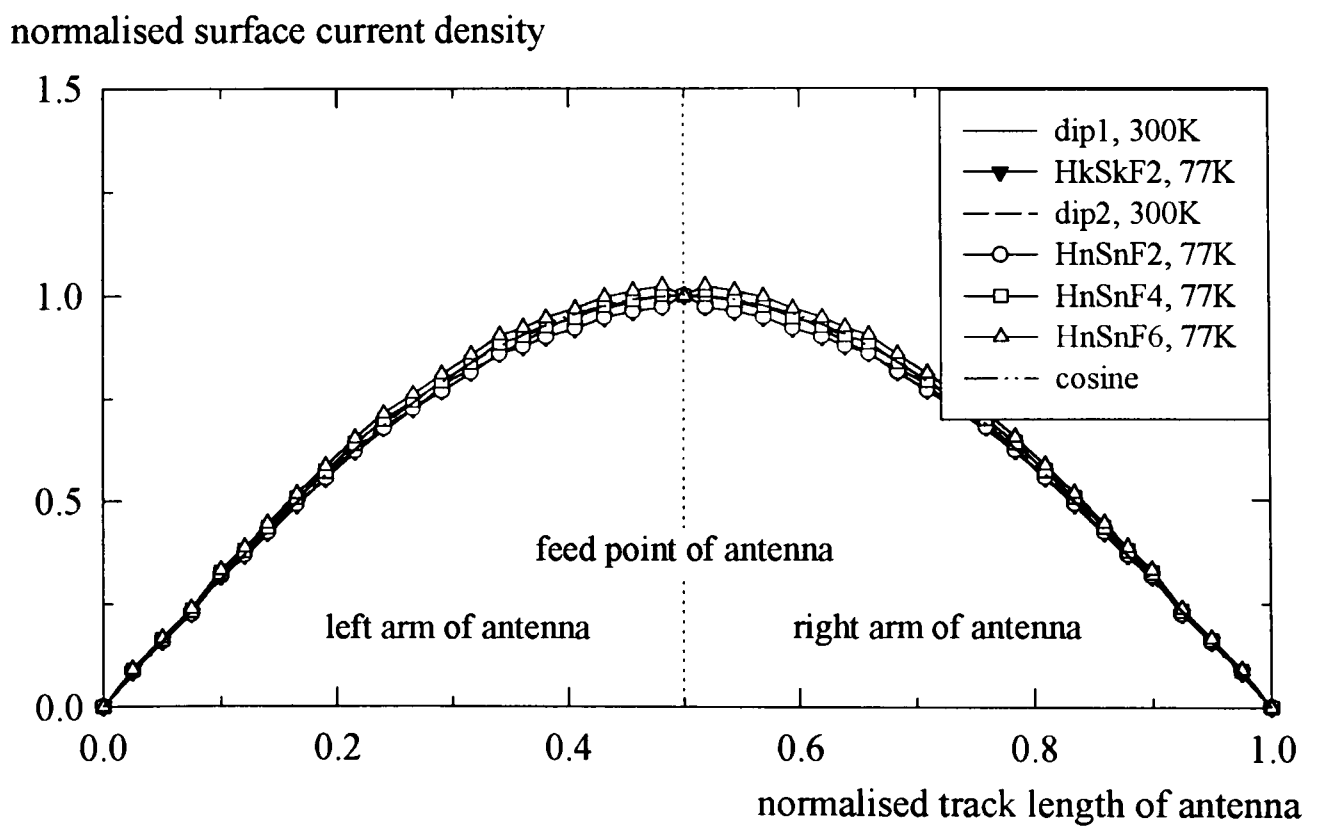

Fig. 8.56. Normalised current distribution along the track length of the HTS and dip antennas, versus the corresponding normalised track length of antenna.

8.2.3 Summary of The Comparison Between The Meander Dipole Structures

From the discussion of the measured and numerically simulated copper anti-symmetrical meander structures of Section 8.2.1, the frequency of operation increases with increasing number of meander sections, whilst the gain and efficiency decreases. The increase in the number of meander sections is proportional to the decrease and increase in the physical and electrical size of the antenna, respectively. As the antenna physically shrinks in size, the frequency of operation approaches that of a short dipole. This in turn increases the electrical size. The far-field radiation patterns show that the anti-symmetrical meander dipole antennas resembles that of the short dipole and having similar beamwidths of 90°. In comparison with the 1 GHz linear $\lambda/2$ reference dipole, the antennas are inefficient due to its small size. In addition, the numerically simulated surface current distribution shows that the variation along the track length and the axial length of the antenna are approximately half-wavelength sinusoidal.

The study proceeds to the design of symmetrical meander structures, initially with copper structures having direct SMA feeds from underneath the circuit, through the substrate. From the discussion of the measured and numerically simulated observations, it was found that all the antennas have almost the same frequency of operation with that of a linear $\lambda/2$ reference dipole. However, the corresponding measured return losses are large and distortion in the measured far-field radiation patterns was observed. The distortion was suspected to be caused by such feeding because all the antennas are physically and electrically small at their operating frequencies. When the experiment was repeated using $\lambda/4$ sleeve balun, it was possible to reduce the return losses and hence the reflection bandwidth can be deduced.

The design proceeds to that having 50 ohm coplanar strip feed lines. The balun was also incorporated in the measurements. Although there are disagreement in the corresponding measured and numerically simulated results, similar constant frequency behaviour was observed. However, reduction in the measured return losses and no

distortion in the measured far-field radiation patterns are observed. Due to the difference in the matching of all the antennas, no correlation between the reflection bandwidth and Q_L with the decreasing number of meander sections can be deduced. Of the three sets of antennas, CuSnF antennas which have the smallest physical and electrical size, exhibit the least gain and efficiency. This is also attributed to the thinnest radiating track width which contributes to the least radiation.

However, with the use of HTS materials in the antenna fabrication, the performance of the antenna is enhanced in terms of gain and efficiency. This was observed with the measured and numerically simulated thick and thin film HTS structures, although they have smaller physical and electrical size. Although discrepancies were observed in the corresponding measured and numerically simulated results, the variation with decreasing number of meander sections are similar. In addition, the far-field radiation patterns are of figure-of-eight shapes with slightly less directive radiation than the corresponding copper structures. The numerically simulated surface current distribution along the track length of the HTS antennas also showed an approximate half-wavelength sinusoidal variation.

CHAPTER 9

CONCLUSION AND FUTURE WORK

9.0 INTRODUCTION

In this chapter, conclusions are drawn. In addition, recommendations for future work are also given.

9.1 CONCLUSION

In this study, two sets of meander antennas have been designed and tested. Numerical simulations have been carried out for comparison with the corresponding experimental results. The first set of antenna is the copper anti-symmetrical meander dipole antennas which demonstrated low gains and are inefficient. This agrees well with the inherent property of small antennas. The gain and efficiency decrease with the number of meander sections. The increase in the number of meander sections is inversely proportional to the physical size of the antenna. The antennas are electrically small, however, as the physical size decreases, the frequency of operation also decreases resulting in an electrical size increase. In addition, the radiation patterns resemble that of a resonant short dipole. No matching network has been designed because the antennas are reasonably well-matched to the input. The numerically simulated surface current distribution along the track length and axial length of the antenna shows an approximate half-wavelength sinusoidal variation.

Due to the low gain and efficiency of the first set of antennas, a second set was designed and tested. This consists of three different sets of copper symmetrical meander dipoles which differ in terms of aspect ratio and track width. In addition, a thick-film and a set of thin-film HTS antennas were also fabricated and tested. For the symmetrical meander dipole antennas, the physical and electrical size are directly proportional. This is attributed to the constant frequency of operation. Initially, all the copper symmetrical meander

antennas were fed from underneath the circuit, through the substrate. However, this causes pattern distortion due to the feeding cable, even though all the antennas operate at almost the same frequency. Furthermore, the return losses was high. No pattern distortion or high return loss were observed from the numerical simulations. Nevertheless, when a quarter-wavelength sleeve balun is incorporated in the measurements, this helps in the matching of the antennas to the input.

Similar meander structures were fabricated, but with a coplanar strip feeding line. The antennas were tested with the incorporation of the balun. It was found that the CuSnF copper antennas which have the smallest size and narrowest track width, exhibit the least gain and efficiency. This agrees well with the inherent property of small antennas. The only thick-film HTS antenna designed has an aspect ratio of 1.0 and track width of 0.5 mm. It demonstrated superior performance than the corresponding copper structure, although it operates at a lower frequency. This was partly due to the relative permittivities of the liquid nitrogen and the YSZ substrate. The latter was a factor of about 3.0 greater than the RT/duroid substrate used for the copper antennas. The thin-film HTS structures have been shown to perform better, although having smaller electrical size than the corresponding copper structures. In addition, all the copper and HTS symmetrical meander antennas showed an approximate half-wavelength sinusoidal current distribution along the track length. All the antennas possess similar bi-directional far-field radiation patterns. However, the HTS structures showed slightly less directive radiation patterns. However, Sonnet was unable to predict the gain of the HTS structures.

The thin film HTS antennas demonstrated the suitability for space-limited applications in the plane parallel to the radiating structure. No other similar printed coplanar meander antennas has been reported to date. With the recent advances in telecommunication, such structures find numerous applications. The designed symmetrical meander dipole is particularly useful for the low frequency applications such as at 100 MHz, where a standard linear dipole will become excessively large. In addition, it is also useful in an array configuration which will perform more efficiently with higher gains. The array can, for example, be placed onto the surface of satellites, aircrafts, spacecrafts, and mobile

communication base stations. In addition, the antenna may be mounted on a ship or spacecraft and used in military defence applications. However, one has to ensure that the spacing between the elements in the array does not introduce problems such as high side-lobe levels [3]. The array configuration may also be designed multi-channel applications. Nevertheless, there is still a problem with the cooling system [48], [50], [62] which will only make the whole system physically large and heavy. In addition, the cooling system also need power and this may not be cost-effective in some applications.

9.2 FUTURE WORK

The potential of realising high performance electrically small high-temperature superconducting antennas is excellent. Recommendations for further developments are:

- reducing the feeding loss with the use of K-connectors, where very narrow centre-pins can be employed,
- further reducing the feeding loss by integrating a printed balun (such as a coplanar hybrid ring) in the antenna structure, which also serves as a matching network,
- further investigation of existing symmetrical meander dipole designs as potential elements in a thin-film high-temperature superconducting antenna array -- the electromagnetic coupling feed using a 50 ohm CPS feed line from underneath the antenna is recommended (Fig. 9.1). This feeding will exclude the existence of a feeding hole completely. The matching network (if designed) may be employed in the feeding structure or it could be integrated into the radiating structure itself.

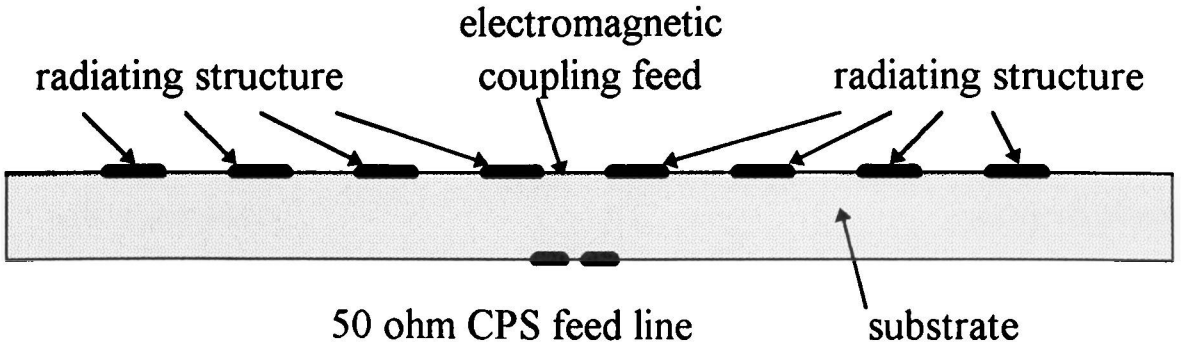

Fig. 9.1. Cross sectional view of a symmetrical meander dipole with CPS electromagnetic-coupling feed.

- further investigation of existing symmetrical meander dipole designs as potential elements in a thin-film high-temperature superconducting microstrip antenna array -- the feeding technique of a single arm may be emphasised and will involve three stages :

  1. In the first stage, microstrip radiating structure of only one arm of the meander dipole has to be fabricated and a direct feed has to be made from underneath the substrate using K-connector (Fig. 9.2). It is expected that the radiation pattern will be normal to the radiating structure plane, instead of bi-directional as with two meander arms. The configuration is similar to that of Chaloupka [68] but with a different feeding technique.

  2. In the next two stages, the antenna will consist of three layers of conducting material, sandwiched by two layers of substrates. The top conducting layer is the radiating structure, the middle conducting layer is the ground plane for the microstrip circuitry and the bottom conducting layer is for the microstrip 50 ohm feeding line with matching network (for connection to the antenna input at one end and to the radiating structure at the other end, through the two substrates). These two stages differ by the feeding technique from the feeding line to the radiating structure through the hole across the layers, that is, (a) direct feed using wire ((Fig. 9.3(a)) and (b) electromagnetic coupling ((Fig. 9.3(b)). These feeding techniques are aimed for preventing spurious radiation from the feeding network and eliminating unwanted coupling between the feed network and the radiating elements. The proposed electromagnetically coupled feeding technique has an added advantage of having no physical connection at all.

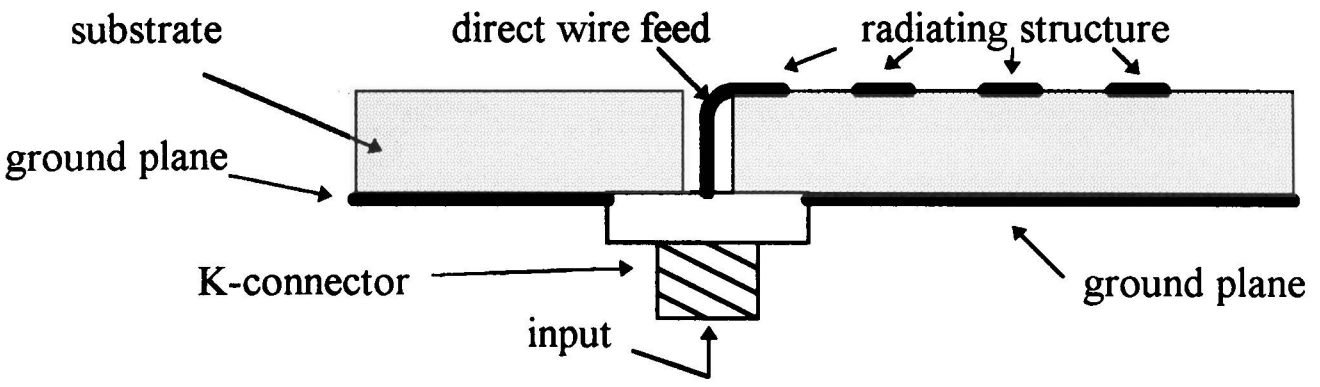

Fig. 9.2. Cross sectional view of a single arm microstrip meander dipole with direct feed. The radiating structure is similar to that of Chaloupka [68] but with a different feeding technique.

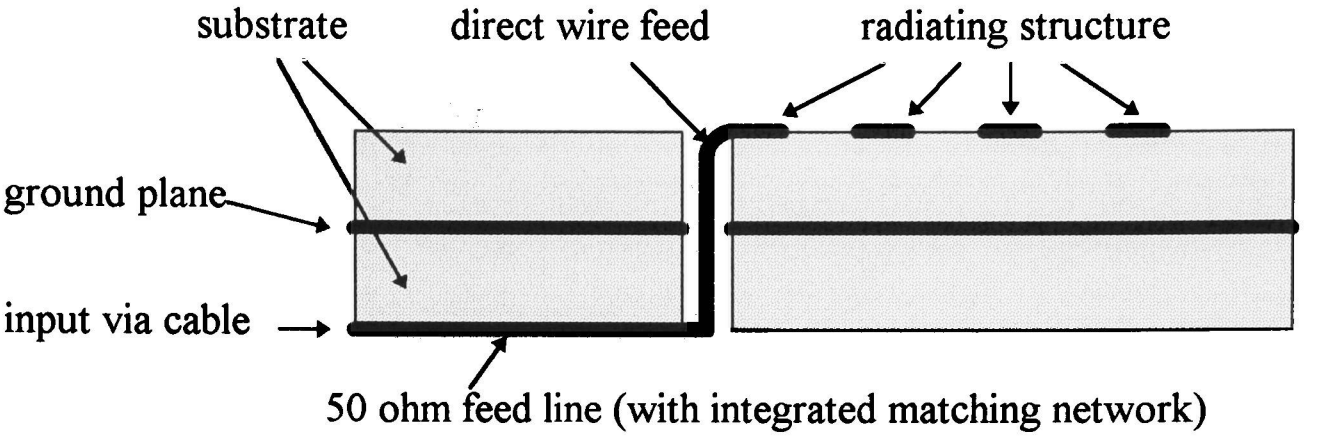

(a)

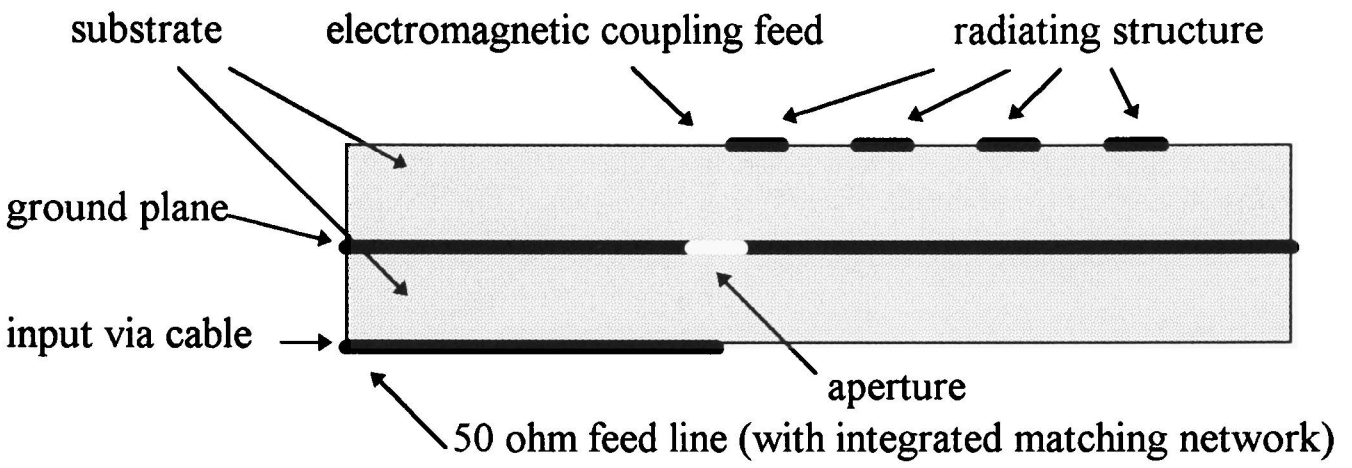

(b)

Fig. 9.3. Cross sectional view of a single arm microstrip meander dipole on two substrates: (a) direct feed using wire, (b) electromagnetic coupling feed.

- investigating other coplanar meander radiating structures such as the meander/triangle shape and the variant of meander/triangle shape. The structures are shown in Figs. 9.4 (a) and (b), respectively. Such structures are similar to a Brown-Woodward (bow-tie) [3], therefore, they will have wide bandwidths.

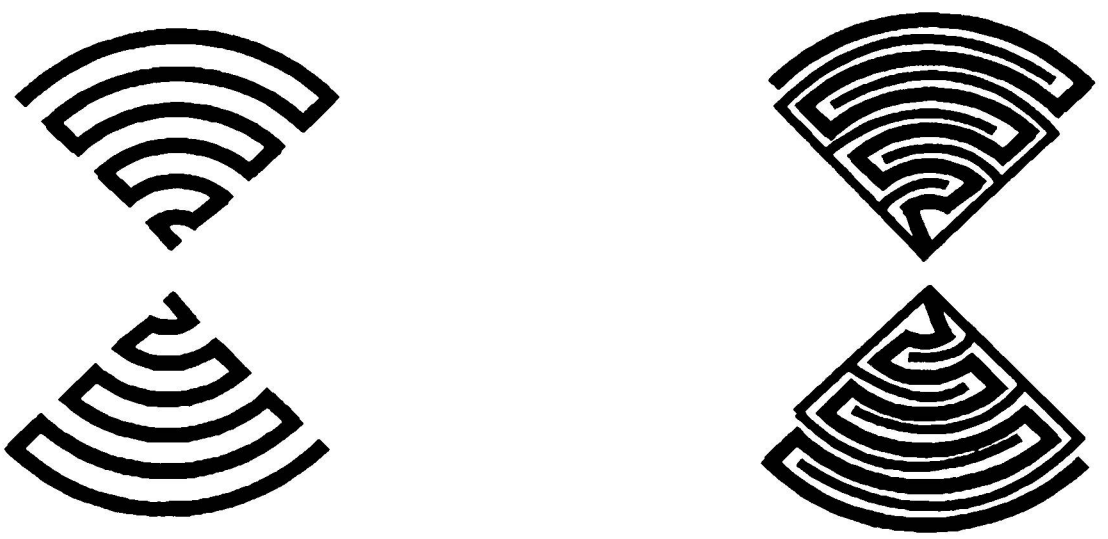

(a) (b)

Fig. 9.4. (a) Meander/triangle shape, (b) variant of meander/triangle shape.

APPENDICES

APPENDIX 1

Design Equations for Coplanar Strips

From eqn. (2.93) of Section 2.8.4,

$$\varepsilon_{eff} = 1.0 + \left(\frac{\varepsilon_r - 1.0}{2.0} \quad \frac{K(m')}{K(m)} \quad \frac{K(m_1)}{K(m_1')} \right) \tag{A1.1}$$

the terms m , m', m_1 and m_1' are defined as follows :

$$m = s / (s+2.0w) \tag{A1.2}$$

$$m' = (1.0 - m^2)^{1/2} \tag{A1.3}$$

$$m_1 = \frac{\sinh(\pi s/4h)}{\sinh(\pi (s + 2w)/4h)} \tag{A1.4}$$

$$m_1' = (1.0 - m_1^2)^{1/2} \tag{A1.5}$$

The complete elliptic integrals of the first kind are $K(m')$, $K(m)$, $K(m_1)$ and $K(m_1')$; where

$$K'(m) = K(m') \text{ and } K'(m_1) = K(m_1') \tag{A1.6}$$

The ratios of complete elliptic integrals of the first kind, namely $K(m) / K(m')$ and $K(m_1) / K(m_1')$, can be found using simple functions but to a very good accuracy. For $1.0 \leq K(m) / K(m') \leq \infty$ and $1.0/ (2.0)^{1/2} \leq m \leq 1.0$:

$$\frac{K(m)}{K(m')} \approx \frac{1.0}{2.0\pi} \ln\left(2.0 \frac{(1.0 + m)^{1/2} + (4.0m)^{1/4}}{(1.0 + m)^{1/2} - (4.0m)^{1/4}} \right) \tag{A1.7}$$

whilst for $0.0 \leq K(m) / K(m') \leq 1.0$ and $0.0 \leq m \leq 1.0/ (2.0)^{1/2}$:

$$\frac{K(m)}{K(m')} \approx \frac{2.0\pi}{\ln\left(2.0 \frac{(1.0 + m)^{1/2} + (4.0m)^{1/4}}{(1.0 + m)^{1/2} - (4.0m)^{1/4}} \right)} \tag{A1.8}$$

Eqns. (A1.7) and (A1.8) can be also used to find the ratio $K(m_1) / K(m_1')$ by substituting m_1 for m and m_1' for m'.

As for both the coplanar strips characteristic impedance and substrate effective permittivity corrected for the strip thickness, eqns. (2.95) and (2.96) of Section 2.8.4 are rewritten here for convenience as

$$\varepsilon_{effi} = \varepsilon_{eff1} - \left(\frac{\varepsilon_{eff1} - 1.0}{[(w / 0.7t)\,[K(m) / K'(m)]] + 1.0} \right) \tag{A1.9}$$

and, $$Z_{st} = 30.0\pi\ \varepsilon_{eff1}^{-1/2}\,[K(m_t') / K(m_t)] \tag{A1.10}$$

The ratio $K(m_t') / K(m_t)$ can be found as the inverse of eqns. (A1.7) and (A1.8), by substituting m_t for m and m_t' for m'. Here, the terms m_t and m_t' are given as

$$m_t = s_t / (s + 2.0w)_t \tag{A1.11}$$

$$m_t' = (1.0 - m_t^2)^{1/2} \tag{A1.12}$$

where $$s_t = s + \frac{1.25t}{\pi}\left[1.0 + \ln\left(\frac{4.0\pi s}{t}\right)\right] \tag{A1.13}$$

and $$(s + 2.0w)_t = (s + 2.0w) - \frac{1.25t}{\pi}\left[1.0 + \ln\left(\frac{4.0\pi s}{t}\right)\right] \tag{A1.14}$$

The term ε_{eff1} can be calculated using eqn. (A1.1) above, but with s_t and $(s + 2.0w)_t$ substituted for s and $(s + 2.0w)$, respectively.

APPENDIX 2

Formulation of the Thick-Film YBCO Surface Resistance

From eqn. (3.27) of Section 3.2,

$$R_s = \frac{\omega \mu_0^{\,2} \sigma_1 \lambda_L^{\,3}(T)}{2} = 4 \pi^2 f^2 \mu_0^{\,2} \lambda^3(T) \sigma_1 / 2 \qquad \text{(A2.1)}$$

By definition, $R_{s\,(YBCO)} = R_{s\,(Cu)}$ at the cross-over frequency $f_{c/o}$, that is,

$$R_{s\,[\,f_{c/o}\,,\,YBCO\,]} = R_{s\,[\,f_{c/o}\,,\,Cu\,]} = 4 \pi^2 f_{c/o}^{\,2} \mu_0^{\,2} \lambda^3(T) \qquad \text{(A2.2)}$$

we get,
$$\sigma_{1\,[\,Cu\,,\,77K\,]} = \frac{2}{\delta^2_{[Cu,\ 77K]}\ \omega\ \mu_0} \qquad \text{(A2.3)}$$

where,
$$\delta_{[\,f_{c/o}\,=\,10.0GHz,\,Cu\,,\,77K\,]} = 0.43\mu m\ [41] \qquad \text{(A2.4)}$$

Substituting eqn. (A2.4) into eqn. (A2.3) gives

$$\sigma_{1\,[\,Cu\,,\,77K\,]} = 136.994 \times 10^6 \qquad \text{(A2.5)}$$

Substituting eqn. (A2.5) into eqn. (2.34) of Section 2.8.1 gives the value of R_s for copper at 77K as a function of frequency as

$$R_{s\,[\,Cu\,,\,77K\,]} \approx (1.7 \times 10^{-9})\, f^{1/2} \qquad \text{(A2.6)}$$

Hence, its value at the cross-over frequency can be given by

$$R_{s\,[\,f_{c/o}\,,\,Cu\,,\,77K\,]} \approx (1.7 \times 10^{-9})\ f_{c/o}^{\,1/2} \qquad \text{(A2.7)}$$

Dividing eqn. (A2.1) by eqn. (A2.7) gives

$$R_{s\,[\,f\,,\,YBCO\,,\,77K\,]} = (R_{s\,[\,f_{c/o}\,,\,Cu\,,\,77K\,]})\ \frac{f^2}{f_{c/o}^{\,2}} \qquad \text{(A2.8)}$$

Finally, substituting eqn. (A2.7) into (A2.8) gives

$$R_{s\,[\,f\,,\,YBCO\,,\,77K\,]} \approx (1.7 \times 10^{-9})\ \frac{f^2}{f_{c/o}^{\,3/2}}\ m\Omega \qquad \text{(A2.9)}$$

or simply,

$$R_{s\,[\,f\,,\,YBCO\,,\,77K\,]} \approx (5.4 \times 10^{-3})\ \frac{f^2}{f_{c/o}^{\,3/2}}\ m\Omega \qquad \text{(A2.10)}$$

where both f and $f_{c/o}$ are in GHz. Note that eqns. (A2.10) and (3.31) of Section 3.2 are the same.

APPENDIX 6

Control File for Pattern Generation on SONNET

This program is the control file for the generation of the far-field radiation pattern of an antenna. It is used by the command *patgen*. The earth co-ordinates is used to generate all the numerically simulated radiation patterns in this study. An example of the pattern is illustrated in Fig. 6.4 of Chapter 6. ANG1 is the variable angle θ in the co-polarisation E-plane radiation pattern. Only the pattern on the upper hemisphere of the co-ordinates can be generated. However, since all the designed antennas have bi-directional radiation patterns, the pattern on the lower hemisphere is assumed to be similar to that on the upper hemisphere. ANG2 refers to the angle ϕ of the pattern. In this study, all the numerically simulated pattern figures are generated by incorporating the simulated pattern data into a commercial spreadsheet software. These are Figs. 8.12, 8.31, 8.37, 8.49 and 8.52. The software generates cartesian plots which are similar to that obtained from the radiation pattern experiments.

```
CTLPG          # Identifies this file - Must be first line
VER 3.0        # Identifies Version - Must be second line
               #
COORD Earth    # Identifies Co-ordinate System - Must be before angles
               #   Sphere = Spherical Co-ordinates
               #   Top    = Top View Co-ordinates
               #   Earth  = Earth View Co-ordinates
               #   Array  = Array Co-ordinates (Van Aulock)
               #
ANG1  -90 90 5 # Angle 1: Theta from -90 to 90 in steps of 2 degrees
               #   May specify one angle:          ANG1 0
               #   or specify two angles:          ANG1 0 90
               #   or specify start, stop, step:   ANG1 0 90 2
               #
               #   CO-ORDINATES    ANGLE1    VALID RANGE
               #   Spherical         Theta       0...180
               #   Earth View        Theta       -90...90
               #   Top View          Alpha       -90...90
               #   Array             u           -1...1
               #
ANG2  -90 90 15# Angle 2: Phi at -90 and 90 degrees
               #   May specify one angle:          ANG2 0
               #   or specify two angles:          ANG2 0 90
               #   or specify start, stop, step:   ANG2 0 90 2
               #
               #   CO-ORDINATES    ANGLE2 VALID RANGE
               #   Spherical         Phi       -180...180
               #   Earth View        Phi       -90...90
               #   Top View          Beta      -90...90
               #   Array             v         -1...1
               #
GHZ            # Specifies units for the following FRE lines
               #   Valid Units: GHz, MHz (default)
```

```
FRE 1.0          # Use all frequencies in the .jxy file (ignores GHZ,MHZ)
                 #   May specify one frequency:      FRE 1
                 #   or specify two frequencies:     FRE 1 10
                 #   or specify start, stop, step:   FRE 1 10 2
                 #   Multiple FRE lines are allowed
                   #
PORT ALL MAG=1 PHASE=0     # Must specify the voltage and phase for each port
                       #   Only one PORT ALL line is allowed
                       #   Only one PORT line for each port: PORT 1 R=5
                       #   May specify any of the following in any order:
                       #   Magnitude (volts)       MAG=1
                       #   Phase (degrees):        PHASE=0
                       #   Resistance (ohms):      R=50
                       #   Reactance (ohms):       X=0
                       #   Inductance (nH):        L=0
                       #   Capacitance (pF):       C=0
```

APPENDIX 8

Properties of Dielectric Substrates Used for Growth of HTS Films [84]

Substrate	*Crystal Structure*	*Growth Surface*	a_0 (Å)*	ε_r (300K)	10^5 x tan δ
M_gO	Cubic	(100)	4.213	10	1.6 (300K, 10 GHz) 0.62 (77K, 10 GHz) 0.61 (20K, 10 GHz)
$SrTiO_3$	Cubic	(100)	3.790	300	30 (300K, 3.2 GHz)
$LaAlO_3$	Rhombohedral	$(110)^+$	3.793	24	2.1 (300K, 10 GHz)
	[Hexagonal]	$[(1\bar{1}02)]$			0.76 (77K, 10 GHz) 0.49 (20K, 10 GHz)
$NdGaO_3$	Orthorhombic	(110)	3.837	23	11.0 (300K, 10 GHz) 32.4 (77K, 10 GHz) 23.2 (20K, 10 GHz)
$LaGaO_3$	Orthorhombic	(110)	3.894	25	180 (300K, 1 MHz)
$YAlO_3$	Orthorhombic	(110)	3.662	16	8.2 (300K, 10 GHz) 1.2 (77K, 10 GHz) 0.49 (20K, 10 GHz)
$NdCaAlO_4$	Tetragonal	(001)	3.69	20	40-250 (5-300K, 200-600 GHz)
$LaSrAlO_4$	Tetragonal	(001)	3.77	27	10 (5K, 8 GHz)
$CaYAlO_4$	Tetragonal	(001)	3.648	20	4 (77K, 5 GHz)
YSZ:	Cubic	(100)	$\sqrt{2}$ x3.635	29	175 (300K, 10 GHz) 74.2 (77K, 10 GHz) 44.5 (20K, 10 GHz)
Al_2O_3	Rhombohedral	(110)	3.48	$9.3^{\diamond}$	0.0038 (80K, 10 GHz)
	[Hexagonal]	$[(1\bar{1}02)]$		11.6^{Δ}	

*Lattice constant for match to HTS films in the cubic or pseudocubic representation.

+Due to twinning, the pseudocubic (100)surface of LaAlO contains regions with four rhombohedral orientations :
(110), $(1\bar{1}0)$, $(\bar{1}10)$ and $(\bar{1}\bar{1}0)$.

: The lattice match to YSZ is rotated 45° with respect to the (100)direction in the surface. While the cubic lattice constant is 5.14, the lattice matches to a repeat distance of 3.635Å.

$^{\diamond}\varepsilon_r \perp$ c.

$^{\Delta}\varepsilon_r \parallel$ c.

APPENDIX 9

Procedure for Patterning YBCO Thin-film on MgO

1. **Cleaning**

   (a) Acetone (2 min. ultrasonic agitation). Make sure that the sample is covered completely. Immediately after taking sample out of the beaker, rinse the sample with IPA from a plastic bottle (blow dry). Make sure that tweezers are dry. Test/adjust air pressure before use as it may be very high.

   (b) Methanol (2 min. ultrasonic agitation). Make sure that the sample is covered completely. Immediately after taking sample out of the beaker, rinse the sample with IPA from a plastic bottle (blow dry).

2. **Spin Photoresist.**

   Give the sample a 'test spin' to adjust the parameters; especially spinning speed (5900 rpm). Cover the whole sample with HOECHST AZ1518 photoresist (~2 drops from pipette; pipette should be cleaned and fresh photoresist should be used after 30 mins. Dry pipette thoroughly before putting in the photoresist as photoresist is dissolved by acetone.) Spin immediately at 5900 rpm for 30 sec.

3. **Bake photoresist.**

   10 min. at 80^0C on hot plate. Then, leave sample for ~3mins. to cool it down (e.g., on a metal surface).

4. **Expose Photoresist.**

   Switch on the UV light source. The control of the UV light is on the left. Power ON and press the START switch. The UV needs about 5-10 mins. to warm up properly. If the UV light source was warmed up before, the START switch will not react immediately - just wait for a minute and try again. Make sure that the photo emulsion of the glass mask faces towards the sample. This means that the green dot on the mask is facing towards you.
   Slide the mask in the appropriate slot and then move it backwards. Position the sample on the vacuum platform. Put the sample on a thin white foil of plastic to increase the contrast between the sample, mask and vacuum platform.
   Pull the mask gently above the sample. Be very careful not to scratch it. Align the sample with the mask. Use mainly your eyes. Suck the sample - both the switches of the control panel should be in the upward position. Adjust the distance between the sample and mask, under the microscope. The microscope is enabled when the two green dots shine down on the mask. Lift the vacuum platform up to the point where fringing lines start to appear. The vacuum platform is lifted by moving the bar with the big black knob to the right.
   Set the exposing time to 7sec. by turning the red 'fire button' on the control panel. Adjust the microscope so that the eye pieces are disabled. A bright green light will shine

down on the entire mask. Press the red 'fire button'. Do not look direct into the UV light.
After the exposure, move the big black knob to the left (its original position). Switch off the suction (both switches of the control panel on the right in downward position). Slide back the mask and remove the sample from the vacuum platform. Take the mask carefully out of the slot and put it back in its box.
Never touch a mask in the middle, only on the edges. Never try to clean a mask with any liquids. Only blow it clean with air. At this stage, photoresist is still light sensitive. Do not remove the sample from the clean room.

5. **Develop Photoresist.**

   Mixture: 1:1 DI H_2O: AZ 312 MIF Developer (HOECHST)
   Take new developer for each single sample. Immerse fully the sample in the developer solution. Leave it unmoved for the first 10 secs. then start to agitate gently. The typical total developing time is 55 sec. Then, rinse the sample in DI H_2O. After rinsing, check that the sample has a nice straight and clean pattern.

6. **Etch YBCO.**

   Mixture: Dissolve 5 spatulas of EDTA in 100ml DI H_2O; filter the saturated (milky) EDTA solution with pH ~2.9. Mix 20 ml of this filtered solution with 200ml DI H_2O to pH<3.8. Adjust pH value between 3.6 and 3.8. Note that if DI H_2O is added to the etching solution, it will become weaker and the pH value will rise.
   Etch for typically 15 mins. with maximal agitation (magnetic stirrer full power). The sample is completely etched when the substrate appears to be bright and shiny. Remove and rinse the sample in DI H_2O.
   It is not recommended to take the sample out of the EDTA solution to check whether it is already completely etched. The exposure to air and/or water will change the etching process. When the sample is completely etched, take a second look under the microscope.

7. **Remove Photoresist.**

   Repeat cleaning procedure 1. Have a final look of the sample under the microscope.

General Comments.

Keep separate the tweezers and beakers for all the chemicals. Keep all the chemicals separate and clearly labelled. Be especially careful not to get any acetone near the photoresist. Wash all beakers by flushing them with the chemical they are used to contain, except the container used for the developer and EDTA which can be cleaned by flushing them with DI H_2O .

APPENDIX 10

Procedure for Applying Silver Contacts on HTS Thin-film Devices in the Evaporator

1. Check that all the valves are closed and all switches are off. Turn on the cooling tap water and switch on the mains power to the evaporator.
2. Switch on the rotary pump (green button) and the pirani gauge (switch). Open fine valve (leave all others closed). When pirani reads $<3x10^{-1}$ Torr, switch on the diffusion pump (red switch). Close the fine valve. The diffusion pump takes 20 mins. to warm up.
3. Open air admittance valve slowly. The pressure inside the chamber comes up to atmosphere. Remove the bell jar. Connect the heater basket across a pair of terminals (there are four choices, select one from a knob on the front panel). Load the basket with cleaned silver wire (with acetone liquid) of 6x1 cm lengths of 1mm diameter wire.
4. Attach the HTS sample onto a glass plate using double-sided sticky tape. Mask the areas not to be covered with silver using thin aluminium foil. Clamp the glass plate into the bracket and hang it face-down from the top of the apparatus. If necessary, grease the vacuum seal and replace the bell jar and safety screen.
5. Close the air admittance valve. Check that the fine valve is closed. Open the roughing valve. The chamber pumps down.
6. If the diffusion pump has warmed up and pirani reads $<3.5x10^{-1}$ Torr (this may take 2 hours), then close the roughing valve and open the fine valve. Open the baffle valve slowly. The pressure of the pirani will rise. Do not let the pump stall. Switch on the penning gauge (switch). Wait until the penning gauge falls to 10^{-5} Torr. It is best to leave it overnight. It is now ready to evaporate.
7. Switch on the current supply to LT. Turn up dial to 100mA for 2 minutes. Silver wire will aglow like the morning sun. Do not look direct onto the glowing silver, but use a dark goggle to check that all the silver has evaporated. It may need to readjust the dial to maintain the current and penning reading will rise. After evaporation has completed, turn the dial to zero and switch off the current supply.
8. Close the baffle valve and then the fine valve. Switch off the diffusion pump followed by the penning gauge. Open air admittance valve slowly. Remove the bell jar. Remove the device and store it in a dessicator.
9. Replace the bell jar and the safety screen. Close the air admittance valve. Then, open the roughing valve. The chamber will be pumped down to $3.5x10^{-1}$ Torr. Close the roughing valve. Switch off the penning gauge and the rotary pump (automatic valve releases). Switch off the mains and turn off the tap water. The diffusion pump and chamber have been left under vacuum. It is important not to let the diffusion pump up to atmospheric pressure, especially when it is hot. This may happen if the baffle valve or both the fine and roughing valves are opened whilst there is air in the chamber, or it the rotary pump is switched off when the fine valve is open.
10. The device with the silver patch should now be annealed to prevent the silver rubbing off.

APPENDIX 12

Program Listing of Far-field Radiation Pattern Measurements using HP Basic

```
10    ! This program controls the HP85107 Network Analyser
20    ! and the PDX15 Indexer for anaechoic chamber pattern measurements.
30    !=================================================
40    !
50    ! Initialise and open RS_232 interface.
60    CONTROL 9,4;IVAL("11000011",2)          !No parity. 8 data bits. 1 stop bit.
70    CONTROL 9,3;9600                        !Baud rate.
80    ASSIGN @Pdx to 9
90    !
100   ! Initialise and open HPIB.
110   REMOTE 7
120   ASSICN @Nwa TO 716
130   CLEAR @Nwa
140   !
150   ! Select turntable parameters.
180   OUTPUT @Pdx;"MN"                        !Mode normal.
190   OUTPUT @Pdx;"MPI"                       !Mode position incremental.
200   OUTPUT @Pdx;"A999"                      !Maximum acceleration.
210   OUTPUT @Pdx;"V2.0"                      !Velocity 1 revs/sec.
220   OUTPUT @Pdx;"MRD4000"                   !Motor resolution definition.
230   OUTPUT @Pdx;"ER4000"                    !Encoder resolution 4000 steps/rev.
240   OUTPUT @Pdx;"D360000"                   !Distance 324000 steps.
250   OUTPUT @Pdx;"GH"                        !Go home.
260   !
270   ! Select Network Analyser parameters.
280   OUTPUT @Nwa,"MENUOFF;"
290   OUTPUT @Nwa,"MARKOFF;"
300   OUTPUT @Nwa,"FRER;"                     !Select frequency domain.
310   INPUT "Enter frequency of operation (GHz): ",Frq$
320   String1$="STAR "&Frq$&" GHz;"
330   String2$="STOP "&Frq$&" GHz;"
340   OUTPUT @Nwa;String1$                    !Start frequency.
350   OUTPUT @Nwa,String2$                    !Stop frequency.
360   OUTPUT @Nwa,"CHAN1"                     !Select Channel 1.
370   OUTPUT @Nwa,"SWET 45S; POIN401; RAMP;"  !Dwel time and points.
380   OUTPUT @Nwa,"S12;LOGM"                  !Log magnitude polar format.
390   OUTPUT @Nwa,"AVERON 256; SMOOOFF"       !Average on. Smoothing off.
400   OUTPUT @Nwa,"REFV 0.0; REFP 10; SCAL 10.0;"      !Scaling.
410   OUTPUT @Nwa,"MARKMAXI;"                 !Marker at maximum.
420   !
430   ! Start far-field radiation pattern measurement.
```

```
431   OUTPUT 1;"Radiation pattern measurement in progress! Please wait."
440   OUTPUT @Nwa,"SING;"                    !S12 Single sweep.
441   OUTPUT @Pdx,"T1.0;"                    !Wait 1.0s
450   OUTPUT @Pdx,"G;"                       !Rotate turn-table.
460   OUTPUT @Pdx,"D-360000;"
461   WAIT 45                                !Wait 45secs for rotation to complete.
463   OUTPUT 1;"Turn-table is rotating back"
464   OUTPUT @Pdx,"G;"                       !Go back.
465   WAIT 45                                !Wait for rotation to end.
470   !
480   !End measurement.
490   OUTPUT 1;"Pattern measurement completed."      !Display message on screen.
491   !
500   !Start saving data.
501   OUTPUT 1;"Do you want to save the data?"
510   INPUT A$
511   IF A$<>"Y" THEN 574
514   OUTPUT @Nwa;"STOIINT"                  !Default drive for disk; internal.
515   OUTPUT @Nwa;"STOR"
525   OUTPUT @Nwa;"DATAFORM"                 !Formatted data in log magnitude.
537   OUTPUT @Nwa;"FORM4;OUTPFORM;"          !Ascii formatted data.
539   OUTPUT 1;"Enter name of file"          !Name file for data.
540   INPUT D$
547   OUTPUT @Nwa;"DISF"&$CHR$(34)&D$(34)
569   OUTPUT 1;"Data is stored into file"
572   WAIT 5                                 !Wait 5sec for data storage.
573   !
574   !Start plotting pattern data
575   OUTPUT 1;"Do you want to plot the data?"
576   INPUT A$
577   IF A$<>"Y" THEN 582
578   OUTPUT @Nwa;"PLOTALL"
579   WAIT 10                                !Wait 10sec for end of plotting.
580   !
582   !End of program
588   OUTPUT 1;"Program ended."
589   STOP
590   END
```

REFERENCES

1. C. A. Balanis, *Antenna Theory: Analysis and Design*, New York: Harper & Row, 1982.
2. R. C. Johnson and H. Jasik, Eds., *Antenna Engineering Handbook*, second edition, New York, London: McGraw, 1984.
3. J. D. Kraus, *Antennas*, New York: McGraw, 1988.
4. J. Rashed and C. T. Tai, "A New Class of Wire Antennas", IEEE Int Symp AP-Dig, pp. 564-67, 1982.
5. J. Rashed-Mohassel and C. T. Tai, "A Foreshortened Resonant Antenna", *Proc ISAE*, pp. 474-76, 1989.
6. J. Rashed and C. T. Tai, "A New Class of Resonant Antennas", *IEEE Trans. Antennas Propagat. (Commun.)*, vol. AP-39, no. 9, pp. 428-30, Sept. 1991.
7. J. Rashed-Mohassel, "The Radiation Characteristics of a Resonant Meander Line Section as a Monopole", M-OT Lett, pp. 537-40, 1991.
8. H. Nakano *et al.*, "Effects of Arm Bend and Asymmetric Feeding on Dipole Antennae", *Int. J. Electron.*, vol. 55, no. 3, pp. 353-64, 1983.
9. H. Nakano, "Shortening Ratios of Modified Dipole Antennas", *IEEE Trans. Antennas Propagat.*, vol. AP-32, no. 4, pp. 385-86, Apr. 1984.
10. H. A. Wheeler, "Fundamental Limitations of Small Antennas", *Proc. IRE*, vol. 35, pp. 1479-84, Dec. 1947.
11. L. J. Chu, "Physical Limitations of Omni-Directional Antennas", *J. Appl. Phys.*, vol. 19, pp. 1163-75, Dec. 1948.
12. R. F. Harrington, "On The Gain and Beamwidth of Directional Antennas", *IRE Trans. Antennas Propagat.*, vol. AP-6, pp. 219-25, July 1958.
13. R. F. Harrington, "Effect of Antenna Size on Gain, Bandwidth, and Efficiency", *J. Res. NBS*, vol. 64D, pp.1-12, Jan.-Feb. 1960.
14. G. Smith, "Efficiency of Electrically Small Antennas Combined with Matching Networks", *IEEE Trans. Antennas Propagat.*, vol. AP-25, no. 3 , pp. 369-73, May. 1977.
15. H. A. Wheeler, "The Radiansphere Around a Small Antenna", *Proc. IRE*, pp. 1325-31, Aug. 1959.
16. H. A. Wheeler, "Small Antennas", *IEEE Trans. Antennas Propagat.*, vol. AP-23, no. 4, pp. 462-69, July 1975.
17. J. S. McLean, "A Re-Examination of the Fundamental Limits on the Radiation Q of Electrically Small Antennas", *IEEE Trans. Antennas Propagat.*, vol. AP-44, no. 5, May 1996.

18. E. H. Newman, P. Bohley and C. H. Walter, "Two Methods for The Measurement of Antenna Efficiency", *IEEE Trans. Antennas Propagat.*, vol. AP-23, no. 4, pp. 457-61, July 1975.

19. T. H. Crowley, "Measurement of Antenna Efficiency by Using Metals with Different Surface Resistivities", Technical Report 478-21, Antenna Lab., Dept. of Electrical Engineering, The Ohio State University, Columbus, Nov. 1953.

20. T. L. Flaig, "Investigation of High Frequency Aircraft Antennas - The Impedance and Efficiency of Multiturn Loop Antennas", Technical Report No. 2235-3, ElectroScience Lab., Dept. of Electrical Engineering, The Ohio State University, Columbus, Apr. 1968.

21. G. Smith, "Radiation Efficiency of Electrically Small Multiturn Loop Antennas", *IEEE Trans. Antennas Propagat.*, vol. AP-20, pp. 656-57, Sept. 1972.

22. L. H. Hoang & M. Fournier, "Signal-to-noise Performance of Cryogenic Electrically Small Receiving Antennas", *IEEE Trans. Antennas Propagat.*, vol. AP-20, pp. 509-11, July 1972.

23. W. L. Weeks, *Antenna Engineering*, New York: McGraw, 1968.

24. G. Smith, "An Analysis of the Wheeler Method for Measuring the Radiating Efficiency of Antennas", *IEEE Trans. Antennas Propagat.*, vol. AP-25, no. 4, pp. 552-56, July 1977.

25. R. C. Hansen, "Fundamental Limitations in Antennas", *Proc. IEEE*, vol. 69, no. 2, pp. 170-82, Feb. 1981.

26. Y. T. Lo, S. W. Lee and Q. H. Lee, "Optimization of Directivity and Signal-to-Noise Ratio of an Arbitrary Antenna Array", *Proc. IEEE*, vol. 54, no. 8, pp. 1033-45, Aug. 1966.

27. E. N. Gilbert and S. P. Morgan, "Optimum Design of Directive Antenna Arrays Subject to Random Variations", *Bell Syst. Tech. J.*, vol. 34, pp. 637-63, May 1955.

28. H. A. Wheeler, "The Wide-Band Matching Area for a Small Antenna", *IEEE Trans. Antennas Propagat.*, vol. AP-31, no. 2, pp. 364-67, Mar. 1983.

29. K. Hikada, "Small Loop Antenna Capable of Changing Matching-frequency over a Wideband", IEEE Int Symp AP-Dig, pp. 556-58, 1982.

30. E. A. Parker and A. N. A. El-Sheikh, "Convoluted Dipole Array Elements", *Electron. Lett.*, vol. 27, no. 4, pp. 322-23, Feb. 1991.

31. G. B. Walker and C. R. Haden, "Superconducting Antennas", *J. Appl. Phys.*, vol. 40, no. 5, pp. 2035-39, 1969.

32. G. B. Walker, C. R. Haden and O. G. Ramer, "Superconducting Superdirectional Antenna Arrays", *IEEE Trans. Antennas Propagat.*, vol. AP-26, no. 6, pp. 885-87, Nov. 1977.

33. R. C. Hansen, Comments on "Superconducting Superdirectional Antenna Arrays", *IEEE Trans. Antennas Propagat.*, vol. AP-25, no. 6, pp. 891, Nov. 1978.

34. IEEE Standard Definitions of Terms for Antennas (IEEE Std 145-1973), *IEEE Trans. Antennas Propagat.*, vol. AP-17, no. 3, May 1969 and vol. AP-22, no. 1, Jan. 1974.

35. B. C. Wadell, *Transmission Line Design Handbook*, Artech, 1991.

36. V. F. Fusco, *Microwave Circuits Analysis and Computer Aided Design*, Englewood Cliffs, New Jersey: Prentice-Hall, 1987.

37. K. Itoh *et al.*, "High-Tc Superconducting Small Antennas", *IEEE Trans. Appl. Superconduct.*, vol. 3, no. 1, pp. 2836-39, Mar. 1993.

38. R. Alm and R. J. Hwu, "Determination of ε_{eff} for Printed Structures on Electrically Thin Substrates", *Microwave J.*, pp. 116-22, Sept. 1994.

39. T. P. Orlando and K. A. Delin, *Foundations of Applied Superconductivity*, Reading, Massachusetts: Addison-Wesley, 1990.

40. R. C. Hansen, "Antenna Applications of Superconductors", *IEEE Trans. Antennas Propagat.*, vol. AP-36, no. 6, pp. 1508-12, Sept. 1991.

41. J. T. Williams and S. A. Long, "High Temperature Superconductors and Their Application in Passive Antenna Systems", *IEEE Antennas Propagat. Mag.*, pp. 7-18, Aug. 1990.

42. H. K. Onnes, "The resistance of pure mercury at helium temperatures", *Leiden Comm.*, 120b, pp. 3, 1911.

43. W. Meissner and R. Ochsenfeld, *Naturwissenschaften*, vol. 21, pp. 987-988, 1933.

44. B. D. Josephson, "Probable new effects in superconductive tunneling", *Phys. Lett.*, vol. 1, pp. 251-253, 1962.

45. J. G. Bednorz and K. A. Müller, "Possible high T_c superconductivity in the Ba-La-Cu-O system", *Z. fur Phys.*, vol. 64, pp. 189, 1986.

46. M. K. Wu, J. R. Ashburn, C. J. Torng, R. L. Meng, L. Gao, Z. J. Huang, Y. Q. Wang, C. W. Chu, "Superconductivity at 93K in a new mixed-phase Y-Ba-Cu-O compound system at ambient pressure", *Phys. Rev. Lett.*, vol. 58, pp. 908-910, 1987.

47. W. G. Lyons and R. S. Withers, "Passive Microwave Devices Applications of High Temperature Superconducting Thin Films", *Microwave J.*, pp. 85-102, Nov. 1990.

48. Z-Y. Shen, *High-Temperature Superconducting Microwave Circuits*, Boston, London: Artech, 1994.

49. A. Schilling, M. Cantoni, G. D. Guo, and H. R. Ott, "Superconductivity above 130K in the Hg-Ba-Ca-Cu-O System", *Nature*, vol. 363, pp. 56-58, 1993.

50. M. J. Lancaster, *Passive Microwave Device Applications of High Temperature Superconductors*, to be published by Oxford University Press, England, 1996.

51. T. van Duzer, T., and C. W. Turner, *Principles of Superconductive Devices and Circuits*, New York: Elsevier, 1981.

52. A. Porch, M. J. Lancaster, R. G. Humphreys and N. G. Chew, "Surface Impedance Measurements of $YBa_2Cu_3O_{7-x}$ Thin Films Using Coplanar Resonators", *IEEE Trans. Appl. Superconduct.*, vol. 3, no. 1, pp. 1719-22, Mar. 1993.

53. N. McN. Alford, T. W. Button, G. E. Peterson, P. A. Smith, L.E. Davis, S. J. Penn. M. J. Lancaster and Z. Wu, "Surface resistance of bulk and thick film $YBa_2Cu_3O_{7-x}$", *IEEE Trans. Magnet.*, vol. 27, no. 2, pp. 1510-18, Mar. 1991.

54. N. Klein, G. Müller, H. Piel, B. Roas, L. Schultz, U. Klein and M. Peiniger, "Millimetre Wave Surface Resistance of Epitaxially Grown $YBa_2Cu_3O_{7-x}$ Thin Films", *Appl. Phys. Lett.*, vol. 54, no. 8, pp. 757-59, 1989.

55. Z. Wu, *et al.*, "Thick Film Printed High-T_c Superconducting Small Loop Antenna", *IEE Coll. on Electrically Small Antennas*, paper 10, Oct. 1990.

56. L. P. Ivrissimtzis, M. J. Lancaster and T. S. M. Maclean, "On the Design and Performance of Electrically Small Printed Thick Film $YBa_2Cu_3O_{7-x}$ Antennas", *IEEE Trans. Appl. Superconduct.*, vol. 4, no. 1, pp. 33-40, Mar. 1994.

57. Z. Wu and L. E. Davis, "Surface Roughness Effect on Surface Impedance of Superconductors", *J. of Appl. Phys.*, vol. 76, no. 6, pp. 3369-72, 1995.

58. R. C. Hansen, "Superconducting Antennas", *IEEE Trans. Aerosp. Electron. Systems*, vol. AES-26, no. 2, pp. 345-55, Mar. 1990.

59. R. J. Dinger and D. J. White, "Theoretical Increase in Radiation Efficiency of a Small Dipole Antenna Made with a High Temperature Superconductor", *IEEE Trans. Antennas Propagat.*, vol. AP-38, no. 8, pp. 1313-16, Aug. 1990.

60. R. J. Dinger and D. J. White, "The Radiation Efficiency of a Small Dipole Antenna Made from High Temperature Superconductor", *IEEE AP-S Dig.*, pp. 724-27, 1990.

61. R. J. Dinger *et al.*, "Radiation Efficiency Measurements of a Thin-Film Y-Ba-Cu-O Superconducting Half-Loop Antenna at 500MHz", *1991 IEEE MTT-S Digest*, pp. 1243-46.

62. R. J. Dinger, D. R. Bowling and A. M. Martin, "A Survey of Possible Passive Antenna Applications of High Temperature Superconductors", *IEEE Trans. Microwave Theory Tech.*, vol. 39, no. 9, pp. 1498-509, Sept. 1991.

63. H. Chaloupka, "High-temperature Superconductors - A Material for Miniaturized of High-Performance Microwave Components", *Frequenz*, vol. 44, no. 5, pp. 141-44, 1990.

64. H. Chaloupka *et al.*, "Miniaturized High Temperature Superconducting Microstrip Patch Antenna", *IEEE Trans. Microwave Theory Tech.*, vol. 39, no. 9, pp. 1513-21, Sept. 1991.

65. V. Palanisamy and R. Garg, "Rectangular Ring and H-Shaped Microstrip Antennas - Alternatives to Rectangular Patch Antenna", *Electron. Lett.*, vol. 21, no. 19, pp.874-76, 1985.

66. A. Pischke *et al.*, "Electrically Small Planar HTS Antennas", *Third Int. Superconductive Electronics Conf.*, Glasgow, Scotland, pp. 340-43, 25-27 June 1991.

67. H. Chaloupka and G. Müller, "Applications of HTSC Thin Films with Low Microwave Losses to Linear Devices", *Physica C*, 180, pp. 259-66, 1991.

68. H. Chaloupka *et al.*, "High-Temperature Superconductor Meander Antenna", *1992 IEEE MTT-S Digest*, pp. 189-92.

69. N. Suzuki *et al.*, "Superconductive Small Antennas Made of EuBaCuO Thin-Films", *Advances in Superconductivity V*, pp. 1127-30, Tokyo: Springer-Verlag, 1993.

70. N. Suzuki *et al.*, "Electromagnetically Coupled Superconductive Thin-Film Small Antennas", *Physica B*, vol. 194/196, NCOM, pp. 129-30, 1994.

71. N. Suzuki *et al.*, "Superconductive Small Antennas with Thin-Film Matching Circuits", *IEICE Trans. Electron*, vol. E75-C, no. 8, pp. 906-10, Aug. 1992.

72. S. K. Khamas *et al.*, "High T_c Superconducting Short Dipole Antenna", *Electron. Lett.*, vol. 24, pp.460-61, 1988.

73. C. E. Gough *et al.*, "Critical Currents in a High- T_c Superconducting Short Dipole Antenna", *IEEE Trans. Magnet.*, 25, pp. 1313-14, 1989.

74. Z. Wu *et al.*, "High-T_c Superconducting Small Loop Antenna", *Physica C*, vol. 162-64, pp. 385-86, 1989.

75. Z. Wu *et al.*, "Supercooled and Superconducting Small Loop Antenna", *IEE Coll. on Microwave Applications of High Temperature Superconductors*, pp. 8/1-/3, Oct. 1989.

76. M. Lancaster *et al.*, "Superconducting Antennas", *Supercond. Sci. Technol.*, vol. 5, pp. 277-79, 1992.

77. M. J. Lancaster *et al.*, "Supercooled and Superconducting Small-loop and Dipole Antennas", *IEE Proc.-H*, vol. 139, no. 3, pp. 264-70, June 1992.

78. M. J. Lancaster *et al.*, "YBCO Thick Film Loop Antenna and Matching Network", 1992 IEEE Applied Superconductivity Conference, *Proc. Appl. Superconduc. Conf.*, Chicago, IL., Aug. 1993.

79. L. P. Ivrissimtzis, M. J. Lancaster and M. Esa, "Miniature Superconducting Coplanar Strip Antennas for Microwave and Mm-Wave Applications", *1995 9th IEE ICAP Conf. Publ.*, vol.1, no. 407, pp. 391-95.

80. M. Esa and M. J. Lancaster, "Electrically Small High-Temperature Superconducting Symmetrical Meander Dipole Antenna", Paper presented at Applied Superconductivity, Edinburgh, 3-6 July 1995, *Ins. Phys. Conf. Ser.*, vol. 2, pp 1191-94, 1995.

81. M. Esa and M. J. Lancaster, "Miniature Superconducting Printed Antennas for Space-Limited Applications", submitted to *Electron. Lett.*, July 1996.

82. G. Drossos, Z. Wu and L. E. Davis, "Miniaturized Microstrip Superconducting Antennas Operating at UHF", Paper presented at Applied Superconductivity, Edinburgh, 3-6 July 1995, *Ins. Phys. Conf. Ser.*, vol. 2, pp 1143-46, 1995.

83. D. Lacey, *et al.*, "Miniaturised HTS Microstrip Patch Antenna with Enhanced Capacitive Loading", Paper presented at *IEE Coll. on Superconducting Microwave Circuits* (Ref: 96/094, pp.4/1-4/6), Savoy Place, London, 19 Apr. 1996.

84. L. P. Ivrissimtzis, M. J. Lancaster and N. McN. Alford, "Supergain Printed Arrays of Closely Spaced Dipoles made of Thick Film High-T_c Superconductors", *IEE Proc.-Microw. Antennas Propag.*, vol. 142, no. 1, pp. 264-70, 1995.

85. K. Fujimoto *et al.*, Small Antennas, England : Research Studies Press, 1987.

86. K. Hirasawa and M. Haneishi, Eds., *Analysis, Design, and Measurement of Small and Low-Profile Antennas*, Boston, London: Artech, 1992.

87. S. Khamas *et al.*, "Significance of Matching Networks in Enhanced Performance of Small Antennas When Supercooled", *Electron. Lett.*, vol. 26, no. 10, pp. 654-55, May 1990.

88. L. P. Ivrissimtzis *et al.*, "High-Gain Series Fed Printed Dipole Arrays Made of High-T_c Superconductors", *IEEE Trans. Antennas Propagat.*, vol. AP-42, no. 10, pp. 1419-29, Oct. 1994.

89. D. M. Pozar and B. Kaufman, "Comparison of Three Methods for the Measurement of Printed Antenna Efficiency", *IEEE Trans. Antennas Propagat.*, vol. AP-36, no. 1, pp. 136-39, Jan. 1988.

90. T. Laverghetta, *Microwave Materials and Fabrication Techniques*, second edition, Boston, London: Artech, 1991.

91. User's Manual, vers. 3.0, Sonnet Software Inc., Liverpool, New York, 1995.

92. P. A. Smith and L. E. Davis, "Dielectric Loss Tangent of Yttria Stabilized Zirconia at 5.6 GHz and 77 K", *Electron. Lett.*, vol. 28, no. 4, pp. 424-25, Feb. 1992.

93. T. W. Button, IRC in Materials for High Performance Applications, University of Birmingham, B15 2TT, *private communications*.

94. T. W. Button, N. McM. Alford and P. Smith, "Melt-processed $YBa_2Cu_3O_7$ thick films", *Proceedings of Eighth Cimtec World Ceramics Congress, Forum on New Materials*, Florence, Italy, 29 June - 4 July 1994, paper SIV - 6.2:L02.

95. T. W. Button, *et al.*, "The Processing and Properties of High T_c Thick Films", *IEEE Trans. Magnet.*, vol. 27, no. 2, pp. 1434-37, Mar. 1991.

96. P. Woodall, University of Birmingham Interdisciplinary Laser Ablation Lab., *private communications*.

97. J. Brannon, "Excimer Laser Ablation and Etching of Materials", Short Course organised by Materials Research Society, IBM Almaden Research Center, USA, 1992.

98. *Pulsed Laser Deposition*, MRS Bulletin, vol. XVII, no. 2, Feb. 1992.

99. HP8510C Network Analyser System Manuals, June 1991.

100. HP9000 Series 200/300 Basic 5.0/5.1 Computer Manuals, 1987.